A DETAILED ANALYSIS OF THE IMPERFECTIONS OF PULSEWIDTH MODULATED WAVEFORMS ON THE OUTPUT STAGE OF A CLASS D AUDIO AMPLIFIER

Francois Koeslag

Dissertation presented in partial fulfilment of the requirements for the degree of Doctor of Philosophy in Engineering at the University of Stellenbosch

Supervisor: Prof. H. du T. Mouton

Co-supervisor: Dr. H.J. Beukes

December 2008

DECLARATION

By submitting this dissertation electronically, I declare that the entirety of the work contained therein is my own, original work, that I am the owner of the copyright thereof (unless to the extent explicitly otherwise stated) and that I have not previously in its entirety or in part submitted it for obtaining any qualification.

SUMMARY

Although the Class D topology offers several advantages, its use in audio amplification has previously been limited by the lack of competitiveness in fidelity compared to its linear counterparts. During the past decade, technological advances in semiconductor technology have awakened new interest since competitive levels of distortion could now be achieved. The output stage of such an amplifier is the primary limiting factor in its performance. In this dissertation, four non-ideal effects existing in this stage are identified and mathematically analysed. The analytical analysis makes use of a well-established mathematical model, based on the double Fourier series method, to model the imperfections introduced into a naturally sampled pulsewidth modulated waveform. The analysis is complemented by simulation using a strategy based on Newton's numerical method. The theory is verified by a comparison between the analytical-, simulated- and experimental results.

OPSOMMING

Die klas D topologie bied verskeie voordele, maar die toepassing daarvan in oudio versterkers was beperk tot op hede as gevolg van onvergelykbare vlakke van distorsie in vergelyking met analoog versterkers. Tegnologiese vooruitgang in halfgeleier tegnologie oor die laaste dekade het tot nuwe belangstelling gelei in die toepassing van die klas D topologie in oudio versterkers, siende dat kompeterende vlakke van distorsie nou haalbaar was. Die uittreestadium van hierdie versterkers is die beperkende faktor in distorsie. Hierdie proefskrif identifiseer en analiseer vier nie-ideale effekte wiskundig. Daar word gebruik gemaak van 'n wel bekende metode, gebaseer op die dubbele Fourier reeksuitbreiding, om die nie-idealiteite in 'n natuurlik gemonsterde pulswydte gemoduleerde golfvorm te modelleer. Die analise word aangevul deur simulasies gebaseer op 'n strategie wat gebruik maak van Newton se numeriese metode. Die teorie word geverifieer deur 'n vergelyking tussen die analitiese-, simulasie- en eksperimentele resultate.

ACKNOWLEDGEMENTS

TABLE OF CONTENTS

SUMMARY OF PAPERS PRESENTED

Conference Papers

F. Koeslag, H. du T. Mouton, H.J. Beukes and P. Midya, "*A Detailed Analysis of the Effect of Dead Time on Harmonic Distortion in a Class D Audio Amplifier*", Africon 2007, Windhoek, Namibia, 26-28 October 2007.

F. Koeslag, H. du T. Mouton and H.J. Beukes, "*The Isolated Effect of Finite Non-Linear Switching Transitions on Harmonic Distortion in a Class D Audio Amplifier*", 17th South African Universities Power Engineering Conference (SAUPEC), Durban, South Africa, January 2008.

F. Koeslag, H. du Toit Mouton, H.J. Beukes, "*An Investigation into the Separate and Combined Effect of Pulse Timing Errors on Harmonic Distortion in a Class D Audio Amplifier*", 39th Annual IEEE Power Electronics Specialists Conference (PESC), Rhodes, Greece, June 2008.

Journal Papers

F. Koeslag, H. du Toit Mouton, H.J. Beukes, "*Analytical Calculation of the Output Harmonics in a Power Electronic Inverter with Current Dependent Pulse Timing Errors*", Submitted to Journal.

LIST OF FIGURES

- xiv -

LIST OF TABLES

LIST OF ACRONYMS

2-D	Two Dimentional
3-D	Three Dimentional
DC	Direct Current
LEPWM	Double Edge Pulsewidth Modulation (Uniform or Natural)
DEUPWM	Double Edge Uniformly Sampled Pulsewidth Modulation
FPGA	Field Programmable Grid Array
HF	High Frequency
LEPWM	Leading Edge Pulsewidth Modulation (Uniform or Natural)
LEUPWM	Leading Edge Uniformly Sampled Pulsewidth Modulation
MOSFET	Metal Oxide Semiconductor Field Effect Transistor
MOSFETs	Metal Oxide Semiconductor Field Effect Transistors
NPWM	Naturally Sampled Pulsewidth Modulation
PAE	Pulse Amplitude Error
PAEs	Pulse Amplitude Errors
PCM	Pulse Code Modulation
PDM	Pulse Duration Modulation
PNPWM	Pseudo Naturally Sampled Pulsewidth Modulation
PTE	Pulse Timing Error
PTEs	Pulse Timing Errors
PWM	Pulsewidth Modulation
TEPWM	Trailing Edge Pulsewidth Modulation (Uniform or Natural)
TENPWM	Trailing Edge Natuarally Sampled Pulsewidth Modulation
TEUPWM	Trailing Edge Uniformly Sampled Pulsewidth Modulation
UPWM	Uniformly Sampled Pulsewidth Modulation
THD	Total Harmonic Distortion

GLOSSARY

BV_{DSS}	breakdown voltage
C_{filt}	demodulation filter capacitor
C_{GD}	gate-to-drain capacitance
C_{GS}	gate-to-source capacitance
C_{iss}	input capacitance
D	duty cycle
D_{A1}	diode of high side switch of phase leg A
D_{B1}	diode of high side switch of phase leg B
D_{A2}	diode of low side switch of phase leg A
D_{B2}	diode of low side switch of phase leg B
f_0	reference frequency
f_c	carrier/switching frequency
g_m	transconductance
i_A	inductor current flowing in phase leg A
i_B	inductor current flowing in phase leg B
Δi_L	inductor current ripple component
i_L	inductor current
I_L	inductor current (scalar)
i_D	drain current
I_D	drain current (scalar)
i_o	output load current
I_o	output load current (scalar)
L_{filt}	demodulation filter inductor
M	modulation index
$r_{DS(on)}$	on-state resistance
R_G	gate resistance
R_{load}	load resistance
T_{A1}	high side switch of phase leg A
T_{B1}	high side switch of phase leg B
T_{A2}	low side switch of phase leg A

T_{B2}	low side switch of phase leg B
t_{dt}	dead time
$t_{d(vr)}$	turn-*on* delay (rising voltage)
$t_{d(vf)}$	turn-*off* delay (falling voltage)
t_{vf}	voltage fall time
t_{vr}	voltage rise time
T_c	switching period
V_d	DC bus voltage
v_{DS}	drain-to-source voltage
v_o	output load voltage
V_{DF}	diode forward voltage
v_{GS}	gate-to-source voltage
V_{GS}	gate-to-source voltage (scalar)
$V_{GS(th)}$	gate-to-source threshold voltage
ω_0	angular modulating frequency (rad/s)
ω_c	angular switching frequency (rad/s)
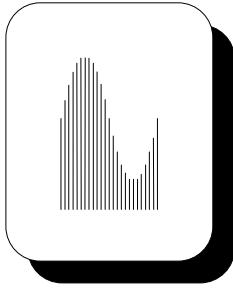
1
LITERATURE

1.1   INTRODUCTION

The Class D mode of operation was originally introduced in 1959 by Baxandall for the potential application in oscillator circuits [1]. Since then it has found several widespread applications in power electronics. More recently, audio amplifiers implementing this topology have emerged on a large scale. Although the Class D topology offers several advantages, its use has previously been limited by the lack of competitiveness in fidelity compared to its linear counterparts. Until recently, this drawback has been the result of limitations in semiconductor technology [2]. Due to technological advances in this field during the past decade, however, new interest has been awakened in the application of this topology in audio amplification, since competitive levels of distortion could now be achieved [2].

Two primary motivations currently drive the research in this field of which efficiency can be regarded as the first and most important [3]. This increased efficiency over conventional analogue amplifiers has the effect of decreasing supply requirements. Moreover, the lower power loss is also decreasing or even eliminating the use of heatsinks. The resultant higher levels of efficiency translate into smaller, lower cost designs. The second motivation is that audio is increasingly derived from digital sources. This is an advantage since the output stage can be driven directly from a digital signal after pulse code modulation (PCM) to pulsewidth modulation (PWM) conversion, creating a purely digital audio amplifier without the need for any digital-to-analogue conversion [4].

1.2   BASIC CONCEPT AND DEVELOPMENT

Class D stages operate in switched mode, which means that the power transistors in the output stage are either fully *on* or fully *off*. Since only two possible states exist, such an output stage relies on the amplification of some binary intermediate signal.

The audio signal thus needs to be modulated in and out of this intermediate signal. PWM is currently the most popular form of this binary signal used in Class D audio amplifiers [5]. Early research in this field was based on this method in combination with Class D power stages to accomplish the amplification [6], [7]. Several modulation methods currently exist for creating PWM, of which the earliest and most basic is called natural sampling. This method utilizes the normal form of analogue signals directly. The analogue audio input is compared to a reference waveform (modulated) whose frequency is multiples higher than that of the audio bandwidth in order to represent the input signal accurately. The resulting switching output is then fed to the power stage, which performs the necessary amplification. The amplified audio signal is then recovered (demodulated) once the output waveform has been passed through a low-pass filter. Alternatively, when digital signals are available, the conventional method is first to convert to analogue and then to proceed with the above mentioned modulation process.

Since audio is increasingly derived from digital sources, the logical next step was to generate the PWM directly from digital code. Early publications on this subject proposed system architectures running at high modulator speeds of tens of GHz [6]. Such systems were clearly impractical due to the limitations posed by the power stage. The digital counter frequency was brought down to several tens of MHz by the introduction of noise shaping techniques, but performance was still limited due to distortions introduced by the modulation process [5]. This problem was addressed by the introduction of a technique called the enhanced concept of power digital-to-analogue conversion [8]. This method relies on pre-processing of the input signal in order to compensate for the distortion introduced by the modulation process. Results from simulations on this subject were published as early as 1990 [9]. The next major advance in this field was the implementation of sigma-delta modulation. However, early research again identified the problem of high pulse frequencies which were degrading audio performance during amplification in the power stage [8]. This problem was addressed by reducing the pulse frequency with a technique called 'bit flipping'. A complete design and implementation of this architecture can be found in [10].

1.3   SYSTEM IMPERFECTIONS

It is well known that PWM introduces harmonic distortion. Early research based on the double Fourier series revealed this fact [11]. The analysis in [11] confirms that the output spectrum captures the input spectrum, but signal dependant harmonics proportional to ordinary Bessel functions are created at multiples of the switching frequency, accompanied by their respective sidebands. These sidebands appear in the audio band if the carrier frequency is not high enough, which results in distortion. However, by selecting a high carrier to fundamental ratio these harmonics can be minimized to negligible values. A switching frequency of more than ten times the modulating frequency results in harmonic levels below −144 dB [12].

From the previous section it is evident that early research paid special attention to the digital implementation of the conversion process to PWM. Several schemes were introduced to minimize and overcome the limitations posed by the uniformly sampled PWM (UPWM) modulation process. Such an example is the 'cross-point detector' found in the enhanced concept of power digital-to-analogue conversion. The original analogue waveform is represented by the uniform samples of the digital signal. However, from the spectral analysis it is evident that uniform sampling introduces distortion within the baseband [1], [13]. The linearizer improves (i.e. reduces) this distortion by approximating natural sampling using a technique called pseudo naturally sampled PWM (PNPWM). This is done by estimating the crossing point of the modulating and reference waveform through interpolation of additional data points using numerical methods. An analogue PWM process is also prone to distortion. This can either be a result of noise appearing in the modulating signal or of non-ideal effects associated with the reference waveform. Carrier non-linearity leads to timing errors within the sampling process. Previous work has shown that minor deviations in carrier linearity influence distortion significantly [14].

It is evident that natural sampling provides a basis for achieving low distortion. This suggests that the power stage is the primary limiting factor in the performance of Class D audio amplifiers [12]. Several imperfections in the output stage contribute to distortion. These non-ideal effects can be categorized into two main groups [15], i.e. pulse-timing errors (PTEs) and pulse-amplitude errors (PAEs). The former group is a result of three sources of which the first is distortion due to power supply imperfections. The output voltage of a Class D audio

amplifier is directly proportional to the supply voltage. Any voltage fluctuations caused as a result of current drawn by the amplifier introduce an error in the output [16]. The second pulse amplitude error (PAE) results from the non-linear switch impedance. Finally, the ringing effect caused by the resonant action between the parasitic inductance and capacitance also leads to amplitude errors. PTEs exist as a result of the non-ideal switching characteristics of the power devices. These errors can be sub-divided into two groups, i.e. errors occurring as a primary or secondary consequence of the non-ideal switching behaviour. Typical PTEs resulting from the primary consequence, assuming a power metal oxide semiconductor field effect transistor (MOSFET) as switching device, include the non-zero turn-*on* and turn-*off* delays, as well as the non-zero, non-linear turn-*on* and turn-*off* switching transitions. The well-known pulse timing error (PTE) resulting from dead time can be classified as a secondary consequence of the switching behaviour. The scope of this dissertation as well as general assumptions are considered in the following section.

1.4   CIRCUIT DEFINITIONS, SCOPE AND GENERAL ASSUMPTIONS

In this dissertation an investigation is launched into the parameters affecting total harmonic distortion (THD) in the output stages of Class D switching audio amplifiers. A general system representation, discussed below, is shown in Figure 1.1.
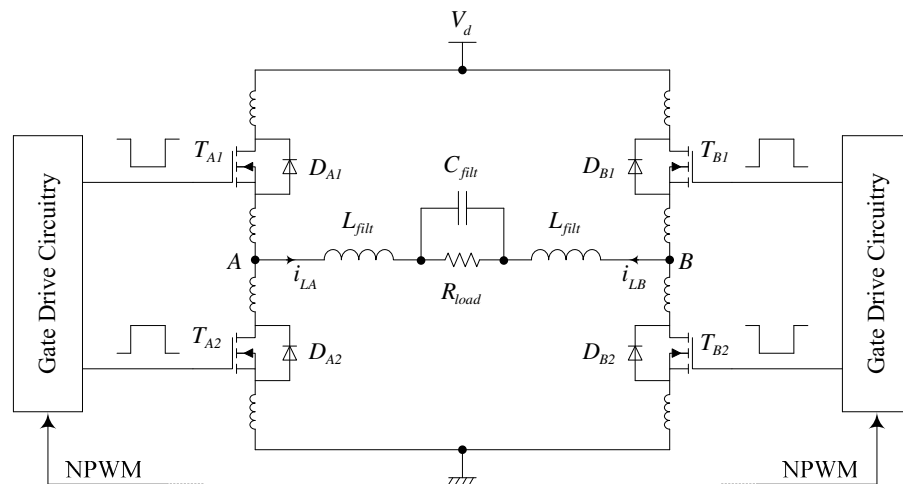
Figure 1.1: Basic circuit parameters and definitions.

The focus of this investigation is limited to a discrete, open loop system. The waveform generated by the digital source is assumed to be a result of a perfect, single-sided, two-level PNPWM process, effectively reproducing NPWM. The output stage topology is assumed to be either a half-bridge or full-bridge configuration with the current flow in each phase leg (denoted *A* and *B*) defined in Figure 1.1. The gate drivers are assumed to be ideal, i.e. they switch in zero time with no propagation delay existing between the gating signals supplied to the upper and lower metal oxide semiconductor field effect transistors (MOSFETs) of each phase. The MOSFETs are considered perfectly matched. The imperfections associated with the power supply and the filter are neglected. The basic definitions of the circuit parameters defined in Figure 1.1 remain unchanged for the rest of this dissertation.

1.5   EXISTING LITERATURE AND CONTRIBUTIONS

A detailed study of existing literature falling within the scope of each aspect investigated in this dissertation will now be considered. This includes a general overview on each subject involved herein, after which a more focussed review of highly relevant reports is presented. Each sub-section concludes with the list of contributions made by this dissertation.

1.5.1   ANALYTICAL DETERMINATION OF THE SPECTRUM OF NPWM

Pulsewidth modulation is a non-linear process which results in a non-periodic pulse train. This means that one-dimentional Fourier analysis cannot be applied. This complicates the analytical determination of the spectrum significantly. W.R. Bennet [11] and H.S. Black [17] introduced a method for determining the modulation products analytically by representing the pulse train as a three-dimensional (3-D) unit area. The analysis was originally proposed for use in communication systems, and expanded to power converter systems by S.R. Bowes [18] and B. Bird [19]. A further study by D.G. Holmes [20] involved the derivation of an expression for uniform and natural sampling where the reference waveform is sinusoidal, requiring only one Bessel function multiplication for each harmonic. An alternative method for determining the spectrum of PWM analytically has been introduced by Z. Song and D.V. Sarwate [21].

The spectrum of PWM can also be found by applying the fast Fourier transform (FFT) to a simulated time-varying switched waveform (such as PSpice). This approach has both advantages and disadvantages. One major advantage is the reduction in mathematical effort compared to analytical computation. The downside is that the time resolution of the simulation has to be very high in order to produce accurate crossing points between the modulating and carrier waveforms. This in turn requires significant computing power, which is very time-consuming. In contrast, the analytical solutions exactly identify the frequency components created by the modulation process. Moreover, the harmonic composition of the waveform is also shown, i.e. the individual contributions of the fundamental low frequency component, baseband harmonics, carrier harmonics as well as sideband harmonics to the spectrum. This information cannot be supplied via simulation.

Relevant Literature

The analytical analysis presented in [22] employs W.R. Bennet's [11] method to establish the harmonic composition of PWM in the presence of a non-zero dead time. The analysis shows how the 3-D unit area can be modified to accommodate this delay. A publication, "*Analytical Calculation of the Output Harmonics in a Power Electronic Inverter with Current Dependent Pulse Timing Errors*", by the author [23] addresses the limitations posed by the current model in [22].

Limitations posed by existing Literature

The investigation in [22] effectively demonstrates the modifications necessary to incorporate constant time delays within the 3-D unit area. However, the proposed model cannot be applied directly to the analysis in this dissertation since the inductor current model in [22] is very limited. Furthermore, as will be discussed later in this section, the majority of PAEs and PTEs are dependent on the current magnitude which results in varying delays. The model in [22] only includes a constant time delay. As mentioned, W.R. Bennet's [11] method has two advantages over the simulation of a time-varying waveform, i.e. the exact magnitudes of the harmonic components can be determined rapidly from the coefficients, and secondly, the harmonic composition of the spectrum can be determined. With the inclusion of non-ideal

effects the analytical integration becomes tedious, which is apparent from the solutions in [22]. As will be shown in Chapter 3, no closed form solution describing the Fourier coefficients can be obtained with the inclusion of a more realistic inductor current model within the 3-D unit area, and should be solved numerically. The first advantage of using this method is thus slightly more complex in the presence of non-ideal effects than for the ideal case. Moreover, as shown in [22], dead time dependent modulation products are created, which mean that the sideband harmonics extending within the audible band might not decay as rapidly as for the ideal case. Since the THD is calculated from the harmonic magnitudes up to a certain frequency (typically 20kHz for audio), each harmonic component should be added individually within this band. This restriction holds for all analytical methods of calculating the spectrum of PWM.

This limitation is overcome by simulation. However, as mentioned, a very accurate crossing point between the natural intersection of the reference and carrier waveforms is required. This is especially true in audio applications where the non-linearities are very subtle. To conclude, both the analytical calculation and the simulation are useful. Whereas the analytical solution gains insight into the harmonic composition, the simulation (if fast and accurate) is more useful in practice.

Contributions in this Dissertation

The analytical analysis for the incorporation of the constant time delay reported in [22] is generalised, after which it is extended to include non-linear current dependent delays with a more realistic inductor current model. A fast, accurate simulation method is introduced, which allows for rapid calculation of the spectrum of PWM with the inclusion of the non-linearities.

1.5.2   DEAD TIME

Dead time, often referred to in the literature as blanking time [24], can be regarded as the most dominant source of distortion in inverters with switching frequencies greater than 150kHz [25]. Since practical switching devices have non-zero turn-*on* and turn-*off* times, an immediate transition in a phase leg results in the flow of a cross-conduction current between the voltage rails. In order to avoid this shoot-through condition, a turn-*on* delay is introduced

at each *on* to *off* transition of the switching devices to prevent simultaneous conduction. This delay is referred to as dead time. Dead time has been an active topic of research within power electronics for many years. Various analytical approaches for the modelling of its effect for different sampling methods have been published to date, notably [22] and [26]. Literature on its effect within switching audio amplification is also well established [15], [25]. Another publication [27] introduces a method in which the dead time is effectively reduced to zero.

Relevant Literature

The analysis in [25] models the dead time within the time domain by varying the input duty cycle and measuring the corresponding output duty cycle. The Fourier transform of the duty cycle error is determined next; from this the harmonic distortion can be calculated. The dead band referred to in [25] is a consequence of a change in current polarity during the dead time. The average duty cycle remains more or less constant in this region, which leaves the output voltage floating. The constant variable *k* (expressed as a percentage of the duty cycle above 50%) describes the level at which the dead band exists.

As a starting point, the initial theory reported in [15] calculates the Fourier transform of the square wave resulting from the average error introduced over a single switching cycle, i.e. for a purely sinusoidal inductor current. The analysis is then extended in which an inductor current model with a non-zero ripple component, expressed as a scaled ratio of the peak output and ripple current, is considered. The initial expression obtained for a purely sinusoidal inductor current is adapted to accommodate the additional constraint.

The analytical analysis presented in [22] utilises the double Fourier series to calculate the harmonic components of naturally sampled PWM (NPWM) with dead time. The analysis is performed for an inductor current which is either purely sinusoidal, or it has a ripple component that satisfies the constraint of only changing polarity once over one half-cycle of the modulating waveform.

Limitations posed by existing Literature

The first complication regarding the direct application of the analysis in [25] within an open loop system is that, in order to achieve acceptable levels of distortion, practical values of

dead time need to be orders of magnitude smaller. This means that the inductor current rarely changes polarity during the dead time, effectively eliminating the dead band. The constraint is met by setting time $t_2=t_1$ in [25]. Secondly, k is directly correlated to the inductor current ripple. This suggests that, for any given circuit, a measurement first needs to be performed in order to establish the value of k before the distortion can be calculated. If it is assumed that $t_2=t_1$, the analysis in [15] corresponds to that proposed in [25] with the indirect relation to the filter inductor expressed in terms of peak current. The shortcoming of both the above mentioned models is that the analysis is performed in the time domain, i.e. by varying the switching frequency while keeping the remaining parameters constant, the distortion will not necessarily remain unaffected. This dependence of the cross modulation products on dead time was noted in [22]. The analytical method considered in [22] overcomes the limitation posed by [15] and [25]. However, the analysis is effectively limited to a purely sinusoidal inductor current. Although the effect of dead time is well established, the limitations posed within current models suggest that there is still no complete model for predicting the isolated effect of dead time on distortion within open loop applications.

Contributions made by this Dissertation

An analytical model is introduced, in which a realistic inductor current model is incorporated. For a given dead time, the harmonic composition of the spectrum can be determined directly from a given set of circuit parameters. The analytical model is accompanied by an equivalent simulation model.

1.5.3 NON-ZERO TURN-ON AND TURN-OFF DELAYS

The turn-*on* and turn-*off* delays exist as a result of the time required for the charge or discharge of the MOSFET's input capacitance. It is well known that the analytical expressions describing these delays are dependent on the current polarity and the current magnitude [24], [28].

Relevant Literature

The fundamental analysis presented in [15] first noted that distortion arises from these delays (referred to as delay distortion). Moreover, it suggested that the distortion exists as a result of two contributions, of which the first is due to the differential delay resulting from the inherent polarity dependency. The second contribution results from the non-linear current modulation. The proposed solution was to minimize the external gate resistance and to optimize the applied gate voltage such that these delays cancel each other out. The current modulation was considered negligible compared to other error sources after which the analysis concluded that delay distortion is generally not a limiting factor in switching output stages.

The time domain analysis of the effect of the turn-*on* and turn-*off* delays presented in [29], respectively referred to as finite speed turn-*on* and finite speed turn-*off*, considers the individual impact of each delay on the average voltage during the dead time. The analysis describes the scenario in which the above mentioned delays offer to minimize the average error voltage within the dead time.

Limitations posed by existing Literature

Although the distortion mechanism was identified in [15], there was no detailed analysis illustrating its exact effect. This shortcoming was addressed in [29] to a cartain degree. However, the analysis focused on the interaction between the timing errors rather than on quantifying the individual effect of the turn-*on* and turn-*off* delays. Although the end goal within a system's design remains low overall distortion, insight is gained into the distortion mechanisms by considering the individual effects. Furthermore, the analysis in [29] was performed in the time domain, which means that the sideband switching harmonics resulting from the modulation process were unknown. This, however, is a concern since the differential delay noted in [15] suggests that an effect similar to dead time exists, which has been shown to influence the modulation products [22].

Contributions made by this Dissertation

The isolated effect of the turn-*on* and turn-*off* delays on THD is established. An simulation model is introduced in which the inherent current polarity and non-linear current magnitude dependencies are modelled.

1.5.4   NON-ZERO TURN-ON AND TURN-OFF SWITCHING TRANSITIONS

The non-zero intrinsic gate-to-drain capacitance within the power MOSFET structure leads to non-zero switching transitions. Since this capacitance is a non-linear function of the drain-to-source voltage, a non-linear switching curve is introduced. Early work in [24], [28] has shown its dependence on both current polarity and magnitude.

Relevant Literature

The non-linear switching characteristic was noted in [15]. However, for purposes of simplicity, a linear transition with equal rise and fall switching times were assumed. A brief analysis followed, which illustrated a moderate influence. The analysis concluded that, in practice, the effect of the switching transitions contributes to noise and distortion, but is less dominant than other error sources.

The analysis in [29] contains an investigation determining the effect of the switching node capacitance on the rising and falling edge transitions during the dead time. This is achieved by establishing the average error voltage at the switching node resulting from a constant capacitance, i.e. a linear transition. Various switching scenarios are presented during the period of dead time from which a time domain representation of the error voltage as a function of the duty cycle can be established.

Limitations posed by existing Literature

Like the methods mentioned in Sections 1.5.2 and 1.5.3, the analysis in [15] and [29] was performed in the time domain. The error at the switching node in [29] was found from the average error resulting from the charge or discharge of the switching node capacitance during

the dead time. This only has an effect on the rising edge for a negative inductor current, and the falling edge for a positive inductor current. The remaining edges were assumed to switch in zero time between the various voltage levels. Moreover, the switching node capacitance's effect becomes less dominant at low current. This, in turn, means that the MOSFET's switching charteristic dominates in this state.

Contributions made by this Dissertation

A closed form solution describing the MOSFET's switching curve in the presence of a non-linear gate-to-drain capacitance is derived, from which a simple approximation to the switching curve for both edges can be established. Distortion analysis of the non-linear switching transition compared to a linear swithing transition is performed via simulation.

1.5.5   PARASITICS AND REVERSE RECOVERY

It is well known that the stray parasitic elements existing within practical power MOSFETs lead to unwanted voltage transients when switched at high speeds. The current literature contains several detailed investigations on the sources giving rise to this effect. Analytical expressions have been derived in which the switching behaviour of the MOSFET is modelled in the presence of both the common source and switching loop inductance, addressing trade-offs between overshoot, switching speed and energy loss [30]. Another publication contains analytical solutions for overshoot in the presence of PCB stray inductances [31]. The analysis of reverse recovery in literature [32], [33] has mostly been limited to the influence on efficiency and switching device ratings. Distortion analysis resulting from its effect has only been mentioned briefly in previous work [15], [32], [33].

Relevant Literature

In [32] it was mentioned that the ringing effect mainly alters the high frequency (HF) spectrum; it was thus concluded that the exact influence is not easily generalized due to its strong dependence on practical implementation.

The effect of the reverse recovery on the switching waveform was considered in [32]. The analysis was limited to the impact on the switching waveforms, and it was concluded that it would only marginally affect system performance. The power loss analysis in [33] included the effect of the parasitic components in the analysis. Reverse recovery was included in [33] as part of a power loss analysis, noting that this effect only occurs during forced commutation, i.e. during the dead time. The distortion analysis included in [33] stated that the effect was not easily quantified theoretically, and it was thus modelled as a current dependent delay prior to the switching transition.

Limitations posed by existing Literature

No analysis was included on either effect in [32]. The above mentioned reports [32], [33] on both subjects were mostly limited to power loss rather than distortion. The inclusion of its effect into the model mentioned in [33] was in terms of a PTE. To knowledge, the effect of reverse recovery as a PAE on distortion has yet to be established.

Contributions made by this Dissertation

The effect of reverse recovery on distortion is determined by means of a simulation model. Its effect is modelled as an additional constraint within the analysis of the parasitics.

1.6   DISSERTATION OUTLINE

This section contains a broad outline of the structure and research methodology used in this dissertation. Firstly, a review of the double Fourier series analytical solution for ideal NPWM is considered. This review is necessary since the integral limits are modified in later chapters to take account of PTEs. An accurate simulation strategy is next developed for NPWM which allows for rapid calculation of the spectra. A general analysis for the incorporation of PTEs within the double Fourier series method of analysis is introduced. The findings achieved are used to extend the analytical NPWM solution as much as possible to account for PTEs. The time based simulation strategy is applied to validate both analysis approaches. When the analytical solution becomes too complex, the simulation strategy can

be applied with confidence because of the match achieved. Finally, the analytical and simulation results are compared to experimental results to verify the validity of the research.

2
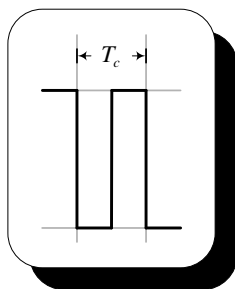
A FUNDAMENTAL
ANALYSIS OF PWM

2.1 INTRODUCTION

Communication systems require a message signal to shift into another frequency range to make it suitable for transmission over a communication channel. Power electronics also utilize such a frequency shift to control the switching device(s) of a converter in order to realize a target reference voltage or current. This frequency shift is termed *modulation* and can be defined as 'the process by which some characteristic of a carrier is varied in accordance with a modulating wave' [36]. The inverse process, corresponding to a shift back into the original frequency range, is known as *demodulation.*

PWM, also referred to in text as pulse duration modulation (PDM) or pulse length modulation [17], is a very well established modulation strategy for controlling the output of power electronic converters. It can be described as the 'modulation of a pulse carrier in which the value of each instantaneous sample of a continuously varying modulating wave is caused to produce a pulse of proportional duration' [17].

This chapter focuses on the fundamental concepts of PWM and serves as a foundation to the following chapters. Firstly, some well-known concepts involving the various methods of modulation are reviewed, after which the double Fourier series method of analysis, originally introduced by W.R. Bennet [11], is considered. A novel simulation strategy, which allows for accurate and rapid calculation of the spectrum, is then introduced.

2.2 FUNDAMENTAL CONCEPTS OF PWM

The primary criterion of all modulation schemes is to create an intermediate signal that has the same fundamental volt-second average as the reference waveform at any instant in time [13]. PWM thus requires the calculation of the exact duration of each pulse, which is necessary to preserve the original modulating waveform.

The pulse width is generated by a simple comparison between the reference waveform and a high frequency carrier (sawtooth or triangular) waveform. The sampling process used to determine the pulse duration can be either natural or uniform, with three possible methods of modulating the pulse width. Either the leading, trailing or both edges of the modulated waveform can be varied to produce the desired pulse width as illustrated in Figure 2.1. The grey lines represent the modulated edges.
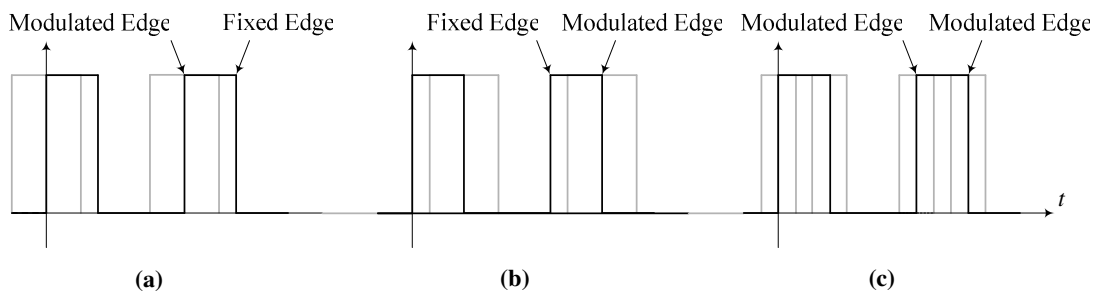
Figure 2.1: (a) Leading edge, (b) trailing edge and (c) double edge modulation [17].

NPWM, sometimes referred to in literature as analog PWM [42], is the earliest and most simple PWM strategy [13]. It is generated whenever the sample instant occurs at the natural intersection of the modulating and carrier waveform. Figure 2.2 illustrates NPWM for leading edge (LENPWM), trailing edge (TENPWM) and double edge (DENPWM) modulation.
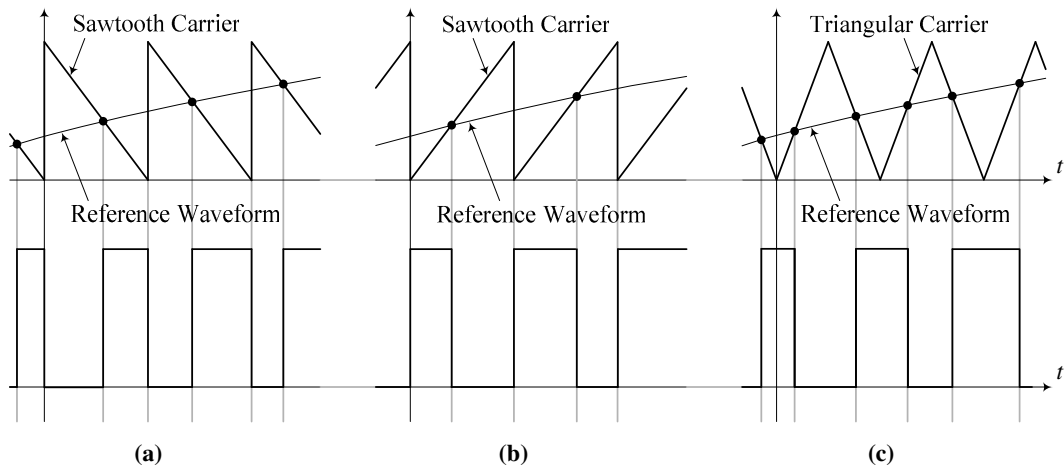
Figure 2.2: Generation of (a) LENPWM, (b) TENPWM and (c) DENPWM.

UPWM is achieved whenever switching occurs at the intersection of a regular or uniformly sampled reference waveform and the carrier waveform. Figure 2.3 shows UPWM for leading edge (LEUPWM), trailing edge (TEUPWM) and double edge (DEUPWM) modulation. For LEUPWM and TEUPWM, illustrated in Figure 2.3 (a) and (b) respectively, sampling of the reference waveform respectively takes place at the vertical rise (leading) or fall (trailing) following the sawtooth ramp. The crosspoint is then determined by directly comparing the amplitude of the sampled reference with the carrier waveform.
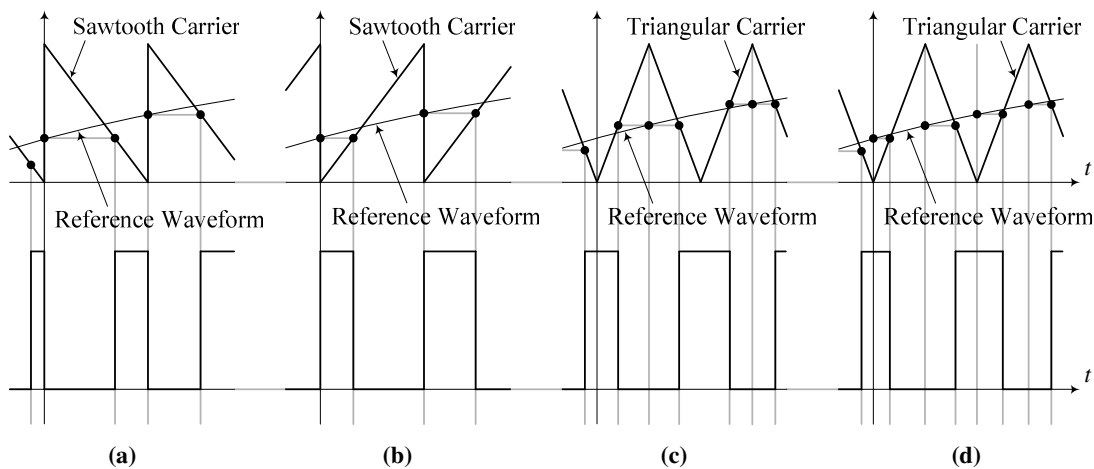
Figure 2.3: (a) LEUPWM, (b) TEUPWM, (c) symmetrical DEUPWM and (d) asymmetrical DEUPWM.

For DEUPWM, sampling can be symmetrical or asymmetrical. Symmetrical UPWM results when the sampled reference is taken at either the positive or negative peak of the triangular waveform with its amplitude held constant over the carrier period. This concept is illustrated in Figure 2.3 (c) and (d). The extent to which a pulse can be modulated is also known as the modulation index. This variable, denoted by *M*, is usually referred to as either a fraction with unity as its maximum value, or as a percentage. Note that, in the following sections, when referring to LEPWM, TEPWM or DEPWM, it is applicable to both natural and uniform sampling. As mentioned in Chapter 1, single-sided NPWM is assumed. The justification of this assumption within Class D applications (employing digital PWM) is that the PNPWM process approximates NPWM using numerical calculation of the intersection between the reference and carrier waveforms. Thus, approximating DENPWM requires twice the amount of intersections, which in turn increases the amount of logic cells required.

2.3   THE ANALYTICAL SPECTRUM OF PWM

The spectrum of a signal provides an alternative viewpoint as a function of frequency that is often more meaningful and revealing than the original function of time. PWM is a non-linear process, which results in distortion of the modulating signal. Determining the spectrum of PWM is thus very helpful, since it creates a better understanding of the non-linearities involved. However, these non-linearities also complicate the analytical analysis significantly. The remainder of this section contains a summary of the double Fourier series method of analysis presented in [17] and [13]. This-well established analytical method was originally introduced by W.R. Bennet [11] for purposes of communication systems [17], [13]. S. Bowes and B. Bird [19] expanded this to power converter systems [13]. The fundamental concept of this theory is explained for ideal two-level PWM. As a starting point, the analysis assumes the existence of two independently periodic time functions given by:

$$x = \omega_c t \tag{2.1}$$

$$y = \omega_0 t \tag{2.2}$$

These two functions of time represent a high frequency carrier wave and low frequency modulating waveform respectively. The pulse train created by the comparison of these two functions is generally non-periodic [17]. This poses a problem for Fourier analysis. W.R. Bennet [11] addressed this problem by representing the pulse train by a 3-D area.
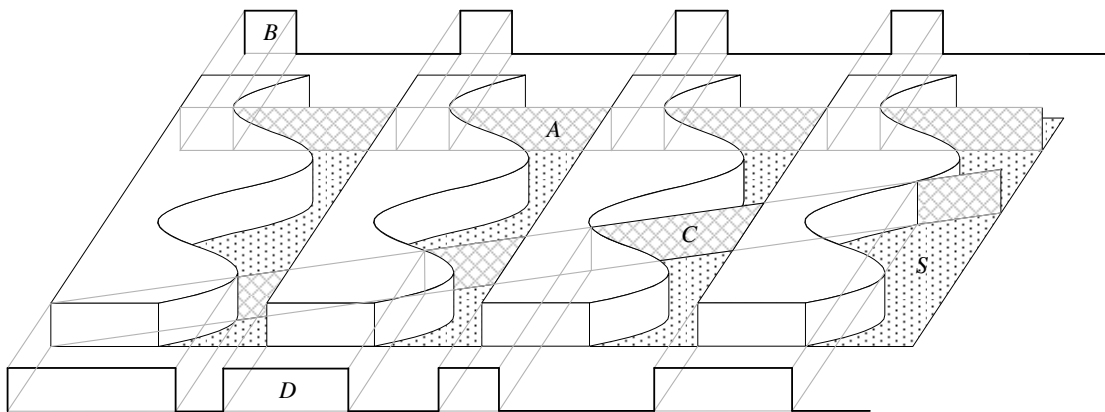
Figure 2.4: Definition of the 3-D area introduced by W.R. Bennet [11].

The configuration defined in Figure 2.4 corresponds to a TENPWM signal and was arbitrarily chosen for purposes of illustration of the concept which will now be explained. The area defined contains identical walls with flat tops at the same height. These walls are parallel to each other and all perpendicular to the surface *S* which they rest upon. Next, assume that the walls are scaled into square cells in such a way that one wall exists for every 2π units in the *x*-direction, and that one complete cycle of the waveform defining the right hand side of each wall exists for every 2π units in the *y*-direction. This makes it possible to represent the height of the cells by a double Fourier series with *x* and *y* as input arguments, denoted by *F(x,y)*. Figure 2.5 shows an extraction of Figure 2.4 with the appropriate scaling.
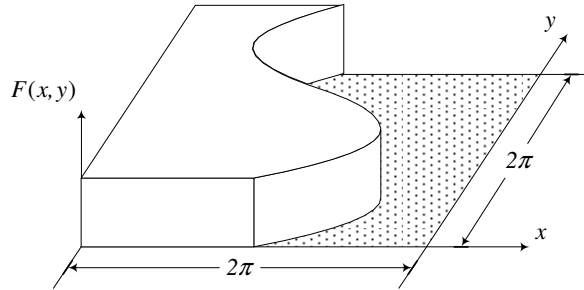
Figure 2.5: Appropriate scaling of the 3-D unit area of Figure 2.4.

The Fourier series can now be developed. Consider two planes that are both perpendicular to plane *S*, denoted by *A* and *B* in Figure 2.4. Both planes are parallel to the *x*-axis. With *B* fixed, the projection of the intersection of plane *A* onto plane *B* produces a series of rectangular pulses in the *x*-direction all with equal duration, shown at the top of Figure 2.4. By moving plane *A* to a new point of intersection on the *y*-axis while still keeping it parallel to the *x*-axis, another projection of equal pulses is created. It can thus be concluded that the intersection the latter plane at any arbitrary point on the *y*-axis (denoted y_1) will always produce a periodic function in the *x*-direction. This makes it possible to describe these pulses with a simple Fourier series:

$$F(x, y_1) = \frac{1}{2}a_0(y_1) + \sum_{m=1}^{\infty}\left[a_m(y_1)\cos(mx) + b_m(y_1)\sin(mx)\right] \tag{2.3}$$

With coefficients:

$$a_m(y_1) = \frac{1}{\pi} \int_0^{2\pi} F(x, y_1) \cos(mx) \, dx, \quad m = 0, 1, 2, ..., \infty \tag{2.4}$$

$$b_m(y_1) = \frac{1}{\pi} \int_0^{2\pi} F(x, y_1) \sin(mx) \, dx, \quad m = 1, 2, 3, ..., \infty \tag{2.5}$$

These coefficients depend on a specific point of intersection with the *y*-axis. Since they are also periodic with respect to *y*, it is possible to represent them with another Fourier series for all possible values of *y*. This is given by:

$$a_m(y) = \frac{1}{2} c_{m0} + \sum_{n=1}^{\infty} \left[c_{mn} \cos(ny) + d_{mn} \sin(ny) \right] \tag{2.6}$$

$$b_m(y) = \frac{1}{2} e_{m0} + \sum_{n=1}^{\infty} \left[e_{mn} \cos(ny) + f_{mn} \sin(ny) \right] \tag{2.7}$$

With the coefficients defined as:

$$c_{mn} = \frac{1}{\pi} \int_0^{2\pi} a_m \cos(ny) \, dy \tag{2.8}$$

$$d_{mn} = \frac{1}{\pi} \int_0^{2\pi} a_m \sin(ny) \, dy \tag{2.9}$$

$$e_{mn} = \frac{1}{\pi} \int_0^{2\pi} b_m \cos(ny) \, dy \tag{2.10}$$

$$f_{mn} = \frac{1}{\pi} \int_0^{2\pi} b_m \sin(ny) \, dy \tag{2.11}$$

By substituting the Fourier expansion for the coefficients in Eq. (2.6) and (2.7) into the original series and expanding for the coefficients in Eqs. (2.8) to (2.11), the double Fourier series can be determined by trigonometric manipulation of the terms as:

$$F(x, y) = \frac{1}{2} A_{00} + \sum_{n=1}^{\infty} \left[A_{0n} \cos(ny) + B_{0n} \sin(ny) \right]$$

$$+ \sum_{m=1}^{\infty} \left[A_{m0} \cos(mx) + B_{m0} \sin(mx) \right] \tag{2.12}$$

$$+ \sum_{m=1}^{\infty} \sum_{n=\pm 1}^{\pm \infty} \left[A_{mn} \cos(mx+ny) + B_{mn} \sin(mx+ny) \right]$$

Where:

$$A_{mn} = \frac{1}{2\pi^2} \int_0^{2\pi} \int_0^{2\pi} F(x,y) \cos(mx+ny) \, dx \, dy \qquad (2.13)$$

$$B_{mn} = \frac{1}{2\pi^2} \int_0^{2\pi} \int_0^{2\pi} F(x,y) \sin(mx+ny) \, dx \, dy \qquad (2.14)$$

The complex form is given by:

$$C_{mn} = A_{mn} + jB_{mn} = \frac{1}{2\pi^2} \int_0^{2\pi} \int_0^{2\pi} F(x,y) e^{j(mx+ny)} \, dx \, dy \qquad (2.15)$$

The Fourier series of Eq. (2.12) can be related to time by substituting for Eqs. (2.1) and (2.2). Also, for each moment of time inserted into Eqs. (2.1) and (2.2), a specific point is defined within the area. The combination of these equations for equal time corresponds to a straight line with slope ω_0/ω_c. Again, consider two planes, denoted by C and D in Figure 2.4. Both these planes are perpendicular to plane S. Plane C includes the origin while plane D is fixed at a point parallel to the x-axis. The projection of the intersection of plane C with the walls onto plane D will produce a series of pulses of varying duration. This projection is shown at the bottom of Figure 2.4. Since the Fourier series represents the height at any point within the defined area, it must also define the height along the straight line corresponding to the time functions of Eqs. (2.1) and (2.2). This makes it possible to represent a series of pulses with varying duration by means of a double Fourier series.

The significance of each term in Eq. (2.12) will now be discussed. The carrier index variable and baseband index variable are defined as m and n respectively. The integer values of these variables define the absolute frequency of the harmonic components by the relation $m\omega_c + n\omega_0$. The first term in Eq. (2.12) exists at a frequency where both m and n are equal to 0. This corresponds to the DC offset of the modulated wave. The frequency components of the second and third term represent special groups of harmonics. For the case where $m=0$ (second term), the harmonics are defined by n alone. This corresponds to the baseband harmonics created by the modulating wave. Note that the desired fundamental output is defined when $n=1$, with all other integer values of n unwanted. In a similar manner, for the case where $n=0$

(third term), the frequency components are defined by *m* alone. This corresponds to the harmonics created by the carrier wave and exists at multiples of the switching frequency. The fourth and final term is formed by a combination of all possible harmonic pairs formed by the sum and difference of the carrier and modulating wave with the exception of the special case where *n*=0. These combinations are generally referred to as sideband harmonics [13]. The analysis and solutions which now follow are summarized from [17] and [13].

The Spectrum of LENPWM

The sawtooth carrier and modulating waveform which will be used to derive an expression for LENPWM are shown in Figure 2.6. The carrier waveform of (a) is defined by:

$$f(x) = -\frac{x}{\pi} + 1 \quad \text{for the region} \quad 0 \le x < 2\pi \tag{2.16}$$

With the modulating waveform of (b) given by:

$$f(y) = M \cos(y) \quad \text{for} \quad 0 < M < 1 \tag{2.17}$$
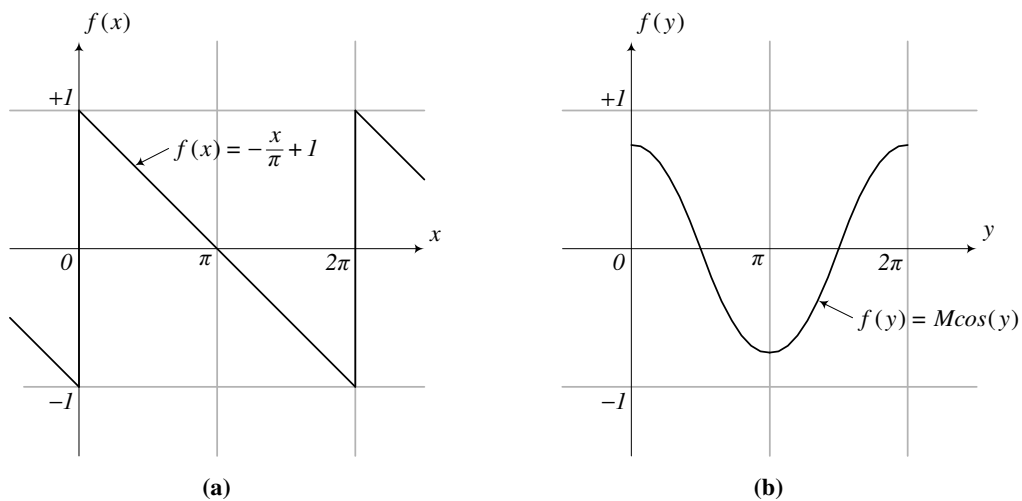
Figure 2.6: (a) Sawtooth carrier waveform and (b) modulating waveform for LENPWM.

The output voltage equals V_d (half-bridge) whenever the reference waveform is greater than the carrier waveform, and it equals zero whenever the carrier waveform is greater than

the reference waveform. As a result of these two conditions $f(x,y)$ can take on two values over the region $0 \leq x \leq 2\pi$. Stated mathematically:

$$f(x,y) = V_d \quad \text{when} \quad M\cos(y) > -\frac{x}{\pi} + 1, \quad \text{or} \quad x > -\pi M\cos(y) + \pi \qquad (2.18)$$

$$f(x,y) = 0 \quad \text{when} \quad M\cos(y) < -\frac{x}{\pi} + 1, \quad \text{or} \quad x < -\pi M\cos(y) + \pi \qquad (2.19)$$

Figure 2.7 illustrates the 3-D unit area defined by Eqs. (2.18) and (2.19).
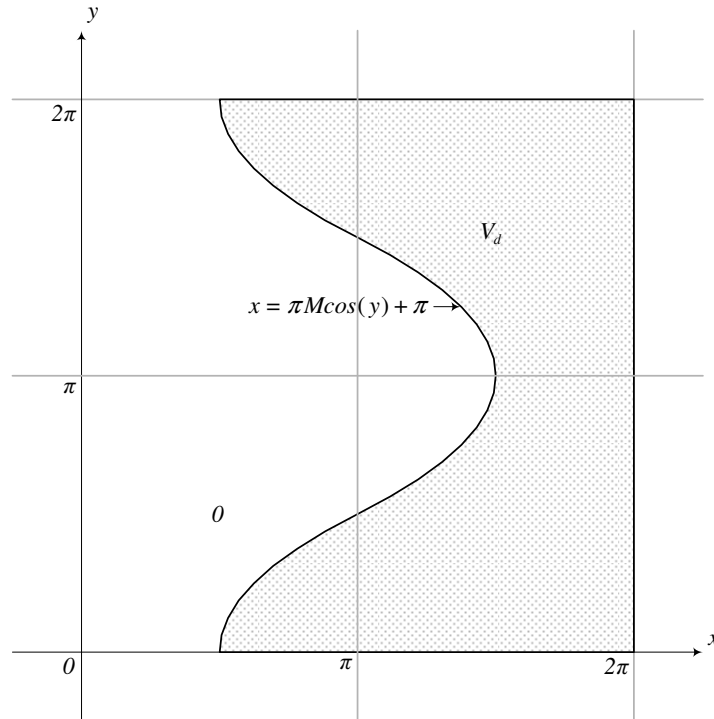
Figure 2.7: 3-D unit area for LENPWM.

The complex Fourier coefficient of Eq. (2.15) can now be evaluated by inserting the limits defined in Figure 2.7. The expression yields:

$$C_{mn} = \frac{V_d}{2\pi^2} \int_0^{2\pi} \left[\int_0^{-\pi M\cos(y)+\pi} e^{jmx} dx + \int_{-\pi M\cos(y)+\pi}^{2\pi} e^{jmx} dx \right] e^{jny} dy \qquad (2.20)$$

Eq. (2.20) can now be evaluated for different values of the index variables m and n. For $m=n=0$, Eq. (2.20) can be simplified to:

$$A_{00} + jB_{00} = \frac{V_d}{2\pi^2} \int\limits_0^{2\pi} \left[\int\limits_0^{-\pi M \cos(y)+\pi} dx + \int\limits_{-\pi M \cos(y)+\pi}^{2\pi} dx \right] dy$$

$$= \frac{V_d M}{2\pi} \int\limits_0^{2\pi} \cos(y)\, dy + 2V_d$$

$$= V_d \tag{2.21}$$

Rewriting Eq. (2.21) into its real and complex parts yield:

$$A_{00} = V_d \text{ and } B_{00} = 0 \tag{2.22}$$

The DC component can now be found by substituting Eq. (2.22) into Eq. (2.12):

$$\frac{A_{00}}{2} = \frac{V_d}{2} \tag{2.23}$$

For $m=0$, $n>0$ the inner integral of Eq. (2.20) gives:

$$A_{0n} + jB_{0n} = \frac{V_d}{2\pi^2} \int\limits_0^{2\pi} \left[\int\limits_0^{\pi M \cos(y)+\pi} dx + \int\limits_{\pi M \cos(y)+\pi}^{2\pi} dx \right] e^{jny}\, dy$$

$$= -\frac{V_d M}{2\pi} \int\limits_0^{2\pi} \cos(y)\, e^{jny}\, dy + \frac{V_d}{2\pi} \int\limits_0^{2\pi} e^{jny}\, dy \tag{2.24}$$

Substituting for $\cos(y)=(e^{jy}+e^{-jy})/2$ Eq. (2.24) leads to:

$$= -\frac{V_d M}{4\pi} \int\limits_0^{2\pi} e^{j(n+1)y}\, dy + \frac{V_d M}{4\pi} \int\limits_0^{2\pi} e^{j(n-1)y}\, dy \tag{2.25}$$

The first term in Eq. (2.25) always integrates to zero for all values of $n>0$. The second term integrates to a non-zero value only when $n=1$. Evaluating the latter for this condition, Eq. (2.25) gives:

$$A_{01} + jB_{01} = -\frac{V_d M}{2} \tag{2.26}$$

Eq. (2.26) represents the magnitude of the fundamental low frequency harmonic component. Note that this is the ideal desired output since the modulating waveform of Eq. (2.17) is preserved with no additional baseband harmonics resulting from the modulation process (Eq. (2.26) equals zero for all $n>1$). For $m>0$, $n=0$, the integral of Eq. (2.20) leads to:

$$A_{m0} + jB_{m0} = \frac{V_d}{2\pi^2} \int_0^{2\pi} \left[\int_0^{-\pi M \cos(y)+\pi} e^{jmx} dx + \int_{-\pi M \cos(y)+\pi}^{2\pi} e^{jmx} dx \right] dy$$

$$= \frac{V_d}{j2\pi^2 m} \int_0^{2\pi} \left[1 - e^{-jm\pi M \cos(y)+jm\pi} \right] dy$$

$$= -j\frac{V_d}{\pi m} + j\frac{V_d}{2\pi^2 m} e^{jm\pi} \int_0^{2\pi} e^{-jm\pi M \cos(y)} dy \tag{2.27}$$

The integral in Eq. (2.27) corresponds to a Bessel function of the first kind. Substituting for the relation in Eq. (A1.11) with $\xi=\pi M$ and $\theta=y$ and noting that:

$$e^{jm\pi} = \cos(\pi m) + j\sin(\pi m) = (-1)^m \tag{2.28}$$

Eq. (2.27) can be simplified to:

$$= -j\frac{V_d}{\pi m} \left[1 - (-1)^m J_0(\pi M m) \right] \tag{2.29}$$

Eq. (2.29) represents the carrier harmonics. For $m>0$, $n\neq0$, Eq. (2.20) can be evaluated:

$$A_{mn} + jB_{mn} = \frac{V_d}{2\pi^2} \int_0^{2\pi} \left[\int_0^{-\pi M \cos(y)+\pi} e^{jmx} dx + \int_{-\pi M \cos(y)+\pi}^{2\pi} e^{jmx} dx \right] e^{jny} dy$$

$$= \frac{V_d}{j2\pi^2 m} \int_0^{2\pi} \left[1 - e^{-jm(-\pi M \cos(y)+\pi)} \right] e^{jny} dy$$

$$= j\frac{V_d}{2\pi^2 m} e^{-jm\pi} \int_0^{2\pi} e^{jm\pi M \cos(y)} e^{jny} dy \tag{2.30}$$

The integral in Eq. (2.30) again corresponds to a Bessel function of the first kind. Substituting for the relation in Eq. (A1.7) results in:

$$= j\frac{V_d}{\pi m} (-1)^m e^{j\frac{\pi}{2}n} J_n(\pi M m) \tag{2.31}$$

Eq. (2.31) defines the sideband harmonics. The complete solution to LENPWM can be found by substituting Eqs. (2.21), (2.26), (2.29) and (2.31) into the double Fourier series of Eq. (2.12) to give:

$$f_{LENPWM}(t) = \frac{V_d}{2} - \frac{V_d M}{2} \cos(\omega_0 t) \tag{2.32}$$

$$- \frac{V_d}{\pi} \sum_{m=1}^{\infty} \frac{1}{m} \left[1 - (-1)^m J_0(\pi M m) \right] \sin(m[\omega_c t])$$

$$+ \frac{V_d}{\pi} \sum_{m=1}^{\infty} \sum_{n=\pm1}^{\pm\infty} \frac{1}{m} (-1)^m J_n(\pi M m) \sin\left(m[\omega_c t] + n[\omega_0 t] - \frac{\pi}{2} n \right)$$

The Spectrum of TENPWM

Figure 2.8 (a) and (b) respectively represent the sawtooth carrier waveform and modulating waveform that will be used to construct the 3-D unit area for TENPWM.
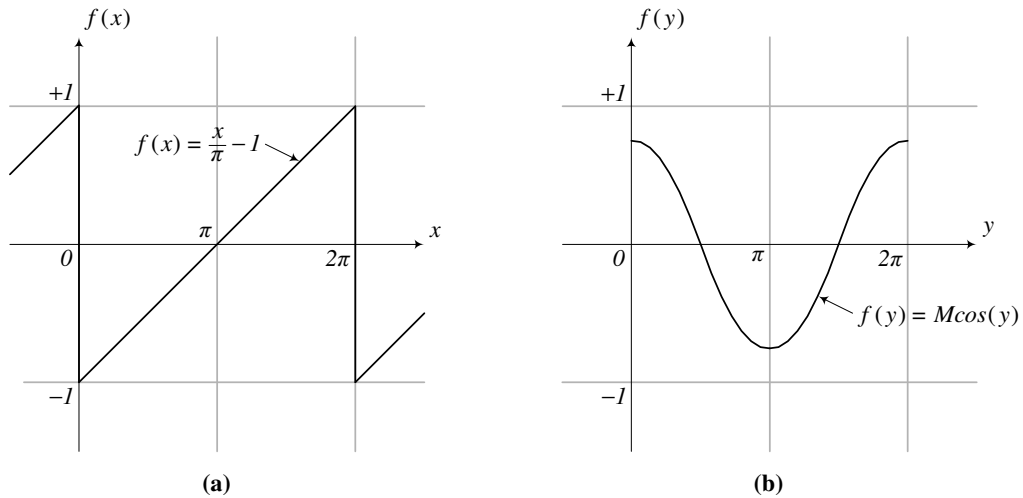
Figure 2.8: (a) Sawtooth carrier waveform and (b) modulating waveform for TENPWM.

The carrier waveform of (a) is defined by:

$$f(x) = \frac{x}{\pi} - 1 \quad \text{for the region} \quad 0 \le x < 2\pi \tag{2.33}$$

While the modulating waveform of (b) is given by:

$$f(y) = M \cos(y) \quad \text{for} \quad 0 < M < 1 \tag{2.34}$$

Using the same switching constraints described in the previous section, the following two mathematical conditions can be constructed:

$$f(x,y) = V_d \quad \text{when} \quad M \cos(y) > \frac{x}{\pi} - 1, \quad \text{or} \quad x < \pi M \cos(y) + \pi \tag{2.35}$$

$$f(x,y) = 0 \quad \text{when} \quad M \cos(y) < \frac{x}{\pi} - 1, \quad \text{or} \quad x > \pi M \cos(y) + \pi \tag{2.36}$$
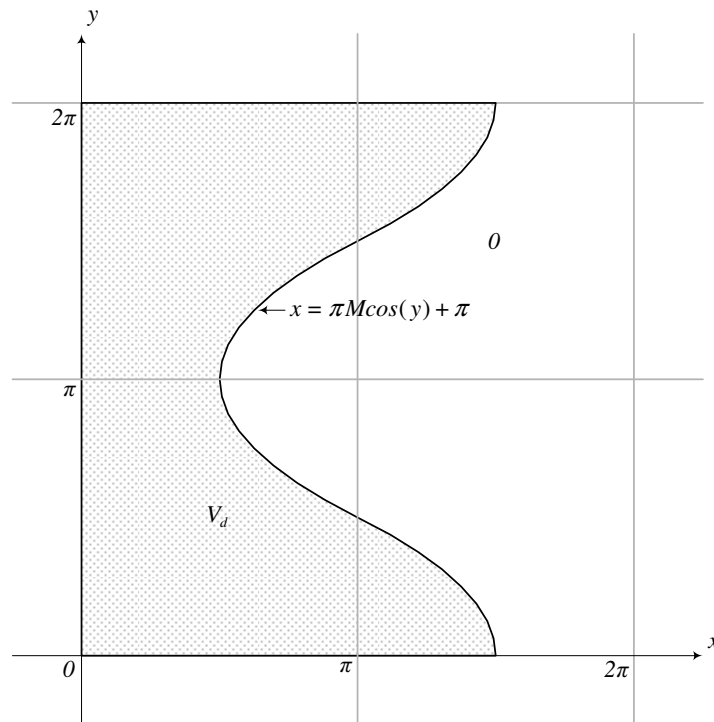
Figure 2.9: 3-D unit area for TENPWM.

The unit area can now be constructed using the constraints defined in Eqs. (2.35) and (2.36). This is illustrated in Figure 2.9.

Rewriting Eq. (2.15) by inserting the limits defined in Figure 2.9, the expression yields:

$$C_{mn} = \frac{V_d}{2\pi^2} \int\limits_0^{2\pi} \left[\int\limits_0^{\pi M \cos(y)+\pi} e^{jmx} dx + \int\limits_{\pi M \cos(y)+\pi}^{2\pi} e^{jmx} dx \right] e^{jny} dy \qquad (2.37)$$

Eq. (2.37) can now be evaluated for different values of the index variables m and n to determine the magnitude of the harmonic components created. For $m=n=0$, Eq. (2.37) can be simplified to:

$$A_{00} + jB_{00} = \frac{V_d}{2\pi^2} \int\limits_0^{2\pi} \left[\int\limits_0^{\pi M \cos(y)+\pi} dx + \int\limits_{\pi M \cos(y)+\pi}^{2\pi} dx \right] dy$$

$$= \frac{V_d M}{2\pi} \int\limits_0^{2\pi} \cos(y) dy + \frac{V_d}{2}$$

$$= \frac{V_d}{2} \qquad (2.38)$$

The result obtained in Eq. (2.38) is exactly the same as that of the previous section. The DC component can thus be written as:

$$\frac{A_{00}}{2} = \frac{V_d}{2} \qquad (2.39)$$

For $m=0$, $n>0$, the inner integral of Eq. (2.37) gives:

$$A_{0n} + jB_{0n} = \frac{V_d}{2\pi^2} \int\limits_0^{2\pi} \left[\int\limits_0^{\pi M \cos(y)+\pi} dx + \int\limits_{\pi M \cos(y)+\pi}^{2\pi} dx \right] e^{jny} dy$$

$$= \frac{V_d M}{2\pi} \int\limits_0^{2\pi} \cos(y) e^{jny} dy + \frac{V_d}{2\pi} \int\limits_0^{2\pi} e^{jny} dy \qquad (2.40)$$

The first term of Eq. (2.24) is the exact negative of the first term of Eq. (2.40). The solution can thus be obtained directly by adapting Eq. (2.26). This gives:

$$A_{01} + jB_{01} = \frac{V_d M}{2} \qquad (2.41)$$

Similar to Eq. (2.26), Eq. (2.41) defines the magnitude of the fundamental low frequency harmonic component.

For *m>0*, *n=0*, Eq. (2.37) can be written as:

$$A_{m0} + jB_{m0} = \frac{V_d}{2\pi^2} \int\limits_0^{2\pi} \left[\int\limits_0^{\pi M \cos(y)+\pi} e^{jmx} dx + \int\limits_{\pi M \cos(y)+\pi}^{2\pi} e^{jmx} dx \right] dy$$

$$= \frac{V_d}{j2\pi^2 m} \int\limits_0^{2\pi} \left[e^{jm\pi M \cos(y)+jm\pi} -1 \right] dy$$

$$= j\frac{2V_d}{2\pi m} - j\frac{V_d}{2\pi^2 m} e^{jm\pi} \int\limits_0^{2\pi} e^{jm\pi M \cos(y)} dy \qquad (2.42)$$

Once again the integral in Eq. (2.42) corresponds to a Bessel function of the first kind. The solution is given by:

$$= j\frac{V_d}{\pi m} \left[1-(-1)^m J_0\left(\pi M m\right) \right] \qquad (2.43)$$

Eq. (2.43) defines the carrier harmonics. For *m>0*, *n≠0*, Eq. (2.37) integrates to:

$$A_{mn} + jB_{mn} = \frac{V_d}{2\pi^2} \int\limits_0^{2\pi} \left[\int\limits_0^{\pi M \cos(y)+\pi} e^{jmx} dx + \int\limits_{\pi M \cos(y)+\pi}^{2\pi} e^{jmx} dx \right] e^{jny} dy$$

$$= \frac{V_d}{j2\pi^2 m} \int\limits_0^{2\pi} \left[e^{jm\pi M \cos(y)+jm\pi} -1 \right] e^{jny} dy$$

$$= -j\frac{V_d}{2\pi^2 m} \int\limits_0^{2\pi} e^{jm\left(\pi M \cos(y)+\pi\right)} e^{jny} dy \qquad (2.44)$$

Again, the integral in Eq. (2.44) represents a Bessel function of the first kind. Substituting for the relation in Eq. (A1.7), Eq. (2.44) can be written as:

$$= -j\frac{V_d}{\pi m}(-1)^m e^{j\frac{\pi}{2}n} J_n\left(\pi M m\right) \qquad (2.45)$$

Eq. (2.45) represents the sideband harmonics situated around multiples of the carrier harmonics.

By next substituting the results achieved in Eqs. (2.38), (2.41), (2.43) and (2.45) into the double Fourier series of Eq. (2.12) and relating the result to time using Eqs. (2.1) and (2.2), the complete solution to TENPWM can be expressed as:

$$f_{TENPWM}(t) = \frac{V_d}{2} + \frac{V_d M}{2}\cos(\omega_0 t)$$

$$+ \frac{V_d}{\pi} \sum_{m=1}^{\infty} \frac{1}{m}\left[1 - (-1)^m J_0(\pi M m)\right]\sin\left(m[\omega_c t]\right)$$

$$- \frac{V_d}{\pi} \sum_{m=1}^{\infty} \sum_{n=\pm 1}^{\pm\infty} \frac{1}{m}(-1)^m J_n(\pi M m)\sin\left(m[\omega_c t] + n[\omega_0 t] - \frac{\pi}{2}n\right)$$

(2.46)

The Spectrum of DENPWM

Figure 2.10 illustrates the carrier waveform and reference waveform that will be used to derive the derivation of the expression for DENPWM.
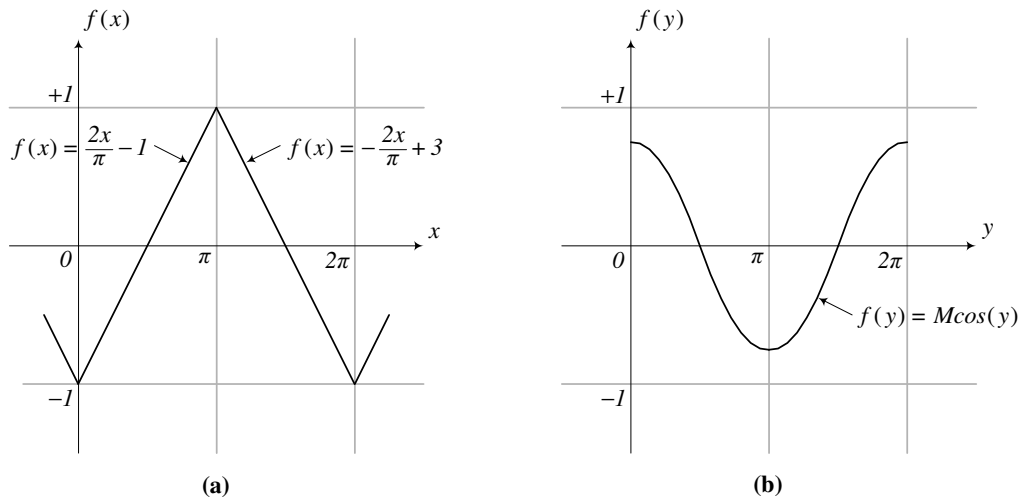
Figure 2.10: (a) Triangular carrier waveform and (b) modulating waveform for DENPWM.

The triangular carrier wave shown in Figure 2.10 (a) is defined over two regions:

$$f(x) = \frac{2x}{\pi} - 1 \qquad \text{for the region} \quad 0 \leq x < \pi$$

(2.47)

$$f(x) = -\frac{2x}{\pi} + 3 \quad \text{for the region} \quad \pi \le x < 2\pi \tag{2.48}$$

The modulating wave illustrated in Figure 2.10 (b) is defined by:

$$f(y) = M\cos(y) \quad \text{for} \quad 0 < M < 1 \tag{2.49}$$ Once again the output voltage switches state under the same conditions as described for LENPWM and TENPWM. For the region defined by $0 \le x < \pi$:

$$f(x,y) = V_d \quad \text{when} \quad M\cos(y) > \frac{2x}{\pi} - 1, \quad \text{or} \quad x < \frac{\pi}{2}M\cos(y) + \frac{\pi}{2} \tag{2.50}$$

$$f(x,y) = 0 \quad \text{when} \quad M\cos(y) < \frac{2x}{\pi} - 1, \quad \text{or} \quad x > \frac{\pi}{2}M\cos(y) + \frac{\pi}{2} \tag{2.51}$$

Also, for the region bounded by $\pi \le x < 2\pi$:

$$f(x,y) = V_d \quad \text{when} \quad M\cos(y) > -\frac{2x}{\pi} + 3, \quad \text{or} \quad x > -\frac{\pi}{2}M\cos(y) + \frac{3\pi}{2} \tag{2.52}$$

$$f(x,y) = 0 \quad \text{when} \quad M\cos(y) < -\frac{2x}{\pi} + 3, \quad \text{or} \quad x < -\frac{\pi}{2}M\cos(y) + \frac{3\pi}{2} \tag{2.53}$$

Eqs. (2.50) to (2.53) define the limits of the unit area shown in Figure 2.11. Inserting the limits defined in Figure 2.11 into the complex Fourier coefficient defined by Eq. (2.15), the expression yields:

$$C_{mn} = \frac{V_d}{2\pi^2} \int_0^{2\pi} \left[\int_0^{\frac{\pi}{2}M\cos(y)+\frac{\pi}{2}} e^{jmx}dx + \int_{\frac{\pi}{2}M\cos(y)+\frac{\pi}{2}}^{-\frac{\pi}{2}M\cos(y)+\frac{3\pi}{2}} e^{jmx}dx + \int_{-\frac{\pi}{2}M\cos(y)+\frac{3\pi}{2}}^{2\pi} e^{jmx}dx \right] e^{jny}dy \tag{2.54}$$

Eq. (2.54) can now be evaluated for the different values of the index variables m and n. For $m=n=0$, the integral of Eq. (2.54) simplified to:

$$A_{00} + jB_{00} = \frac{V_d}{2\pi^2} \int_0^{2\pi} \left[\int_0^{\frac{\pi}{2}M\cos(y)+\frac{\pi}{2}} dx + \int_{\frac{\pi}{2}M\cos(y)+\frac{\pi}{2}}^{-\frac{\pi}{2}M\cos(y)+\frac{3\pi}{2}} dx + \int_{-\frac{\pi}{2}M\cos(y)+\frac{3\pi}{2}}^{2\pi} dx \right] dy$$

$$= \frac{V_d M}{2\pi} \int_0^{2\pi} \cos(y)\,dy + V_d$$

$$= V_d \tag{2.55}$$
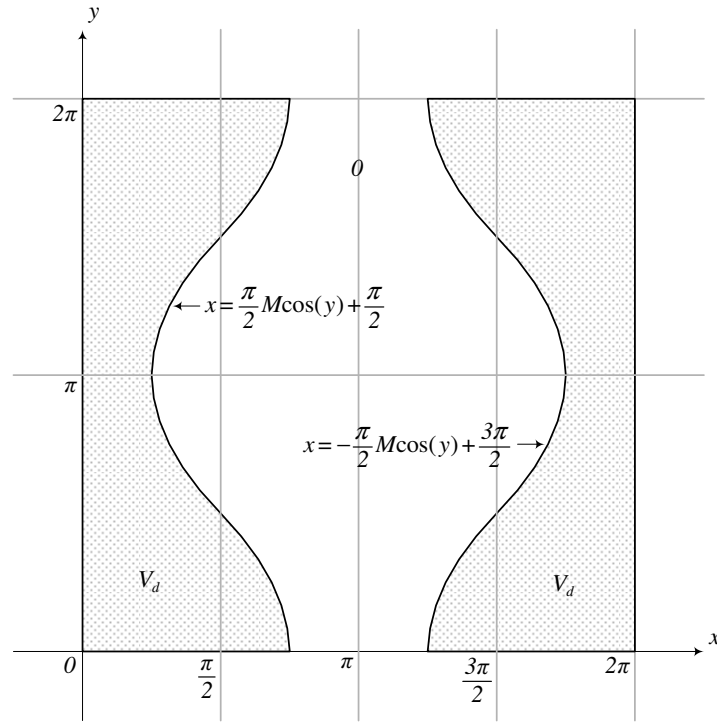
Figure 2.11: 3-D unit area for DENPWM.

The result achieved in Eq. (2.55) is exactly the same as that of the previous two sections. The DC component can thus once again be written as:

$$\frac{A_{00}}{2} = \frac{V_d}{2}$$

(2.56)

For $m=0$, $n>0$, evaluation of Eq. (2.54) leads to:

$$A_{0n} + jB_{0n} = \frac{V_d}{2\pi^2} \int_0^{2\pi} \left[\int_0^{\frac{\pi}{2}M\cos(y)+\frac{\pi}{2}} dx + \int_{\frac{\pi}{2}M\cos(y)+\frac{\pi}{2}}^{-\frac{\pi}{2}M\cos(y)+\frac{3\pi}{2}} dx + \int_{-\frac{\pi}{2}M\cos(y)+\frac{3\pi}{2}}^{2\pi} dx \right] e^{jny} dy$$

$$= \frac{V_d M}{2\pi} \int_0^{2\pi} \cos(y) e^{jny} dy + \frac{V_d}{2\pi} \int_0^{2\pi} e^{jny} dy$$

(2.57)

The integral of Eq. (2.57) corresponds to that of Eq. (2.40).

Evaluating Eq. (2.57) using the same technique discussed in the previous section gives:

$$A_{01} + jB_{01} = \frac{V_d M}{2} \tag{2.58}$$

The latter solution represents the fundamental low frequency harmonic component. For $m>0$, $n=0$, Eq. (2.54) can be written as:

$$
A_{m0} + jB_{m0} = \frac{V_d}{2\pi^2} \int_0^{2\pi} \left[\int_0^{\frac{\pi}{2}M\cos(y)+\frac{\pi}{2}} e^{jmx} dx + \int_{\frac{\pi}{2}M\cos(y)+\frac{\pi}{2}}^{-\frac{\pi}{2}M\cos(y)+\frac{3\pi}{2}} e^{jmx} dx + \int_{-\frac{\pi}{2}M\cos(y)+\frac{3\pi}{2}}^{2\pi} e^{jmx} dx \right] dy
$$

$$
= \frac{V_d}{j2\pi^2 m} \int_0^{2\pi} \left[e^{j\frac{\pi}{2}mM\cos(y)} e^{j\frac{\pi}{2}m} - e^{-j\frac{\pi}{2}mM\cos(y)} e^{j\frac{3\pi}{2}m} \right] dy
$$

$$
= -j\frac{V_d}{2\pi^2 m} e^{j\frac{\pi}{2}m} \int_0^{2\pi} e^{j\frac{\pi}{2}mM\cos(y)} dy + j\frac{V_{sw}}{2\pi^2 m} e^{j\frac{3\pi}{2}m} \int_0^{2\pi} e^{-j\frac{\pi}{2}mM\cos(y)} dy \tag{2.59}
$$

Both integrals in Eq. (2.59) correspond to Bessel functions of the first kind. By substituting again for the relation in Eq. (A1.11) results in:

$$
= j\frac{V_d}{\pi m} J_0\left(\frac{\pi}{2}Mm\right)\left[e^{j\frac{3\pi}{2}m} - e^{j\frac{\pi}{2}m} \right] \tag{2.60}
$$

Rewriting the exponential functions in brackets as the sum of sine and cosine functions, Eq. (2.60) can be simplified to:

$$
= \frac{2V_d}{\pi m} J_0\left(\frac{\pi}{2}Mm\right)\sin\left(\frac{\pi}{2}m\right) \tag{2.61}
$$

Eq. (2.61) represents the carrier harmonics. For $m>0$, $n\neq0$, Eq. (2.54) integrates to:

$$
A_{mn} + jB_{mn} = \frac{V_d}{2\pi^2} \int_0^{2\pi} \left[\int_0^{\frac{\pi}{2}M\cos(y)+\frac{\pi}{2}} e^{jmx} dx + \int_{\frac{\pi}{2}M\cos(y)+\frac{\pi}{2}}^{-\frac{\pi}{2}M\cos(y)+\frac{3\pi}{2}} e^{jmx} dx + \int_{-\frac{\pi}{2}M\cos(y)+\frac{3\pi}{2}}^{2\pi} e^{jmx} dx \right] e^{jny} dy
$$

$$
= \frac{V_d}{j2\pi^2 m} \int_0^{2\pi} \left[e^{j\frac{\pi}{2}mM\cos(y)} e^{j\frac{\pi}{2}m} - e^{-j\frac{\pi}{2}mM\cos(y)} e^{j\frac{3\pi}{2}m} \right] e^{jny} dy
$$

$$
= -j\frac{V_d}{2\pi^2 m} e^{j\frac{\pi}{2}m} \int_0^{2\pi} e^{j\frac{\pi}{2}mM\cos(y)} e^{jny} dy + j\frac{V_d}{\pi^2 m} e^{j\frac{\pi}{2}m} \int_0^{2\pi} e^{-j\frac{\pi}{2}mM\cos(y)} e^{jny} dy \tag{2.62}
$$

By substituting for the Bessel function relation given in Eq. (A1.7), Eq. (2.62) can be written as:

$$= j\frac{V_d}{\pi m}J_n\left(\frac{\pi}{2}Mm\right)\left[e^{j\left(\frac{3\pi}{2}m-\frac{\pi}{2}n\right)}-e^{j\left(\frac{\pi}{2}m+\frac{\pi}{2}n\right)}\right] \tag{2.63}$$

Eq. (2.63) in turn can be simplified to:

$$= \frac{2V_d}{\pi m}J_n\left(\frac{\pi}{2}Mm\right)\sin\left(\frac{\pi}{2}m+\frac{\pi}{2}n\right) \tag{2.64}$$

The latter solution represents the sideband harmonics. Substituting for Eqs. (2.55), (2.58), (2.59) and (2.64) the double Fourier series describing the unit area of Figure 2.11 can be found:

$$f_{DENPWM}(t) = \frac{V_d}{2}+\frac{V_dM}{2}\cos\left(\omega_0 t\right) \tag{2.65}$$

$$+\frac{2V_d}{\pi}\sum_{m=1}^{\infty}\frac{1}{m}J_0\left(\frac{\pi}{2}Mm\right)\sin\left(\frac{\pi}{2}m\right)\cos\left(m[\omega_c t]\right)$$

$$+\frac{2V_d}{\pi}\sum_{m=1}^{\infty}\sum_{n=\pm1}^{\pm\infty}\frac{1}{m}J_n\left(\frac{\pi}{2}Mm\right)\sin\left(\frac{\pi}{2}m+\frac{\pi}{2}n\right)\cos\left(m[\omega_c t]+n[\omega_0 t]\right)$$

2.4   SPECTRAL PLOTS AND GENERAL DISCUSSION

The spectra for the analytical method described in the previous section will now be briefly discussed. The results presented in this section are once again summarized from [17] and [13]. The Fourier coefficients defined in Eq. (2.15) represent the magnitudes of the harmonic components. The spectrum can thus easily be found through evaluation of the index variables m and n for the different values described in Section 2.3. Note that the parameters used in this section correspond to $M=0.85$, $V_d=10V$ and a carrier to fundamental ratio $\omega_c/\omega_0=384$. The voltage spectrum for LENPWM is shown in Figure 2.12 (a). From this illustration the fundamental low frequency harmonic component can be seen to be present at order 1. The first two carrier harmonics existing at integer multiples of the switching frequency, together with their respective sidebands are also shown in this spectral plot.

(a)   **(b)**
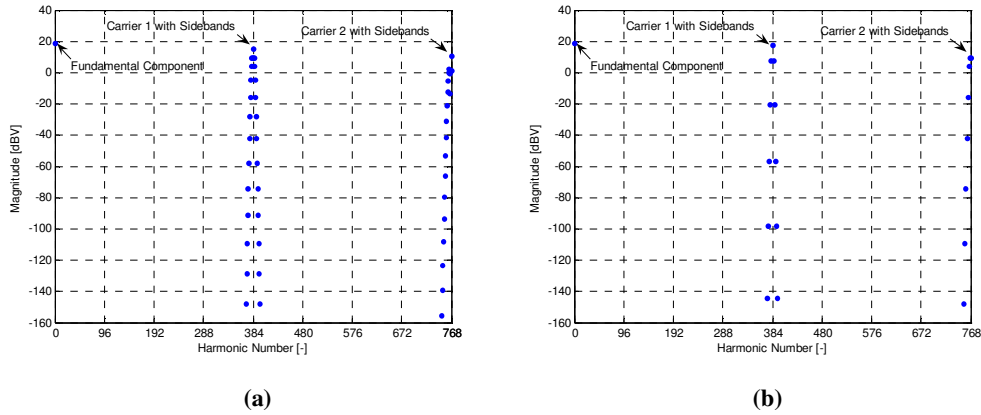
Figure 2.12: Analytical voltage spectrum of (a) LENPWM (or TENPWM), and (b) DENPWM.

Upon examination of Figure 2.1 it is evident that LENPWM is achieved when reversing the time scale of TENPWM and vice versa [17]. Stated mathematically:

$$f_{LENPWM}\left(t\right) = f_{TENPWM}\left(-t\right), \quad \text{and} \quad f_{TENPWM}\left(t\right) = f_{LENPWM}\left(-t\right) \tag{2.66}$$

As a result TENPWM produces exactly the same magnitude spectrum as LENPWM. Figure 2.12 (b) represents the harmonic voltage spectrum for DENPWM. The fundamental low frequency harmonic component represented by Eq. (2.58) is shown together with the carrier and sideband harmonics at multiples one and two of the switching frequency. Note that, upon inspection of Eq. (2.61), it is evident that the sine function equals zero for all even values of the index variable *m*. Similarly, Eq. (2.64) equals zero when either both *m* and *n* are even or when both of them are odd. This has the net effect of eliminating all even sideband harmonics around even multiples of the carrier frequency as well as cancelling all odd sideband harmonics around odd multiples of the carrier frequency.

2.5   SIMULATION STRATEGY

The analytical solutions obtained in Section 2.3 identify exactly the frequency components created by the modulation process. These harmonic components can also be found by applying the FFT to a simulated time-varying switched waveform (such as PSpice) [13]. This approach has both advantages and disadvantages. One major advantage is the reduction in mathematical effort compared to analytical computation. The downside is that the

time resolution of the simulation has to be very high in order to produce accurate crossing points between the reference and carrier waveforms. This in turn requires significant computing power, which is very time-consuming. The use of this simulation strategy is eliminated for application in this dissertation since the errors in pulse width introduced by a lack of precision could exceed the subtle non-ideal effects that some of the less dominant sources of distortion might have. The latter requirement calls for a very precise, time effective simulation method to insure accurate modelling of the non-ideal effects. In this section a novel simulation strategy based on accurate cross-point calculation using Newton−Raphson's numerical method is introduced to meet the simulation requirement.

2.5.1   THE NEWTON-RAPHSON NUMERICAL METHOD

In general, the solution to the roots of a non-linear equation cannot be found analytically and the equation is solved by approximate methods [37]. These estimates are usually based on the concept of iteration which, as a starting point, requires an initial guess. From this initial value an iterative procedure generates a set of approximations, which are assumed to presumably converge to the desired root. The Newton-Raphson method, also referred to in literature as Newton's method [38], utilizes a straight-line approximation to obtain the roots of a non-linear equation. Figure 2.13 shows an arbitrarily chosen non-linear function $f(t)$ for which a single root exists. The fundamental concept of Newton's method is to replace this non-linear function with a linear approximation in the vicinity of the root and then to solve for the latter. This linear function is chosen to be the tangent line to $f(t)$. Assume that t_0 represents the initial guess to the root of $f(t)$. The intersection of the tangent line to $f(t_0)$ with the x-axis produces a better estimate to the root than that of the initial guess. A convergent set of approximations can thus be formed by calculating the tangent at each new point of intersection produced by the previous iteration.
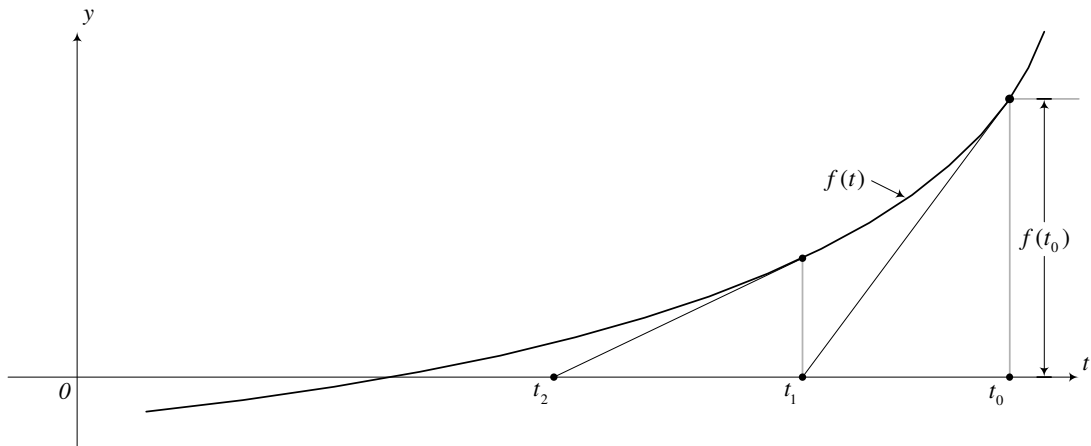
Figure 2.13: Geometric representation of the Newton-Raphson numerical method.

Through geometric analysis of Figure 2.13 an expression for the approximation to the root can now be derived. The slope of the line tangent to $f(t_0)$ can be found by calculating the ratio of variation in both the t and y direction ($\Delta y / \Delta t$). By noting that the derivative of $f(t_0)$, denoted by $f'(t_0)$. also represents the gradient the following can be stated:

$$\frac{0 - f(t_0)}{(t_0 - t_1)} = f'(t_0) \tag{2.67}$$

Solving Eq. (2.67) for t_1 leads to:

$$t_1 = t_0 - \frac{f(t_0)}{f'(t_0)} \tag{2.68}$$

The general case of Eq. (2.68) can be written as:

$$t_{n+1} = t_n - \frac{f(t_n)}{f'(t_n)} \tag{2.69}$$

Eq. (2.69) represents the solution to Newton-Raphson's numerical method. Note that the number of iterations depends on the required accuracy. By defining an error criterion $|t_{n+1} - t_n|$ to which each iteration can be compared, the process can terminate as soon as the error becomes smaller than the required accuracy.

2.5.2   CROSS-POINT CALCULATION USING NEWTON-RAPHSON'S METHOD

This section will show how Newton-Raphson's numerical method can be utilized to determine the spectra of TENPWM and DENPWM.

TENPWM

The single pulse illustrated in Figure 2.14 corresponds to the pth pulse of a TENPWM waveform, denoted by p_{TENPWM}. The low frequency modulating wave is represented by $m_{TENPWM}(t)$ while the carrier waveform is denoted by $c_{TENPWM}(t)$. The output switches to the positive rail whenever the modulating wave is greater than the carrier waveform with the inverse situation corresponding to a transition to the negative rail.

Since the leading edge of the switched output voltage remains fixed for TENPWM the width of the pulse is solely determined by the trailing edge. The crossing point of the latter two waveforms is given by:

$$m_{TENPWM}(t) = c_{TENPWM}(t), \quad \text{or alternatively} \quad m_{TENPWM}(t) - c_{TENPWM}(t) = 0 \tag{2.70}$$
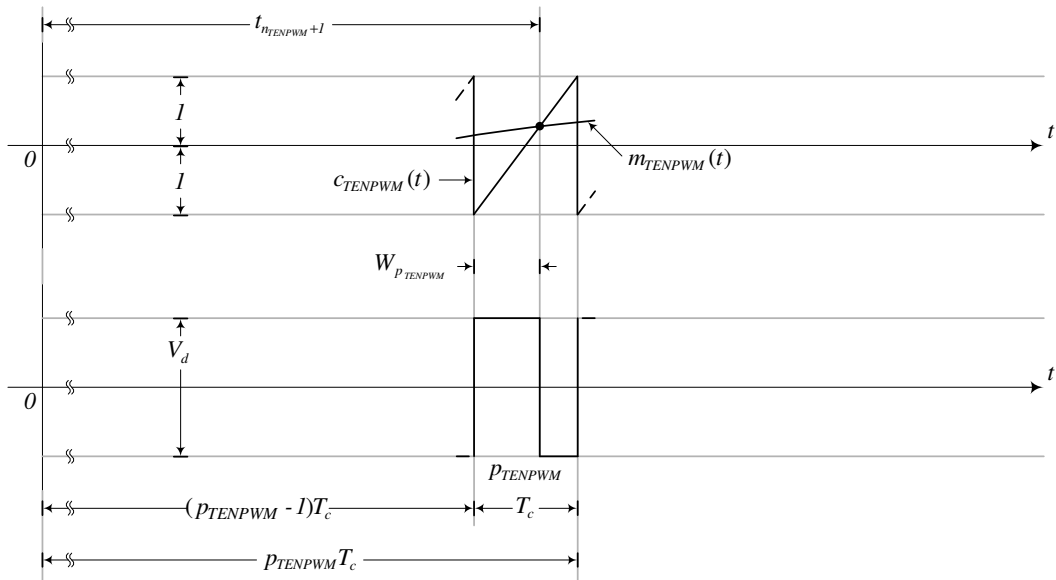
Figure 2.14: Generation of TENPWM.

The modulating wave of Eq. (2.70) is defined by:

$$m_{TENPWM}(t) = M\cos(\omega_0 t) \quad \text{with} \quad 0 < M < 1 \tag{2.71}$$

The carrier waveform, which produces the pth pulse of the switched output voltage, can be written directly from Figure 2. as:

$$c_{TENPWM}(t) = \frac{2}{T_c}t - (2p_{TENPWM} - 1) \quad \text{for} \quad (p_{TENPWM} - 1)T_c < t < p_{TENPWM}T_c \tag{2.72}$$

The nonlinear function $f_{TENPWM}(t)$ can now be defined in such a way that:

$$f_{TENPWM}(t) = m_{TENPWM}(t) - c_{TENPWM}(t) \tag{2.73}$$

Substituting for Eqs. (2.71) and (2.72), Eq. (2.73) can be simplified to:

$$= M\cos(\omega_0 t) - \frac{2}{T_c}t + (2p_{TENPWM} - 1) \quad \text{for} \quad (p_{TENPWM} - 1)T_c < t < p_{TENPWM}T_c \tag{2.74}$$

The roots of Eq. (2.74) can be determined by using the general solution to the Newton−Raphson numerical method described in Eq. (2.69). The approximation to the crossing point for TENPWM for the same limits bounding Eq. (2.74) is given by:

$$t_{n_{TENPWM}+1} = t_{n_{TENPWM}} - \frac{M\cos(\omega_0 t_{n_{TENPWM}}) - \dfrac{2}{T_c}t_{n_{TENPWM}} + (2p_{TENPWM} - 1)}{-\omega_0 M\sin(\omega_0 t_{n_{TENPWM}}) - \dfrac{2}{T_c}} \tag{2.75}$$

With the origin taken as reference, Eq. (2.75) represents the intersection of the modulating wave with the pth pulse of the carrier waveform. The width of the corresponding switched output voltage can thus be found through geometric analysis of Figure 2.14 as:

$$W_{p_{TENPWM}} = t_{n_{TENPWM}+1} - (p_{TENPWM} - 1)T_c \tag{2.76}$$

According to the definition of the carrier waveform given by Eq. (2.72), the point of intersection of the pth pulse can occur anywhere within the interval bounded by $(p_{TENPWM}-1)T_c < t < p_{TENPWM}T_c$. With the initial guess ($n=1$) chosen as one half of the latter interval quick convergence to the root will be assured.

Thus:

$$t_{1_{TENPWM}} = \left(p_{TENPWM} - \frac{1}{2} \right) T_c \tag{2.77}$$

DENPWM

Consider the pth pulse of the DENPWM waveform shown in Figure 2.15. The switching conditions are exactly the same as for TENPWM. The carrier waveform is denoted by $c_{DENPWM}(t)$, while the reference wave is represented by $m_{DENPWM}(t)$. For this method of modulation the pulse width is determined by the points of intersection of both the leading and trailing edge of the modulated waveform. The crossing point can be determined by:

$$m_{DENPWM}(t) = c_{DENPWM}(t), \quad \text{or alternatively} \quad m_{DENPWM}(t) - c_{DENPWM}(t) = 0 \tag{2.78}$$
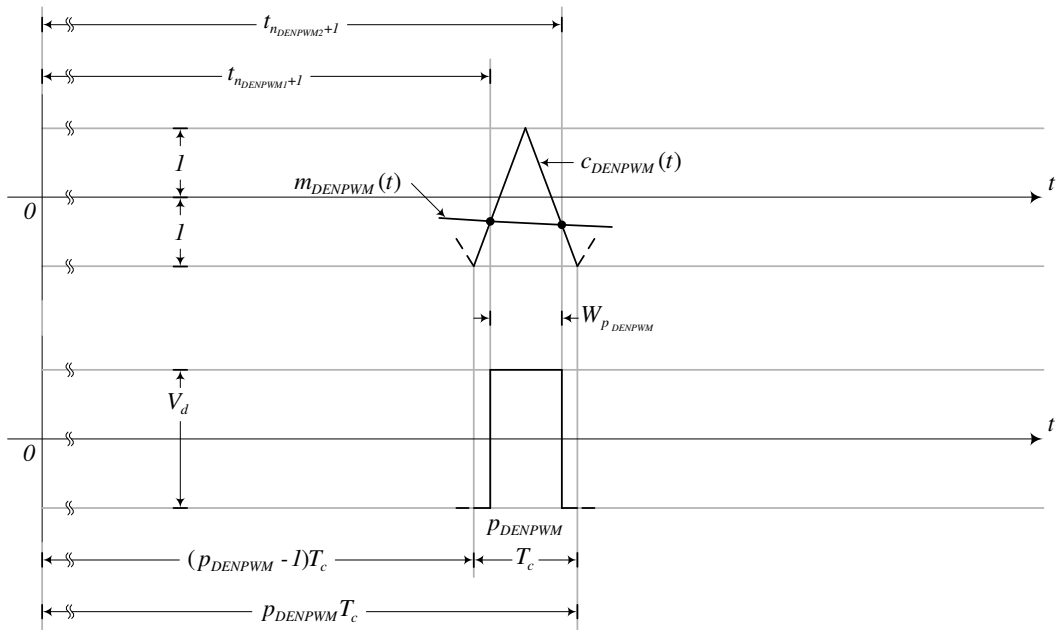
Figure 2.15: Generation of DENPWM.

With the reference waveform of Eq. (2.78) defined by:

$$m_{DENPWM}(t) = M \cos(\omega_0 t) \quad \text{with} \quad 0 < M < 1 \tag{2.79}$$

Since the carrier consist of two line segments, it must be defined over two regions as:

$$c_{DENPWM}(t) = \begin{cases} \dfrac{4}{T_c}t - \left[4(p_{DENPWM}-1)+1\right] \\[2ex] -\dfrac{4}{T_c}t + (4p_{DENPWM}-1) \end{cases} \tag{2.80}$$

For the respective regions:

$$= \begin{cases} (p_{DENPWM}-1)T_c < t < (2p_{DENPWM}-1)\dfrac{T_c}{2} \\[2ex] (2p_{DENPWM}-1)\dfrac{T_c}{2} < t < p_{DENPWM}T_c \end{cases} \tag{2.81}$$

Defining the non-linear function $f_{DENPWM}(t)$ gives:

$$f_{DENPWM}(t) = m_{DENPWM}(t) - c_{DENPWM}(t) \tag{2.82}$$

By substituting for the modulating and carrier waveforms respectively defined in Eqs. (2.79) and (2.80), Eq. (2.82) can be defined over the two intervals as:

$$= \begin{cases} M\cos(\omega_0 t) - \dfrac{4}{T_c}t + \left[4(p_{DENPWM}-1)+1\right] \\[2ex] M\cos(\omega_0 t) + \dfrac{4}{T_c}t - (4p_{DENPWM}-1) \end{cases} \tag{2.83}$$

For the respective regions:

$$= \begin{cases} (p_{DENPWM}-1)T_c < t < (2p_{DENPWM}-1)\dfrac{T_c}{2} \\[2ex] (2p_{DENPWM}-1)\dfrac{T_c}{2} < t < p_{DENPWM}T_c \end{cases} \tag{2.84}$$

An approximation to the roots of Eqs. (2.83) can be found by applying Newton's method in Eq. (2.69).

Thus, the estimate of the intersection of the modulating and carrier waveforms for DENPWM over the region $(p_{DENPWM}-1)T_c<t<(2p_{DENPWM}-1)T_c/2$ can be defined as:

$$t_{n_{DENPWM1}+1}=t_{n_{DENPWM1}}-\frac{M\cos\left(\omega_0 t_{n_{DENPWM1}}\right)-\frac{4}{T_c}t_{n_{DENPWM1}}+\left[4\left(p_{DENPWM}-1\right)+1\right]}{-\omega_0 M\sin\left(\omega_0 t_{n_{DENPWM1}}\right)-\frac{4}{T_c}} \qquad (2.85)$$

For the interval bounded by $(2p_{DENPWM}-1)T_c/2<t<p_{DENPWM}T_c$ the intersection is given by:

$$t_{n_{DENPWM2}+1}=t_{n_{DENPWM2}}-\frac{M\cos\left(\omega_0 t_{n_{DENPWM2}}\right)-\frac{4}{T_c}t_{n_{DENPWM2}}-\left(4p_{DENPWM}-1\right)}{-\omega_0 M\sin\left(\omega_0 t_{n_{DENPWM2}}\right)-\frac{4}{T_c}} \qquad (2.86)$$

From Figure 2.15 it is evident that the width of the pth pulse can be found by calculating the difference between Eqs. (2.85) and (2.86), which leads to the expression:

$$W_{p\,DENPWM}=t_{n_{DENPWM2}+1}-t_{n_{DENPWM1}+1} \qquad (2.87)$$

Using a similar argument as for TENPWM, the initial guess' ($n=1$) of Eqs. (2.85) and (2.86) can be established as:

$$t_{1_{DENPWM1}}=\frac{T_c}{4}\left[4\left(p_{DENPWM}-1\right)+1\right] \qquad (2.88)$$

$$t_{1_{DENPWM2}}=\frac{T_c}{4}\left(4p_{DENPWM}-1\right) \qquad (2.89)$$

Spectra of TENPWM and DENPWM

Consider the single rectangular pulse, denoted by $g_i(t)$ where $-\infty<i<+\infty$, with amplitude V_d and width W_p illustrated in Figure 2.16 (a), generated as a result of a NPWM process. In order to simplify the mathematical representation and analysis of this function, $g_i(t)$ was chosen to be situated around the origin with a DC offset equal to $V_d/2$.
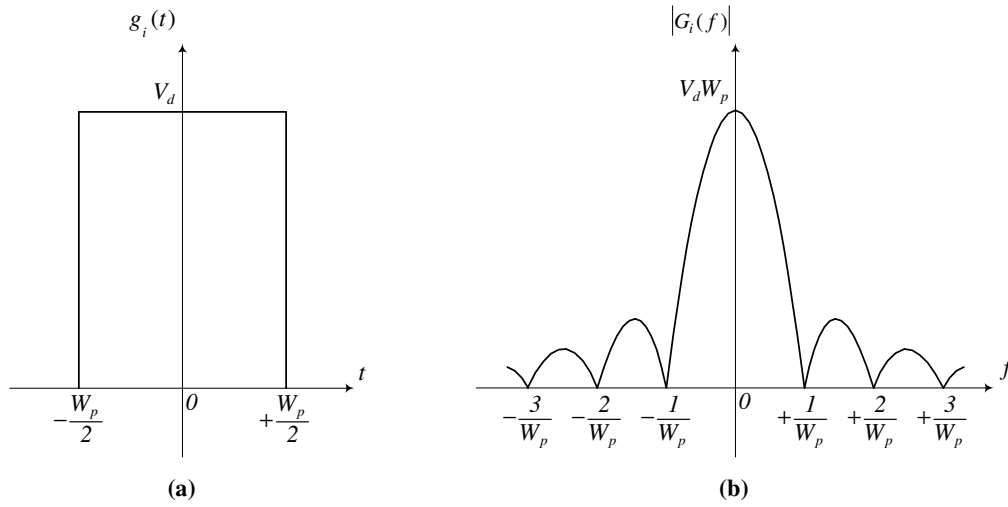
Figure 2.16: (a) Time domain and (b) magnitude spectrum representation of a rectangular pulse.

The rectangular function of Figure 2.16 (a) can be described mathematically by:

$$g_i(t) = \begin{cases} V_d & \text{for the region} \quad -\frac{W_p}{2} < t < \frac{W_p}{2} \\ 0 & \text{elsewhere} \end{cases}$$

(2.90)

The Fourier Transform of $g_i(t)$, denoted by $G_i(f)$, can be computed as:

$$G_i(f) = \int_{-\frac{W_p}{2}}^{\frac{W_p}{2}} V_d e^{-j2\pi ft} dt$$

$$= V_d W_p \left[\frac{\sin(\pi f W_p)}{\pi f W_p} \right]$$

(2.91)

To simplify the result, the function in brackets can be further reduced by defining the sinc function often found in communications theory [40]. It is defined as:

$$\text{sinc}(\lambda) = \frac{\sin(\pi\lambda)}{\pi\lambda}$$

(2.92)

Where λ represents the independent variable. As shown in Figure 2.17, the function decays as λ increases, oscillating through positive and negative values with its zero crossings existing at integer values of λ.
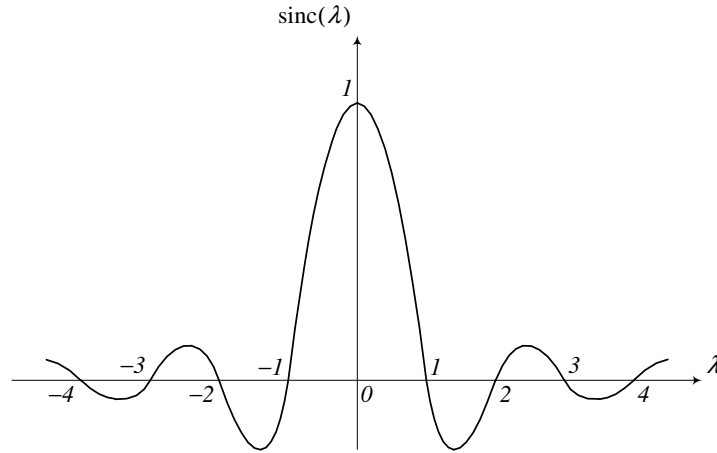
Figure 2.17: The sinc function.

It has a maximum value of unity at $\lambda=0$. By noting that $\lambda=fW_p$ Eq. (2.91) reduces to:

$$G_i(f) = V_d W_p \text{sinc}(fW_p) \tag{2.93}$$

Figure 2.16 (b) shows the magnitude spectrum $|G_i(f)|$ of the rectangular pulse $g_i(t)$. Consider the pulse of Figure 2.18 (a). Suppose that this pulse is shifted by a constant time t_0 in such a way that its leading edge coincides with that of Figure 2.18. For the pth pulse of a TENPWM waveform this time shift t_0 corresponds to:

$$t_0 = (p_{TENPWM} - 1)T_c + \frac{W_{p\,TENPWM}}{2} \tag{2.94}$$

In a similar manner the DENPWM of Figure 2.15 can also be related to the pulse of Figure 2.16 (a). This is given by:

$$t_0 = t_{n_{DENPWM}+1} + \frac{W_{p\,DENPWM}}{2} \tag{2.95}$$

Figure 2.18 illustrates the time shifting of the rectangular pulse of Figure 2.16 (a) by a constant amount t_0. Depending on the method of modulation, the width W_p can either correspond to Eq. (2.76) or (2.87).
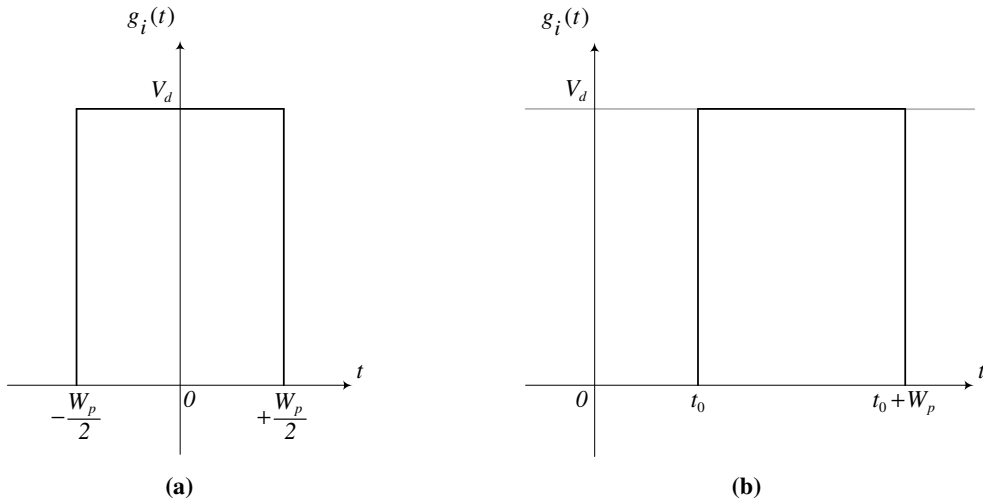
Figure 2.18: Time shifting of the rectangular pulse of Figure 2.16 (a).

The effect of the time shift on the spectrum can be determined by calculating the Fourier Transform of the pulse illustrated in Figure 2.18 (b) as:

$$G_i(f) = \int_{t_0}^{t_0+W_p} V_d e^{-j2\pi ft} dt$$

$$= V_d W_p \text{sinc}(fW_p) e^{-j2\pi ft_0} \tag{2.96}$$

From Eq. (2.96) it is evident that, if the function $g_i(t)$ is shifted by a positive constant time t_0, it is the equivalent of multiplying its Fourier Transform by a factor $\exp(-2\pi ft_0)$ [40]. The multiplication has the effect of only altering the phase of $G_i(f)$ by an amount corresponding to $-2\pi ft_0$ while the magnitude remains unaffected. From this discussion it is evident that each individual pulse of a PWM waveform can be represented by a rectangular wave shifted by some constant time t_0. The complete pulse train, denoted by $g(t)$, can be found as:

$$g(t) = \sum_{i=-\infty}^{\infty} g_i(t) \tag{2.97}$$

Where $g_i(t)$ is defined in Eq. (2.96). Applying the Fourier Transform, the result yields:

$$\Im[g(t)] = \Im\left[\sum_{i=-\infty}^{\infty} g_i(t)\right] \tag{2.98}$$

From Lebesgue's Convergence Theorem 15 [41] it can be shown that:

$$\Im\big[g(t)\big] = \sum_{i=-\infty}^{\infty} \Im\big[g_i(t)\big] \tag{2.99}$$

2.5.3 SIMULATION RESULTS

Table 2.1 and Table 2.2 respectively compare the analytical results to the simulations for TENPWM and DENPWM using the proposed strategy. The conditions used correspond to those of Section 2.4. The fundamental component and first carrier with its respective sideband harmonis are shown in both tables.

TABLE 2.1

COMPARISON OF ANALYTICAL AND SIMULATION RESULTS FOR TENPWM.

Harmonic Number [-]	Analytical Magnitude [V]	Simulated Magnitude [V]
1	8.5000	8.5000
…	…	…
382	2.9709	2.9709
383	2.8683	2.8683
384	5.5435	5.5435
385	2.8683	2.8683
386	2.9709	2.9709

The results of the simulations of both TENPWM and DENPWM are consistent with the analytical solutions, which confirms the validity of the proposed model. Note that the simulations were performed with ten iterations of Newton's method (accurate to −280 dB). As already mentioned in Section 2.4, all even sideband harmonics around even multiples of the carrier frequency as well as all odd sidebands around odd multiples of the carrier frequency are eliminated for ideal DENPWM.

TABLE 2.2

COMPARISON OF ANALYTICAL AND SIMULATION RESULTS FOR DENPWM.

Harmonic Number [-]	Analytical Magnitude [V]	Simulated Magnitude [V]
1	8.5000	8.5000
…	…	…
382	2.4385	2.4385
383	0.0000	0.0000
384	7.6596	7.6596
385	0.0000	0.0000
386	2.4385	2.4385

2.6   GENERAL DISCUSSION

Consider the analytical and simulated spectra of TENPWM respectively shown in Figure 2.19 (a) and (b) for $\omega_c/\omega_0=8$. The remaining parameters correspond to those of the previous section. The fundamental low frequency harmonic component and the first two carrier harmonics ($m=1$ and $m=2$) together with their respective sidebands are shown. Since the index variables of the analytical solutions of Section 2.4 define a specific harmonic according to the relation $m\omega_c+n\omega_0$ it is possible to plot the individual contribution of $m=1$ and $m=2$ with its respective sidebands. This is shown in Figure 2.19 (a).
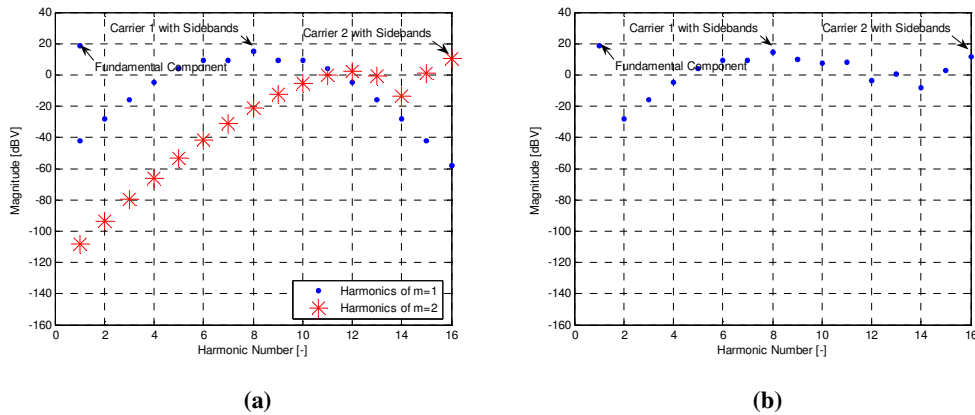
Figure 2.19: (a) Analytical and (b) simulated spectrum of TENPWM with $\omega_c/\omega_0=8$.

The spectrum shown in Figure 2.19 (b) differs significantly from that shown in (a). The reason for this is that the various overlapping harmonics of the analytical solution have been plotted individually, and not summed. The harmonic magnitudes of the spectra of Figure 2.19 (a) and (b) are compared in Table 2.3. Note that the analytical solution in (a) will produce the same result as in (b) if the various overlapping harmonics are summed. The value of ω_c/ω_0 used was merely for purposes of illustration of the concept and is not realistic for implementation in practical systems. Moreover, the phasor summation of the harmonic components is not of great concern when considering the ideal case at high carrier to fundamental ratios due to its negligible amplitude caused by the rapid decay of the sidebands. However, as will be shown in Chapters 5 to 9, when considering non-ideal effects these sidebands do not decay as quickly.

TABLE 2.3

ANALYTICAL AND SIMULATED HARMONIC MAGNITUDES OF THE SPECTRUM SHOWN IN FIGURE 2.19.

Harmonic Number [-]	Analytical Magnitude [V]	Simulated Magnitude [V]
1	8.5000	8.5074
…	…	…
6	2.9709	2.9626
7	2.8683	2.8394
8	5.5435	5.4544
9	2.8683	3.1061
10	2.9709	2.4372

The analytical analysis provides a tool with which the sole contribution of each harmonic component is established, more specifically, the individual contribution of the baseband and sideband harmonics within the audible band.

2.7 SUMMARY

Fundamental concepts of PWM were considered, after which the double Fourier series method of analysis for calculating the spectrum of PWM analytically was reviewed. A simulation strategy, based on Newton's numerical method, was introduced which allows for

rapid and accurate calculation of the spectrum of PWM. The results of the proposed simulation strategy correlated to those of the analytical method, verifying its validity.

3
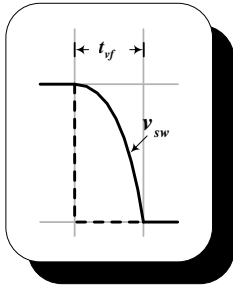
INCORPORATION OF PTES IN THE

DOUBLE FOURIER SERIES METHOD

3.1   INTRODUCTION

A method, introduced in the paper "*Analytical Calculation of the Output Harmonics in a Power Electronic Inverter with Current Dependent Pulse Timing Errors*" [34] by the author, for the incorporation of current dependent PTEs within the double Fourier series method of analysis is considered in this chapter.

The incorporation of dead time within W.R. Bennet's [11] method has been reported in [22], which effectively includes a current polarity dependent delay within the ideal analysis. In this chapter the analysis in [22] is generalised and extended. This serves as a general analytical tool in which the harmonic components of a NPWM waveform can be calculated in the presence of current dependent PTEs. The analysis starts off with a brief overview of a known approximation to the inductor ripple current in Section 3.2. The analysis presented in Sections 3.3 to 3.6 covers the incorporation of the PTEs within the 3-D unit area. A general analysis of that presented in [22] for the inclusion of a constant delay which is independent of current is given in Section 3.3. A purely sinusoidal current dependency is included in Sections 3.4 and 3.5, respectively covering a polarity dependency and non-linear magnitude dependency. In addition to the analysis in [22] the former section distinguishes between sampling on the leading or trailing edge of the NPWM waveform. Section 3.6 shows how the inductor current model of Section 3.2 can be incorporated into the 3-D unit area.

3.2   REALISTIC INDUCTOR CURRENT MODEL

Since the expressions describing the various PTEs and PAEs are current dependent, it is imperative that a proper and accurate inductor current model first be established before proceeding with the construction of the analytical and simulation models in Chapters 5 to 9.

Consider the inductor voltage $v_{L(ideal)}$ and current $i_{L(ideal)}$ waveforms for an ideal switching transition illustrated in Figure 3.1. This illustration represents a half-bridge topology with V_d being the applied bus voltage.
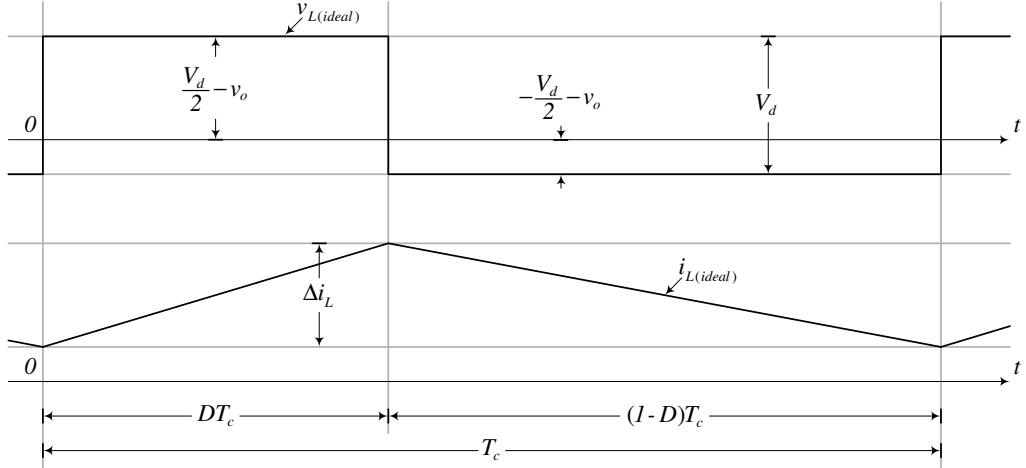
Figure 3.1: Voltage across and current through the inductor.

By next assuming that v_o remains constant over one cycle of the switching period an expression describing Δi_L can be constructed from Figure 3.1 as:

$$\Delta i_L = \frac{1}{L_{filt}} \int_0^{DT_c} \left(\frac{V_d}{2} - v_o \right) dt = \frac{1}{L_{filt}} \left(\frac{V_d}{2} - v_o \right) DT_c \tag{3.1}$$

Where v_o is assumed to follow the reference voltage exactly. Thus:

$$v_o = \frac{V_d M}{2} \cos\left(2\pi f_0 t\right) \tag{3.2}$$

By next substituting Eq. (3.2) into Eq. (3.1) and noting that $D=((1+M\cos(2\pi f_0 t)/2)$, the expression in Eq. (3.1) is simplified to:

$$\Delta i_L = \frac{V_d}{2 L_{filt} f_c} \left(D - D^2 \right) \tag{3.3}$$

The result achieved was also noted in [33]. From Eq. (3.3) it can be seen that the maximum deviation in Δi_L occurs at $D=50\%$ while the minimum is established at either the

maximum or minimum value of D. The remainder of this section identifies two possible scenarios in which the inductor current can manifest itself. Figure 3.2 defines the upper and lower envelope of the inductor current which is respectively represented by $i_{L(upper\_env)}$ and $i_{L(lower\_env)}$. Current i_o is assumed to be purely sinusoidal as well as in phase with the output voltage. Variables $i_{L(upper\_env)}$ and $i_{L(lower\_env)}$ can respectively be defined as:

$$i_{L(upper\_env)} = I_o \cos\left(2\pi f_0 t\right) + \frac{\Delta i_L}{2} \tag{3.4}$$

$$i_{L(lower\_env)} = I_o \cos\left(2\pi f_0 t\right) - \frac{\Delta i_L}{2} \tag{3.5}$$

Where Δi_L is defined in Eq. (3.3) and:

$$I_o = \frac{V_d M}{2 R_{load}} \tag{3.6}$$

From Figure 3.2 (a) and (b) two scenarios of the inductor current can be defined. For (a) M was chosen such that $i_{L(upper\_env)}$ is always distinctly positive and $i_{L(lower\_env)}$ is always distinctly negative. This condition governs inductor current Scenario ①.

| (a) | (b) |
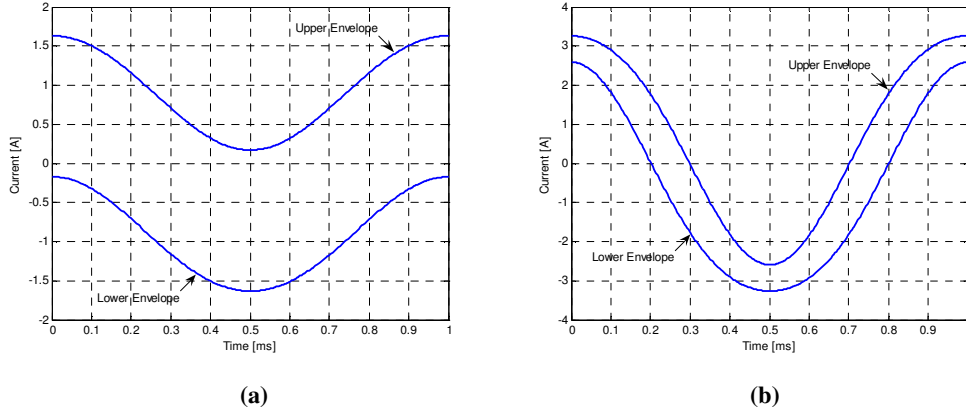
Figure 3.2: Definition of the inductor current for (a) Scenario ① and (a) Scenario ②.

Scenario ② occurs when both $i_{L(upper\_env)}$ and $i_{L(lower\_env)}$ cross through zero at some point in time over one complete cycle of the modulating waveform. This is shown in Figure 3.2 (b). Note that during this state $i_{L(upper\_env)}$ and $i_{L(lower\_env)}$ are still defined by Eqs. (3.4) and (3.5).

TABLE 3.1

DEFINITION OF THE BASIC VARIABLES USED THROUGHOUT THIS CHAPTER.

Variable	Value
V_d	10 V
R_L	8.2 Ω
L_{filt}	10.4 uH
f_0	1 kHz
f_c	384 kHz

Unless stated otherwise, the basic variables used within the rest of this chapter correspond to those defined in Table 3.1. When referring to results *within Scenario* ① or *within Scenario* ②, the governing condition described holds.

3.3   INCORPORATION OF TIME DELAYS

Suppose that the duty cycle of an ideal TENPWM waveform needs to be altered in order to produce a constant positive DC offset $V_{DC(offset)}$ with respect to the ideal case. A possible solution for achieving this requirement is to adapt the switching strategy in such a way that the modulated (trailing) edge of the switched output voltage's turn-*on* is delayed by some constant time t_d. Similarly, still for a TENPWM waveform, assume that the same negative constant DC offset $-V_{DC(offset)}$ relative to the ideal case is required. This can be achieved by delaying the unmodulated (leading) edge by t_d. The relation between $V_{DC(offset)}$ and t_d for the two scenarios can be found by averaging the delay over a complete switching cycle which results in:

$$V_{DC(offset)} = \begin{cases} +t_d V_d f_c & \text{for the trailing edge} \\ -t_d V_d f_c & \text{for the leading edge} \end{cases} \tag{3.7}$$

The following two sub-sections show how these requirements can be incorporated into the 3-D unit area.

3.3.1 MODULATED EDGE

Figure 3.3 illustrates an extract of pulses of a TENPWM waveform with the modulated edge delayed by t_d. The ideal modulated edge is represented by the dashed line.
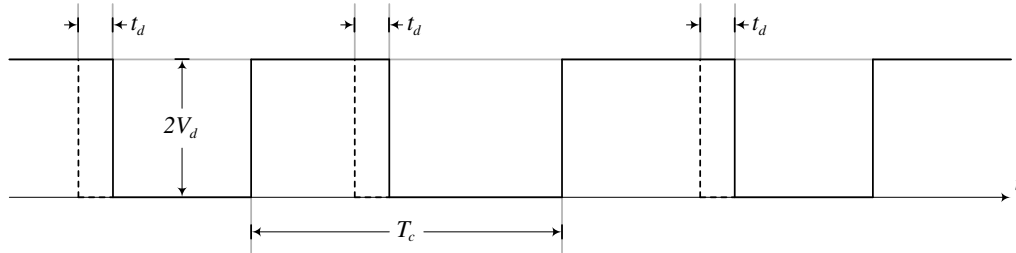
Figure 3.3: Definition of t_d introduced on the modulated edge.

The incorporation of time delays within the double Fourier series method of analysis necessitates a slight modification within the unit area. Since the pulse train is defined along the intersection of the straight line $y=(\omega_0/\omega_c)x$ with the various walls within the 3-D unit area, the corresponding mapping of t_d (in radians) Φ_d' needs to be defined along the this line. Figure 3.4 shows a visual representation of this concept.
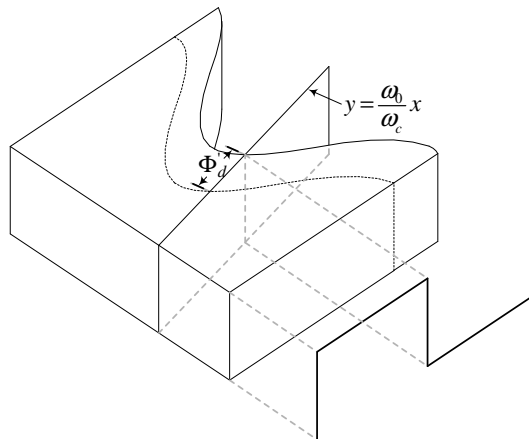
Figure 3.4: Definition of the constant time delay mapping Φ_d' within the 3-D unit area.

Consider Figure 3.5 which shows a two-dimensional (2-D) representation of Figure 3.4. The function defining the modulated edge thus needs to be shifted in both the *x* and *y*

directions in such a way that point *A* is now located at *A'* with the distance from *A* to *A'* equaling Φ_d'. However, since the pulse train is represented by the projection of the intersection of the function defined along the straight line $y=(\omega_0/\omega_c)x$ onto a plane parallel to the *x*-axis the actual time delay introduced is Φ_d instead of Φ_d'. This results in an error Φ_{err} being introduced.
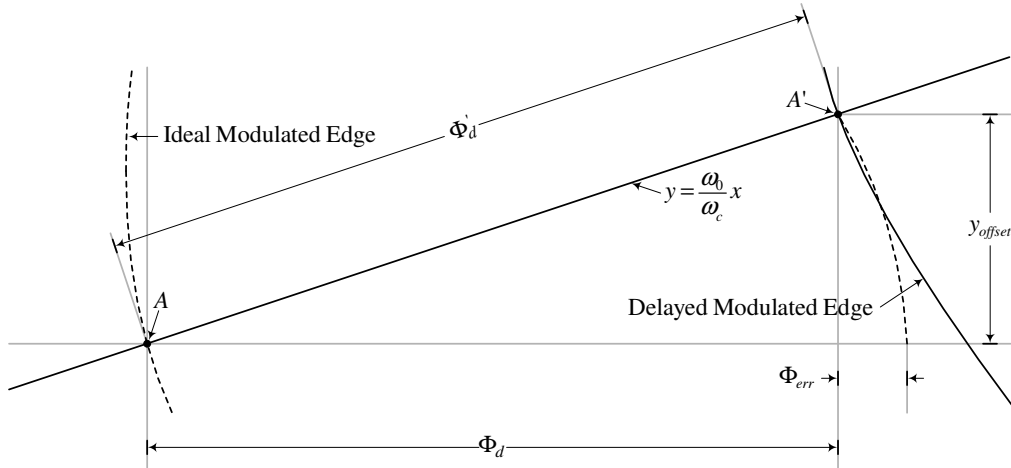
Figure 3.5: 2-D representation of the error introduced for the modulated edge.

The correct delay can be included into the unit area by shifting the ideal modulated edge by the corresponding radians $\Phi_d=2\pi f_c t_d$ (since the mapping of $T_c=2\pi$ within the unit area) in the positive *x*-direction, and adjusting the *y*-offset (denoted y_{offset}) in such a way that point *A* coincides with *A'*, i.e. $y_{offset}=(\omega_0/\omega_c)\Phi_d$. If it is assumed that the ideal modulated edge is described by $x=\pi M\cos(y)+\pi$, the delayed edge is given by:

$$x = \pi M \cos\left(y - y_{offset}\right) + \pi + \Phi_d \tag{3.8}$$

This is illustrated in Figure 3.6. By next inserting the limits defined in Figure 3.6 the complex Fourier coefficient of Eq. (2.15) can be written as:

$$C_{mn} = \frac{V_d}{\pi^2} \int\limits_0^{2\pi} \left[\int\limits_0^{\pi M \cos\left(y - y_{offset}\right) + \pi + \Phi_d} e^{jmx} dx \right] e^{jny} dy \tag{3.9}$$
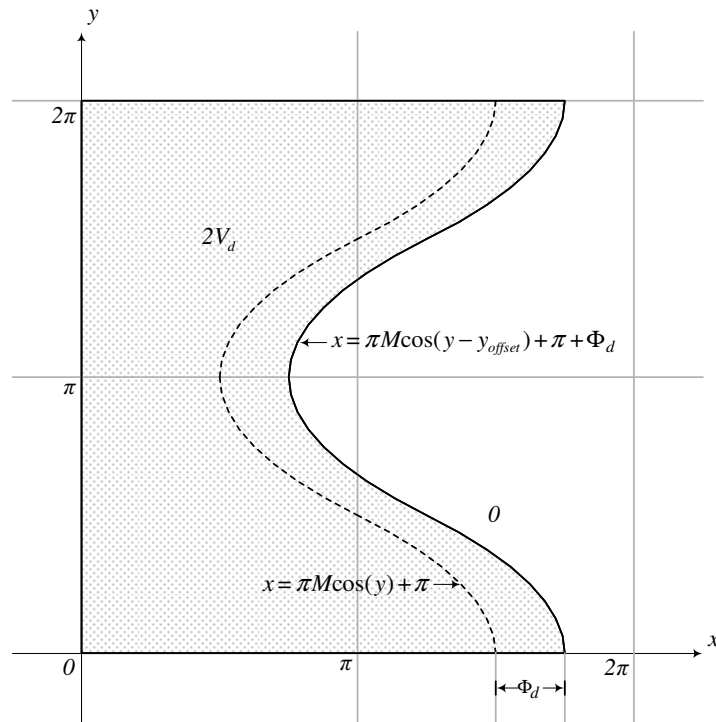
Figure 3.6: 3-D unit area for TENPWM with delay Φ_d.

Table 3.2 compares the analytical and simulation results for TENPWM with the addition of the delay. Note that t_d=10ns and M=0.8. It is evident that the harmonic magnitudes of the analytical and simulation results correlate, which verifies the validity of the argument.

TABLE 3.2

COMPARISON OF ANALYTICAL AND SIMULATION RESULTS FOR TENPWM WITH A CONSTANT TIME DELAY

INTRODUCED ON THE MODULATED EDGE.

Harmonic Number	Analytical Magnitude [V]	Simulated Magnitude [V]
1	8.0000	8.0000
…	…	…
383	3.1435	3.1435
384	6.0866	6.0866
385	3.1435	3.1435

3.3.2 UNMODULATED EDGE

Figure 3.7 shows an extract of the pulses of a TENPWM waveform with the leading edge delayed by t_d. The ideal modulated edge is once again represented by the dashed line.
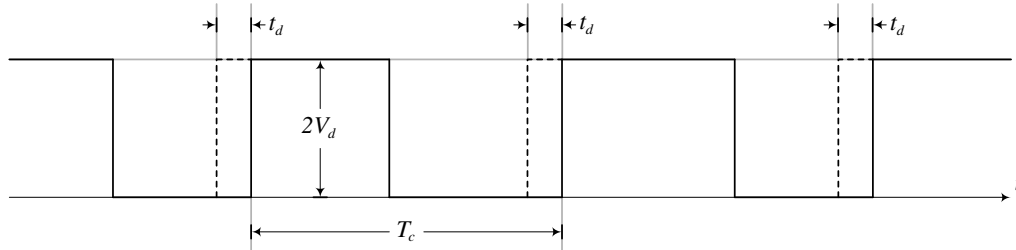
Figure 3.7: Definition of t_d introduced on the unmodulated edge.

Consider Figure 3.8 which represents a 2-D sketch of the error introduced on the unmodulated edge of a TENPWM waveform. In a similar manner as described in Section 3.3.1, the unmodulated edge needs to be shifted in the x direction by an amount Φ_d. However, since the leading edge is unmodulated, i.e. independent of y, the projection of the intersection of the function defined along the straight line $y=(\omega_0/\omega_c)x$ with point A' produces the same projected distance Φ_d onto a plane parallel to the x-axis as the projection of the intersection of a function defined along a line parallel to the x-axis and point B.
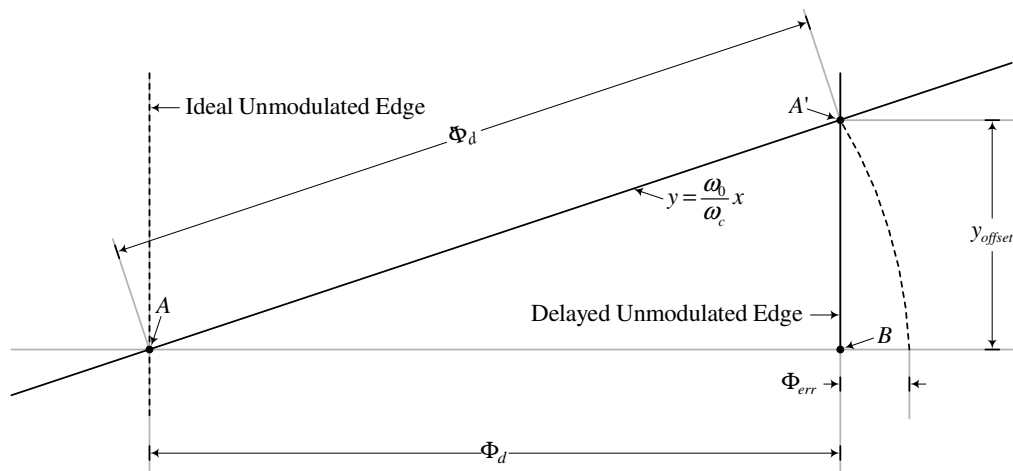
Figure 3.8: 2-D representation of the error introduced for the unmodulated edge.

It is thus evident that, for an unmodulated edge (no *y*-dependency), no correction is necessary in the *y* direction. The corresponding delay within the unit area is thus simply defined by $\Phi_d = 2\pi f_c t_d$.

3.4   INCORPORATION OF A SINUSOIDAL CURRENT POLARITY DEPENDENCY

Consider a TENPWM waveform which is governed by some inductor current polarity dependency. Suppose that, during the negative half-cycle of a purely sinusoidal inductor current, the trailing edge is delayed by an arbitrarily chosen time (denoted t_d). This section shows how this condition can be incorporated into the 3-D unit area. Since the current polarity can be sampled on either edge of the TENPWM waveform the analysis needs to be divided into two parts.

3.4.1   POLARITY DEPENDENCY SAMPLED ON THE TRAILING EDGE

In this section it is assumed that the current polarity is sampled on the time instant of switching of the ideal modulated trailing edge. This sampling process is illustrated in Figure 3.9 for a carrier to fundamental ratio chosen as $\omega_c/\omega_0=5$. Note that the ideal modulated edge is represented by the dashed line.
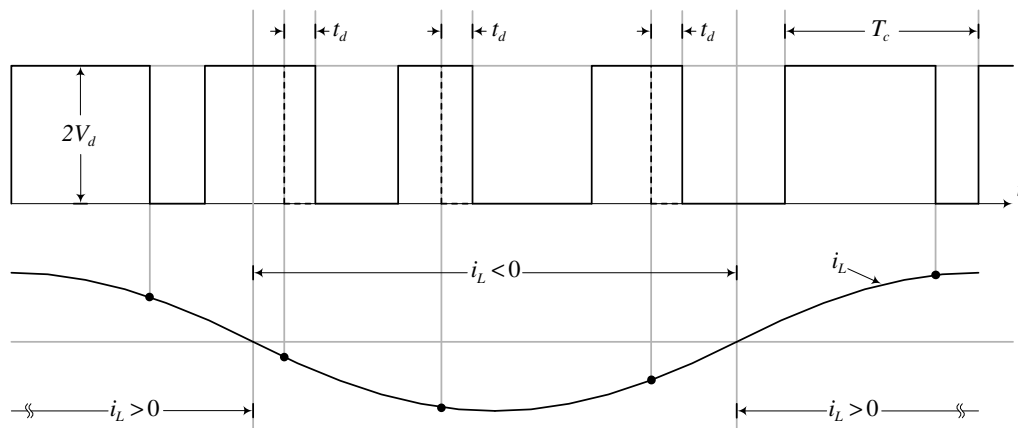
Figure 3.9: Proposed arbitrary inductor current polarity dependency sampled on the ideal trailing edge.

This condition can next be integrated into the 3-D unit area. Firstly, the various areas within the unit area, during which the inductor current is positive and negative, need to be identified. Since the polarity is assumed to be sampled on the switching instant of the ideal modulated edge the current polarity can be defined over the regions as shown in Figure 3.10.
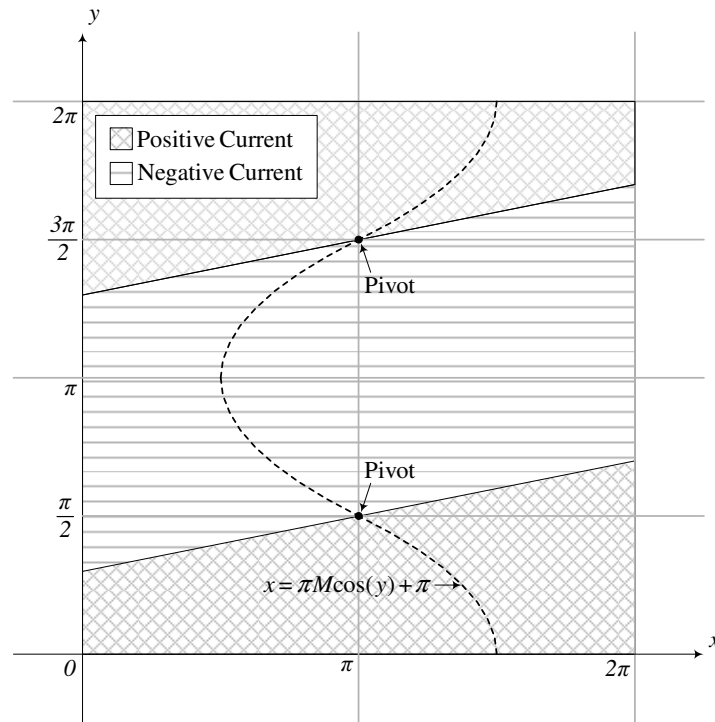
Figure 3.10: Definition of the various current zones within the 3-D unit area.

The slope with pivots existing at the polarity transition sampled on the trailing edge illustrated ($y=\pi/2$ and $y=3\pi/2$) is necessary in order to keep the sampled current polarity constant over the region $0<x\leq2\pi$. Figure 3.11 represents a combination of Figure 3.9 and Figure 3.10 with the required mapping. The relation within the 3-D unit area using the proposed polarity sampling process is clearly visible from this illustration. Consider the region within Figure 3.11 for which the inductor current is negative. In this area the trailing edge is delayed by t_d in accordance with the original requirement. A corresponding mapping equalling $\Phi_d=2\pi f_c t_d$ thus needs to be introduced in accordance with the analysis described in Section 3.3.1. In the region where the inductor current is positive, both the leading and trailing edges correspond to those of ideal TENPWM.
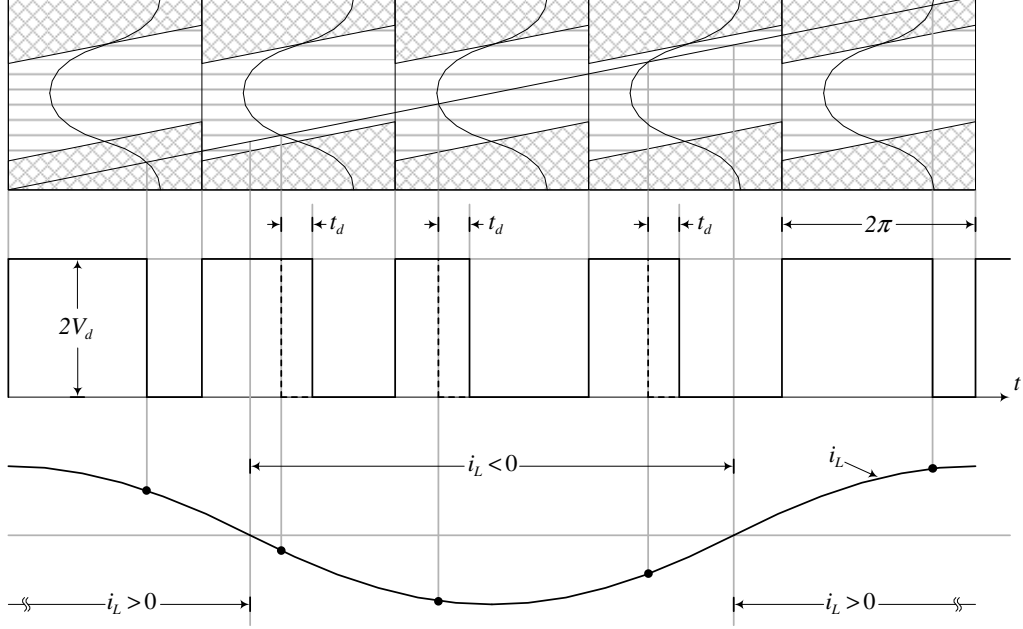
Figure 3.11: Combination of Figure 3.9 and Figure 3.10 illustrating the sampling process.

The 3-D unit area describing these conditions is shown in Figure 3.12. Note that the linear sections existing within intervals $y_1 < y \leq y_2$ and $y_3 < y \leq y_4$ are defined at a slope ω_0/ω_c to ensure a single crossing point at the intersection of line $y = (\omega_0/\omega_c)x$ with the walls. The complex Fourier coefficient of Eq. (2.15) can next be written by inserting the limits defined in Figure 3.12 such that:

$$C_{mn} = \frac{V_d}{\pi^2} \left[\int_0^{y_1} \left[\int_0^{\pi M \cos(y)+\pi} e^{jmx} dx \right] e^{jny} dy + \int_{y_1}^{y_2} \left[\int_0^{\frac{\omega_c}{\omega_0}(y-y_1)+\pi} e^{jmx} dx \right] e^{jny} dy + \right. \tag{3.10}$$

$$\left. + \int_{y_2}^{y_3} \left[\int_0^{\pi M \cos(y-y_{offset})+\pi+\Phi_d} e^{jmx} dx \right] e^{jny} dy + \int_{y_3}^{2\pi} \left[\int_0^{\pi M \cos(y)+\pi} e^{jmx} dx \right] e^{jny} dy + \int_{y_3}^{y_4} \left[\int_0^{\frac{\omega_c}{\omega_0}(y-y_3)+\pi} e^{jmx} dx \right] e^{jny} dy \right]$$

Where $y_1 = \pi/2$, $y_2 = \pi/2 + (\omega_0/\omega_c)\Phi_d$, $y_3 = 3\pi/2$ and $y_4 = 3\pi/2 + (\omega_0/\omega_c)\Phi_d$.
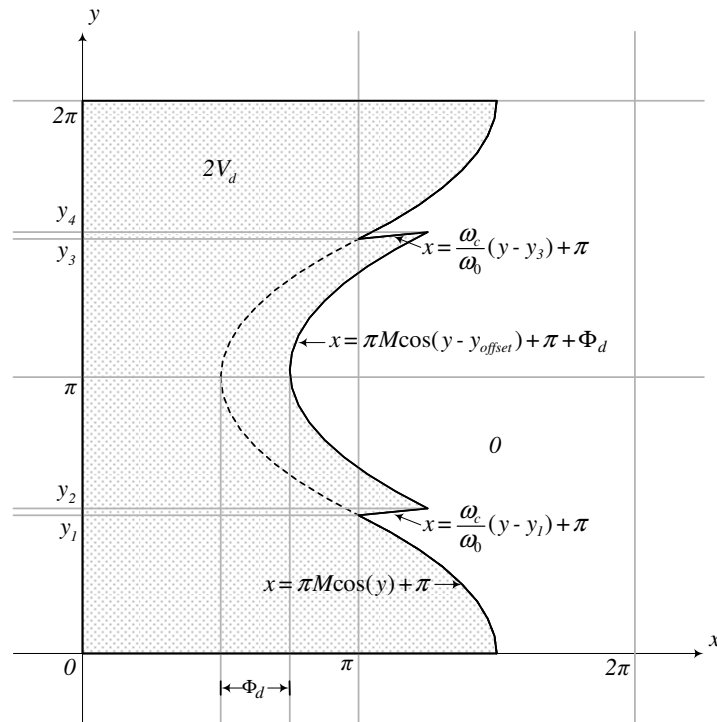
Figure 3.12: 3-D unit area for TENPWM with current polarity dependency.

Table 3.3 shows a comparison between the analytical and simulation results for TENPWM including the current polarity conditions. The parameters used correspond to $t_d=10\text{ns}$ and $M=0.8$. The analytical and simulation results correlate.

TABLE 3.3

COMPARISON OF ANALYTICAL AND SIMULATION RESULTS FOR TENPWM WITH INDUCTOR CURRENT POLARITY

CONDITION SAMPLED ON THE TRAILING EDGE.

Harmonic Number	Analytical Magnitude [V]	Simulated Magnitude [V]
1	7.9511	7.9511
2	0.0002	0.0002
3	0.0163	0.0163
…	…	…
383	3.1609	3.1609
384	6.0722	6.0722
385	3.1613	3.1613

3.4.2   POLARITY DEPENDENCY SAMPLED ON THE LEADING EDGE

In this section it is assumed that the current polarity is sampled on the time instant of switching of the ideal unmodulated leading edge. This is shown in Figure 3.13 for a carrier to fundamental ratio $\omega_c/\omega_0=5$. The ideal modulated edge is represented by the dashed line.
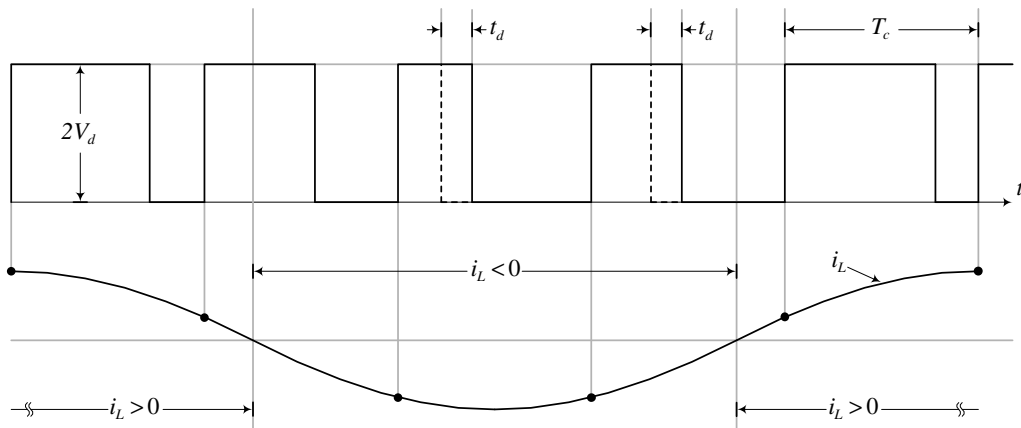
Figure 3.13: Proposed arbitrary inductor current polarity dependency sampled on the ideal leading edge.

Similar to methodology followed in Section 3.4.1, the first step in integrating the condition described in Figure 3.13 into the 3-D unit area is to define the various regions for which the inductor current is positive and negative. Since the current polarity is assumed to be sampled on the leading edge the various regions need to be defined at a slope ω_0/ω_c as shown in Figure 3.14, with the pivot point as indicated. This ensures that the polarity sample is held constant over a single switching period $0<x\leq2\pi$.
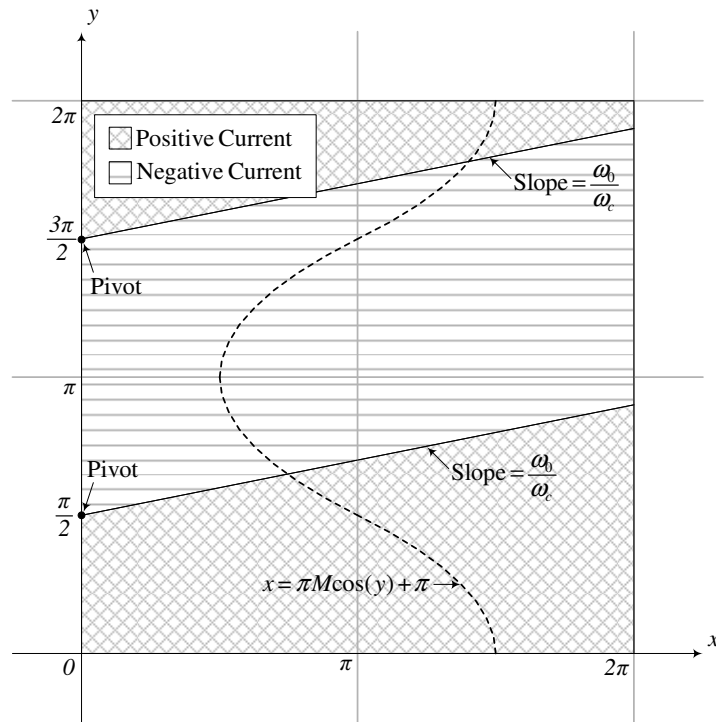
Figure 3.14: Definition of the various current zones within the 3-D unit area.

A combination of Figure 3.13 and Figure 3.14 is shown in Figure 3.15. From this illustration it can be seen how the polarity is sampled and held over a single switching period. From Figure 3.13 it is evident that the trailing edge need to be delayed by t_d if the current polarity is negative on the switching instant of the ideal unmodulated leading edge. Once again a corresponding mapping of $\Phi_d = 2\pi t_d f_c$ needs to be introduced within the region in Figure 3.14 for which the inductor current is negative.
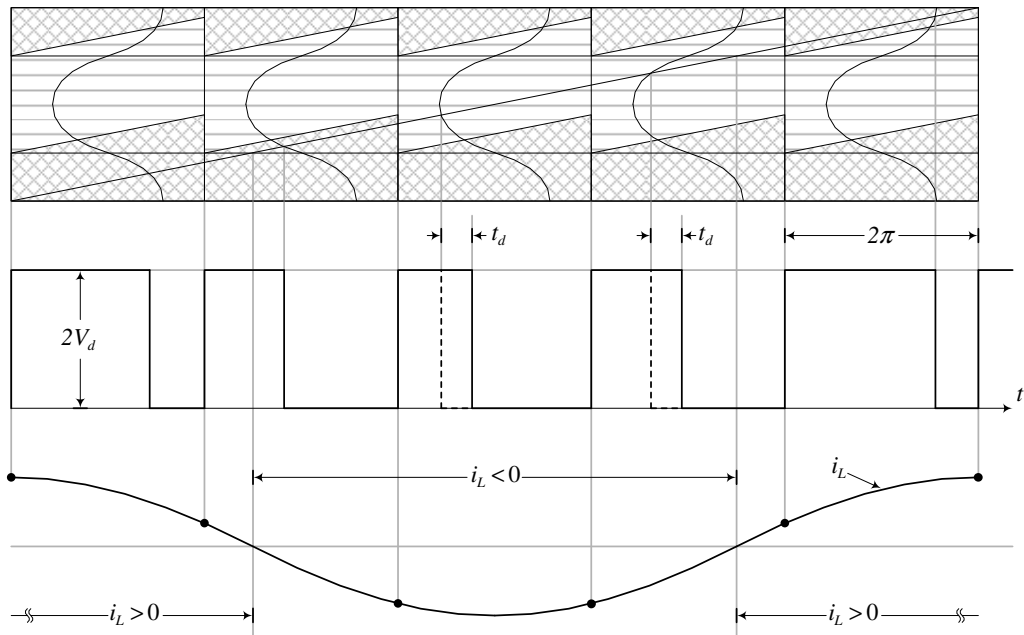
Figure 3.15: Combination of Figure 3.13 and Figure 3.14 illustrating the sampling process.

The 3-D unit area representing this condition described is shown in Figure 3.16. No closed form solution for variables $y_{1...4}$ can be achieved and thus needs to be solved numerically. Variable y_1 can be calculated from $x=\pi M\cos(y)+\pi$ and $y=(\omega_0/\omega_c)x+\pi/2$. Also, y_3 can be determined from $x=\pi M\cos(y)+\pi$ and $y=(\omega_0/\omega_c)x+3\pi/2$. The remaining variables y_2 and y_4 are found by respectively adding $(\omega_0/\omega_c)\Phi_d$ to y_1 and y_3. The limits of Figure 3.16 correspond to those defined in Eq. (3.10) with only $y_{1...4}$ being different.

Figure 3.16: 3-D unit area for TENPWM with current polarity dependency.

Table 3.4 shows a comparison between the analytical and simulation results for TENPWM including the current polarity conditions. The parameters used correspond to t_d=10ns and M=0.8. It can be seen that similar results are produced.

TABLE 3.4

COMPARISON OF ANALYTICAL AND SIMULATION RESULTS FOR TENPWM WITH INDUCTOR CURRENT POLARITY

CONDITION SAMPLED ON THE LEADING EDGE.

Harmonic Number	Analytical Magnitude [V]	Simulated Magnitude [V]
1	7.8727	7.8727
2	0.0006	0.0006
3	0.0424	0.0424
…	…	…
383	3.1879	3.1879
384	6.1619	6.1619
385	3.1887	3.1888

Figure 3.17: Simulated TENPWM spectra for sampling on the (a) trailing and (b) leading edge.

Figure 3.17 (a) shows the simulated spectra using the sampling process of Section 3.4.1 while (b) shows the spectra with sampling on the leading edge described in this section. The difference in clearly visible.

3.5   INCORPORATION OF A PURELY SINUSOIDAL NON-LINEAR INDUCTOR CURRENT MAGNITUDE DEPENDENCY IN THE 3-D UNIT AREA

Consider a TENPWM waveform of which either the leading or trailing edge is governed by some non-linear purely sinusoidal inductor current magnitude dependency. The current dependent delay t_d introduced is assumed to be governed by the arbitrarily chosen relation:

$$t_d = k_{scaling} \left| I_0 \cos(\omega_0 t) \right|^2 \tag{3.11}$$

Where $k_{scaling}$ is a constant scaling variable. In this section it is shown how this condition can be incorporated into the 3-D unit area by applying the methodology introduced in Sections 3.3 and 3.4. Note that the current magnitude is assumed to be sampled on the same edge on which the error is being introduced.

3.5.1   THE UNMODULATED LEADING EDGE

In this section the unmodulated leading edge is delayed in accordance with the relation defined in Eq. (3.11). Since the current magnitude is sampled on the leading edge, the current

polarity zones defined in Figure 3.14 hold. Next, the equivalent mapping of Eq. (3.11) within the unit area can be established as $\Phi_d = 2\pi f_c k_{scaling}$ and $y = \omega_0 t$. As mentioned in Section 3.3.2, the ideal leading edge of a TENPWM waveform is independent of y. By adding Eq. (3.11) to the leading edge a y dependency is introduced. This means that the adjustment (y_{offset}) discussed in Section 3.3 must be included. The expression describing the current dependent leading edge is thus given by:

$$\Phi_d = \Phi_{scaling} \left| I_0 \cos\left(y - y_{offset} \right) \right|^2 \tag{3.12}$$

Where $y_{offset} = (\omega_0/\omega_c)\Phi_d$. This allows for the 3-D unit area to be constructed, which is illustrated in Figure 3.18.
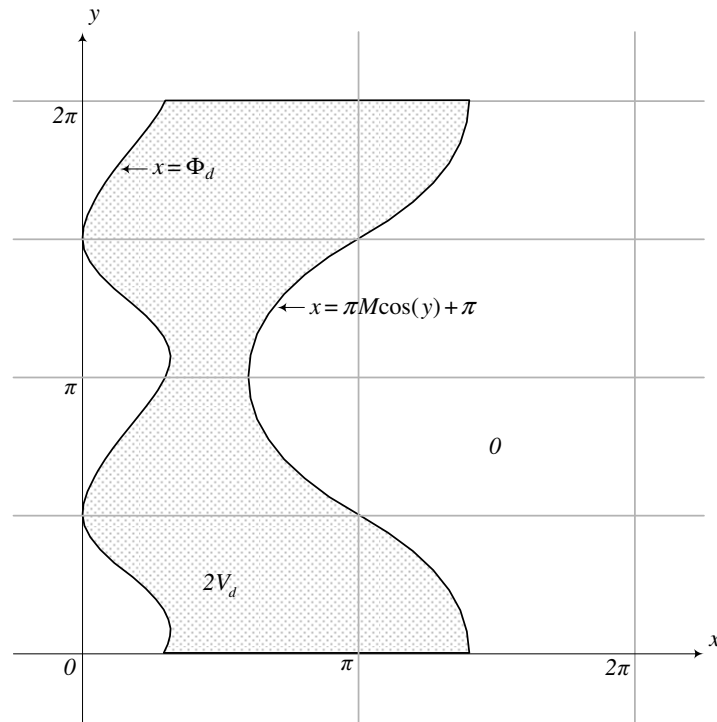
Figure 3.18: 3-D unit area for TENPWM with current magnitude dependency.

By inserting the limits defined in Figure 3.18 into Eq. (2.15) yields:

$$C_{mn} = \frac{V_d}{2\pi^2} \int_0^{2\pi} \left[\int_{\Phi_d}^{\pi M \cos(y - y_{offset}) + \pi} e^{jmx} dx \right] e^{jny} dy \tag{3.13}$$

Table 3.5 shows a comparison between the analytical and simulation results for TENPWM including the current polarity conditions. The parameters used correspond to t_d=10ns, M=0.8. The analytical and simulation results correlate well.

TABLE 3.5

COMPARISON OF ANALYTICAL AND SIMULATION RESULTS FOR TENPWM WITH INDUCTOR CURRENT MAGNITUDE

DEPENDENCY SAMPLED ON THE TRAILING EDGE.

Harmonic Number	Analytical Magnitude [V]	Simulated Magnitude [V]
1	8.0000	8.0000
2	0.0326	0.0326
3	0.0000	0.0001
…	…	…
383	3.1435	3.1435
384	6.0169	6.0169
385	3.1435	3.1435

3.5.2   THE MODULATED TRAILING EDGE

In this section the modulated trailing edge is considered. The current magnitude is sampled on the ideal trailing edge which means that the polarity zones defined in Figure 3.10 apply. The equivalent mapping of Eq. (3.12) within the unit area is the same as in Section 3.5.1. The 3-D unit area representing these conditions is shown in Figure 3.19. The complex Fourier coefficient of Eq. (2.15) can be written as:

$$C_{mn} = \frac{V_d}{2\pi^2} \int_0^{2\pi} \left[\int_{\Phi_d}^{\pi M \cos(y - y_{offset}) + \pi} e^{jmx} dx \right] e^{jny} dy \tag{3.14}$$

Where Φ_d is defined in Eq. (3.12). A comparison between the analytical an simulation results are shown in Table 3.6.
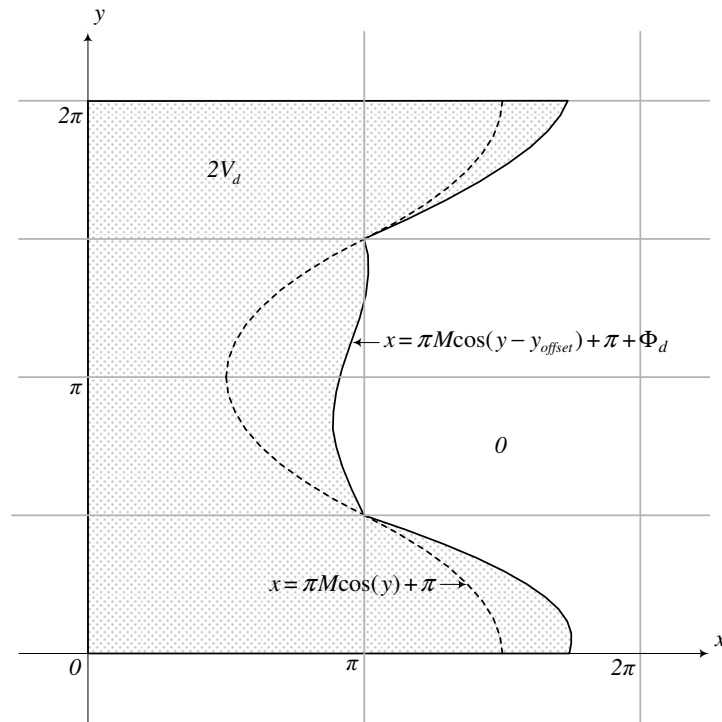
Figure 3.19: 3-D unit area for TENPWM with current magnitude dependency.

The conditions correspond to those of Section 3.5.1. From Table 3.6 it can be seen that the analytical and simulation results correlate well.

TABLE 3.6

COMPARISON OF ANALYTICAL AND SIMULATION RESULTS FOR TENPWM WITH INDUCTOR CURRENT MAGNITUDE

DEPENDENCY SAMPLED ON THE LEADING EDGE.

Harmonic Number	Analytical Magnitude [V]	Simulated Magnitude [V]
1	8.0000	8.0000
2	0.0326	0.0326
3	0.0000	0.0001
…	…	…
383	3.1435	3.1435
384	6.0169	6.0169
385	3.1435	3.1435

3.6   INCORPORATION OF SECTION 3.2 WITHIN THE 3-D UNIT AREA

The previous section assumed a purely sinusoidal inductor current. In this section it will be shown how the current model of Section 3.2 can be integrated into the unit area to provide a tool where the ripple current can be parsed as a parameter to model more realistic polarity dependencies. The objective is achieved via simple manipulation of Eq. (3.3) in which D needs to be described as a continuous function with the required mapping of $T_c=2\pi$ within the unit area. Since $y=2\pi f_0 t$ and $D=((1+M\cos(2\pi f_0 t))/2)$ Eq. (3.3) can be rewritten as:

$$\Delta i_L = \frac{V_d}{8 L_{filt} f_c}\left[1-M^2\cos^2(y)\right] \tag{3.15}$$

Since $i_{L(upper\_env)}$ and $i_{L(lower\_env)}$ are respectively defined on the trailing and leading edges the implementation has to be done with Section 3.4 in mind. Figure 3.20 defines the various current polarity zones for $i_{L(upper\_env)}$ within the 3-D unit area according to the analysis of Section 3.4.1.
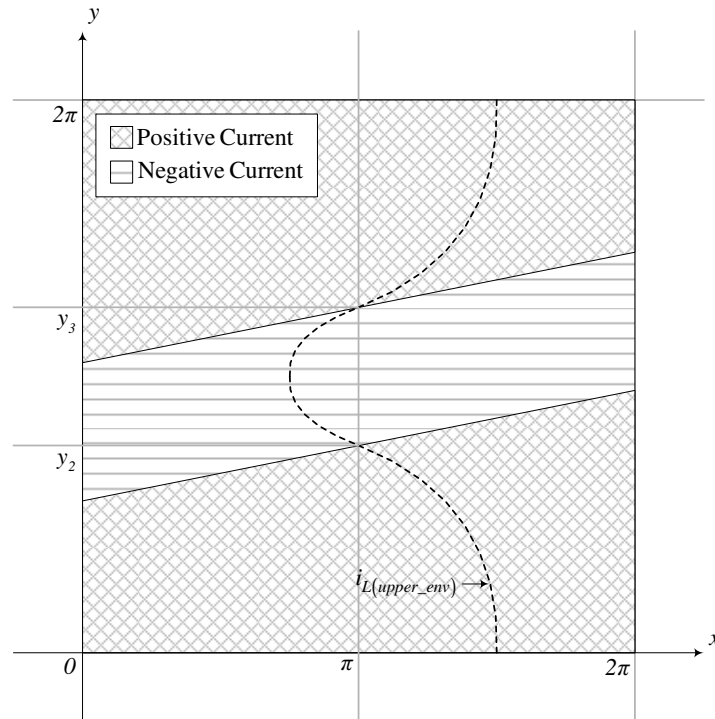
Figure 3.20: Definition of the various current zones for $i_{L(upper\_env)}$ within the 3-D unit area.

In a similar manner Figure 3.21 defines the various current polarity zones for $i_{L(lower\_env)}$ within the 3-D unit area according to the analysis of Section 3.4.2. Note that no closed form solution can be achieved for variables $y_{1...4}$ and that it must thus be solved numerically.
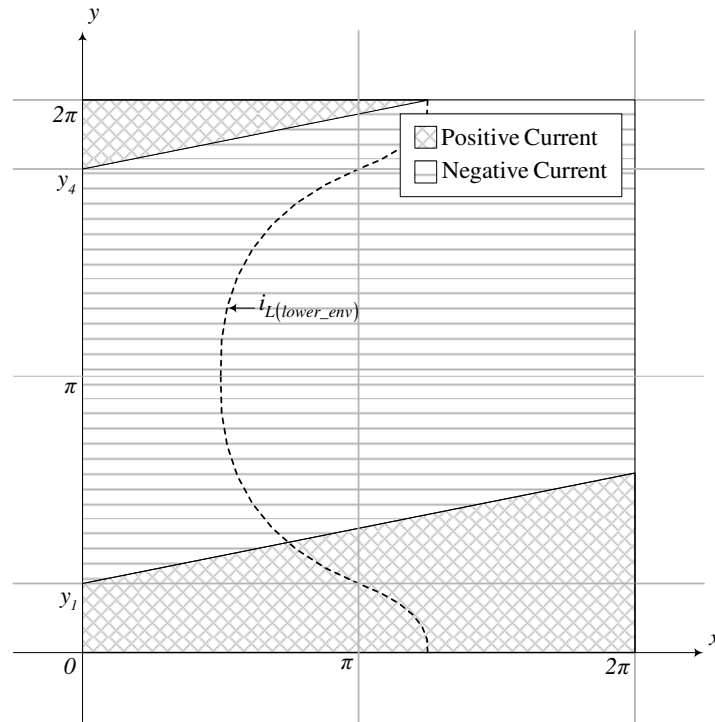
Figure 3.21: Definition of the various current zones for $i_{L(lower\_env)}$ within the 3-D unit area.

A general power electronic tool has been introduced in this chapter. However, within switching audio applications, the analysis can be simplified by noting that $y_{offset} \approx 0$ if $f_c >> f_0$. This assumption will be applied for the rest of this dissertation.

3.7   SUMMARY

A general analytical tool has been developed which allows for the calculation of the harmonic composition of naturally sampled PWM in the presence of current dependent pulse timing errors. The analysis was verified by simulation. The analysis firstly considered a purely sinusoidal inductor current after which a more realistic current model with a non-zero ripple was included. The proposed analytical models and simulation results correlated.

4
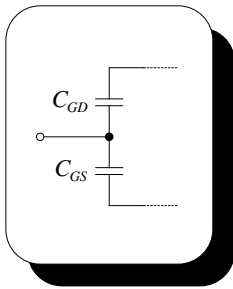
SWITCHING DEVICE

CHARACTERISTICS

4.1 INTRODUCTION

The power MOSFET has been available since the early 1980's [24]. Even though the power BJT was developed during the 1950's [28] and has continued to evolve ever since, fundamental drawbacks exist in its operating characteristics. The development of the power MOSFET was primarily driven by the limitations posed by the power BJT.

The BJT is a current controlled device. This means that a continuous current must be applied to its base in order to keep the device in the *on* state. Even larger reverse base currents are required to ensure rapid turn-*off*. The base drive circuitry required thus tends to be complex and expensive. The required gate drive characteristics compromise both efficiency and linearity. The power BJT's safe operating area is limited by its inability to handle high voltages and currents simultaneously. Another limitation is the difficulties of using the devices in parallel. This can be ascribed to the decrease in forward voltage drop for increasing temperature, which in turn leads to current diversion to a single device.

In contrast, the MOSFET is a voltage controlled device. Its insulated gate structure need only be supplied with current in order to charge and discharge the input capacitance during switching transitions. This means that no steady state current is required in the *on* or *off* state. The gate drive requirements are thus greatly simplified as a result of the high input impedance. Furthermore, since current conduction occurs only through transport of majority carriers, no delays are introduced as a result of the recombination process associated with the injection of minority carriers. This leads to faster switching times than the power BJT. Since the power MOSFET is not subject to second breakdown, the safe operating area is also much greater than that of the power BJT. Lastly, these devices can easily be mounted in parallel because the forward voltage drop increases with increasing temperature. This results in even current distribution amongst paralleled devices.

From the brief discussion above it is evident that the power MOSFET represents a closer approximation to an ideal switch than the power BJT. It thus finds its application in audio switching amplifiers in which fidelity is the primary design parameter. This chapter describes the fundamental operation of the power MOSFET on a semiconductor level. The inclusion of this overview is essential since the non-ideal effects investigated in Chapters 5 to 8 are either a primary or secondary consequence of its operation. The first four sections of this chapter (4.2 to 4.5) contain a fundamental overview of the basic structure, operation and dynamic characteristics, which are summarized from [24]. Section 4.6 describes the operation within a single phase leg, in which all non-ideal effects considered in this dissertation are included. Note that the above mentioned analysis is adapted and summarized from [32].

4.2   POWER MOSFET STRUCTURE

Figure 4.1 illustrates a vertical diffused MOSFET (VDMOS). This device is fabricated using a n^+ pn^- n^+ structure and is termed an *enhancement mode n-channel MOSFET*. This vertical structure consists of alternating *n*-type and *p*-type doped semiconductor layers with the n^+ top layer labelled the *source* and the n^+ bottom termed the *drain*. The *p*-type region is known as the *body* with the n^- layer called the *drift region*.
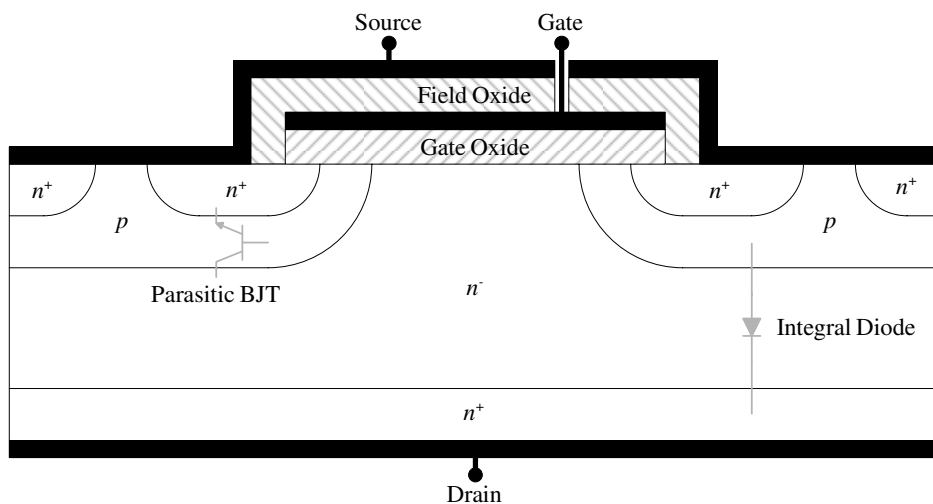
Figure 4.1: Vertical cross-sectional view of a power MOSFET [24].

From Figure 4.1 it should be noted that a parasitic BJT exists within the $n^+ pn^- n^+$ structure with the *p* body region representing its base. This BJT must be kept in the *off* state at all times, since forward biasing would lead to unwanted conduction, which in turn can result in device breakdown. The source metallization connects the *p* body region to that of the n^+ top layer, creating a short circuit between the base and the emitter of the parasitic BJT. This short leads to an integral diode being connected between the drain and source regions.

4.3   POWER MOSFET OPERATION

From Figure 4.1 it seems that current flow between the gate and source terminals is impossible since one of the *pn* junctions will always be reverse biased. Moreover, the gate metallization is isolated by a layer of silicon dioxide (SiO_2), which rules out the possibility of minority carrier injection. In order to have current flow between the drain and source terminals, it is imperative to establish a conductive path between the n^+ source and n^- drift regions. This path is created by applying a positive voltage to the gate terminal (with respect to the source). The positive charge existing on the gate electrode requires an equal but inverse negative charge on the silicon beneath the SiO_2 layer. The electric field established in this way attracts electrons to the *p* base region just beneath the SiO_2 while repelling majority carriers (holes). This creates a depletion region. An increased gate voltage attracts more electrons to the surface while repelling more holes. This results in an increased depletion region with the holes pushed into the *p* base area beyond the depletion boundary. These additional holes are neutralized by electrons from the n^+ source region. An equilibrium is established once the density of the free electrons beneath the gate oxide is equal to the density of free holes beyond the depletion region. This channel of free electrons beneath the SiO_2 is known as the inversion layer. The value of applied gate voltage at which this inversion layer is formed is known as the gate-to-source threshold voltage. In this state the free electrons just below the gate oxide are highly conductive and can be regarded as a *n*-type semiconductor. The application of a drain voltage will result in current flow through the channel region. The power MOSFET is switched into the *off* state by turning the gate voltage back to zero. This is done by creating a short circuit between the gate and source terminals. Since the electrons are no longer attracted by the induced electric field, the channel between the n^+ source and n^- drift region is broken.

4.4   CHARACTERISTIC CURVES

Figure 4.2 (a) shows a plot of i_D as a function of v_{DS} for various values of the V_{GS} for a *n*-channel device. The power MOSFET is cut off whenever v_{GS} is smaller than $V_{GS(th)}$. In this *off* state the *pn*-junction is reverse biased and the device is able to block any voltage smaller than BV_{DSS}. As shown in Figure 4.2 (a), when operating in the active region the drain current is only dependent on v_{DS}. The power MOSFET enters the ohmic region whenever $v_{GS}-V_{GS(th)}>v_{DS}>0$.
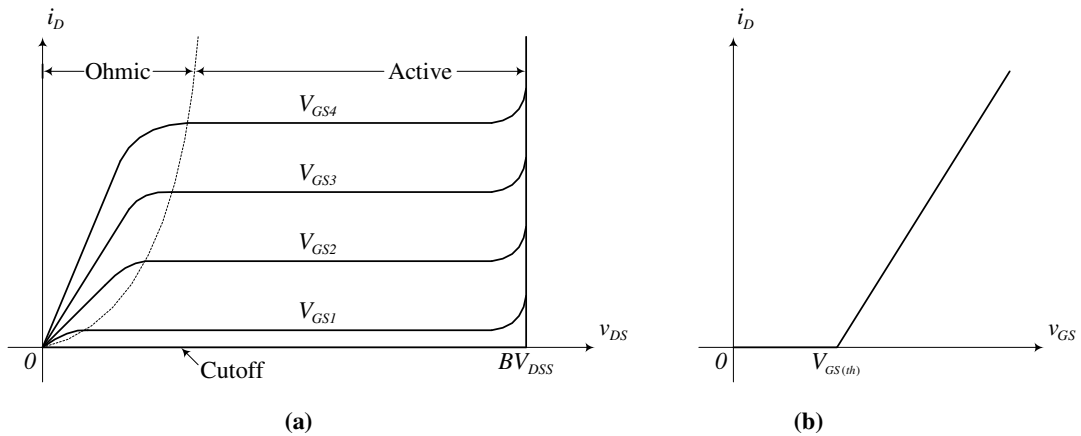
Figure 4.2: (a) Output and (b) transfer characteristic curves [24].

This condition is achieved by driving the device with a relatively large V_{GS}. In this state v_{DS} is small, and it is determined by the device's on-state resistance and operating current. Figure 4.2 (b) illustrates i_D as a function of v_{GS}.

4.5   POWER MOSFET DYNAMIC MODEL

The switching speed of the power MOSFET is limited to the charge and discharge of the input gate capacitance due to its insulated gate structure. Figure 4.3 shows a cross-sectional view of the power MOSFET structure, illustrating the location of the parasitic capacitances. These capacitances can be divided into two primary groups of which the first is labelled C_{GS} and the second of which is labelled C_{GD}. The former capacitance can again be subdivided into three separate components. The first two components of C_{GS} arise as a result of the overlap of

the gate electrode with the n^+ source and p base regions, respectively denoted as C_{n+} and C_p. The third capacitance exists due to the overlap of the gate electrode with the source metallization, labelled C_m. Note that the latter is determined by the type of insulator used between the gate electrode and the source metallization as well as its thickness.
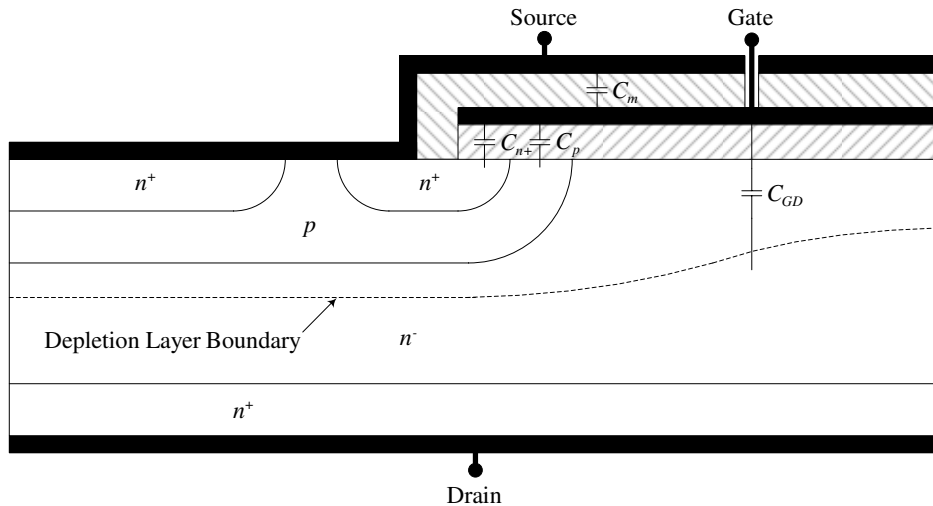
Figure 4.3: Vertical cross-sectional view of a power MOSFET with parasitic capacitances [24].

The second capacitance exists as a result of the overlap of the gate electrode with the n^- drift region. As mentioned, it is labelled C_{GD} and consists of two components in series. The first component arises from the capacitance created by the gate electrode and oxide layer, which is once again determined by the thickness and type of insulating material used. The second component is a result of the capacitance introduced by the depletion layer. With zero voltage applied to the gate electrode, the depletion layer beneath the gate oxide will be at a minimum. By applying a positive gate voltage, the depletion layer will start forming, increasing for higher values of applied voltage. This in turn leads to a decrease in the capacitance of the depletion layer because it is widened. This process continues until the surface inversion layer is formed and the depletion layer is at its maximum value. In this state the depletion layer capacitance exhibits its lowest value. It is thus evident that these capacitances are not constant and change with voltage due to the partial contribution from the depletion layer. Figure 4.4 shows a plot of C_{GD} as a function of v_{DS}.
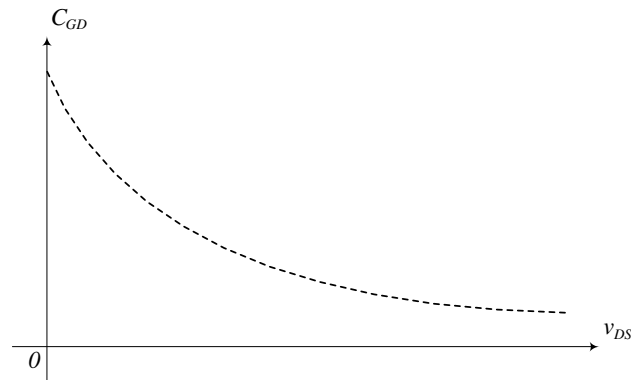
Figure 4.4: C_{GD} as a function of v_{DS} [24].

Figure 4.5 shows the circuit diagrams used to model the parasitic capacitances, with (a) representing the MOSFET when it is either cutoff or in the active region. During the interval when $v_{GS} < V_{GS(th)}$ the MOSFET is cut off and $i_D = 0$. Once the threshold voltage is reached the device enters the active region and the current increases according to the current-voltage transfer characteristic of Figure 4.2 (b) with the MOSFET's transconductance g_m defining the slope. In this state the drain current is thus defined by $g_m(v_{GS} < V_{GS(th)})$.

(a)   **(b)**
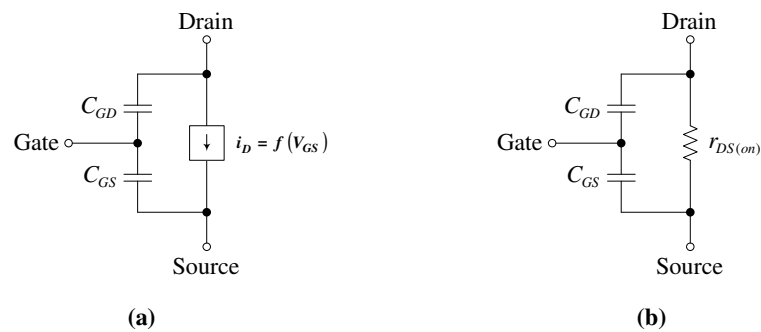
Figure 4.5: Circuit model when power MOSFET is in the (a) active and (b) ohmic region [24].

The MOSFET enters the ohmic region once $v_{GS} - V_{GS(th)} > v_{DS} > 0$. In this state the inversion layer has a nearly uniform thickness and effectively shorts the drain and source terminals. This means that the circuit model of Figure 4.5 (a) is no longer valid. Figure 4.5 (b) shows the equivalent circuit in the ohmic region. Note the inclusion of a non-zero $r_{DS(on)}$ between the drain and source terminals. This is a result of the resistances associated with the different regions of the semiconductor material.

4.6   POWER MOSFET SWITCHING WAVEFORMS

This sub-section is adapted and summarized from [32] and serves as a brief overview of the MOSFET switching characteristics. Figure 4.6 illustrates the switching waveforms within one leg of a single phase inverter for a positive i_L.
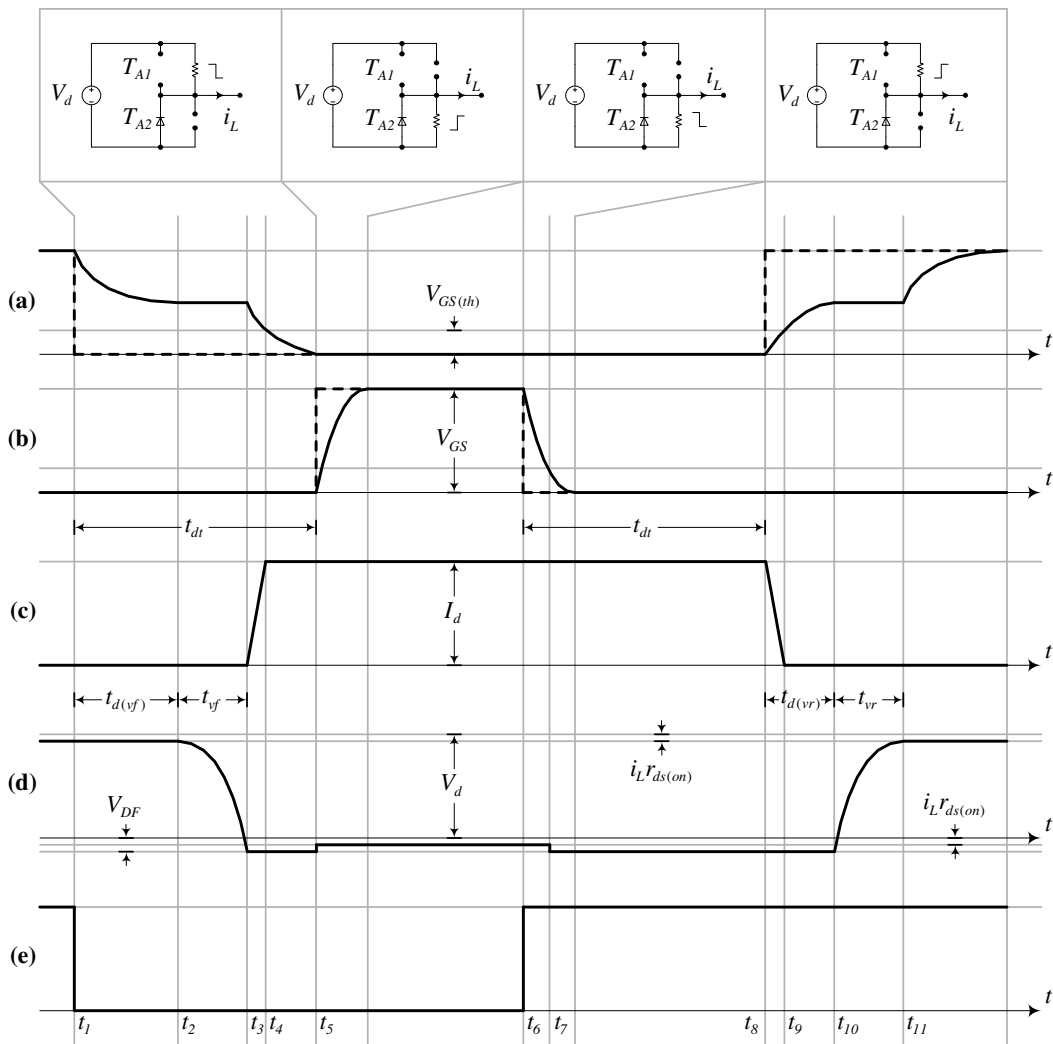
Figure 4.6: Switching characteristics in a single phase leg for a positive inductor current [32].

The solid bold waveforms of Figure 4.6 (a) and (b) respectively represent the practical gating signals of the high side and low side MOSFETs, whereas the dashed lines represent the

ideal waveforms. The low side MOSFET's i_D is shown in Figure 4.6 (c) with v_{DS} represented by (d). The ideal switching output measured over T_{A2} is shown in Figure 4.6 (e). With the circuit diagrams representing the devices in play during the specified intervals a detailed description of each interval can now be constructed. This is given in Table 4.1.

TABLE 4.1

DESCRIPTION OF THE ACTION ON THE VARIOUS TIME INSTANTS OF FIGURE 4.6.

Time	Description
t_1	The gating signal of T_{A1} switches from high to low and the discharge of C_{GS} results in $t_{d(off)}$.
t_2	v_{GS} becomes temporarily clamped to a fixed value needed to maintain I_L according to the transfer characteristic of Figure 4.2 (b). Since v_{GS} remains constant during this interval, all of the input current supplied by V_{GS} flows through C_{GD}. This causes the v_{DS} to drop rapidly as it transverses through the active toward the ohmic region of Figure 4.2 (a).
t_3	D_{A2} starts its commutation sequence once v_{DS} of T_{A2} goes low enough, which in turn causes v_{GS} to fall rapidly. V_{DF} of D_{A2} causes v_{DS} of T_{A2} to fall to a value $-V_{DF.}$
t_4	$v_{GS}=V_{GS(th)}$ and T_{A1} is cut off. i_L now flows completely through $D_{A2.}$
t_5	t_{dt} is over and the gating signal of T_{A2} transitions from low to high. Since the inception of this interval both v_{DS} and v_{GD} equals zero, which means that T_{A2} never enters the active region. This results in rapid switching. The only requirement is the shift of charge from the D_{A2} to T_{A2}. Once the complete current is transferred to T_{A2} voltage v_{DS} falls to $-i_L r_{DS(on)}$.
t_6	The gating signal of T_{A2} transitions from high to low.
t_7	$v_{GS}=V_{GS(th)}$ and T_{A2} is cutoff. Due to the current polarity the current will transfer directly to D_{A2} again allowing for a rapid transition. V_{DF} causes v_{DS} to fall to $-V_{DF}$.
t_8	After t_{dt} the gating signal of T_{A1} changes from low to high.
t_9	$v_{GS}=V_{GS(th)}$ and thus T_{A1} enters the active region. The combination of intervals t_8 and t_9 leads to $t_{d(on).}$
t_{10}	v_{GS} becomes temporarily clamped to a fixed value needed to maintain I_L according to the transfer characteristic of Figure 4.2 (b). Since v_{GS} remains constant during this interval all of the input current supplied by V_{GS} flows through C_{GD}. This causes the v_{DS} to rise rapidly as it transverses through the active to the ohmic region.
t_{11}	T_{A2} enters the final interval once v_{DS} has reached its on-state value at $i_L r_{DS(on)}$ below V_d.

Figure 4.7 shows the switching waveforms within one leg of a single phase inverter for a negative i_L. The different switching intervals can be determined in a similar manner as for the positive inductor current. As a result, it is not necessary to discuss it in detail. The non-ideal switching characteristics described in Figure 4.6 and Figure 4.7 serve as a basis for the analysis which follows in the remainder of this dissertation.
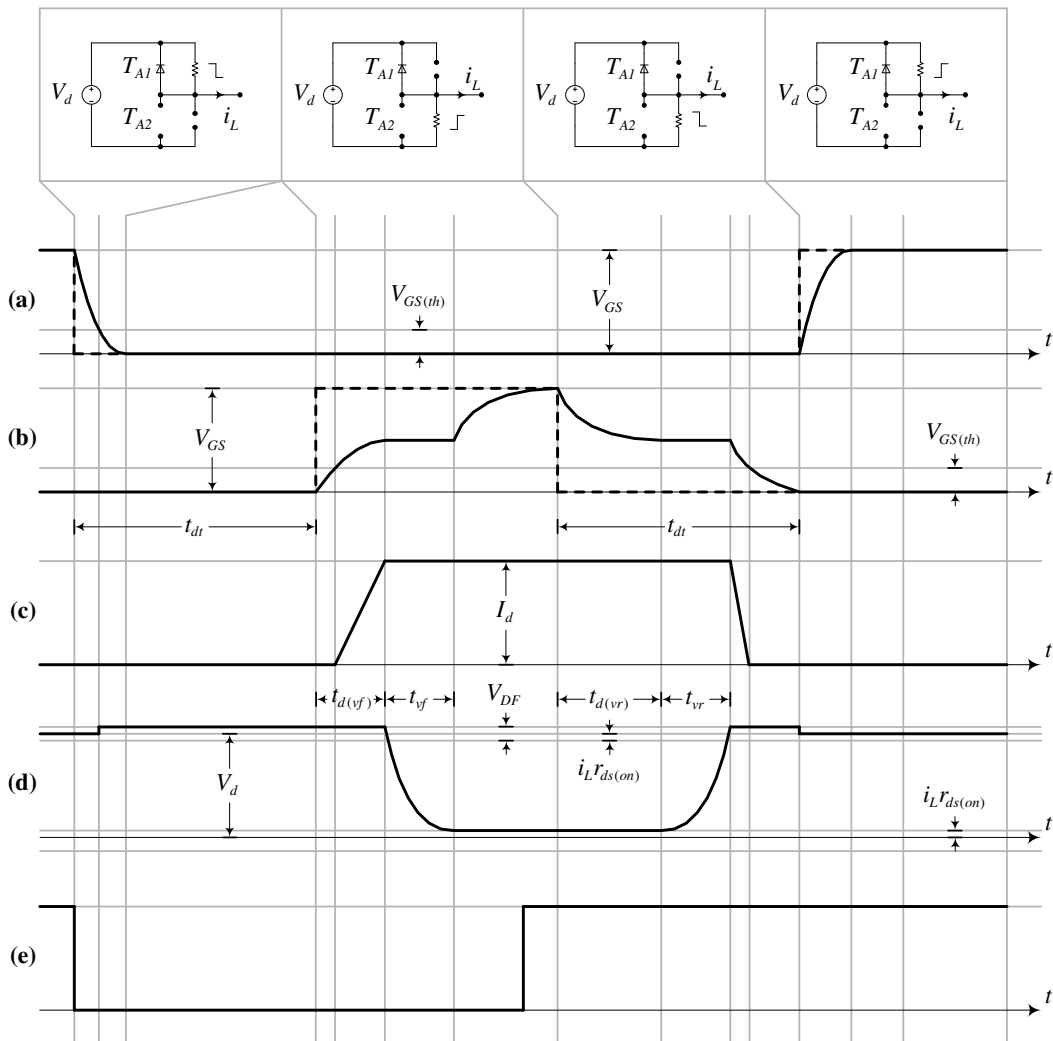
Figure 4.7: Switching characteristics in a single phase leg for a negative inductor current [32].

4.7   SUMMARY

The first part of this chapter (Sections 4.2 to 4.5) summarized the basic structure, operation and dynamic characteristics of the power MOSFET, which have been summarized from [24]. The final part (Section 4.6) was adapted from [32] and considered the non-ideal switching behaviour within a single phase leg. This chapter thus served as a foundation in which the primary and secondary consequences of its operation on the switching waveform within a single phase leg were considered.

5
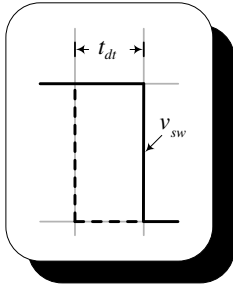
THE EFFECT

OF DEAD TIME

5.1 INTRODUCTION

This chapter contains a detailed analysis of the effect of dead time on harmonic distortion in open loop class D audio amplifiers, adapted from the papers in [23] and [46] by the author. A fundamental analysis is considered in Section 5.2. Employing the findings in Chapter 3, an analytical model describing TENPWM with dead time is proposed in Section 5.3. A simulation model based on the strategy introduced in Chapter 2.5 is considered in Section 5.4, after which a detailed discussion of the analytical and simulation results follows in Section 5.5. This chapter concludes with a summary.

5.2 ANALYSIS OF DEAD TIME

The analysis will be divided into two sections. Section 5.2.1 contains a detailed analysis for the region during which both $i_{L(upper\_env)}$ and $i_{L(lower\_env)}$ are positive or both of them are negative (inductor current Scenario ② in Section 3.2). In Section 5.2.2 the remaining region where $i_{L(upper\_env)}$ is positive and $i_{L(lower\_env)}$ is negative is investigated (inductor current Scenario ① in Section 3.2).

5.2.1 A DISTINCTLY POSITIVE AND NEGATIVE INDUCTOR CURRENT (SCENARIO ②)

The effect of dead time on the switched output voltage can best be described using one leg of the single phase inverter shown in Figure 5.1. Through simple inspection of the this illustration it is evident that the output voltage depends on the polarity of the output current when both switches (T_{A1} and T_{A2}) are *off*. Additional states exist when the switches transition from *off* to *on* and vice versa.

Consider Figure 5.1 (a), which represents the region during which i_{LA} is distinctly positive in the presence of a non-zero dead time. Referring to the illustration in (a), consider the transition of T_{A1} from *on* (current direction ①) to *off* and T_{A2} from *off* to *on*. During t_{dt} diode D_{A2} conducts (current direction ②) while diode D_{A1} blocks the current flow to the positive rail. This results in the same output voltage as for an immediate transition of T_{A2} from *off* to *on*, which in turn corresponds to the correct output voltage. Next, with the output current still positive, consider the change of T_{A2} from *on* (current direction ③) to *off* and T_{A1} from *off* to *on*. Again, D_{A2} conducts (current direction ④) while D_{A1} blocks the current flow to the positive rail. This condition leads to a loss of voltage, since the output remains clamped to the negative rail during t_{dt}.
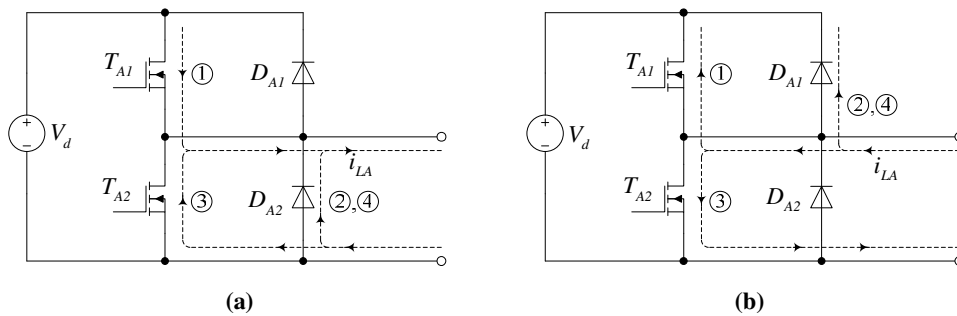
Figure 5.1: Commutation sequence in a single phase leg for (a) $i_{LA}>0$ and (b) $i_{LA}<0$.

The remaining two conditions exist when the output current is distinctly negative. Refer to Figure 5.1 (b). For a transition of T_{A2} from *on* (current direction ③) to *off* and T_{A1} from *off* to *on* with the addition of t_{dt}, D_{A1} conducts (current direction ②) while D_{A2} is reverse biased. This results in the correct voltage at the output terminals, since the same result is achieved for a transition with zero dead time. The final condition is given by a transition of T_{A1} from *on* (current direction ①) to *off* and T_{A2} from *off* to *on* for a negative output current. The conduction sequence of D_{A1} and D_{A2} during t_{dt} (current direction ④) is exactly the same as for the latter case. Since the voltage is clamped to the positive rail during t_{dt} instead of a transition to the negative rail, a voltage gain is achieved. Figure 5.2 illustrates the switching waveforms influencing t_{dt} for a positive inductor current. Since only t_{dt} is considered, the remaining waveforms are considered as ideal. During the transition of $v_{GS(high\_side)}$ from *on* to *off* the voltage is assumed to switch instantly from V_{GS} to zero.
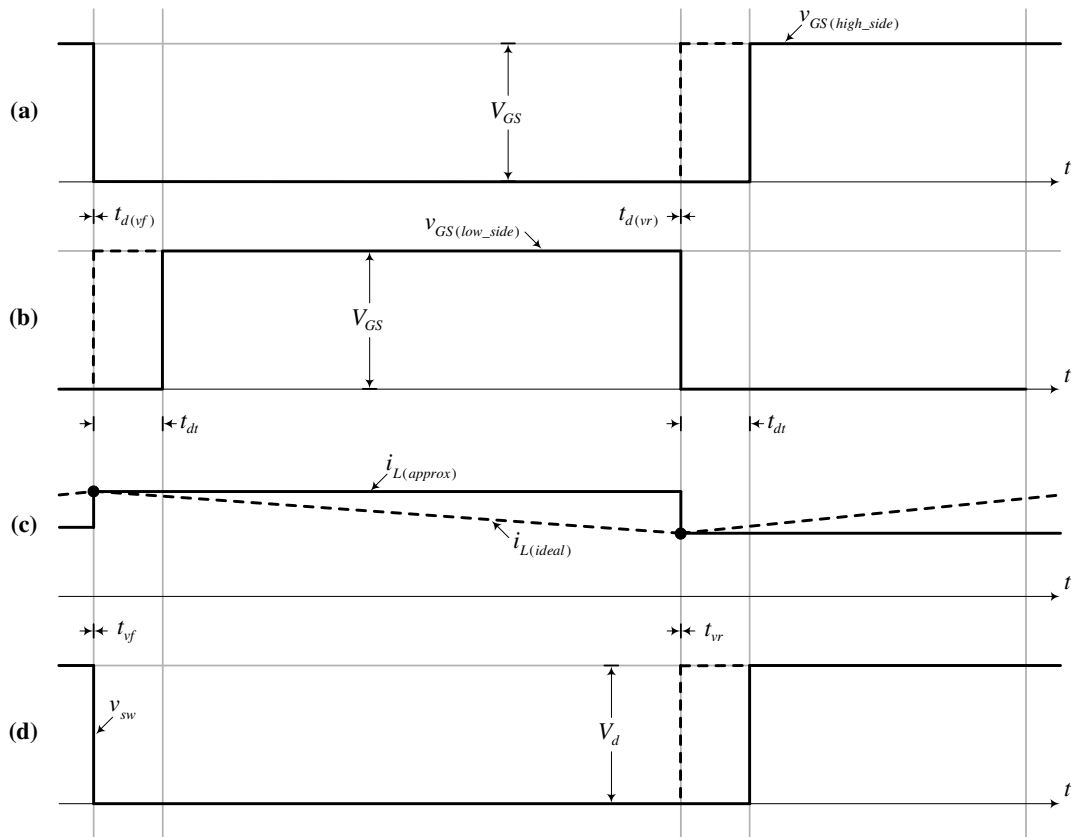
Figure 5.2: Switching waveforms for a positive inductor current. (a) Low side gate-to-source voltage. (b) High side gate-to-source voltage. (c) Inductor current. (d) Switched output voltage.

This leads to a value of $t_{d(vf)}=0$. Using similar conditions $v_{GS(high\_side)}$ results in $t_{d(vr)}=0$ during a change of $v_{GS(high\_side)}$ from *off* to *on*. This also results in instantaneous switching transitions, i.e. $t_{vr}=t_{vf}=0$. The inductor current polarity is sampled at the time instant of switching on the ideal output voltage transition, which occurs on either $i_{L(upper\_env)}$ or $i_{L(lower\_env)}$. This results in an approximation $i_{L(approx)}$ within region t_{dt} as shown in Figure 5.2 (c). The voltage loss associated with $i_L>0$ is shown in in Figure 5.2 (d). Figure 5.3 illustrates the switching waveforms affecting t_{dt} for a negative inductor current. The switching waveforms are idealized in exactly the same way as for Figure 5.2. The voltage gain associated with $i_L<0$ is shown in in Figure 5.3 (d).
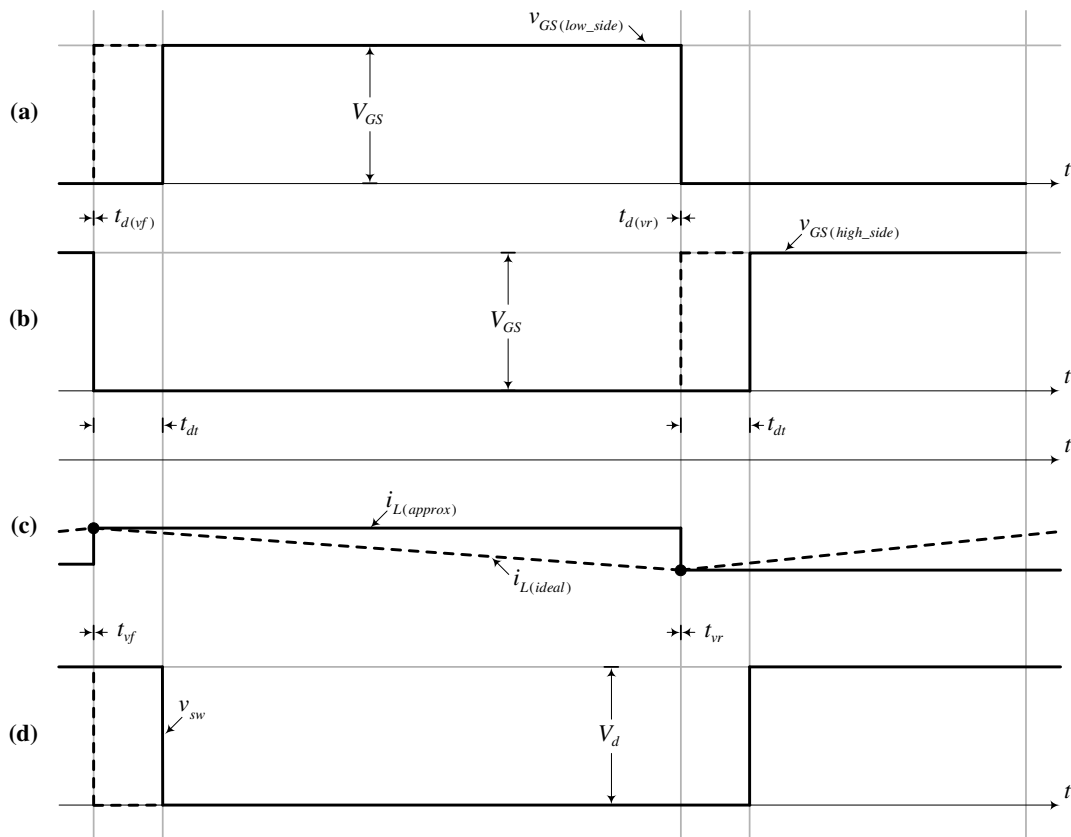
Figure 5.3: Switching waveforms for a negative inductor current. (a) High side gate-to-source voltage. (b) Low side gate-to-source voltage. (c) Inductor current. (d) Switched output voltage.

5.2.2   NEITHER DISTINCTLY POSITIVE NOR NEGATIVE INDUCTOR CURRENT (SCENARIO ①)

Two possible sub-scenarios exist in the region where the inductor current is neither distinctly positive nor negative. Firstly, consider Figure 5.4 (a) which illustrates a change in polarity of i_L occurring within the region $LE+t_{dt}<t<TE$ or $TE+t_{dt}<t<LE$. From the analysis in the previous section it is evident that the commutation sequence results in reproducing the ideal switching waveform, i.e. the dead time has no effect. The remaining sub-scenario exists when i_L changes polarity during t_{dt}. This is shown in Figure 5.4 (b) for a practical system, with the magenta and turquoise waveform respectively representing the switched output voltage and inductor current.
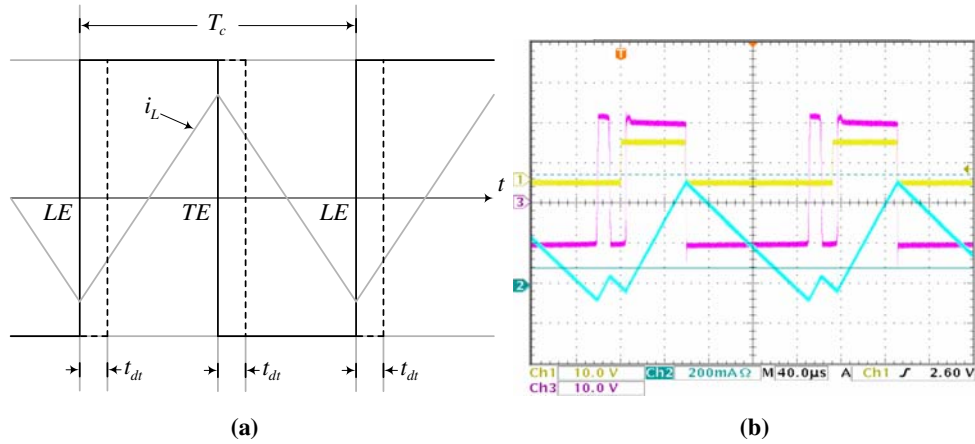
Figure 5.4: Change in current polarity (a) outside interval t_{dt} and (b) within interval t_{dt} [35].

The change in switching state of the output voltage is a result of reverse recovery. However, this dissertation assumes open loop systems $t_{dt} << T_c$ and, as a result, the latter scenario will be ignored in the analysis.

5.3   ANALYTICAL MODEL

In this section a model is introduced for TENPWM which allows for the harmonic components created by the dead time to be calculated analytically. Since inductor current Scenario ① reproduces the ideal case under the assumption described in the previous section, it is only necessary to consider Scenario ②. Implementing the findings in Chapter 3 the unit area for TENPWM with dead time can be constructed. The leading edge with polarity sampled on $i_{L(lower\_env)}$ needs to be delayed by the corresponding mapping $\Phi_{dt}=2\pi f_c t_{dt}$ within the region where both $i_{L(upper\_env)}$ and $i_{L(lower\_env)}$ are positive. In the region where both $i_{L(upper\_env)}$ and $i_{L(lower\_env)}$ are negative, the trailing edge needs to be delayed by Φ_{dt}. The 3-D unit area representing these conditions is shown in Figure 5.5. Note that variables y_1, y_2, y_3 and y_4 are solved numerically, as mentioned in Chapter 3.
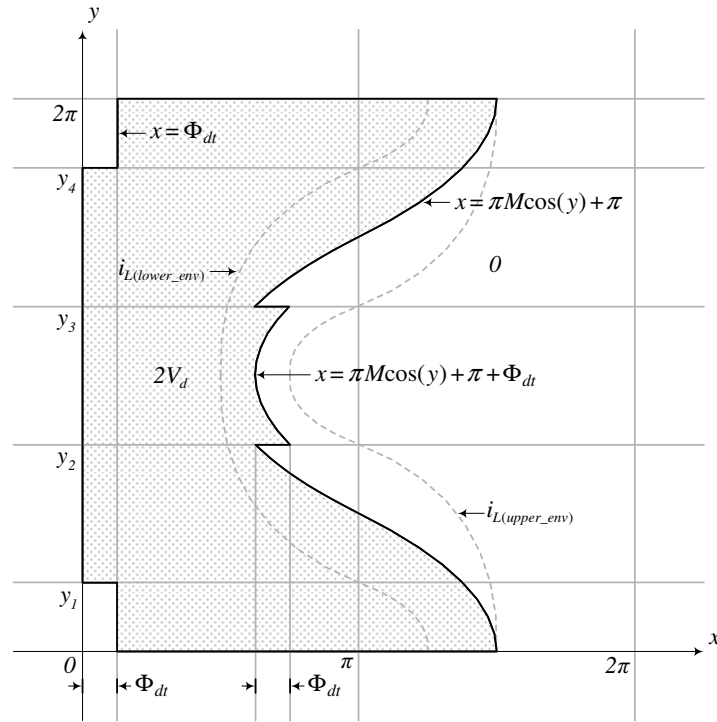
Figure 5.5: 3-D unit area for TENPWM with dead time.

By next inserting the limits defined in Figure 5.5, the complex Fourier coefficient of Eq. (2.15) can be written as:

$$C_{mn} = \frac{V_d}{\pi^2}\left[\int_0^{y_1}\left[\int_{\Phi_{dt}}^{\pi+\pi M\cos(y)} e^{j(mx+ny)}dx \right]dy + \int_{y_1}^{y_2}\left[\int_0^{\pi+\pi M\cos(y)} e^{j(mx+ny)}dx \right]dy \right.$$

$$+ \int_{y_2}^{y_3}\left[\int_0^{\pi+\pi M\cos(y)+\Phi_{dt}} e^{j(mx+ny)}dx \right] + \int_{y_3}^{y_4}\left[\int_0^{\pi+\pi M\cos(y)} e^{j(mx+ny)}dx \right]dy$$

$$\left. + \int_{y_4}^{2\pi}\left[\int_{\Phi_{dt}}^{\pi+\pi M\cos(y)} e^{j(mx+ny)}dxdy \right]dy \right] \tag{5.1}$$

The complete solution defining the unit area for TENPWM with dead time is achieved by substituting Eq. (5.1) into Eq. (2.12). Note that Eq. (5.1) is solved numerically.

5.4   SIMULATION STRATEGY

The simulation technique introduced in Section 2.5 will now be adapted to determine the spectrum of TENPWM with dead time. The remainder of this sub-section describes the alterations necessary to the ideal simulation strategy of Section 2.5 to represent the pulses with dead time. The voltage loss and gain introduced in the TENPWM waveform with dead time is respectively shown in Figure 5.6 (a) and (b). Note that the parameters used in Figure 5.6 correspond to those of the ideal case originally introduced in Figure 2.14.
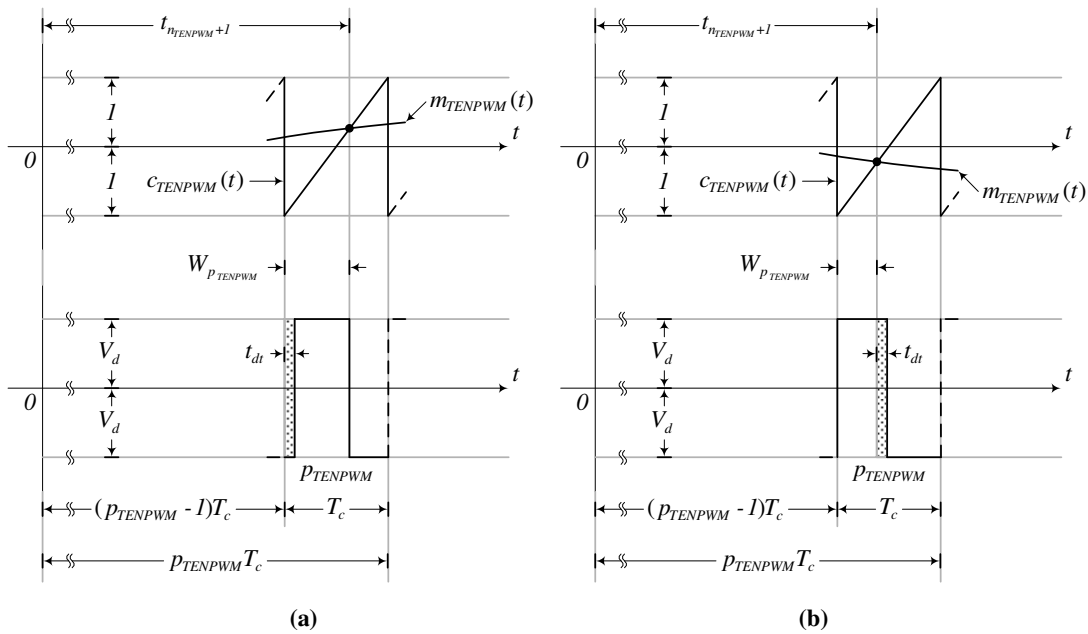
Figure 5.6: Generation of TENPWM with dead time for (a) $i_L>0$ and (b) $i_L<0$.

Through evaluation of Figure 5.6 (a) and (b) an expression for the width of the pth pulse can be found. Since the width is dependent on the current polarity, it must be defined over two regions. This leads to the equality:

$$W_{P_{TENPWM},dt} = \begin{cases} W_{P_{TENPWM}} - t_{dt} & \text{when} \quad i_L > 0 \\ W_{P_{TENPWM}} + t_{dt} & \text{when} \quad i_L < 0 \end{cases} \tag{5.2}$$

Note that the time shift for the ideal case of Eq. (2.94) is also dependent on the pulse width. Thus, redefining the time shift in the presence of blanking time yields:

$$
t_0 = \begin{cases} \left(p_{TENPWM} - 1\right)T_c + \dfrac{W_{p_{TENPWM,dt}}}{2} - \dfrac{t_{dt}}{2} & \text{when} \quad i_L > 0 \\[2em] \left(p_{TENPWM} - 1\right)T_c + \dfrac{W_{p_{TENPWM,dt}}}{2} + \dfrac{t_{dt}}{2} & \text{when} \quad i_L < 0 \end{cases} \tag{5.3}
$$

5.5   ANALYTICAL AND SIMULATION RESULTS

The analytical solutions derived in Section 5.3 and the simulation model of Section 5.4 will now be compared and discussed for TENPWM. The parameters used correspond to those defined in Chapter 1.1 unless stated otherwise. The parameters used in this section correspond to V_d=30V M=0.8, L_{filt}=10.4µH and ω_c/ω_0=384 unless stated otherwise.

5.5.1   HARMONIC COMPOSITION OF TENPWM WITH DEAD TIME

In this section the effect of t_{dt} within the audible band is considered. The plot shown in Figure 5.7 (a) was constructed using Eq. (5.1) in which only the baseband harmonics were considered, i.e. m=0. The simulation strategy of Section 5.4 was employed to construct the spectrum of Figure 5.7 (b). Note that t_{dt}=15ns in both plots.

(a)   (b)
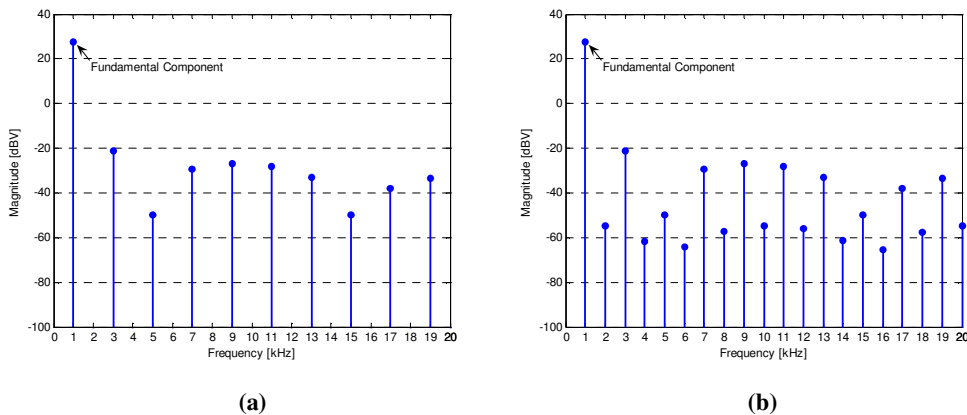
Figure 5.7: (a) Analytical (m=0) and (b) simulated baseband harmonics for TENPWM.

From (a) it can be seen that the analytical spectrum only contains baseband harmonics at odd orders of the modulating waveform. The simulation in (b), however, contains additional even order harmonics. This suggests that the sideband switching harmonics appear as distortion in the audible band.

(a)   **(b)**
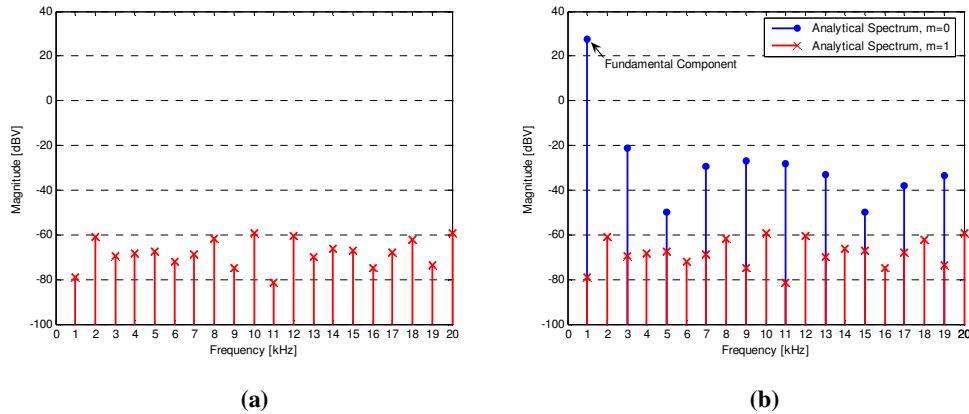
Figure 5.8: Analytical spectrum for (a) $m=1$ and $-383 \leq n \leq -364$ and (b) combination with Figure 5.7 (a).

The contribution of the cross modulation products of the first carrier ($m=1$ and $-383 < n < -364$) is shown in Figure 5.8 (a). A combination of Figure 5.7 (a) and Figure 5.8 (a) is illustrates in Figure 5.8 (b). The latter plot was constructed by simply plotting Figure 5.7 (a) on top of Figure 5.8 (a), thus not allowing for phasor summation of the various harmonics.

TABLE 5.1

ANALYTICAL AND SIMULATED MAGNITUDE OF THE BASEBAND HARMONICS FOR TENPWM.

Harmonic Number [-]	Analytical Magnitude [dBV]	Simulated Magnitude [dBV]
1	27.45107002	27.45106552
3	-21.03326378	-21.03015820
5	-49.89322182	-49.75868863
7	-29.29112361	-29.29778067
9	-26.85678341	-26.85776145
11	-28.19841313	-28.19412432
13	-32.99759418	-32.98354673
15	-49.90858282	-49.80020594
17	-38.05197260	-38.06822963
19	-33.62642316	-33.62593163

The analytical spectrum of Figure 5.8 (b) correlates very well with the simulation of Figure 5.7 (b). Note that, theoretically, the complete analytical spectrum within the specified range can be obtained by phasor summation of all the modulation products within the baseband. Table 5.1 compares the magnitudes of the analytical and simulation results of the odd order harmonics of Figure 5.7, which correlate very well.
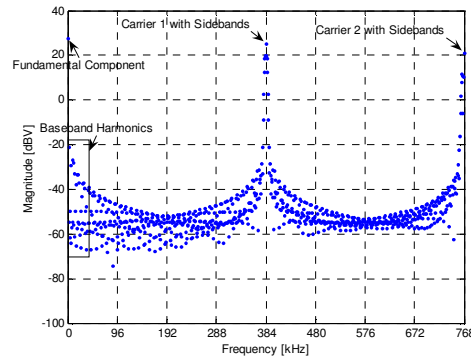
Figure 5.9: Simulated spectrum showing the first two carrier harmonics and its respective sidebands.

Figure 5.9 is a spectral plot constructed using the simulation strategy of Section 5.4. The first two carrier harmonics with its respective sidebands are shown. From this illustration it is evident that the sideband switching harmonics do not decay at such a rapid rate in the presence of t_{dt} as occurs in the ideal case discussed in Chapter 2. This confirms the findings.

5.5.2   GENERAL RELATION TO CIRCUIT PARAMETERS

Figure 5.10 (a) plots the simulated percentage THD as a function of t_{dt} (which is represented as a percentage of the switching period) for M=0.8. The increase in distortion for increasing t_{dt} is a well known result. Figure 5.10 (b) illustrates the relation between the THD and M. Since the dead time only has an effect within inductor current Scenario ②, the lower limit of M equals 0.25 to avoid Scenario ① being entering. From this plot it is apparent that distortion resulting from the dead time cannot be lowered by lowering M, also noted in [25].
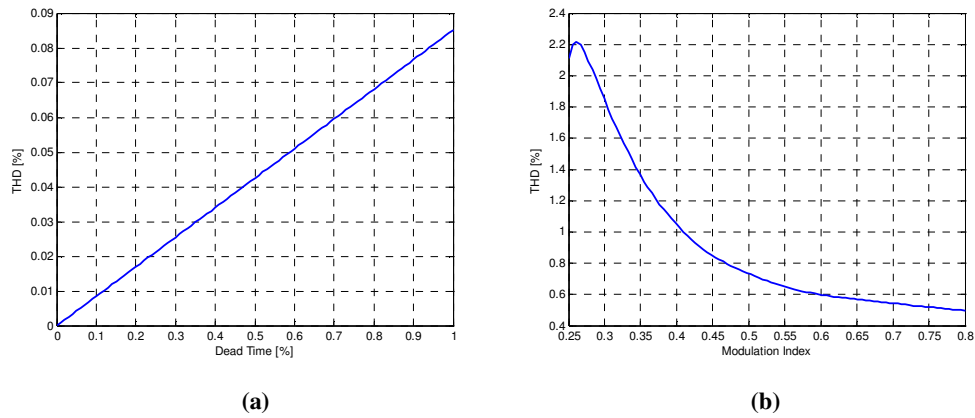
Figure 5.10: Simulated THD as a function of (a) t_{dt} and (b) M.

The percentage THD as a function of L_{filt} for t_{dt}=15ns is illustrated in Figure 5.11 (a). Consider the initial decrease in distortion between L_{filt}=2μH and L_{filt}=7μH. In this region the various harmonics within the baseband add in such a way that the THD decreases for increasing values of L_{filt}. Above L_{filt}=7μH they add in such a way to increase the overall distortion.
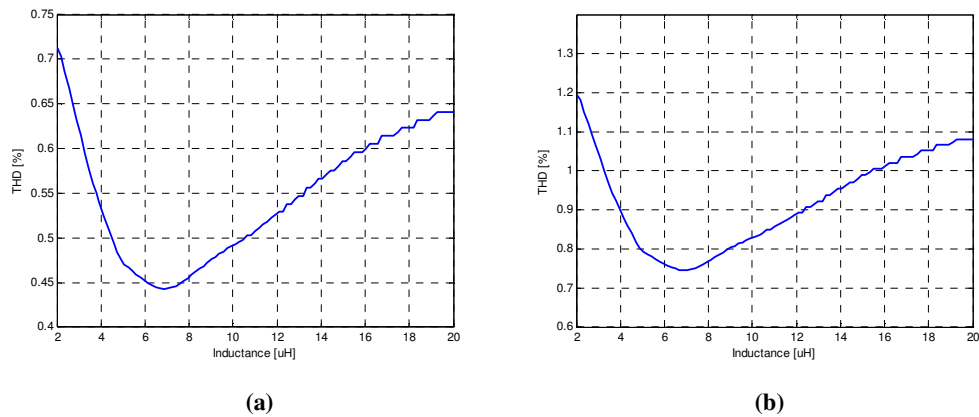
Figure 5.11: Simulated THD as a function of L_{filt} for (a) t_{dt}=15ns and (b) t_{dt}=25ns.

A similar plot to Figure 5.11 (a) is shown in Figure 5.11 (b) for t_{dt}=25ns. The same relation holds. Neglecting all other effects, this suggests that for a given dead time, an optimum value of L_{filt} can be determined.

5.6   SUMMARY

The analysis in this chapter considered the isolated effect of dead time on harmonic distortion. An overview was given of this well-known effect, after which an analytical model based on the double Fourier series method of analysis was introduced for TENPWM. A simulation model was next constructed. The proposed analytical and simulation models allow for L_{filt} as well as f_c to be parsed as parameters. The analytical and simulation results achieved showed very good correlation. It was shown that the dead time produces even, as well as odd order harmonics within the audible band. Moreover, it was established that the former harmonics are a result of the modulation products, which in turn dependend on the switching frequency. It was also shown that, for a specific dead time, the THD can be optimized by varying L_{filt}.

6
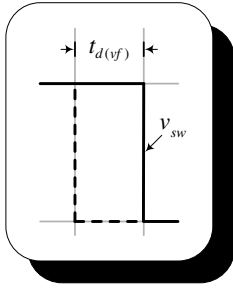
THE EFFECT OF THE MOSFET

TURN-ON AND TURN-OFF DELAYS

6.1 INTRODUCTION

It will be shown in this chapter that the MOSFET turn-*on* and turn-*off* delays lead to distortion within the baseband. A simulation model is presented, which is followed by a detailed discussion of the results achieved for TENPWM. This chapter contains a more detailed analysis of that presented in [46] by the author.

6.2 ANALYSIS OF THE TURN-ON AND TURN-OFF DELAYS

Figure 6.1 illustrates various switching waveforms for a positive inductor current. Since only the turn-*on* and turn-*off* delays are considered, the remainder of the switching waveform is idealized in an attempt to isolate the non-ideal effect under investigation. Two separate values of dead time, denoted $t_{dt(low\_side)}$ and $t_{dt(high\_side)}$ are assumed where the respective values represent the dead time introduced for the low side and high side MOSFET. The waveform is idealized if $t_{dt(low\_side)}=t_{d(vf)}$ and $t_{dt(high\_side)}=0$. This is necessary to avoid simultaneous conduction of the switching devices. The switching transition of $v_{GS(low\_side)}$ is also considered to be ideal. If all amplitude errors are neglected, for a positive inductor current, the switched output voltage of Figure 6.1 (d) within the turn-*on* and turn-*off* delay is independent of $v_{GS(low\_side)}$. This waveform has however been included in Figure 6.1 as (b) to clarify the above mentioned timing requirements.Later in this section it will be shown that the inverse situation holds for a negative inductor current, i.e. the switched output voltage within the turn-*on* and turn-*off* delay is independent of $v_{GS(high\_side)}$. Since the current polarity determines whether $v_{GS(low\_side)}$ or $v_{GS(high\_side)}$ switches the output voltage, the turn-*on* and turn-*off* delays are labelled in accordance with the switched output voltage rather than relating them to $v_{GS(low\_side)}$ or $v_{GS(high\_side)}$. The designations used are $t_{d(vf)}$ and $t_{d(vr)}$ (voltage fall and voltage rise).
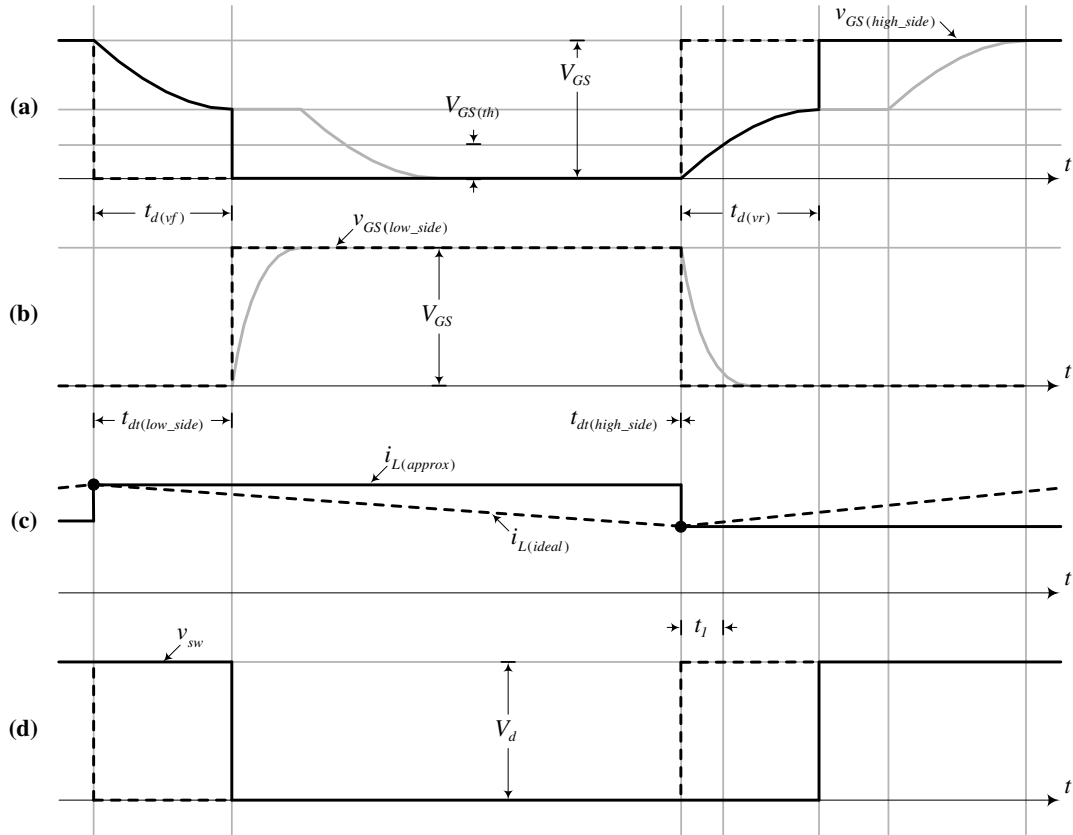
Figure 6.1: Switching waveforms for a positive inductor current. (a) High side gate-to-source voltage. (b) Low side gate-to-source voltage. (c) Inductor current. (d) Switched output voltage.

Consider $v_{GS(high\_side)}$ shown in Figure 6.1 (a). An instantaneous transition in gate drive from $v_{GS}=V_{GS}$ to $v_{GS}=0$ and vice versa is assumed, with V_{GS} well above $V_{GS(th)}$ according to the analysis in [24]. This ideal characteristic is represented by the dashed line in Figure 6.1 (a). The solid line represents the actual part of v_{GS} which leads to $t_{d(vf)}$ and $t_{d(vr)}$. Firstly, consider $t_{d(vf)}$. Once v_{GS} transitions from V_{GS} to zero, the actual gate-to-source voltage decreases exponentially as a result of the discharge of C_{iss} through R_G. This is given by the relation [28]:

$$v_{GS} = V_{GS}\, e^{-\frac{t}{R_G C_{iss}}} \tag{6.1}$$

The gate-to-source voltage decreases up to the point where the drain current equals the inductor current. Similar to the analysis in Chapter 5, i_L is approximated by a constant value within the interval $t_{d(vf)}$. This value is calculated on the ideal switching transition of the output

voltage, which occurs on $i_{L(upper\_env)}$ and is represented by $i_{L(approx)}$ in Figure 6.1 (c). The relation between v_{GS} and I_L can be found from the transfer characteristic of the MOSFET as:

$$v_{GS} = V_{GS(th)} + \frac{I_L}{g_{fs}} \tag{6.2}$$

From Eqs. (6.1) and (6.2) $t_{d(vf)}$ can be calculated as:

$$t_{d(vf)} = R_G C_{iss} \ln\left(\frac{V_{GS}}{V_{GS(th)} + \frac{I_L}{g_{fs}}}\right) \quad \text{for} \quad I_L > 0 \tag{6.3}$$

Using a similar approach, an expression for $t_{d(vr)}$ can be found for a positive inductor current. Again, an immediate transition in the applied gate drive voltage from zero to V_{GS} results in the charge of C_{iss} through R_G by the exponential relation:

$$v_{GS} = V_{GS}\left(1 - e^{-\frac{t}{R_G C_{iss}}}\right) \tag{6.4}$$

During the initial rising period (defined as t_1) the MOSFET is in the cut-off region since $v_{GS} < V_{GS(th)}$. This interval ends once $v_{GS} = V_{GS(th)}$ which yields:

$$t_1 = R_G C_{iss} \ln\left(\frac{V_{GS}}{V_{GS} - V_{GS(th)}}\right) \tag{6.5}$$

At the latter instant in time the drain current will start to flow in the MOSFET and v_{GS} will continue to increase in relation with Eq. (6.4). The drain-to-source voltage will increase in accordance with the transfer characteristic of the MOSFET up to the point where $I_D = I_L$. Substituting for Eq. (6.2) the equality in (6.5) can be written as:

$$t_{d(vr)} = R_G C_{iss} \ln\left(\frac{V_{GS}}{V_{GS} - V_{GS(th)} - \frac{I_L}{g_{fs}}}\right) \quad \text{for} \quad I_L > 0 \tag{6.6}$$

Using minor alterations to those of the previous analysis, similar expressions defining $t_{d(vf)}$ and $t_{d(vr)}$ can now be constructed for a negative inductor current. Figure 6.2 illustrates the switching waveforms.
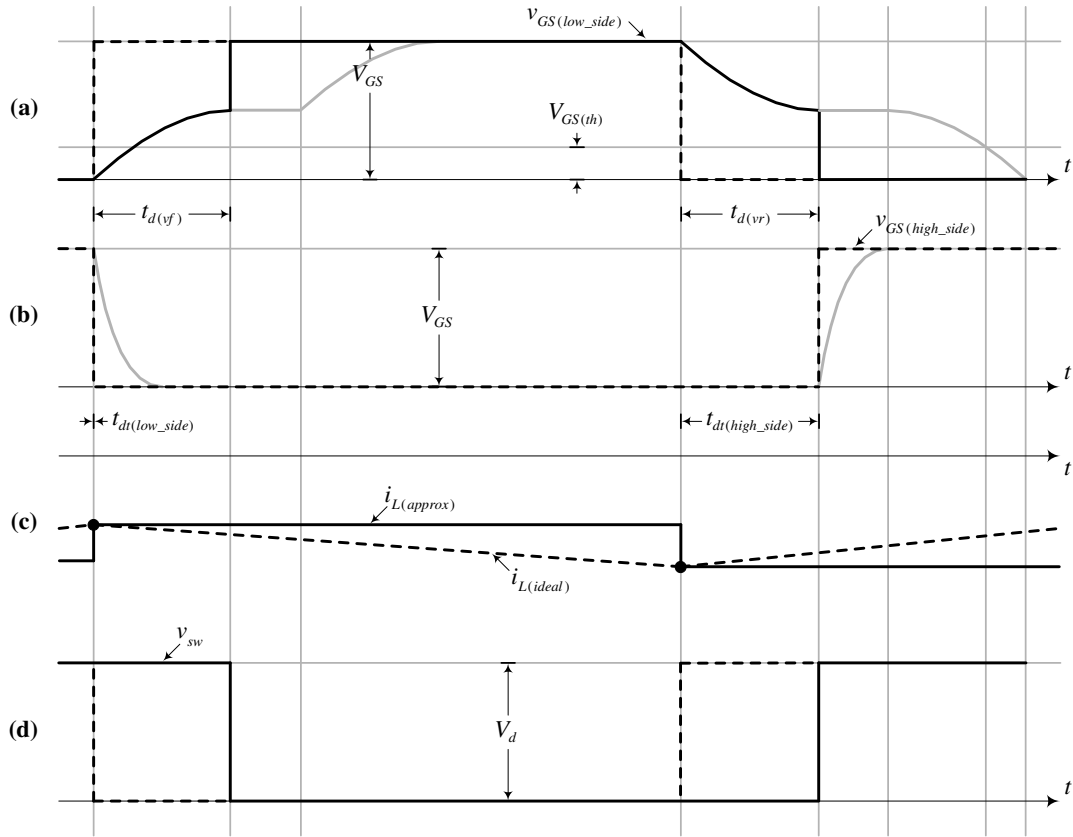
Figure 6.2: Switching waveforms for a negative inductor current. (a) Low side gate-to-source voltage. (b) High side gate-to-source voltage. (c) Inductor current. (d) Switched output voltage.

In order to idealize the switching waveforms the dead time requirements change to $t_{dt(low\_side)}=0$ and $t_{dt(high\_side)}=t_{d(vr)}$. The switching waveform of $v_{GS(high\_side)}$ is assumed to be ideal. As already mentioned, for a negative inductor current the output voltage within the turn-*on* and turn-*off* delays is independent of $v_{GS(high\_side)}$. The relation defining $t_{d(vf)}$ for a negative inductor current is:

$$t_{d(vf)} = R_G C_{iss} \ln\left(\frac{V_{GS}}{V_{GS} - V_{GS(th)} - \frac{I_L}{g_{fs}}} \right) \quad \text{for} \quad I_L < 0 \tag{6.7}$$

While $t_{d(vr)}$ can be defined as:

$$t_{d(vr)} = R_G C_{iss} \ln\left(\frac{V_{GS}}{V_{GS(th)} + \frac{I_L}{g_{fs}}}\right) \quad \text{for} \quad I_L < 0 \tag{6.8}$$

6.3   ERROR DESCRIPTION

The solutions obtained in Section 6.2 are analysed in this section. The parameters used for the remainder of this chapter correspond to V_d=10V M=0.85, R_G=10Ω, V_{GS}=10V, $V_{GS(th)}$=4.9V, g_{fs}=11, C_{iss}=810pF, L=10.7µH and ω_c/ω_0=384 unless stated otherwise. The plots illustrated in Figure 6.3 (a) and (b) respectively represent $t_{d(vr)}$ for Scenario ① (R_L=120Ω) and Scenario ② (R_L=8.2Ω).

(a)   (b)
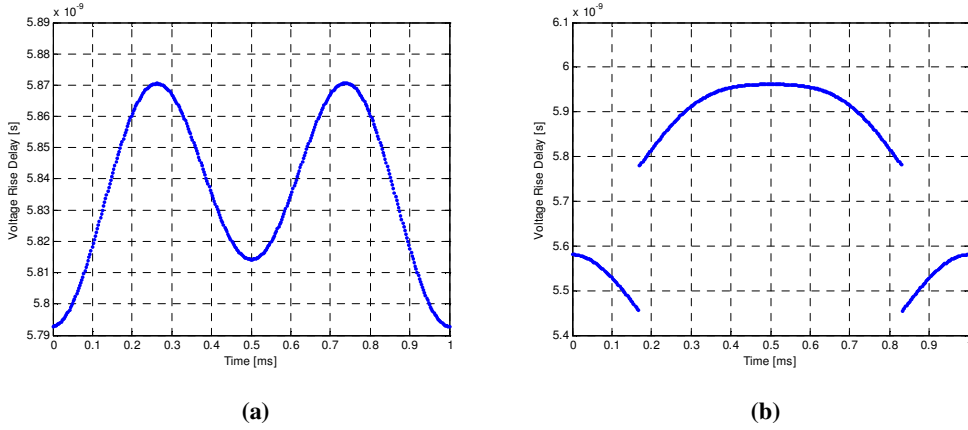
Figure 6.3: $t_{d(vr)}$ for (a) Scenario ① and (b) Scenario ②.

From Figure 6.3 (a) it is evident that Scenario ① results in a continuous curve. This can be ascribed to the fact that $i_{L(lower\_env)}$ remains negative over the complete switching cycle, which in turn results in $t_{d(vr)}$ being only defined by Eq. (6.8). For Scenario ② the current changes polarity, which means that $t_{d(vr)}$ is either defined by Eq. (6.6) or Eq. (6.8), leading to the abrupt change in $t_{d(vr)}$ illustrated in Figure 6.3 (b).

(a)   (b)
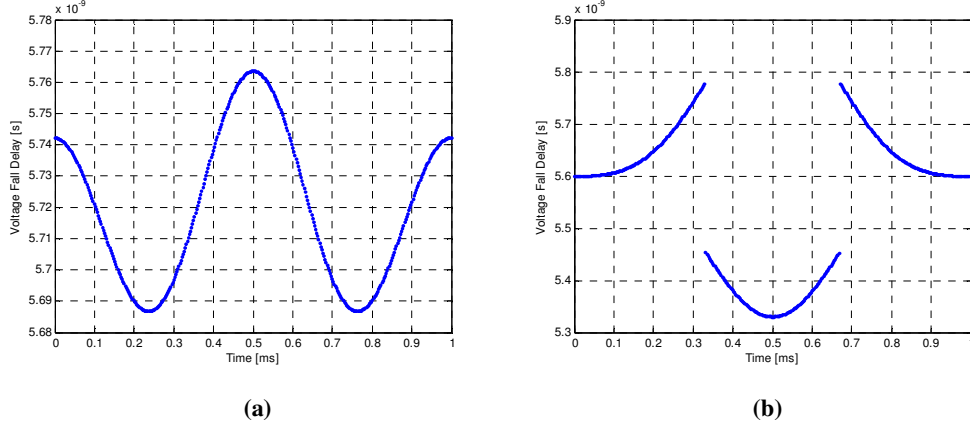
Figure 6.4: $t_{d(vf)}$ for for (a) Scenario ① and (b) Scenario ②.

Figure 6.4 shows a plot of $t_{d(vf)}$ for the various scenarios of the inductor current. Similar to Figure 6.3 the curve in Figure 6.4 (a) is only defined by Eq. (6.3) since $i_{L(upper\_env)}$ remains positive over the complete switching cycle. For Scenario ② shown in Figure 6.4 (b) the solution is either described by Eq. (6.3) or Eq. (6.7). The analytical solutions of Eqs. (6.3), (6.6), (6.7) and (6.8) can next be used to construct the simulation model.

6.4   SIMULATION STRATEGY

With the solutions for $t_{d(vf)}$ and $t_{d(vr)}$ defined in Section 6.2 it is now possible to incorporate the delays into the simulation strategy introduced in Section 2.5. The pulse in Figure 6.5 represents the pth pulse of a TENPWM waveform with the addition of a non-zero turn-*on* and turn-*off* delay. The remaining parameters correspond to those used in Figure 2.14. From Figure 6.5 it can be seen that the pulse width changes to:

$$W_{p_{TENPWM(vr\_vf)}} = W_{p_{TENPWM}} - t_{d(vr)} + t_{d(vf)} \tag{6.9}$$

Since the time shift of Eq. (2.94) is also dependent on the pulse width, it needs to be adapted. Substituting for Eq. (6.9) the time shift of Eq. (2.94) can be written as:

$$t_0 = \left(p_{TENPWM} - 1 \right) T_c + \frac{W_{p_{TENPWM}} - t_{d(vr)} + t_{d(vf)}}{2} \tag{6.10}$$
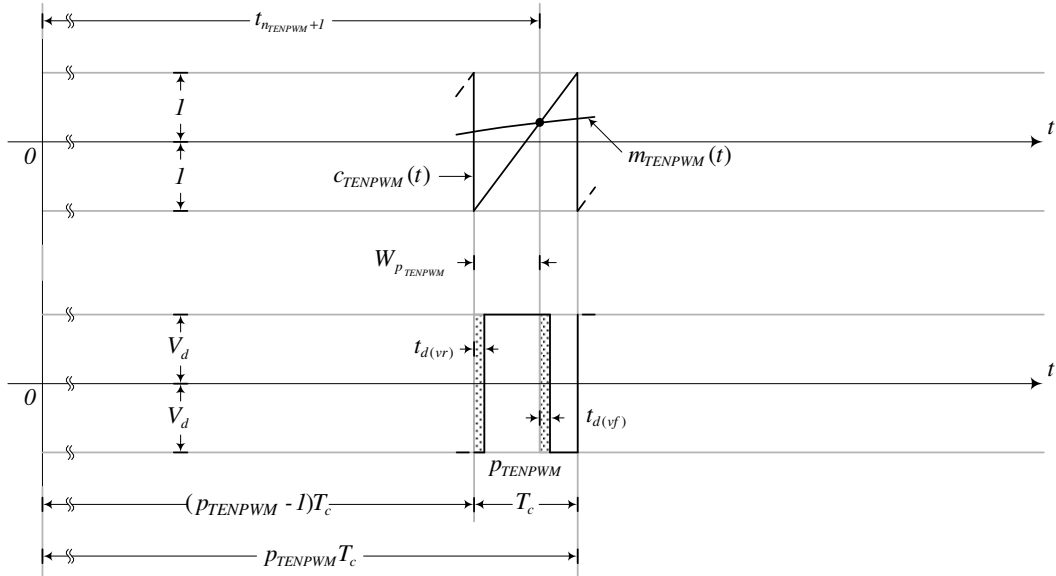
Figure 6.5: Generation of TENPWM with turn-*on* and turn-*off* delays.

6.5   SIMULATION RESULTS

In this section the simulation model of Section 6.4 will be utilized to determine the effect of the non-zero $t_{d(vr)}$ and $t_{d(vf)}$ on distortion. The results achieved will be discussed for both scenarios of the inductor current. Furthermore, note that the parameters used correspond to those defined in Section 6.3 unless stated otherwise.

6.5.1   BASEBAND HARMONICS

Firstly, the effect within the baseband is determined in this section. Figure 6.6 (a) shows a spectral plot of the baseband harmonics for inductor current Scenario ①. From Figure 6.6 it can be seen that Scenario ② produces a much higher level of distortion than that of Scenario ①. The reason for the distortion in Figure 6.6 (b) being so much higher than that of (a) can be explained when referring to Figure 6.3 and Figure 6.4. The abrupt change in $t_{d(vr)}$ and $t_{d(vf)}$ associated with Scenario ② (Figure 6.3 (b) and Figure 6.4 (b)) results in the more prominent baseband harmonics shown in Figure 6.6 (b) than those in (a).

(a)   **(b)**
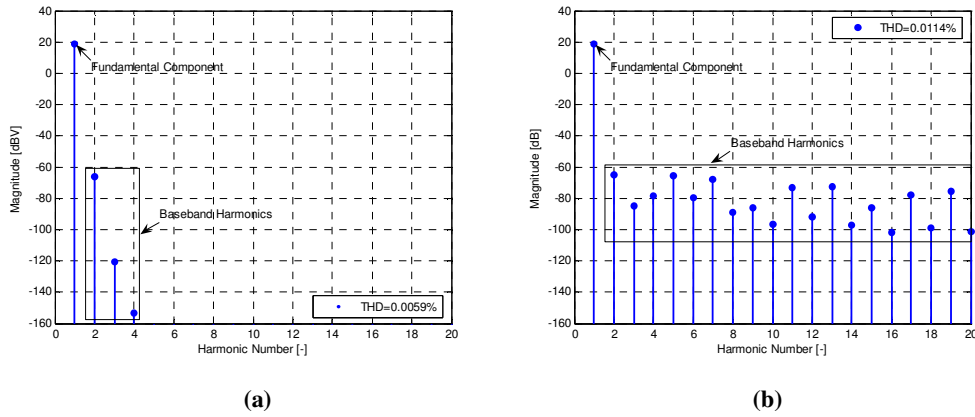
Figure 6.6: Simulated TENPWM baseband harmonics for (a) Scenario ① and (b) Scenario ②.

Table 6.1 compares the THD of Scenario ① and ② for various values of R_G. It can be seen that the distortion increases for increasing values of R_G. This is a result from the fact that $t_{d(vr)}$ and $t_{d(vf)}$ increase for increasing values of R_G, which is evident upon simple inspection of Eqs. (6.3), (6.6), (6.7) and (6.8).

TABLE 6.1

SIMULATED THD FOR TENPWM FOR VARIOUS R_G.

R_G [Ω]	Simulated THD, Scenario 1 [%]	Simulated THD, Scenario 2 [%]
10	0.005969	0.011438
22	0.013132	0.025153
27	0.016116	0.030864
47	0.028054	0.053691
100	0.059690	0.114039
120	0.071628	0.136758

Table 6.2 shows a comparison between Scenario ① and ② for various values of V_{GS}. Since Eqs. (6.3) and (6.8) are independent of V_{GS} for Scenario ① the THD remains constant. For Scenario ② the distortion increases for increasing values of V_{GS}. The following section focuses on the contribution of the sideband switching harmonics within the baseband.

TABLE 6.2

SIMULATED THD FOR TENPWM FOR VARIOUS V_{GS}.

V_{GS} [V]	Simulated THD, Scenario 1 [%]	Simulated THD, Scenario 2 [%]
10	0.005969	0.011438
11	0.005969	0.050100
12	0.005969	0.084282
13	0.005969	0.113984
14	0.005969	0.140197
15	0.005969	0.163643

6.5.2   SIDEBAND HARMONICS

In this section the analysis focuses on the sideband harmonics. Figure 6.7 compares the spectra for Scenario ① and ②. From the latter illustration it can be seen that the sideband harmonics decay at a rapid rate for Scenario ①.
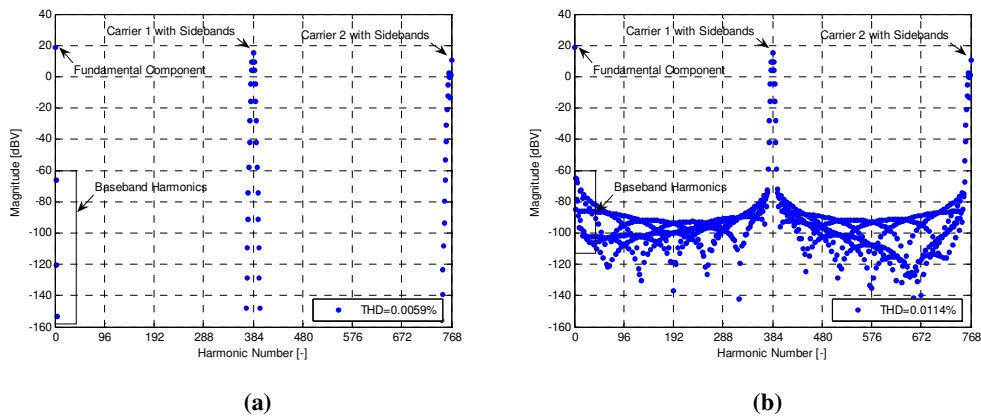
Figure 6.7: Simulated TENPWM spectra for (a) Scenario ① and (b) Scenario ②.

For Scenario ② the sidebands do not roll off that quickly and thus contribute to distortion within the baseband, yielding an effect similar to that of dead time.

6.6   SUMMARY

The isolated effect of the MOSFET turn-*on* and turn-*off* delay on harmonic distortion was considered in this chapter. Well-known analytical expressions describing these delays [24], [28] were implemented into a simulation model for TENPWM.

The simulation results obtained for TENPWM showed that inductor current Scenario ② produces much higher levels of distortion than Scenario ① due to the abrupt change in the delays upon a change in current polarity. Furthermore, it was shown that the THD increases for increasing values of the delays. Lastly, the analysis showed that the sideband switching harmonics only increase distortion under Scenario ②.

7
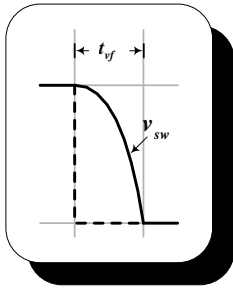
THE EFFECT OF NON-ZERO

NON-LINEAR SWITCHING TRANSITIONS

7.1 INTRODUCTION

This chapter contains the analysis presented in [47] by the author, in which the isolated effect of the non-zero switching transitions is investigated. The analysis is based on well-known analytical expressions describing the switching behaviour [24], [28]. A method for the modelling of the non-linear switching curve based on a specific MOSFET case study is then introduced and compared to that of a linear transition to determine its significance. A simulation model is also introduced, which is followed by a detailed discussion of the results achieved. The analysis shows that the distortion is highly dependent on current polarity rather than modulation and that it increases for longer switching times. Furthermore, the proposed non-linear switching model results in significantly higher levels of distortion than those of the linear transitions.

7.2 ANALYSIS OF NON-ZERO RISE AND FALL SWITCHING TRANSITIONS

The switching waveforms that influence intervals t_{vf} and t_{vr} are shown in Figure 7.1 for a positive inductor current. The analysis in this chapter is only concerned with the effect of the non-zero rise and fall transitions, and thus only the portions of the switching waveforms falling within these intervals are considered to be non-ideal. This requires conditions in which the remainder of the waveform is idealized.

Firstly, during the initial transition of $v_{GS(high\_side)}$ from *on* to *off* the voltage is assumed to switch in zero time from V_{GS} to $v_{GS(I_L)}$. This leads to a value of $t_{d(on)}=0$. Using similar conditions $v_{GS(high\_side)}$ results in $t_{d(off)}=0$ during a change of $v_{GS(high\_side)}$ from *off* to *on*. In order to avoid simultaneous conduction of the switching devices, the dead time requirement has to be adapted in such a way that $t_{dt(low\_side)}=t_{vf}$ and $t_{dt(high\_side)}=0$ as shown in Figure 7.1.
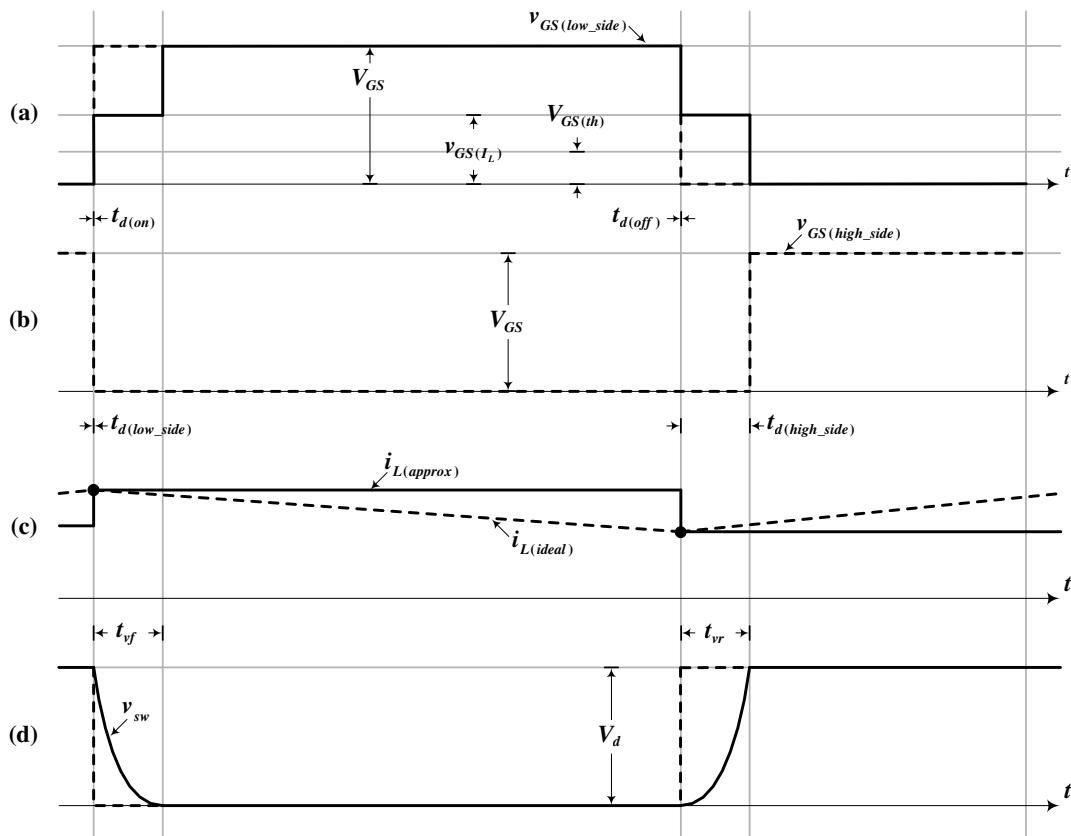
Figure 7.1: Switching waveforms for a positive inductor current. (a) High side gate-to-source voltage. (b) Low side gate-to-source voltage. (c) Inductor current. (d) Switched output voltage.

As already mentioned in Chapter 6, for a positive inductor current with all amplitude errors neglected, the output voltage is independent of $v_{GS(low\_side)}$. However, it has once again been included in Figure 7.1 (b) to clarify the timing requirements of the dead time. Consider t_{vf}. Upon completion of interval $t_{d(on)}$ the switched output voltage starts to fall. As in the analysis of Chapter 6, i_L is again approximated by $i_{L(approx)}$ within region t_{vf}. This value is

calculated on the ideal output switching transition from *off* to *on* which occurs on $i_{L(upper\_env)}$. This is shown in Figure 7.1 (c). According to the MOSFET transfer characteristic v_{GS} will also remain constant at a value:

$$v_{GS(I_L)} = V_{GS(th)} + \frac{I_L}{g_{fs}} \tag{7.1}$$

Since $v_{GS(I_L)}$ is constant, the full gate current will charge C_{GD}. The expression describing I_G can thus be written as:

$$I_G = -\frac{v_{GS(I_L)}}{R_G} = -\frac{\left(V_{GS(th)} + \frac{I_L}{g_{fs}}\right)}{R_G} \tag{7.2}$$

The voltage v_{DG} across C_{GD} is given by:

$$\frac{dv_{DG}}{dt} = \frac{I_G}{C_{GD}} \tag{7.3}$$

Since v_{GS} is constant, the rate of change of v_{DS} equals the rate of change of the v_{DG}. Stated mathematically:

$$\frac{dv_{DS}}{dt} = \frac{dv_{DG}}{dt} \tag{7.4}$$

Substituting for Eq. (7.3) the equality in Eq. (7.4) leads to the expression:

$$\frac{dv_{DS}}{dt} = -\frac{\left(V_{GS(th)} + \frac{I_L}{g_{fs}}\right)}{R_G C_{GD}} \quad \text{for} \quad I_L > 0 \tag{7.5}$$

An expression describing v_{DS} during t_{vr} can now be found in a similar manner. Since the drain current remains constant at a value calculated on $i_{L(lower\_env)}$ the gate voltage is still given by Eq. (7.1), which in turn results in the complete I_G flowing through C_{GD}. The gate current is given by:

$$I_G = \frac{V_{GS} - V_{GS(I_L)}}{R_G} = \frac{V_{GS} - V_{GS(th)} - \frac{I_L}{g_{fs}}}{R_G} \tag{7.6}$$

Note that $v_{GS(I_L)}$ is defined in Eq. (7.1). The voltage v_{DG} across C_{GD} is given by Eq. (7.3) and since the rate of change of v_{DS} equals the rate of change of v_{DG} the expression for v_{DG} during interval t_{vr} can be constructed from Eqs. (7.3) and (7.6) as:

$$\frac{dv_{DS}}{dt} = \frac{V_{GS} - V_{GS(th)} - \frac{I_L}{g_{fs}}}{R_G C_{GD}} \quad \text{for} \quad I_L > 0 \tag{7.7}$$
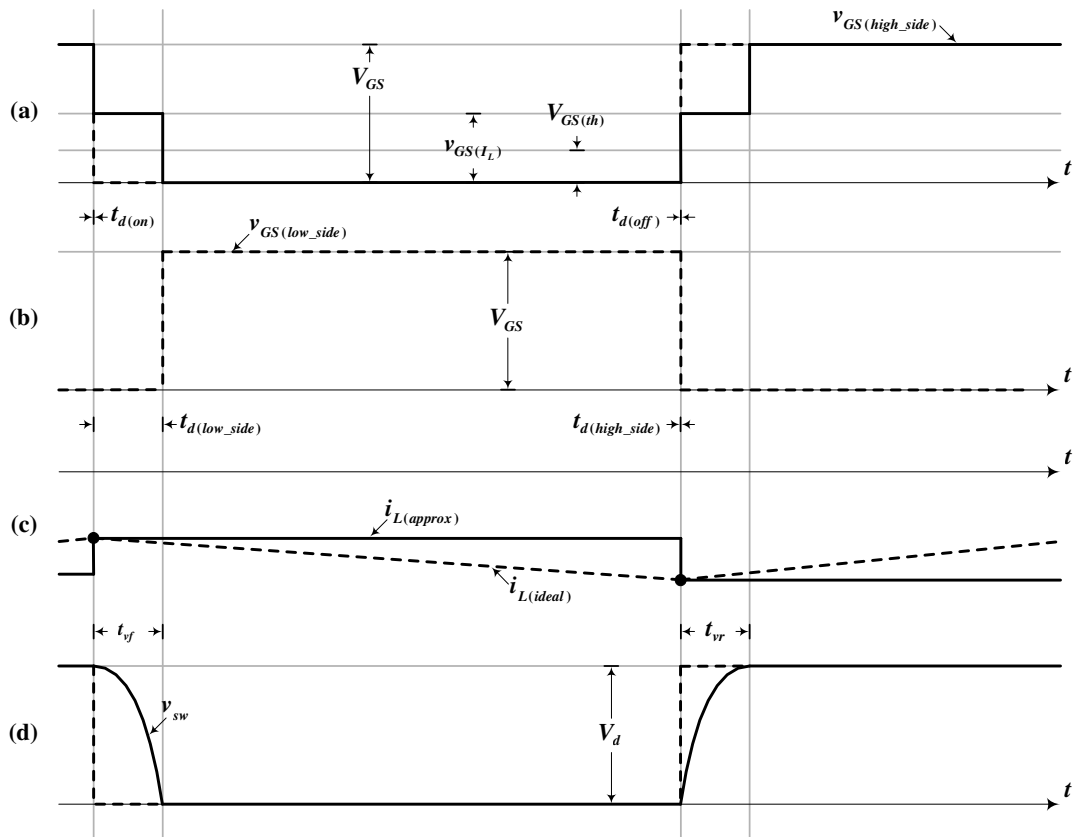
Figure 7.2: Switching waveforms for a negative inductor current. (a) Low side gate-to-source voltage. (b) High side gate-to-source voltage. (c) Inductor current. (d) Switched output voltage.

Figure 7.2 illustrates the switching waveforms affecting intervals t_{vf} and t_{vr}. For a negative inductor current the dead time changes to $t_{dt(low\_side)}=0$ and $t_{dt(high\_side)}=t_{vr}$ in order to isolate the switching transitions from the remaining non-ideal effects. Note that $v_{GS(high\_side)}$ is assumed to be ideal and that it is once again included to state the dead time requirements.

Following a similar approach to that of the previous analysis for a positive inductor current, an expression describing v_{DS} during t_{vf} can be constructed as:

$$\frac{dv_{DS}}{dt} = -\frac{\left(V_{GS} - V_{GS(th)} - \frac{I_L}{g_{fs}}\right)}{R_G C_{GD}} \quad \text{for} \quad I_L < 0 \tag{7.8}$$

In a similar manner, an expression for v_{DS} for interval t_{vr} can be obtained as:

$$\frac{dv_{DS}}{dt} = \frac{V_{GS(th)} + \frac{I_L}{g_{fs}}}{R_G C_{GD}} \quad \text{for} \quad I_L < 0 \tag{7.9}$$

The expressions describing the switched output voltage during intervals t_{vr} and t_{vf} obtained will be solved in the following section.

7.3   SOLUTIONS TO THE EXPRESSIONS OF THE SWITCHING CURVES

The solutions to the expressions of the switching curves derived in the previous section will now be determined. Initially, a solution for a constant C_{GD} is obtained, after which a more realistic solution for a dynamic C_{GD} is considered. As will be shown in Section 7.3.1, a constant C_{GD} results in a linear switching curve, whereas the proposed dynamic approximation of C_{GD} leads to a non-linear switching characteristic. The reasoning behind the inclusion of both models is to show how the proposed model differs from that introduced in previous work [29], as well as to determine whether the non-linear switching characteristic has a negligible effect on distortion compared to the linear switching curve. Note that the solutions obtained in this section are applicable to both half-bridge and full-bridge topologies.

7.3.1   CONSTANT GATE-TO-DRAIN CAPACITANCE

Since C_{GD} is dependent on v_{DS} it is necessary to establish an approximation to achieve the objective of a linear switching characteristic in this section. By defining C_{GD1} at $v_{DS}=0$ and C_{GD2} at $v_{DS}=V_d$ the best constant approximation is achieved by:

$$C_{GD} = \frac{C_{GD1} - C_{GD2}}{2} \tag{7.10}$$

Consider a positive inductor current. The solution to v_{DS} during t_{vf} can be found through integration of Eq. (7.5) as:

$$v_{DS} = V_d - \left[\frac{V_{GS(th)} + \frac{I_L}{g_{fs}}}{R_G C_{GD}} \right] t \quad \text{for} \quad I_L > 0 \tag{7.11}$$

By noting that $t = t_{vf}$ if v_{DS} is zero, the solution to t_{vf} can be found as:

$$t_{vf} = \frac{V_d R_G C_{GD}}{V_{GS(th)} + \frac{I_L}{g_{fs}}} \quad \text{for} \quad I_L > 0 \tag{7.12}$$

The solution to v_{DS} during t_{vr} can be found through integration of Eq. (7.7), which yields:

$$v_{DS} = \left[\frac{V_{GS} - V_{GS(th)} - \frac{I_L}{g_{fs}}}{R_G C_{GD}} \right] t \quad \text{for} \quad I_L > 0 \tag{7.13}$$

Since $v_{DS} = V_d$ when $t = t_{vr}$ the solultion to t_{vr} can be expressed as:

$$t_{vr} = \frac{V_d R_G C_{GD}}{V_{GS} - V_{GS(th)} - \frac{I_L}{g_{fs}}} \quad \text{for} \quad I_L > 0 \tag{7.14}$$

Using a similar approach the solutions to v_{DS} during t_{vr} and t_{vf} can now also be determined for a negative inductor current. The solution to v_{DS} during t_{vf} can be found through integration of Eq. (7.8) as:

$$v_{DS} = V_d - \left[\frac{V_{GS} - V_{GS(th)} - \frac{I_L}{g_{fs}}}{R_G C_{GD}} \right] t \quad \text{for} \quad I_L < 0 \tag{7.15}$$

Since v_{DS} equals zero when $t = t_{vf}$ the solution to t_{vf} can be written as:

$$t_{vf} = \frac{V_d R_G C_{GD}}{V_{GS} - V_{GS(th)} - \frac{I_L}{g_{fs}}} \quad \text{for} \quad I_L < 0 \tag{7.16}$$

The solution to v_{DS} during t_{vr} can be found through integration of Eq. (7.9), which leads to:

$$v_{DS} = \left[\frac{V_{GS(th)} + \frac{I_L}{g_{fs}}}{R_G C_{GD}} \right] t \quad \text{for} \quad I_L < 0 \tag{7.17}$$

By next noting that $v_{DS}=V_d$ when $t=t_{vr}$ the solultion can be expressed as:

$$t_{vr} = \frac{V_d R_G C_{GD}}{V_{GS(th)} + \frac{I_L}{g_{fs}}} \quad \text{for} \quad I_L < 0 \tag{7.18}$$

The following section contains a more complex model of C_{GD}. It is shown that the prosposed model leads to a non-linear solution to v_{DS} during the switching intervals.

7.3.2 DYNAMIC GATE-TO-DRAIN CAPACITANCE

Since the C_{GD} vs. v_{DS} characteristic is MOSFET specific, a case study approach will be used in this section to obtain the solution to the switching curves for a varying C_{GD}. Consider Figure 7.3. The bold curve in (a) represents the actual C_{GD} vs. v_{DS} characteristic for part IRFI4019H-117P obtained from the device's datasheet [48].

(a)   **(b)**
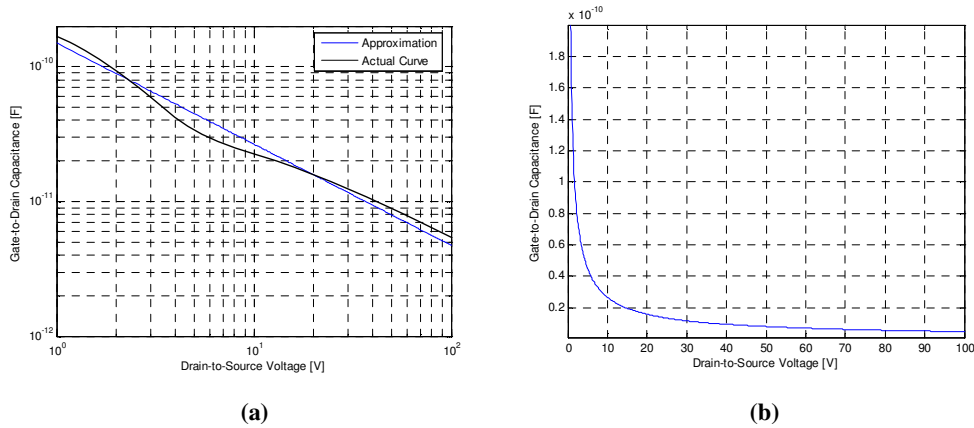
Figure 7.3: (a) Approximate and actual curve of C_{GD} as a function of v_{DS} on a log scale. (b) Approximate curve of C_{GD} as a function of v_{DS} on a linear scale for part IRFI4019H-117P.

From Figure 7.3 (a) it can be seen that a good approximation to the actual curve is achieved via a power law of the form:

$$C_{GD} = m_{C_{GD}} v_{DS}^{\,k_{C_{GD}}} \tag{7.19}$$

The approximation is shown in (a) with parameters corresponding to $m_{C_{GD}} = 150\,\text{pF}$ and $k_{C_{GD}} = -0.75$. Figure 7.3 (b) represents the plot of (a) on a linear scale. The relation in Eq.

(7.19) can next be used to obtain the solutions to the expressions derived in Section 7.2. Firstly, consider a positive inductor current. The solution to v_{DS} during t_{vf} can be found through integration of Eq. (7.5) as:

$$v_{DS} = V_d - \left[\frac{\left(k_{C_{GD}} + 1\right)\left(V_{GS(th)} g_{fs} + I_L\right)}{R_G g_{fs} m_{C_{GD}}} t \right]^{\left(\frac{1}{k_{C_{GD}}+1}\right)} \quad \text{for} \quad I_L > 0 \tag{7.20}$$

Since $v_{DS}=0$ when $t=t_{vf}$ the solution to t_{vf} can be written as:

$$t_{vf} = \frac{R_G g_{fs} m_{C_{GD}} V_d^{\left(k_{C_{GD}}+1\right)}}{\left(k_{C_{GD}} + 1\right)\left(V_{GS(th)} g_{fs} + I_L\right)} \quad \text{for} \quad I_L > 0 \tag{7.21}$$

Eq. (7.20) can next be written in terms of t_{vf} by rewriting Eq. (7.21) and substituting the result into Eq. (7.20). Since $k_{C_{GD}} = -0.75$ Eq. (7.20) simplifies to:

$$v_{DS} = V_d - \frac{V_d}{t_{vf}^4} t^4 \quad \text{for} \quad I_L > 0 \tag{7.22}$$

From Eq. (7.22) it is evident that the switching curve can be approximated by a polynomial of order four. Using result of this, the remaining solutions can easily be obtained. For a positive inductor current, v_{DS} during t_{vr} is given by:

$$v_{DS} = V_d - \frac{V_d}{t_{vr}^4} \left(t - t_{vr}\right)^4 \quad \text{for} \quad I_L > 0 \tag{7.23}$$

Where t_{vr} can be written as:

$$t_{vr} = \frac{4 R_G g_{fs} m_{C_{GD}} V_d^{\frac{1}{4}}}{\left(V_{GS} g_{fs} - V_{GS(th)} g_{fs} - I_L\right)} \quad \text{for} \quad I_L > 0 \tag{7.24}$$

Consider a negative inductor current. The solution to v_{DS} within interval t_{vf} can be written as:

$$v_{DS} = \frac{V_d}{t_{vf}^4} \left(t - t_{vf}\right)^4 \quad \text{for} \quad I_L < 0 \tag{7.25}$$

With t_{vf} defined by:

$$t_{vf} = \frac{4 R_G g_{fs} m_{C_{GD}} V_d^{\frac{1}{4}}}{\left(V_{GS} g_{fs} - V_{GS(th)} g_{fs} - I_L\right)} \quad \text{for} \quad I_L < 0 \tag{7.26}$$

Finally, the solution to v_{DS} during interval t_{vr} is given by:

$$v_{DS} = \frac{V_d}{t_{vr}^4} t^4 \quad \text{for} \quad I_L < 0 \tag{7.27}$$

While t_{vr} in Eq. (7.27) can be written as:

$$t_{vr} = \frac{4 R_G g_{fs} m_{C_{GD}} V_d^{\frac{1}{4}}}{\left(V_{GS(th)} g_{fs} + I_L\right)} \quad \text{for} \quad I_L < 0 \tag{7.28}$$

7.4   ERROR DESCRIPTION

In this section the solutions of the switching curves obtained in Section 7.3 are analysed. Note that the parameters used for the remainder of this chapter correspond to V_d=10V M=0.85, R_G=10Ω, V_{GS}=10V, $V_{GS(th)}$=4.9V, g_{fs}=11, L=10.7µH and ω_c/ω_0=384 unless stated otherwise. Figure 7.4 (a) and (b) respectively show a plot of t_{vr} for Scenario ① (R_L=120Ω) and Scenario ② (R_L=8.2Ω) using the solutions obtained in Section 7.3.2.

(a)   **(b)**
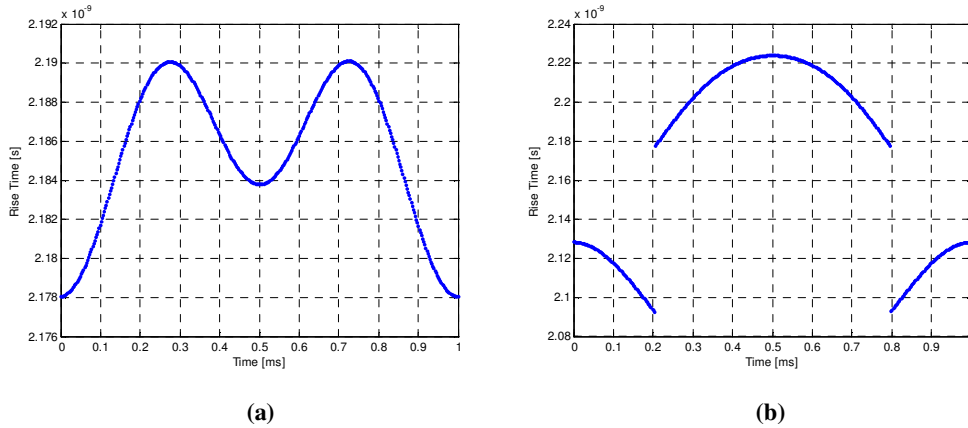
Figure 7.4: Rise time for (a) Scenario ① and (b) Scenario ②.

From Figure 7.4 (a) it can be seen that Scenario ① results in a continuous curve. This can be ascribed to the fact that $i_{L(lower\_env)}$ remains negative over the complete switching cycle which in turn results in t_{vr} being only defined by Eq. (7.28). For Scenario ② the current changes polarity, which means that t_{vr} is either defined by Eq. (7.24) or Eq. (7.28), leading to the abrupt change in t_{vr} shown in Figure 7.4 (b).

(a)   (b)
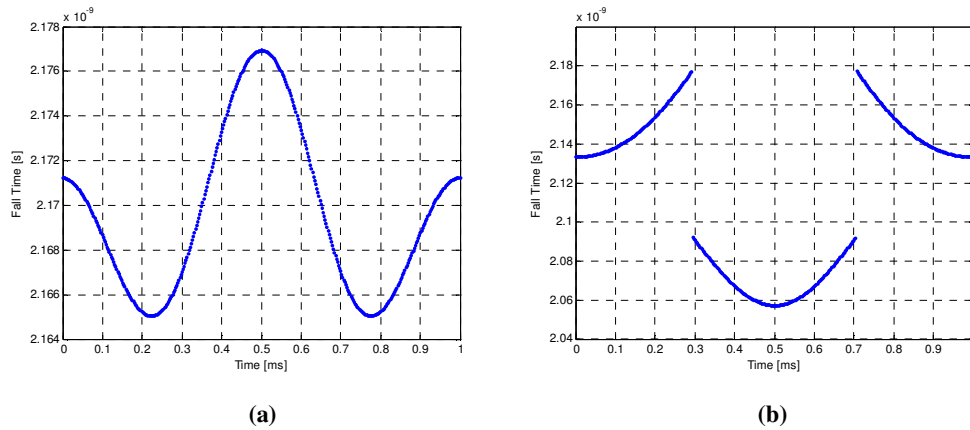
Figure 7.5: Fall time for (a) Scenario ① and (b) Scenario ②.

Figure 7.5 shows a plot of t_{vf} for the various scenarios of the inductor current. Similar to Figure 7.4 the curve in (a) is only defined by Eq. (7.21) since $i_{L(upper\_env)}$ remains positive over the complete switching cycle. For Scenario ② shown in Figure 7.5 (b) the solution is either described by Eq. (7.21) or Eq. (7.26).

(a)   (b)
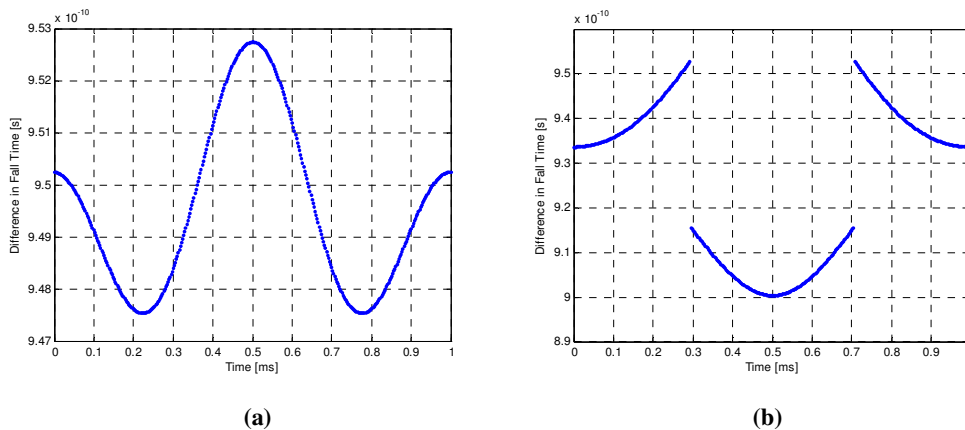
Figure 7.6: Difference in fall time for (a) Scenario ① and (b) Scenario ②.

Figure 7.6 illustrates a plot of the difference in t_{vf} for the solutions obtained in Section 7.3.2 and Section 7.3.1. This serves as a reference for discussing of the results, which follows in Section 7.6.

7.5   SIMULATION STRATEGY

The simulation strategy of Section 2.5 can now be adapted to accommodate for t_{vr} and t_{vf}. Since a comparison between the linear and non-linear switching characteristic will be included, the simulation model needs to be set up for both sets of solutions obtained in Section 7.3. Note that models for both TENPWM and DENPWM are presented.

TENPWM

The pth pulse of a TENPWM waveform in the presence of a non-zero turn-*on* and turn-*off* switching transition is shown in Figure 7.7. The solid curves represent the non-linear transitions for a positive inductor current during t_{vr} and t_{vf}, whereas the dashed curves represent switching for a negative inductor current. The linear transitions are shown as grey lines within the latter intervals.
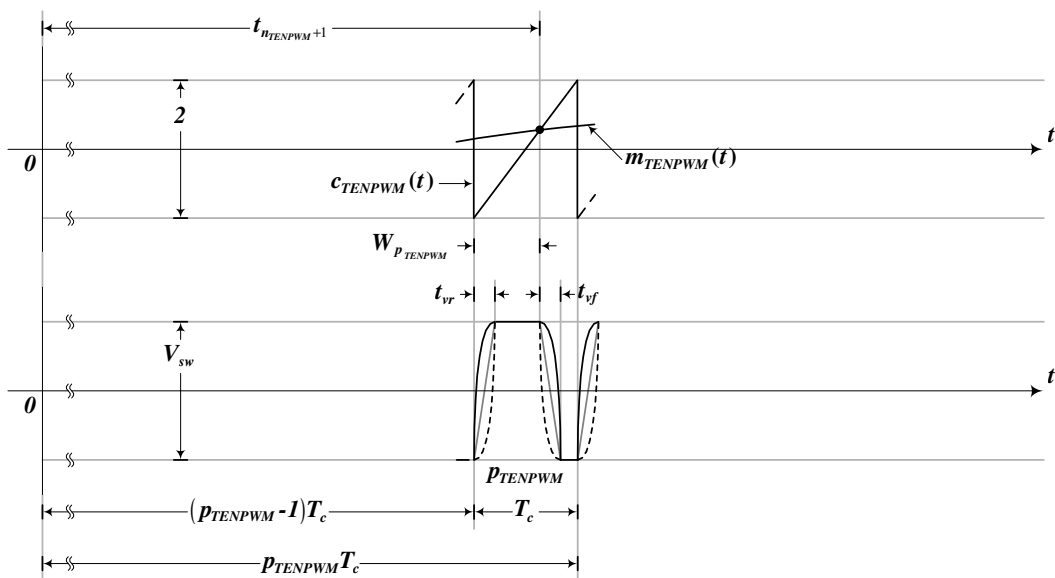
Figure 7.7: Generation of TENPWM with non-zero rise and fall times.

The Fourier Transform of $v_{DS}(t)$ during t_{vr} including the necessary time shift t_0 is given by:

$$\Im\left[v_{DS}\left(t\right)\right]e^{-j2\pi ft_0} = \left[\int_0^{t_{vr}} v_{DS}\left(t\right)e^{-j2\pi ft}dt\right]e^{-j2\pi ft_0} \tag{7.29}$$

Where:

$$t_0 = \left(p_{TENPWM} - 1\right)T_c \tag{7.30}$$

Depending on the current polarity, $v_{DS}(t)$ in Eq. (7.29) is defined by Eqs. (7.14) or (7.17) for linear switching curves and Eq. (7.23) or (7.27) for the non-linear approximation. The Fourier Transform of $v_{DS}(t)$ for interval t_{vf} is given by:

$$\Im\left[v_{DS}\left(t\right)\right]e^{-j2\pi ft_0} = \left[\int_0^{t_{vf}} v_{DS}\left(t\right)e^{-j2\pi ft}dt\right]e^{-j2\pi ft_0} \tag{7.31}$$

With t_0 defined as:

$$t_0 = \left(p_{TENPWM} - 1\right)T_c + W_{p_{TENPWM}} \tag{7.32}$$

In a similar manner as for t_{vr} $v_{DS}(t)$ is defined by Eq. (7.11) or (7.15) for a linear switching curve, whereas Eq. (7.22) or (7.25) defines it for a non-linear transition. From Figure 7.7 it is evident that the pulse width also needs to be adapted to:

$$W_{p_{TENPWM\,(t_{vr}\_t_{vf})}} = W_{p_{TENPWM}} - t_{vr} \tag{7.33}$$

The time shift of Eq. (2.94) is a function of the pulse width and thus needs to be altered as well. By substituting for Eq. (7.33) the time shift of Eq. (2.94) changes to:

$$t_0 = \left(p_{TENPWM} - 1\right)T_c + \frac{W_{p_{TENPWM}} - t_{vr}}{2} \tag{7.34}$$

7.6   SIMULATION RESULTS

The simulation model introduced in the previous section can next be implemented. In this section a detailed analysis of the results achieved will be considered for TENPWM. A discussion of the difference between the linear and non-linear switching transitions is also

included. Once again, throughout this section the results will be discussed for both scenarios of the inductor current. The parameters used correspond to those defined in Section 7.4, unless stated otherwise.

7.6.1   BASEBAND HARMONICS

The effect of t_{vr} and t_{vf} within the baseband is considered in this section. Figure 7.8 is a comparative spectral plot of the baseband harmonics of both linear and non-linear switching transitions, which were plotted using the respective solutions derived in Sections 7.3.1 and 7.3.2. From Figure 7.8 it can be seen that Scenario ② produces much higher levels of distortion than Scenario ①. The reason why the distortion in Figure 7.8 (b) is so much more prominent can be explained when referring to Figure 7.4 and Figure 7.5. The abrupt change in t_{vr} and t_{vf} associated with Scenario ② (Figure 7.4 (b) and Figure 7.5 (b)) results in more prominent baseband harmonics shown in Figure 7.8 (b) than in (a).

(a)   **(b)**
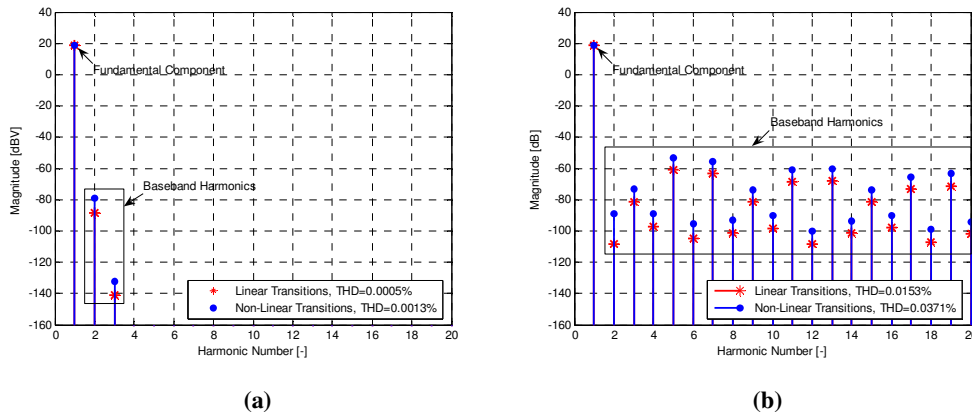
Figure 7.8: Simulated TENPWM baseband harmonics for (a) Scenario ① and (b) Scenario ②.

A comparison between the linear and non-linear switching transitions for various values of R_G is represented in Table 7.1. It is evident that the distortion increases for increasing values of R_G. Through simple inspection of the solutions in Section 7.3 it can be observed that t_{vr} and t_{vf} increase for increasing values of R_G, suggesting that longer switching transitions result in higher levels of distortion.

TABLE 7.1

SIMULATED THD FOR LINEAR AND NON-LINEAR SWITCHING TRANSITIONS FOR TENPWM FOR VARIOUS R_G.

R_G [Ω]	Scenario 1		Scenario 2	
	Simulated THD, Linear [%]	Simulated THD, Non-Linear [%]	Simulated THD, Linear [%]	Simulated THD, Non-Linear [%]
10	0.000451	0.001284	0.015269	0.037130
22	0.000993	0.002824	0.033570	0.081557
27	0.001218	0.003466	0.041188	0.100026
47	0.002121	0.006034	0.071619	0.173658
100	0.004512	0.012838	0.151942	0.366910
120	0.005415	0.015406	0.182132	0.439136

Table 7.2 shows a similar comparison as Table 7.1, only for various values of V_{GS}. The solutions in Section 7.3 describing t_{vr} (Eqs. (7.18) and (7.28)) and t_{vf} (Eqs. (7.12) and (7.21)) for Scenario ① are independent of V_{GS}, which results in a THD that remains constant.

TABLE 7.2

SIMULATED THD FOR LINEAR AND NON-LINEAR SWITCHING TRANSITIONS FOR TENPWM FOR VARIOUS V_{GS}.

V_{GS} [Ω]	Scenario 1		Scenario 2	
	Simulated THD, Linear [%]	Simulated THD, Non-Linear [%]	Simulated THD, Linear [%]	Simulated THD, Non-Linear [%]
10	0.000451	0.001284	0.015269	0.037130
11	0.000451	0.001284	0.015224	0.039050
12	0.000451	0.001284	0.015177	0.040430
13	0.000451	0.001284	0.015128	0.041469
14	0.000451	0.001284	0.015077	0.042279
15	0.000451	0.001284	0.015023	0.042929

For Scenario ② the distortion decreases for increasing values of V_{GS} for the linear transitions, while the inverse holds for the non-linear switching transitions. In both Table 7.1 and Table 7.2 it can be seen that the proposed non-linear model of Section 7.3.2 results in higher levels of distortion than the linear model of Section 7.3.1. This can partially be explained when referring to Figure 7.6 which shows the difference in t_{vf} between the linear and non-linear cases. The solutions of the proposed non-linear model yields higher switching

times than that of the linear model, which in turn results in higher levels of distortion, as suggested in Table 7.1. The following section focuses on the contribution of the sideband switching harmonics within the baseband.

7.6.2   SIDEBAND HARMONICS

The following analysis shows under which circumstances the sideband harmonics are most likely to deteriorate distortion by contributing to the baseband harmonics. Figure 7.9 compares the spectra of the linear and non-linear switching transitions for the various scenarios of the inductor current. From the latter illustration it can be seen that the sideband harmonics decay at a rapid rate for Scenario ①.
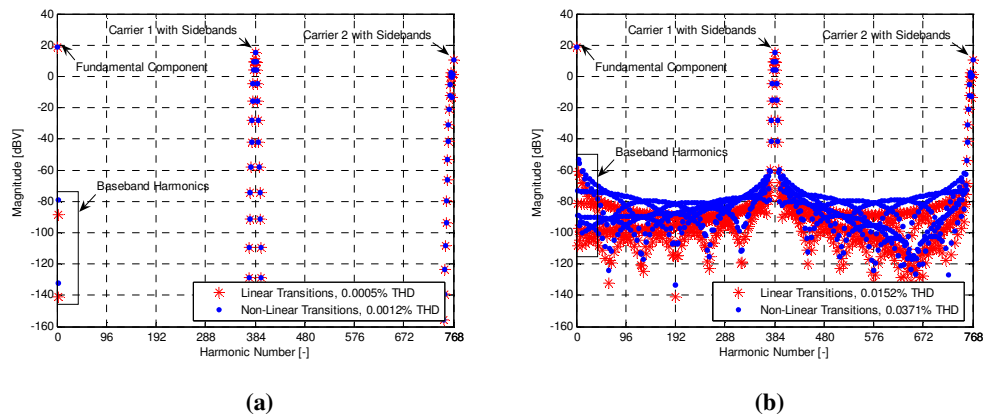
Figure 7.9: Simulated TENPWM spectra for (a) Scenario ① and (b) Scenario ②.

However, for Scenario ② the sidebands of the first carrier do not roll off at such a rapid rate and thus contribute to distortion within the baseband. This slow decay associated with Scenario ② can be ascribed to abrupt change in t_{vr} and t_{vf} upon transition, as described in the previous section.

7.7   SUMMARY

This chapter focussed on the isolated effect of non-zero linear, as well as non-zero non-linear switching transitions on harmonic distortion. The analysis included a linear model

based on well-known analytical expressions [24], [28] as well as a newly proposed non-linear model based on an approximation of the non-linear v_{DS} vs. C_{GD} curve of a specific power MOSFET. A simulation model was constructed for TENPWM.

From the results obtained for TENPWM it was shown that inductor current Scenario ② yields much higher levels of distortion than Scenario ① due to the abrupt change in transition times upon a change in current polarity. It was also shown that the THD increases for increasing switching times. For Scenario ② the sideband harmonics contribute to distortion within the baseband. The proposed non-linear model resulted in much higher levels of distortion than the linear model for both cases of the inductor current.

8
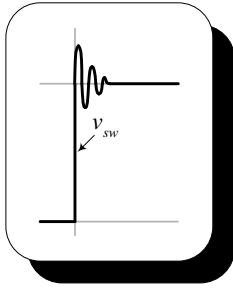
THE EFFECT OF PARASITICS

AND REVERSE RECOVERY

8.1 INTRODUCTION

This chapter focusses on the effects of the turn-*on* and turn-*off* voltage transients on harmonic distortion. Due to the vast amount of variables involved, as well as the dependence on practical implementation, it is very difficult to characterise the voltage transient's exact parameters [31], [32]. Thus, the proposed analysis makes use of an existing analytical solution and focus is shifted towards the parameters that give rise to distortion within the baseband rather than predicting the exact characteristic of the overvoltage for a given practical setup. The conditions under which the reverse recovery increases distortion are then determined, after which a method for modelling its effect is established. A simulation models is introduced for TENPWM after which a detailed discussion of the results achieved are considered.

8.2 ANALYSIS OF THE PARASITICS AND REVERSE RECOVERY

As mentioned in the previous section, the analysis will focus on the mechanism giving rise to distortion within an existing practical setup rather than analytically estimating the amplitude and frequency of the ringing effect for that specific circuit. This approach calls for some existing analytical solution describing the overvoltage within current literature. The analysis in [31] contains a detailed study of the MOSFET turn-*off* overvoltage transient in the presence of various parasitics. A closed form analytical solution for this voltage is obtained from equivalent circuit models of the power MOSFET and the PCB. A brief summary of the analysis and solution obtained in [31] now follows.
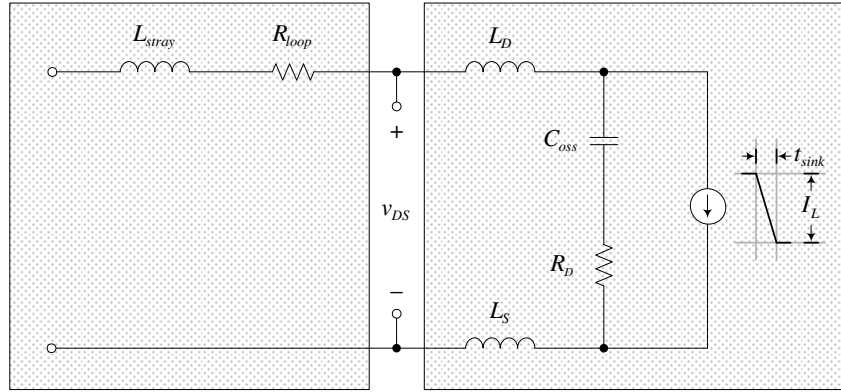
Figure 8.1: Equivalent circuit model of the turn-*off* process [31].

In order to obtain an analytical expression the analysis utilizes a relatively simple MOSFET model in which essential design parameters are included. This model's simplicity is based on the assumption that C_{oss} is fully charged to the supply voltage (and thus constant during the ringing phase) before the current starts to fall. This MOSFET model is shown in the right hand side rectangle of Figure 8.1. Both the PCB and the component leads contribute to the total stray inductance. The former is modelled using a computer aided design (CAD) tool (InCa) in which a method (the Partial Element Equivalent Circuit) is implemented that permits modelling of the interconnections. The various self-and-mutual partial inductances and resistances are respectively represented by a single inductance and a single resistance, all connected in series. This circuit is shown in the left hand rectangle of Figure 8.1. The stray inductance L_{stray} is a combination of the total self-and-mutual partial inductances together with the lead inductances of the upper switching device while R_{loop} is the total partial resistance of the PCB tracks. From Figure 8.1 the expression describing the MOSFET's external overvoltage takes the general form [31]:

$$\Delta v_{DS} = \frac{L_{stray} I_L}{t_{sink} \sqrt{1 - \zeta^2}} e^{(-\omega_{ov} \zeta t)} \sin\left(\omega_{ov} \left[\sqrt{1 - \zeta^2} \right] t \right) \tag{8.1}$$

Where:

$$\zeta = \frac{R_{tot}}{2} \sqrt{\frac{C_{oss}}{L_{tot}}}, \quad \omega_{ov} = \frac{1}{\sqrt{L_{tot} C_{oss}}} \quad \text{and} \quad L_{tot} = L_{stray} + L_D + L_S \tag{8.2}$$

A single switching phase leg is considered as a starting point from where the analysis is extended to a full-bridge topology. It will be shown that the analytical solution of Eq. (8.1) is applicable to both scenarios of the inductor current as well as both topologies, hence the reason for it being introduced as a general solution at enception of this section. The analysis of the half-bridge topology now follows.

8.2.1   ANALYSIS OF A HALF-BRIDGE TOPOLOGY

The half-bridge topology provides a simple starting point for modelling the effect of the parasitics and reverse recovery. The two scenarios of the inductor current introduced in Chapter 3 once again govern the analysis, resulting in it being divided into two sub-sections.

Inductor Current Scenario ①

Figure 8.2 illustrates a practical switched output voltage with a duty cycle of 50% measured within a single phase leg of a full-bridge inverter. Figure 8.2 (a) represents a switching transition of the lower switch from *on* to *off* while (b) shows a transition from *off* to *on*. Note that *D* was chosen at 50% since it provides a simple measurement environment of the waveforms in which Scenario ① is reproduced.

(a)   **(b)**
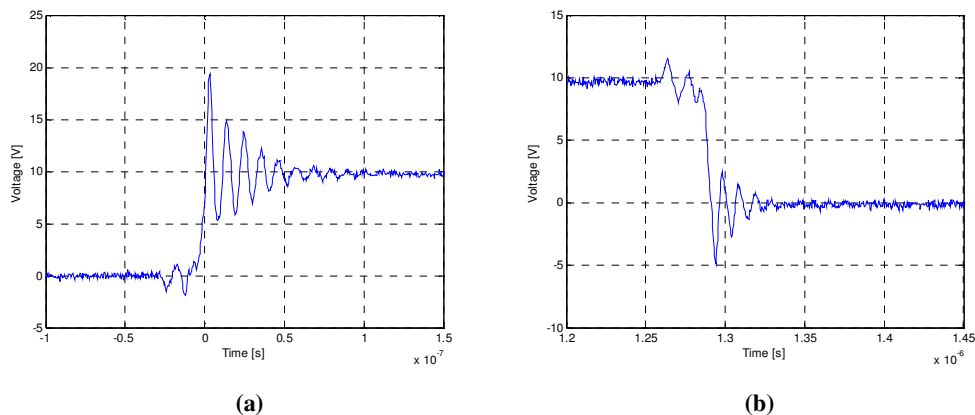
Figure 8.2: Measured switching output voltage transitions from (a) *on* to *off* and (b) *off* to *on*.

The values of the circuit parameters used correspond to V_d=10V, R_G=10Ω, V_{GS}=14V, L_{filt}=10.4µH, C=470nF and f_c=384kHz. The waveforms of Figure 8.2 (a) and (b) can next be matched using the analytical solution of Eq. (8.1). Firstly, consider Figure 8.2 (a). The required damping and frequency of the oscillation can be determined iteratively from R_{tot}, C_{oss} and L_{tot} as 5Ω, 70pF and 40nH respectively. The peak overvoltage is measured at 9.3V and exists at time t_{peak}=2.6ns (relative to inception of the ringing period). Substituting for $t=t_{peak}$ into Eq. (8.1) with $\Delta v_{DS}=\Delta v_{DS(peak)}$=9.3V and noting that the standing current produced corresponds to I_L=0.31A, the only unknown variables are L_{stray} and $t_{sink}=t_{if}$. Assuming a value of L_{stray}=30nH, t_{if} can be determined as 0.85ns.
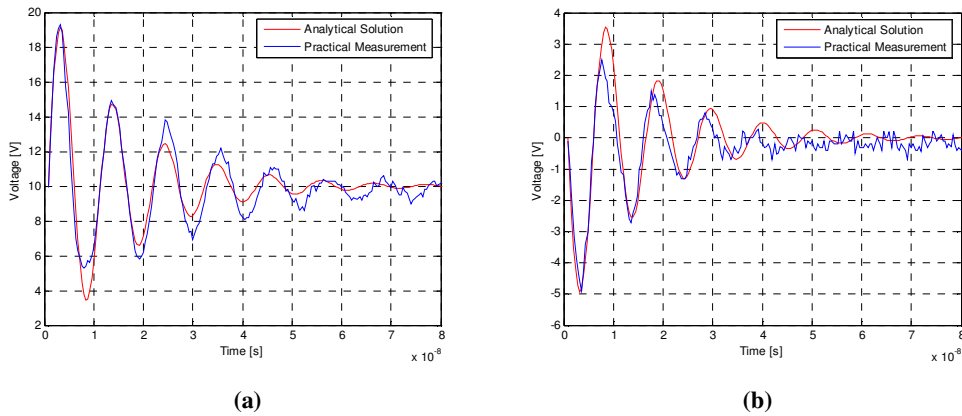
Figure 8.3: Analytically matched waveforms of (a) Figure 8.2 (a), and (b) Figure 8.2 (b).

Using a similar approach, the measured undervoltage of Figure 8.2 (b) can next be matched. The parameters used for the damping and frequency of the ringing effect are the same as for Figure 8.3 (a). The peak overvoltage is measured at 4.9V and once again exists at 2.6ns due to the frequency being the same. Substituting for the latter peak undervoltage and noting that the standing current again corresponds to I_L=0.31A, $t_{sink}=t_{ir}$ can be determined as 1.62ns. It is thus evident that Eq. (8.1) provides an accurate solution for the modelling of both the over- and undervoltage. In both Figure 8.3 (a) and (b) the frequency and damping of the oscillation correlate well. Since I_L is known and t_{peak} is constant, the latter argument suggests that the required waveform can be determined by simply establishing the practical relation between $\Delta v_{DS(peak)}$ and t_{sink} for a given setup.

(a)   (b)

(c)   (d)
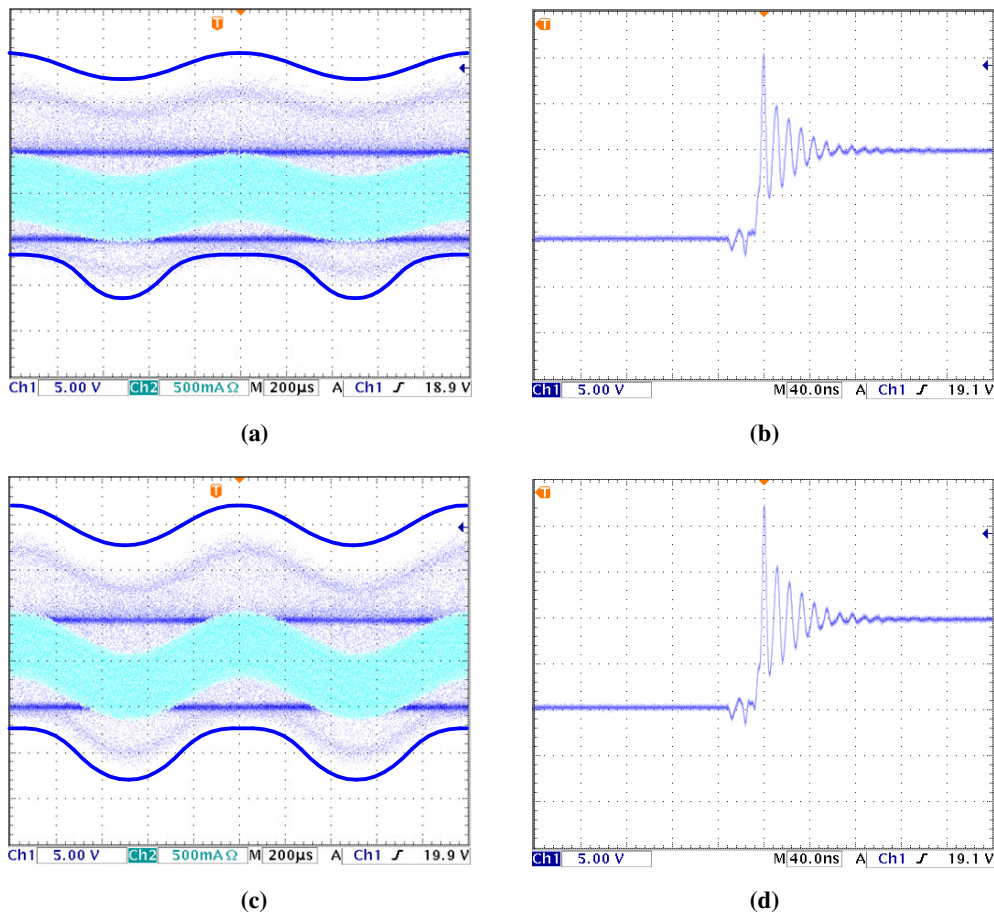
Figure 8.4: Measured voltage envelopes and inductor current for (a) *M*=0.1 and (c) *M*=0.2. Measured peak overvoltage at the crest of the overvoltage envelope for (b) *M*=0.1 and (d) *M*=0.2.

Figure 8.4 illustrates the measured envelopes of the over- and undervoltage as well as the inductor current for (a) *M*=0.1 and (c) *M*=0.2 over two cycles of a 1kHz modulating waveform. Note that the latter values of *M* were chosen in such a way as to ensure that the inductor current remains within the boundaries of Scenario ①. The corresponding peak overvoltage transients measured on the crest of $\Delta v_{DS(upper\_env)}$ are respectively shown in (b) and (d). These measurements are included since the aliasing effect of the oscilloscope results in a possible misinterpretation of the actual measurement. The solid curves shown in (a) and (c) have been included in order to illustrate the exact measured envelopes. From both Figure 8.4 (a) and (c) it is apparent that a direct relation exists between the envelopes of the over- and undervoltage and the inductor current.

This relation will now be established. Firstly, consider the overvoltage. Upon inspection of Figure 8.4 a general expression defining $\Delta v_{DS(upper\_env)}$ can be determined by offsetting $i_{L(lower\_env)}$ by some constant value and applying the appropriate scaling, that is:

$$\Delta v_{DS(upper\_env)} = k_{offset} + k_{scaling} i_{L(lower\_env)} \tag{8.3}$$

The two unknown constants k_{offset} and $k_{scaling}$ can be solved by measuring the peak overvoltage at the crest of $\Delta v_{DS(upper\_env)}$ and the corresponding I_L, which is determined at the trough of $i_{L(lower\_env)}$. Another measurement of the peak overvoltage at the trough of $\Delta v_{DS(upper\_env)}$ and the corresponding I_L at the crest of $i_{L(lower\_env)}$ makes it possible to solve Eq. (8.3).

TABLE 8.1

VARIOUS VARIABLES FOR EXPRESSING THE UPPER ENVELOPE OF THE OVERVOLTAGE FOR SCENARIO ①.

M	Measured Peak Voltage [V]		Current Magnitude [A]		k_{offset}	$k_{scaling}$
	Crest	Trough	Crest	Trough		
0.1	20.80	17.60	0.4318	0.1879	23.27	13.12
0.2	22.80	16.40	0.0566	0.5444	23.54	13.12

The various variables established for M=0.1 and M=0.2 are summarized in Table 8.1. Note that the magnitude of the current was calculated using the solution obtained in Eq. (3.5). Next, consider the undervotage. From Figure 8.4 (a) and (c) it is evident that a similar relation to that established for the overvoltage exists for the undervoltage, which means that:

$$\Delta v_{DS(lower\_env)} = k_{offset} + k_{scaling} i_{L(upper\_env)} \tag{8.4}$$

However, for some part of the interval displayed in Figure 8.4 (a) and (b) it can be seen that $\Delta v_{DS(lower\_env)}$ becomes saturated (respective measured peak undervolatage levels of 1.5V and 2.2V for M=0.1 and M=0.2), and thus does not follow $i_{L(upper\_env)}$ according to the relation defined in Eq. (8.4). Assuming that the same latter linear relation exists during saturation, the crest of $\Delta v_{DS(lower\_env)}$ can be estimated. This allows for the calculation of k_{offset} and $k_{scaling}$.

For the remaining region a simple condition can be applied to $\Delta v_{DS(lower\_env)}$ in order to clamp it to the corresponding voltage during clipping. Table 8.2 contains a summary of the various variables.

<div align="center">TABLE 8.2</div>

<div align="center">VARIOUS VARIABLES FOR EXPRESSING THE LOWER ENVELOPE OF THE UNDERVOLTAGE FOR SCENARIO ①.</div>

M	Measured Peak Voltage [V]		Current Magnitude [A]		k_{offset}	$k_{scaling}$
	Crest (est.)	Trough	Crest	Trough		
0.1	1.00	-6.80	0.4318	0.1879	-12.81	31.98
0.2	2.00	-8.10	0.5444	0.0566	-9.27	20.71

Figure 8.5 illustrates the analytical reconstruction if the measurements obtained in Figure 8.4 are using the parameters obtained in Table 8.1 and Table 8.2.

<div align="center">(a)   (b)</div>
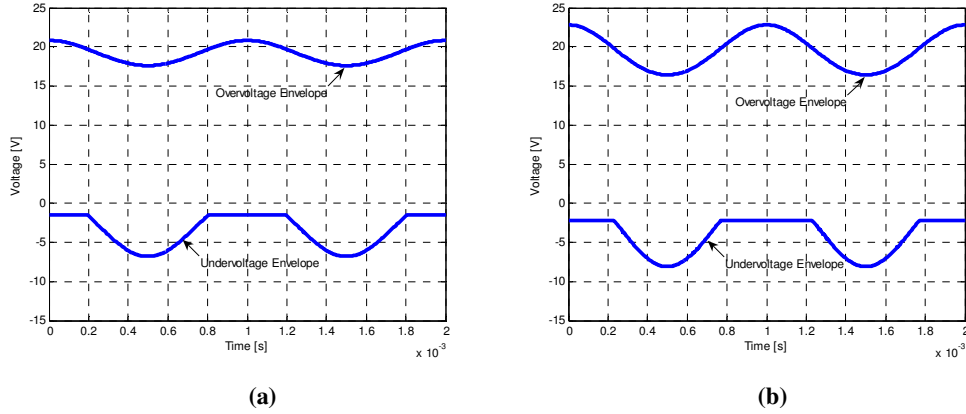
Figure 8.5: Analytically reconstructed voltage envelopes of Figure 8.4 for (a) *M*=0.1 and (b) *M*=0.2.

Since $\Delta v_{DS(upper\_env)}$ and $\Delta v_{DS(lower\_env)}$ define $\Delta v_{DS(peak)}$ the appropriate scaling needs to be applied in accordance with Eq. (8.1) in order to derive an expression for Δv_{DS}. This requires the derivation of an expression for t_{sink} as a function of time. Since $\Delta v_{DS(peak)}=\Delta v_{DS(upper\_env)}$ at $t=t_{peak}$ an expression defining $t_{sink}=t_{if}$ can be found from Eq. (8.1):

$$t_{if} = \frac{L_{stray}i_{L(lower\_env)}}{\Delta v_{DS(upper\_env)}\sqrt{1-\zeta^2}} e^{\left(-\omega_{ov}\zeta t_{peak}\right)} \sin\left(\omega_{ov}\left[\sqrt{1-\zeta^2}\right]t_{peak}\right) \tag{8.5}$$

In a similar manner $\Delta v_{DS(peak)}=\Delta v_{DS(lower\_env)}$ which means that an expression defining $t_{sink}=t_{ir}$ can be established from Eq. (8.1):

$$t_{ir} = \frac{L_{stray}i_{L(upper\_env)}}{\Delta v_{DS(lower\_env)}\sqrt{1-\zeta^2}}\, e^{\left(-\omega_{ov}\zeta t_{peak}\right)} \sin\left(\omega_{ov}\left[\sqrt{1-\zeta^2}\right]t_{peak}\right) \tag{8.6}$$

By next substituting the results of Eqs. (8.5) and (8.6) into Eq. (8.1) an expression for Δv_{DS} can be determined for inductor current Scenario ①.

Inductor Current Scenario ②

Figure 8.6 illustrates measurements of the voltage envelopes as well as the inductor current for (a) M=0.5 and (c) M=0.8. In both cases Scenario ② is reproduced at some stage of the switching interval. Note that the remaining conditions used correspond to those of Figure 8.4. Figure 8.6 (b) and (d) respectively represent the corresponding overvoltage transisients of (a) and (c) measured on the crest of $\Delta v_{DS(upper\_env)}$. Consider both measurements of $\Delta v_{DS(upper\_env)}$ and $\Delta v_{DS(lower\_env)}$. In the region where the inductor current falls within the limits governing Scenario ①, the same linear relation introduced in the previous section holds. However, in Scenario ② it can be observed that $\Delta v_{DS(upper\_env)}$ and $\Delta v_{DS(lower\_env)}$ are governed by some other constraint. This is evident by noting that the peak overvoltage measurements shown in (b) and (d) are both more or less equal.

(a)

(b)

(c)   (d)
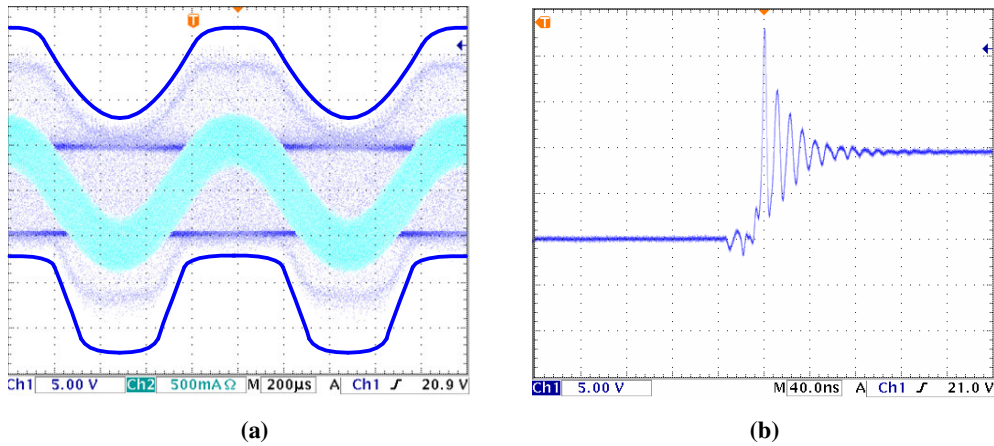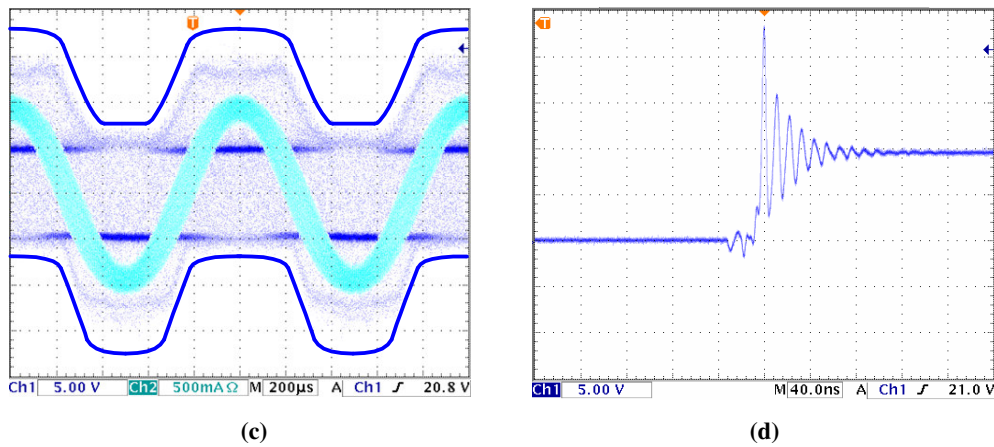
Figure 8.6: Measured voltage envelopes and inductor current for (a) *M*=0.5 and (c) *M*=0.8. Measured peak overvoltage at the crest of the overvoltage envelope for (b) *M*=0.5 and (d) *M*=0.8.

Figure 8.7 (a) and (b) show a measurement similar to that of Figure 8.6 (c) and (d) with M=0.8 and V_d=20V. Note that the bus voltage was increased in order to magnify the effect observed. The additional curves inserted onto $\Delta v_{DS(upper\_env)}$ will now be explained.

(a)   (b)
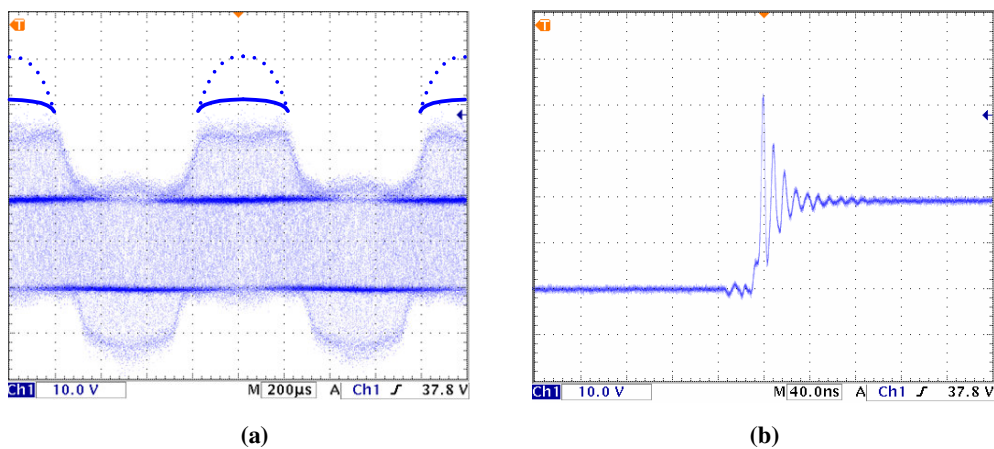
Figure 8.7: (a) Measured voltage envelopes for *M*=0.8. (b) Measured peak overvoltage at the crest of the overvoltage envelope with *V$_d$*=20V.

The dashed curves in Figure 8.7 (a) represent an extension of the estimate of the relation described for Scenario ① within the boundaries of Scenario ② while the solid curves denote the actual measured value of $\Delta v_{DS(upper\_env)}$. It is clear that a mechanism different to that observed for Scenario ① governs $\Delta v_{DS(upper\_env)}$ in this region. Note that the same phenomenon

is observed for $\Delta v_{DS(lower\_env)}$. An indication as to which non-ideal effect is responsible within the latter interval can be established by noting that it occurs within the conditions of the dead time mentioned in Chapter 5, or during forced commutation as also observed and described by F. Nyboe [33]. For a distinctly positive inductor current the voltage loss occurs on the leading edge (the edge at which the overvoltage is produced). Refer to Figure 5.1 (a). At the time instant just before T_{A1} switches from *off* to *on* D_{A2} conducts. Once the complete current flows through T_{A1}, a minority carrier reverse recovery charge Q_{rr} must be removed before D_{A2} becomes reverse biased. An inevitable shoot through current is produced until the latter charge is removed. In a similar manner the voltage gain occurs on the trailing edge (the edge at which the undervoltage is produced). Following the same methology as for a distinctly positive inductor current, it can be concluded from Figure 5.1 (b) that the shoot through current results from the reverse recovery of D_{A1}. A relation once again exists between $\Delta v_{DS(upper\_env)}$ and $i_{L(lower\_env)}$, as well as between $\Delta v_{DS(lower\_env)}$ and $i_{L(upper\_env)}$, and it will now be established.
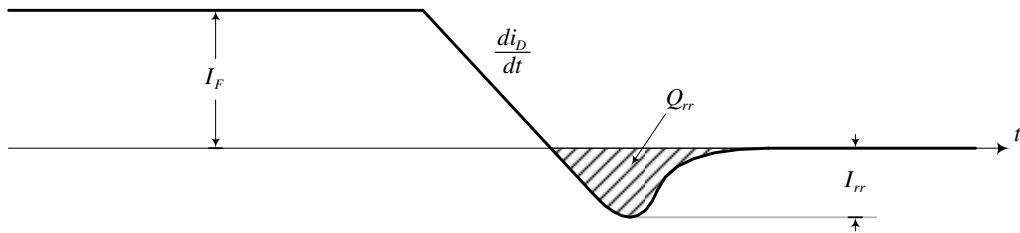
Figure 8.8: Intrinsic power diode current switching characteristic during turn-*off* [24].

The turn-*off* switching characteristics of the intrinsic power diode is shown in Figure 8.8. A well known approximate expression describing I_{rr} is given by [24]:

$$I_{rr} \approx 2.8 \times 10^{-6} BV_{DSS} \sqrt{I_F \frac{di_D}{dt}} \tag{8.7}$$

The switching times as well as the waveform of Figure 8.8 are dependent on the properties of the semiconductor as well as the practical circuit in which it finds itself [24]. Moreover, as emphasized in [24], the solution in Eq. (8.7) is based on various assumptions and thus represents a very rough estimate that essentially summarizes the trade-offs between the respective variables involved. Attempting to analyze the reverse recovery effect

analytically with the given amount of unknown factors will thus be tedious. One very useful observation, however, can be made from Eq. (8.7) by noting that I_{rr} is directly proportional to the square root of I_F for an assumed constant value of di_D/dt. This allows for $\Delta v_{DS(upper\_env)}$ and $i_{L(lower\_env)}$ to be interrelated once again. Adapting Eq. (8.3) the expression yields:

$$\Delta v_{DS(upper\_env)} = k_{offset} + k_{scaling} \sqrt{i_{L(lower\_env)}} \tag{8.8}$$

Variable k_{offset} can be determined by noting that $i_{L(lower\_env)}=0$ upon a transition from inductor current Scenario ① to Scenario ②. Thus, by simply measuring the peak overvoltage of $\Delta v_{DS(upper\_env)}$ at the time instant where $i_{L(lower\_env)}$ changes polarity from negative to positive, k_{offset} can be found. The remaining unknown variable $k_{scaling}$ can be established by measuring the peak overvoltage at the crest of $\Delta v_{DS(upper\_env)}$ and the corresponding value of I_L.

TABLE 8.3

VARIOUS VARIABLES FOR EXPRESSING THE UPPER ENVELOPE OF THE OVERVOLTAGE FOR SCENARIO ②.

M	Measured Peak Voltage [V]		Current Magnitude [A]		k_{offset}	$k_{scaling}$
	Crest	$i_{L(lower\_env)}=0$	Crest	$i_{L(lower\_env)}=0$		
0.5	23.80	23.20	0.3750	0	23.20	0.98
0.8	23.20	22.80	0.8629	0	22.80	0.43

The various variables for $M=0.5$ and $M=0.8$ are summarized in Table 8.3. In a similar way the relation describing the undervoltage can be written as:

$$\Delta v_{DS(lower\_env)} = k_{offset} + k_{scaling} \sqrt{i_{L(upper\_env)}} \tag{8.9}$$

The unknown variables k_{offset} and $k_{scaling}$ are determined from measurement in the same way as for $\Delta v_{DS(upper\_env)}$.

TABLE 8.4

VARIOUS VARIABLES FOR EXPRESSING THE LOWER ENVELOPE OF THE UNDERVOLTAGE FOR SCENARIO ②.

M	Measured Peak Voltage [V]		Current Magnitude [A]		k_{offset}	$k_{scaling}$
	Trough	$i_{L(lower\_env)}=0$	Trough	$i_{L(lower\_env)}=0$		
0.5	-13.00	-12.60	0.3749	0	-12.60	0.65
0.8	-12.80	-12.40	0.8628	0	-12.40	0.43

The various variables obtained for the undervoltage are summarized in Table 8.4 for M=0.5 and M=0.8. Before $\Delta v_{DS(upper\_env)}$ and $\Delta v_{DS(lower\_env)}$ can be reconstructed it is first necessary to determine the values of k_{offset} and $k_{scaling}$ for Scenario ①. A simple way of determining k_{offset} is to note that it serves as the boundary condition between Scenario ① and Scenario ② and is thus equal to each other. The remaining variable $k_{scaling}$ can next be established from a simple measurement of $\Delta v_{DS(upper\_env)}$ and $\Delta v_{DS(lower\_env)}$ with its corresponding current during Scenario ①. Two further measurements need to be made to determine the level at which the over-and-undervoltage clip during Scenario ①. This allows for the analytical reconstruction of the measured voltage envelopes of Figure 8.6 which is shown in Figure 8.9.

(a)   **(b)**
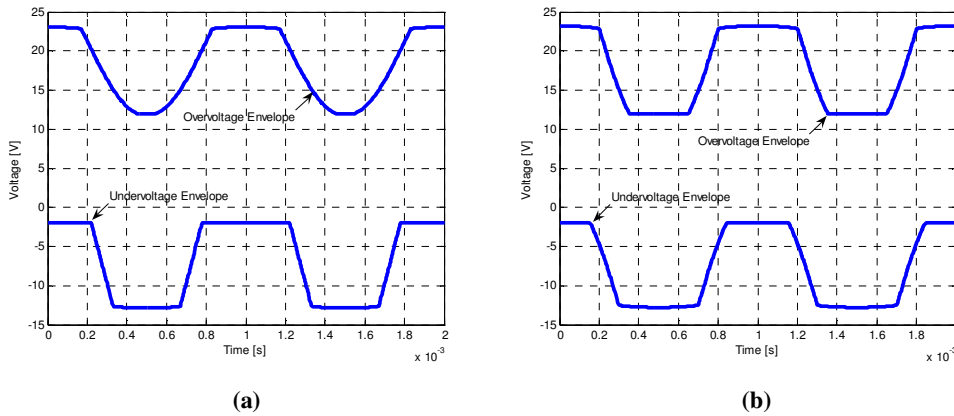
Figure 8.9: Analytically reconstructed voltage envelopes of Figure 8.6 for (a) M=0.5 and (b) M=0.8.

Consider Figure 8.6 (b) and (d). A final remark can be made by observing that the frequency and waveform of the ringing effect during Scenario ② correlate well to those of Scenario ① shown in Figure 8.4 (b) and (d). This implies that the analytical solution of Eq. (8.1) can once again be applied to describe the over- and undervoltage waveforms.

8.2.2 ANALYSIS FOR A FULL-BRIDGE TOPOLOGY

Figure 8.10 illustrates a switched output voltage at D=50% measured within a full-bridge inverter for a switching transition of the low side switch from (a) *on* to *off* and (b) *off* to *on*.

(a)   **(b)**
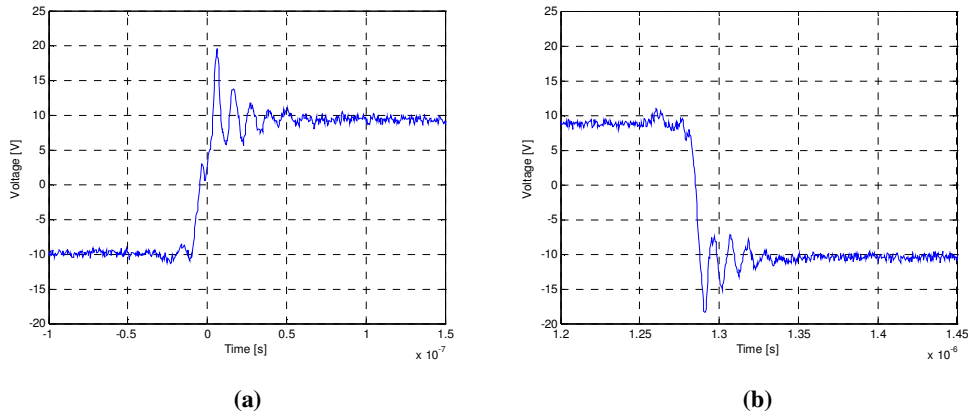
Figure 8.10: Measured switching output voltage transitions from (a) *on* to *off* and (b) *off* to *on*.

It will now be determined whether the solution of Eq. (8.1) can still be used to match the measured waveform within this topology. Figure 8.11 (a) and (b) respectively show a close-up of the waveforms illustrated in Figure 8.10 (a) and (b). The values of the circuit parameters correspond to those used in Section 8.2.1.

(a)   **(b)**
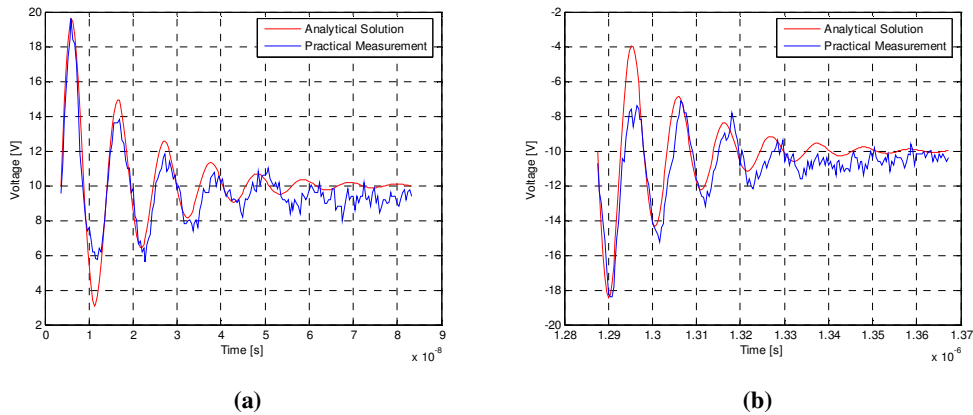
Figure 8.11: Analytically matched waveforms of (a) Figure 8.10 (a), and (b) Figure 8.10 (b).

Using the same approach as for a single phase leg, the measured waveform of Figure 8.10 (a) can be matched. The parameters determining the frequency and damping are the same as for a single phase leg. The peak overvoltage is measured at 9.6V and exists at time t_{peak}=2.6ns. Since I_L=0.62A t_{if} can be determined as 1.66ns if L_{stray} is assumed to take on a value of 30nH. Next, consider Figure 8.10 (b). Using the same parameters for the frequency

and damping as for (a), the undervoltage can be matched by measuring its peak value, which corresponds to 8.4V. Since the magnitude of I_L equals 0.62A, t_{ir} can be determined as 1.89ns. It is thus evident that the solution of Eq. (8.1) still serves as an accurate approximation to the over-and undervoltage curve within the full-bridge topology.

(a)	(b)
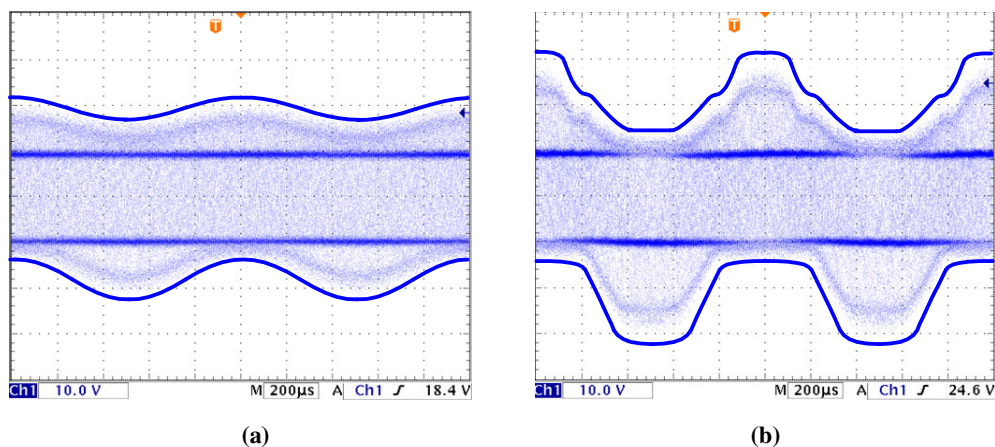
Figure 8.12: Measured voltage envelopes for (a) *M*=0.2 and (b) *M*=0.8.

Consider the measurements of $\Delta v_{DS(upper\_env)}$ and $\Delta v_{DS(lower\_env)}$ shown in Figure 8.12 for (a) *M*=0.2 and (b) *M*=0.8. These measurements respectively reproduce inductor current Scenario ① and Scenario ②. From Figure 8.12 (a) it is evident that the relation between $\Delta v_{DS(upper\_env)}$ (or $\Delta v_{DS(lower\_env)}$) and $i_{L(lower\_env)}$ (or $i_{L(upper\_env)}$) established within a single phase leg in Section 8.2.1 also holds within the full-bridge topology. Next, consider Figure 8.12 (b). The relation between $\Delta v_{DS(lower\_env)}$ and $i_{L(upper\_env)}$ correlates with that achieved within a single phase leg. The slight kink observed in the curve of $\Delta v_{DS(upper\_env)}$ is a result of the switching transitions of the various phase legs not executing on the exact same time instant. This mismatch is also observed in Figure 8.10 (a).

8.3   GENERAL OBSERVATIONS AND COMMENTS

The analysis in Section 8.2 was performed for a given practical setup in which the parameters were mostly kept constant. In this section V_{GS} and V_d will be varied in order to establish whether the approach used in the above analysis still holds. Note that the remaining parameters correspond to those of the previous section. Figure 8.13 (a) and (b) respectively

represent the measured voltage envelopes within a single leg of a full-bridge inverter for M=0.2 and M=0.8 at V_d=20V.
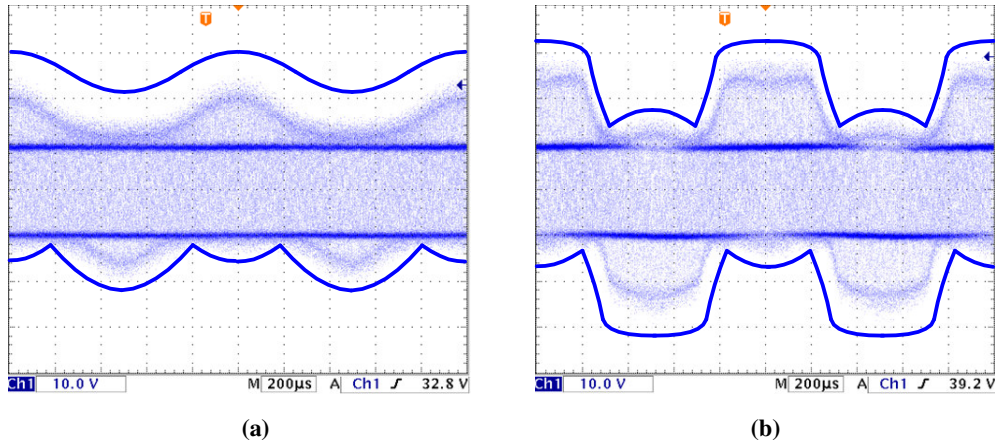
Figure 8.13: Measured voltage envelopes at (a) M=0.2 and (b) M=0.8 for V_d=20V.

From these measurements it is apparent that the same relation established in Section 8.2 holds at higher output power levels too. However, in the region where $\Delta v_{DS(upper\_env)}$ and $\Delta v_{DS(lower\_env)}$ were constant for V_d=10V (Figure 8.5 and Figure 8.9) it can now be observed that some relation to $i_{L(lower\_env)}$ and $i_{L(upper\_env)}$ once again exist. This relation can easily be established by simply determining whether switching occurs during the conditions of reverse recovery or not, i.e., during a transition from *on* to *off* under the condition $i_{L(lower\_env)}$>0 (or a transition from *off* to *on* under the condition $i_{L(upper\_env)}$<0) $\Delta v_{DS(upper\_env)}$ and $\Delta v_{DS(lower\_env)}$ is respectively described by Eqs. (8.8) and (8.9). For all other transitions a direct relation in accordance with Eqs. (8.3) and (8.4) can be established. Figure 8.14 (a) and (b) respectively represent a measurement of the voltage envelopes within a full-bridge topology for V_{GS}=11.5V and V_{GS}=12V, with M equalling 0.8 in both illustrations.
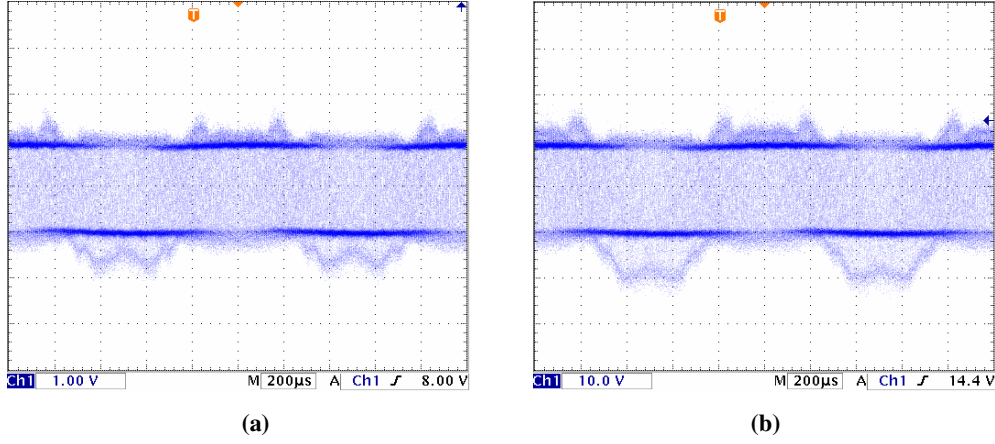
Figure 8.14: Measured voltage envelopes for M=0.8 for (a) V_{GS}=11.5V and (b) V_{GS}=12V.

By varying V_{GS} the switching characteristic of each phase leg is altered, which results in the cancellation of $\Delta v_{DS(upper\_env)}$ and $\Delta v_{DS(lower\_env)}$ to a certain extent. This was also briefly mentioned by F. Nyboe [29]. However, the degree to which the parasitics contribute to distortion remains unknown. Furthermore, optimizing V_{GS} to minimize the latter effect alters $t_{d(on)}$, $t_{d(off)}$, t_{vr} and t_{vf}, which might have a more dominant effect on the distortion.

8.4   SIMULATION STRATEGY

In this section it is shown how the solutions of Δv_{DS} obtained in Section 8.2 can next be incorporated into the simulation strategy of Section 2.5. Consider the pth pulse of a TENPWM waveform shown in Figure 8.15, in which Δv_{DS} is included. The Fourier Transform of the overvoltage during interval $W_{P_{TENPWM}}$ including the necessary time shift t_0 is given by:

$$\Im\left[\Delta v_{DS}\right]e^{-j2\pi ft_0} = \left[\int_0^{W_{P_{TENPWM}}}\left[\frac{V_d}{2}+\Delta v_{DS}\right]e^{-j2\pi ft}dt\right]e^{-j2\pi ft_0} \tag{8.10}$$

Where:

$$t_0 = \left(p_{TENPWM}-1\right)T_c \tag{8.11}$$

Note that Δv_{DS} is defined in Eq. (8.1) with $t_{sink}=t_{if}$ which is defined by Eq. (8.5).
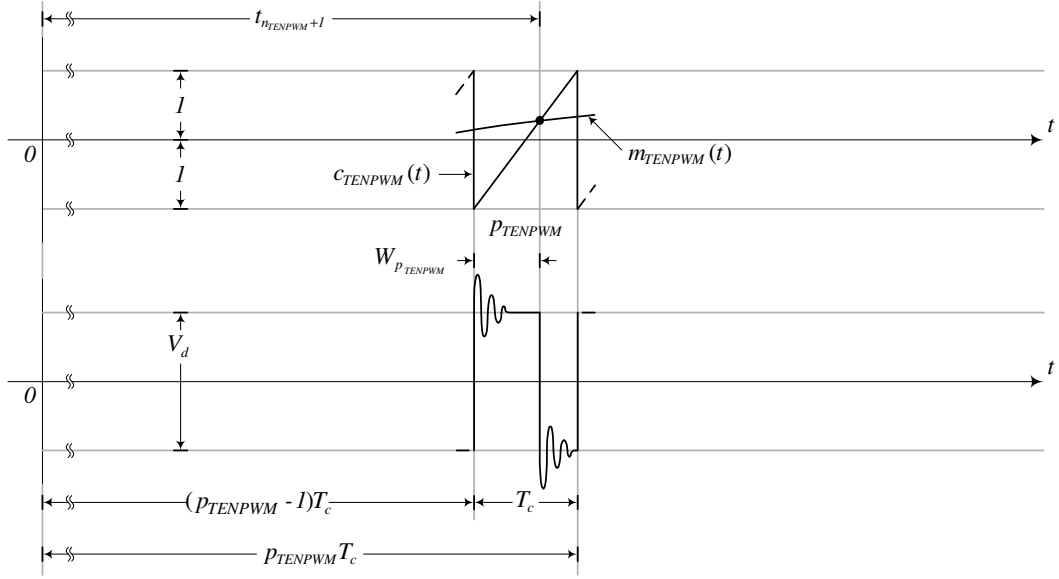
Figure 8.15: Generation of TENPWM with Δv_{DS}.

In a similar way the Fourier Transform of the undervoltage Δv_{DS} can be determined Figure 8.15 as:

$$\Im\left[\Delta v_{DS}\right]e^{-j2\pi ft_0} = -\left[\int_{0}^{T_c - W_{PTENPWM}} \left[\frac{V_d}{2} + \Delta v_{DS}\right]e^{-j2\pi ft}dt\right]e^{-j2\pi ft_0} \tag{8.12}$$

Where:

$$t_0 = \left(p_{TENPWM} - 1\right)T_c + W_{PTENPWM} \tag{8.13}$$

The undervoltage Δv_{DS} is once again defined in Eq. (8.1) with $t_{sink}=t_{ir}$, which is defined in Eq. (8.6). Closed form solutions can be obtained for both Eqs. (8.10) and (8.12).

8.5   SIMULATION RESULTS

The simulation strategy of the previous section is implemented in this section to show how the parasitics and reverse recovery affect distortion. As mentioned and illustrated in Section 8.3, the exact curvature adopted by $\Delta v_{DS(upper\_env)}$ and $\Delta v_{DS(lower\_env)}$ within a full-bridge topology is highly dependent on V_{GS}. Determining an analytical expression describing $\Delta v_{DS(upper\_env)}$ and $\Delta v_{DS(lower\_env)}$ within Scenario ② is a tedious exercise. Instead, the simulation

results will be limited to a single phase leg. Although this does not predict the distortion within a full-bridge topology, it does provide insight into the distortion levels produced, as well as the circumstances under which distortion occurs. Since different conditions govern Scenario ① and ②, the analysis once again needs to be divided into two sections.

8.5.1   BASEBAND HARMONICS

This sub-section considers the effect of Δv_{DS} within the baseband. Figure 8.16 (a) illustrates the baseband harmonics resulting from Δv_{DS} for M=0.2. The simulation was constructed using the respective parameters of $\Delta v_{DS(upper\_env)}$ and $\Delta v_{DS(lower\_env)}$ defined in Table 8.1 and Table 8.2. Figure 8.16 (b) shows the baseband harmonics within the limits of Scenario ② (M=0.8), constructed from the variables obtained in Table 8.3 and Table 8.4.
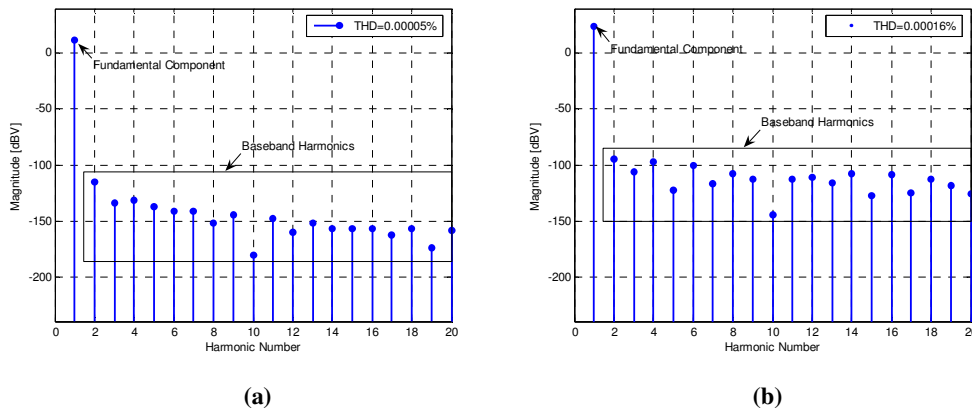
Figure 8.16: Simulated baseband harmonics with Δv_{DS} for (a) Scenario ① and (b) Scenario ②.

The baseband harmonics produced for Scenario ① are a result of the constant region within $\Delta v_{DS(lower\_env)}$, shown in Figure 8.5 (b). In this region the linear relation to $i_{L(upper\_env)}$ defined in Eq. (8.4) no longer holds, resulting in distortion. A similar mechanism governs Scenario ②. In addition to the constant region also being present in both $\Delta v_{DS(upper\_env)}$ and $\Delta v_{DS(lower\_env)}$ shown in Figure 8.9 (b), the non-linear relation established during diode conduction results in additional harmonics. However, the distortion produced is not as prominent compared to the PTE's analyzed in Chapters 5 to 7, especially under the conditions of Scenario ②.

8.5.2   SIDEBAND HARMONICS

In this sub-section the effect of the sideband harmonics within the audible band is considered. Figure 8.17 (a) and (b) respectively illustrate the spectrum of Figure 8.16 (a) and (b) over a larger frequency range.

(a)   **(b)**
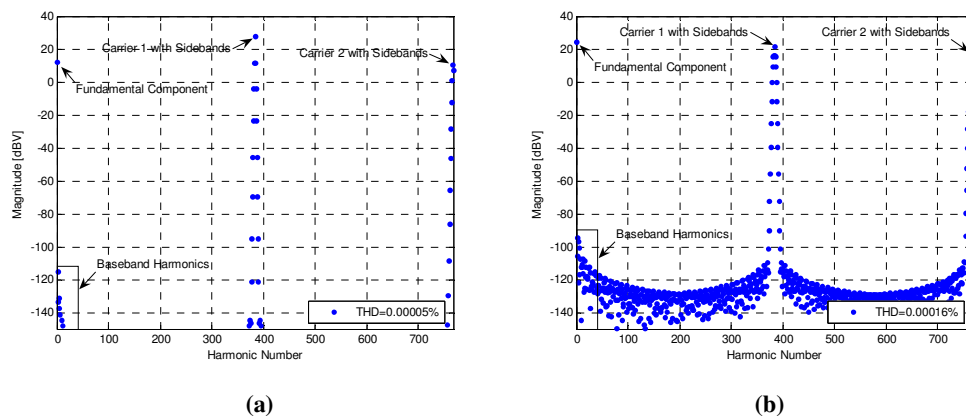
Figure 8.17: Simulated sideband harmonics with Δv_{DS} for (a) Scenario ① and (b) Scenario ②.

From (a) it is evident that the sideband harmonics decay at a rapid rate for Scenario ①. From both Figure 8.16 (a) and (b) it is apparent that the the sidebands do not roll off at such a rapid rate and thus contribute to distortion within the baseband.

8.6   SUMMARY

This chapter considered the effects of the parasitics and reverse recovery on harmonic distortion. The analysis made use of an existing solution to model the overvoltage and undervoltage ringing effect. A simulation model was constructed for TENPWM, after which the results were considered for a half-bridge topology. It was shown that, for both scenarios of the inductor current, that the PAE introduced is negligible compared to the PTEs considered in Chapters 5 to 7.

9
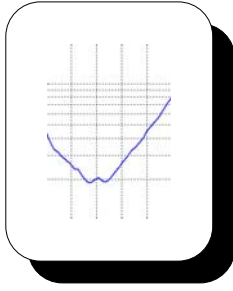
COMBINATION MODEL AND

EXPERIMENTAL VERIFICATION

9.1   INTRODUCTION

The aim of this chapter is to verify the theory that was proposed in the previous chapters. Section 9.2 contains a brief overview of each individual non-linearity analysed in this dissertation, as well as establish the validity of the proposed analytical solutions within a practical environment. The analytical and simulation models describing the combined effect of the individual error sources are constructed in Section 9.3. These models are compared to experimental measurements in Section 9.4, after which a summary follows in Section 9.5.

9.2   OVERVIEW OF THE INDIVIDUAL NON-LINEARITIES

Before the analytical and simulation models can be constructed, it is first necessary to consider the practical significance of the analytical solutions introduced in Chapters 5 to 8. The following sub-sections contain a brief overview of each individual non-ideal effect, after which the alterations that need to be made, if any, are identified. Unless stated otherwise, the parameters used in the rest of this chapter correspond to those defined in Table 9.1.

TABLE 9.1

DEFINITION OF THE BASIC VARIABLES USED THROUGHOUT THIS CHAPTER.

Variable	Value	Variable	Value
V_d	30 V	f_0	1 kHz
L_{filt}	10.4 µH	f_c	384 kHz
R_{load}	8.2 Ω	$V_{GS(th)}$	4.9 V
V_{GS}	14 V	C_{iss}	810 pF
R_G	12.5 Ω	g_{fs}	11 S

9.2.1   THE DEAD TIME

Figure 9.1 illustrates two simulated plots of the THD as a function of the modulation index with t_{dt}=15ns. In Figure 9.1 (a) the inductor current falls within the boundaries of Scenario ①. As mentioned in Chapter 5, ideal TENPWM is produced in this region. The distortion shown is a result of the numerical error of the simulation.
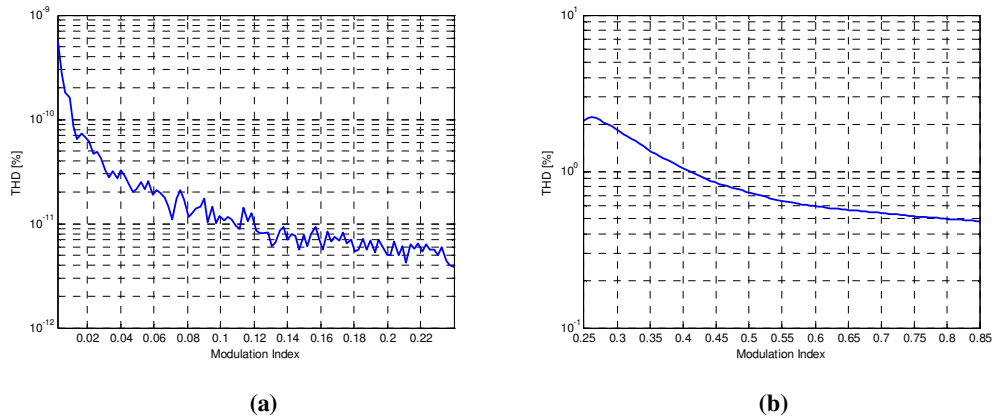
Figure 9.1: Simulated THD vs. *M* with non-zero t_{dt} for (a) Scenario ① and (b) Scenario ②.

Once Scenario ② is entered, the distortion resulting from the dead time increases rapidly. The decrease in THD for increasing *M* is a result of the increase in the ratio of the fundamental low frequency component compared to the average error resulting from t_{dt}.

9.2.2   THE TURN-ON AND TURN-OFF DELAYS

Figure 9.2 illustrates two simulated plots of THD vs. *M* for non-zero values of $t_{d(vr)}$ and $t_{d(vf)}$. The distortion shown in (a) is a result of the non-linear current modulation, as mentioned in Chapter 6 which, intuitively, increases for increasing *M* (increasing current magnitude). The curves of Figure 9.1 (b) and Figure 9.2 (b) correlate. This similarity is a result of the polarity dependency of $t_{d(vr)}$ and $t_{d(vf)}$, which leads to an abrupt change in these delays as the current changes polarity. This polarity dependency produces an effect similar to dead time.

(a)   (b)
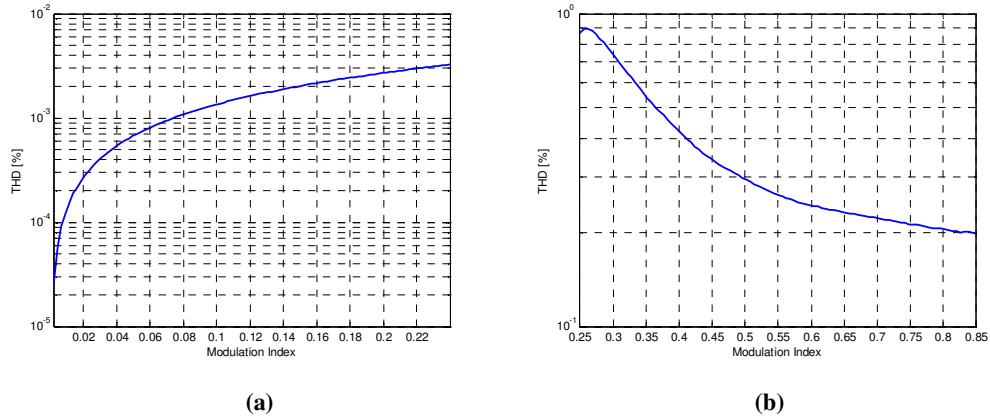
Figure 9.2: Simulated THD vs. M with non-zero $t_{d(vr)}$ and $t_{d(vf)}$ for (a) Scenario ① and (b) Scenario ②.

9.2.3   THE NON-ZERO, NON-LINEAR SWITCHING TRANSITIONS

Consider the measured switching waveforms shown in Figure 9.3. From the solutions derived in Chapter 7 for t_{vr} (Eqs. (7.18) and (7.28)) and t_{vf} (Eqs. (7.12) and (7.21)), it is apparent that the analytical switching times (≈2ns) are not realistic within a practical enviroment. The objective of this sub-section is to determine realistic values of t_{vr} and t_{vf} for the given practical setup. Consider inductor current Scenario ①. The waveforms in Figure 9.3 were measured at a duty cycle of 50%, with the demodulation filter disconnected, i.e. $L_{filt}=\infty$. However, it is assumed that a very small standing current still exists.

(a)   (b)
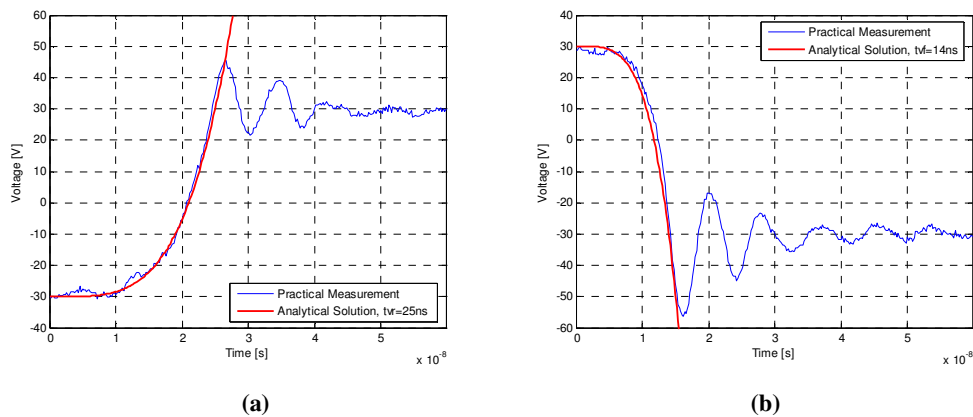
Figure 9.3: (a) Rising and (b) falling switching transition curves for $L_{filt}=\infty$.

The reason for this assumption is that the switching curves are dependent on the current polarity, and since the focus is initially within Scenario ①, the switching curves within intervals t_{vr} and t_{vf} need to be defined by Eq. (7.27) and Eq. (7.22), respectively. Using these equations, the measured waveforms of Figure 9.3 (a) and (b) can be matched. For this measurement, t_{vr}=25ns and t_{vf}=14ns.
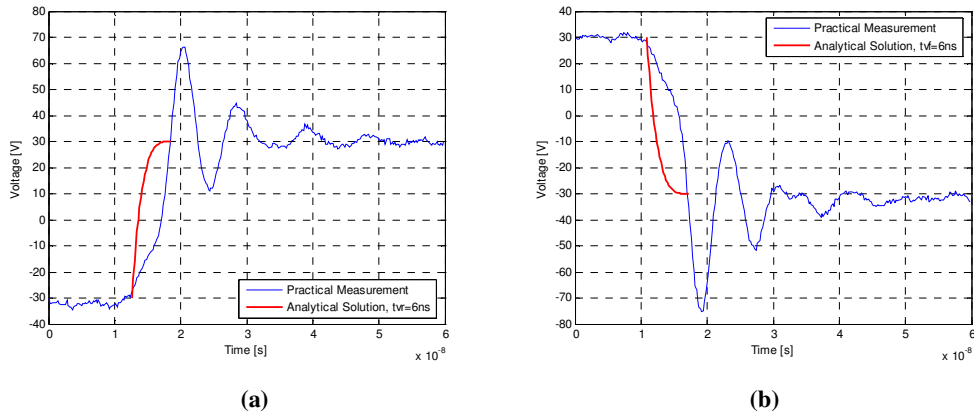
Figure 9.4: (a) Rising and (b) falling switching transition curves for Scenario ②.

Consider inductor current Scenario ②. Figure 9.4 (a) shows the rising edge transition for $i_{L(lower\_env)}$>0, while (b) illustrates the falling edge transition for $i_{L(upper\_env)}$<0. The analytical curves included in Figure 9.4 (a) and (b) were constructed using the solutions of Eq. (7.23) and Eq. (7.25), respectively. It is apparent that these solutions no longer provide a means of estimating the switching curve within a practical environment. Consider the non-linear switching curves shown at the top of Figure 9.5. These curves were obtained from the solutions derived in Chapter 7. In order to construct an analytical model, the analysis in Chapter 3 requires that the PTE be expressed in terms of a delay. This can be achieved by calculating the average error voltage, and then mapping it to an equivalent delay, as shown in Figure 9.5. Consider Figure 9.5 (a). The non-linear switching curve within interval t_{vr} is defined by Eq. (7.27). The equivalent delay Δ_1 can be calculated from the expression:

$$\Delta_1 = 1 - \left(\frac{1}{t_{vr}^4}\right)\int_0^{t_{vr}} t^4 dt = 0.8 t_{vr} \tag{9.1}$$
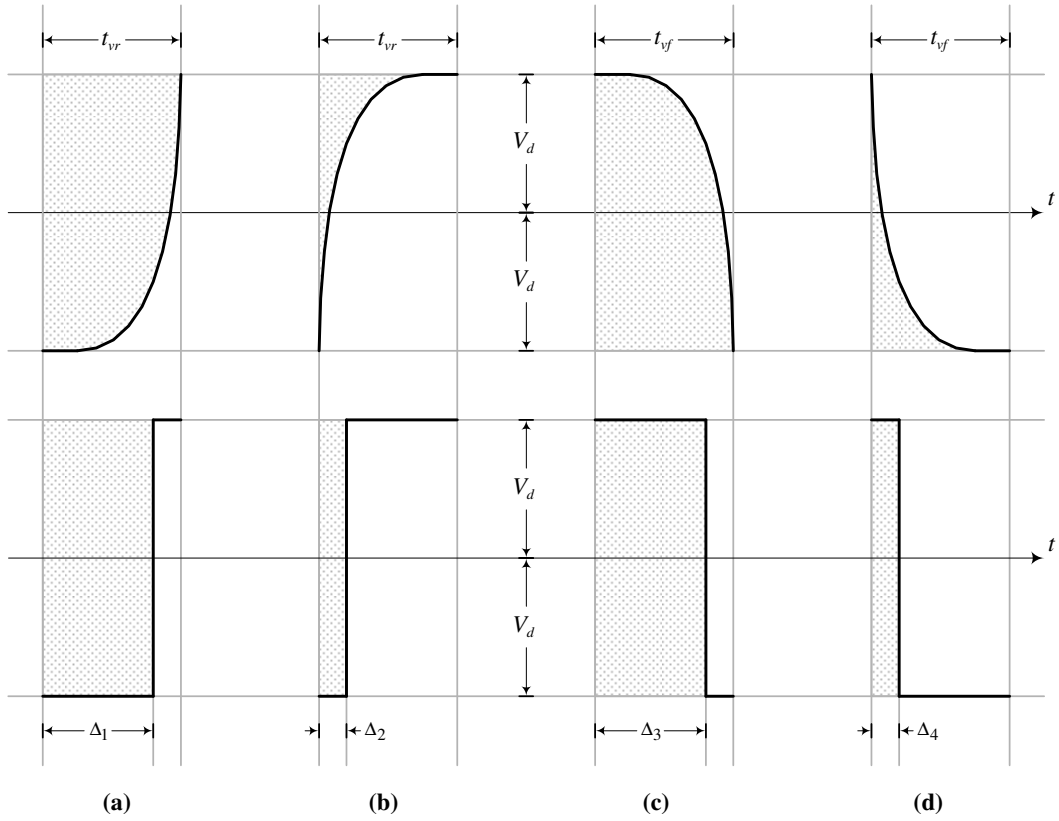
Figure 9.5: Switching curves during (a) t_{vr} for $i_L<0$, (b) t_{vr} for $i_L>0$, (c) t_{vf} for $i_L>0$ and (d) t_{vf} for $i_L<0$.

The relation to the inductor current is given by Eq. (7.28), which takes the general form:

$$\Delta_1 = \frac{k_1}{k_2 + k_{scaling(t_{vr})}I_L} \tag{9.2}$$

By noting that $\Delta_1=k_1$ when $I_L=0$ and $k_2=1$, the expression in Eq. (9.2) simplifies to:

$$\Delta_1 = \frac{0.8t_{vr(I_L=0)}}{1 + k_{scaling(t_{vr})}I_L} \tag{9.3}$$

Where $t_{vr(I_L=0)}$ is the transition time at $I_L=0$, which is established by measurement and $k_{scaling(t_{vr})}$ an arbitrary scaling factor. Similarly, the equivalent delay Δ_3 can be found as:

$$\Delta_3 = \frac{0.8t_{vf(I_L=0)}}{1 + k_{scaling(t_{vf})}I_L} \tag{9.4}$$

The remaining variables Δ_2 and Δ_4 are calculated using symmetry, i.e. $\Delta_2 = 0.2t_{vr}$ and $\Delta_4 = 0.2t_{vf}$. The measured values $t_{vr(I_L=0)}$ and $t_{vf(I_L=0)}$ thus basically serve as initial conditions. In reality, the boundary condition governing the transition between Scenario ① and ② is much more complex. A method for the modelling of the transition between Scenario ① and Scenario ② for short amounts of dead time is presented in Section 9.3.

9.2.4 THE PARASITICS AND REVERSE RECOVERY

The analysis in Chapter 8 concluded that the parasitics and reverse recovery only pose to deteriorate fidelity within Scenario ① due to its negligible effect compared to other error sources within Scenario ②. However, in the next section it will be shown that the noise is orders of magnitude larger in the former region compared to the effect of the parasitics and reverse recovery. As a result its effect will be omitted.

9.2.5 THE INCLUSION OF NOISE

A measurement of THD+N does not distinguish between harmonic distortion and noise. Thus, at low levels of the input signal, noise will dominate the THD+N measurement, decreasing as the fundamental low frequency component increases.

| (a) | (b) |
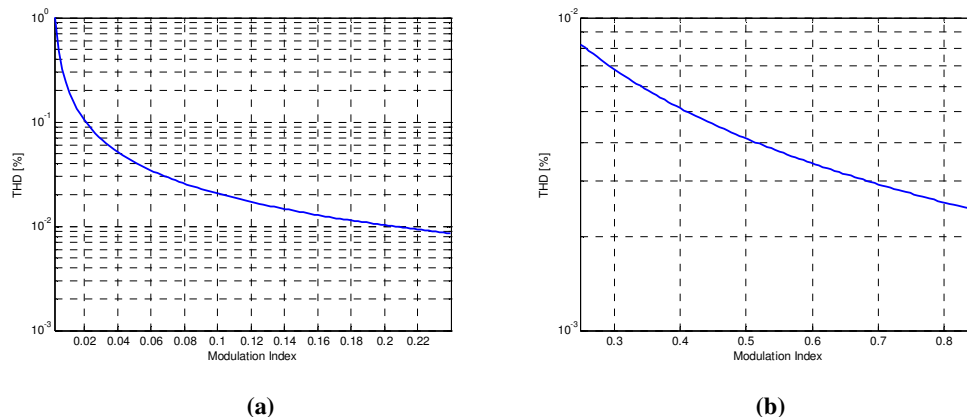
Figure 9.6: Noise vs. *M* for (a) Scenario ① and (b) Scenario ②.

Figure 9.6 (a) and (b) illustrates the distortion resulting from noise (20nW) for Scenario ① and Scenario ②, respectively, with an ideal TENPWM applied as input. This concludes the basic configuration of the individual non-ideal effects. The following section introduces the combination model.

9.3   COMBINATION MODELS

In this section analytical and simulation models are introduced for TENPWM from which the harmonic components of the combination of the various individual sources of distortion can be determined. The analysis performed in the previous section illustrated that the most dominant non-linearities considered in this dissertation can be modelled by means of current dependent delays. This means that the findings in Chapter 3 can once again be applied for the analytical implementation. As a starting point, inductor current Scenario ① is considered after which a method for the modelling of the transition into Scenario ② is introduced.

9.3.1   INDUCTOR CURRENT SCENARIO ①

In this section the analytical and simulation models are constructed which describe the combined effect of the non-linearities within the boundaries of Scenario ①. Of the non-ideal effects considered, only $t_{d(vr)}$, $t_{d(vf)}$, t_{vr} and t_{vf} influence distortion within this region.

Analytical Model

The findings in Chapter 3 can now be implemented to construct the 3-D unit area for the combination model. By noting that the corresponding error mapping of the leading edge is $\Phi_{d(LE)}=2\pi f_c(t_{d(vr)}+t_{vr})$ and the trailing edge $\Phi_{d(TE)}=2\pi f_c(t_{d(vf)}+t_{vf})$, the 3-D unit area representing the combination model can be defined. This is shown in Figure 9.7. Note that the various delays $t_{d(vr)}$, $t_{d(vf)}$, t_{vr} and t_{vf} are respectively defined by Eq. (6.8), (6.3), (9.3) and (9.4).
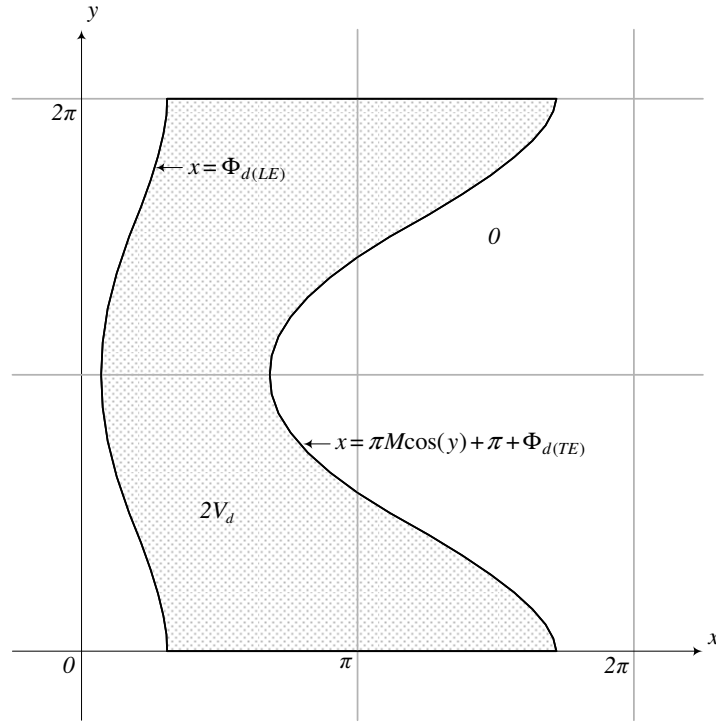
Figure 9.7: Combination 3-D unit area for TENPWM for Scenario ①.

By next inserting the limits defined in Figure 9.7, the complex Fourier coefficient of Eq. (2.15) can be written as:

$$C_{mn} = \frac{V_d}{\pi^2} \int_0^{2\pi} \left[\int_{\Phi_{d(LE)}}^{\pi + \pi M \cos(y) + \Phi_{d(TE)}} e^{j(mx+ny)} dx \right] dy \qquad (9.5)$$

Where:

$$\Phi_{d(LE)} = 2\pi f_c \left[R_G C_{iss} \ln\left(\frac{V_{GS}}{V_{GS(th)} + \frac{I_L}{g_{fs}}} \right) + \frac{0.8 t_{vr(I_L=0)}}{1 + k_{scaling(t_{vr})} I_L} \right] \qquad (9.6)$$

And:

$$\Phi_{d(TE)} = 2\pi f_c \left[R_G C_{iss} \ln\left(\frac{V_{GS}}{V_{GS(th)} + \frac{I_L}{g_{fs}}} \right) + \frac{0.8 t_{vf(I_L=0)}}{1 + k_{scaling(t_{vf})} I_L} \right] \qquad (9.7)$$

The complete solution describing the unit area for the combination of the error sources is achieved by substituting Eq. (9.5) into Eq. (2.12). Note that Eq. (9.5) is solved numerically.

Simulation Strategy

The simulation technique introduced in Section 2.5 will now be adapted to determine the spectrum of the combination model for TENPWM within Scenario ①. The remainder of this sub-section describes the alterations necessary to the ideal simulation strategy of Section 2.5 to represent the pulses with the added constraints. Figure 9.8 represents the pth pulse of a TENPWM waveform within the boundaries of inductor current Scenario ①, in which the non-zero values of $t_{d(vr)}$, $t_{d(vf)}$, t_{vr} and t_{vf} are included. Note that the rest of the parameters used correspond to those of the ideal case originally introduced in Figure 2.14.
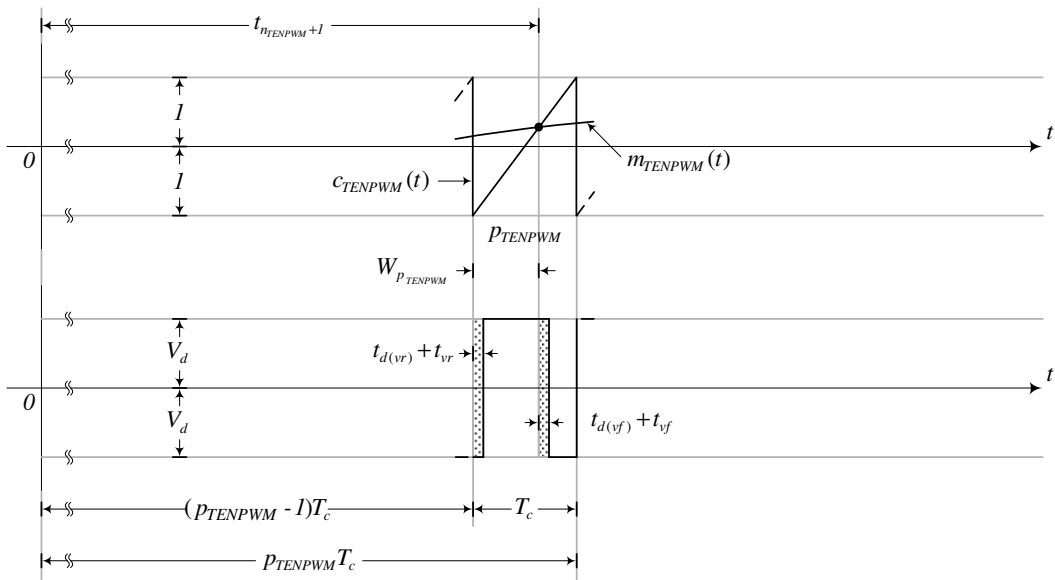
Figure 9.8: Combination simulation model for Scenario ①.

The ideal TENPWM model of Figure 2.14 can next be adapted to include the necessary delays shown in Figure 9.8. Firstly, the pulse width changes to:

$$W_{p_{TENPWM\,(combo)}} = W_{p_{TENPWM}} - \left[t_{d(vr)} + t_{vr} \right] + \left[t_{d(vf)} + t_{vf} \right]$$ (9.8)

The time shift of Eq. (2.94) is dependent on the pulse width and thus also needs to be adapted.

Substituting for Eq. (9.8) the time shift of Eq. (2.94) can be rewritten as:

$$t_0 = \left(p_{TENPWM} - 1 \right) T_c + \frac{W_{p_{TENPWM}} - \left[t_{d(vr)} + t_{vr} \right] + \left[t_{d(vf)} + t_{vf} \right]}{2} \tag{9.9}$$

Where the various delays $t_{d(vr)}$, $t_{d(vf)}$, t_{vr} and t_{vf} are respectively defined by Eq. (6.8), (6.3), (9.3) and (9.4).

### *Verification of the Proposed Analytical and Simulation Models*

The aim of this sub-section is to determine whether the proposed analytical and simulation models of the previous two sub-sections yield similar results. Figure 9.9 (a) was constructed using Eq. (9.5).

(a)   **(b)**
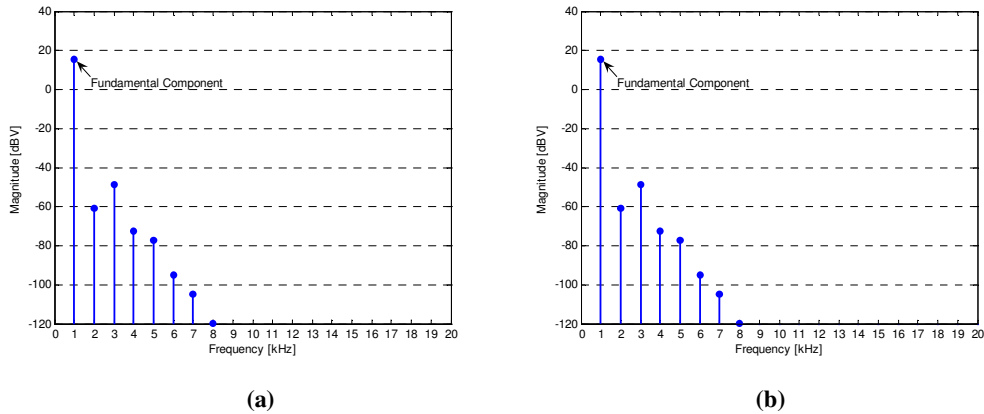
Figure 9.9: (a) Analytical (*m*=0) and (b) simulated baseband harmonics for TENPWM for *M*=0.2.

The simulation strategy was employed to construct the spectrum of Figure 9.9 (b). The variables used correspond to M=0.2, $t_{vr(I_L=0)}$=20ns, $t_{vf(I_L=0)}$=10ns, $k_{scaling(t_{vr})}$=0.5 and $k_{scaling(t_{vf})}$=1. It can be seen that the analytical and simulation results correlate very well.

9.3.2 INDUCTOR CURRENT SCENARIO ➁

The aim of this section is to construct the analytical and simulation models which describe the combined effect of the individual non-linearities within the boundaries of

Scenario ②. The non-ideal effects influencing distortion in this region are $t_{d(vr)}$, $t_{d(vf)}$, t_{vr}, t_{vf} and t_{dt}. However, before these models can be constructed, it is first necessary to consider the boundary between the two scenarios of the inductor current.
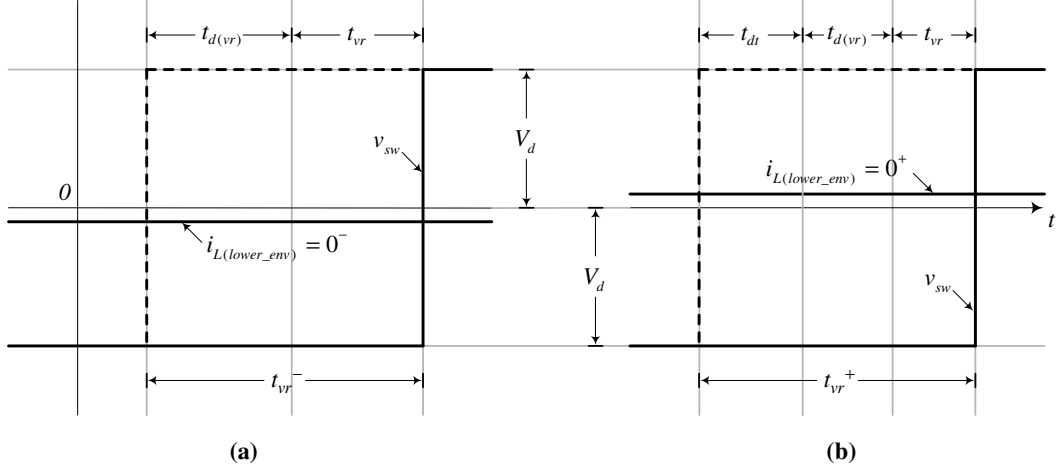
Figure 9.10: Rising egde transition at (a) $i_{L(lower\_env)}= 0^-$ and (b) $i_{L(lower\_env)}= 0^+$.

Figure 9.10 (a) illustrates the non-ideal effects governing the rising edge transition at the limit of the transition of $i_{L(lower\_env)}$ from negative to positive ($i_{L(lower\_env)}=0^-$). At this boundary the total delay, denoted by t_{vr}^-, describing the transition of the rising edge can be found from the equivalent time domain representation of Eq. (9.7) by substituting for $I_L=0$, which yields:

$$t_{vr}^{-} = R_G C_{iss} \ln\left(\frac{V_{GS}}{V_{GS(th)}}\right) + 0.8 t_{vr(I_L=0)} \tag{9.10}$$

The rising edge transition at the limit just after $i_{L(lower\_env)}$ changed polarity from negative to positive ($i_{L(lower\_env)}=0^+$) is shown in Figure 9.10 (b). Consider the expressions describing $t_{d(vr)}$ for a negative and positive inductor current, repectively defined by Eqs. (6.8) and (6.6). The difference in these delays at $I_L=0$, denoted by $t_{d(I_L=0)}$, is given by:

$$t_{d(I_L=0)} = R_G C_{iss} \ln\left(\frac{V_{GS} - V_{GS(th)}}{V_{GS(th)}}\right) \tag{9.11}$$

Thus, the transition of $i_{L(lower\_env)}$ from negative to positive causes an abrupt decrease in $t_{d(vr)}$. A typical value of $t_{d(I_L=0)}$ (using the parameters defined in Table 9.1) is in the vicinity of

6ns. This abrupt change in $t_{d(vr)}$ effectively decreases t_{dt}. Thus, in order to ensure a smooth transition between Scenario ① and Scenario ②, t_{vr}^+ must be equal to t_{vr}^-, which leads to the following definition of t_{vr} within Scenario ②:

$$t_{vr(I_L=0)} = t_{vr}^- - \left(t_{dt} + t_{d(vr)}\right) \tag{9.12}$$

Where t_{vr}^- is defined in Eq. (9.11), and $t_{d(vr)}$ given by Eq. (6.6). In a similar way, it can be shown that the abrupt change in $t_{d(vf)}$ decreases t_{dt} by adding a constant delay, defined in Eq. (9.11), to the trailing edge. The expression for t_{vf} within Scenario ② is given by:

$$t_{vf(I_L=0)} = t_{vf}^- - \left(t_{dt} + t_{d(vf)}\right) \tag{9.13}$$

Where:

$$t_{vf}^- = R_G C_{iss} \ln\left(\frac{V_{GS}}{V_{GS(th)}}\right) + 0.8 t_{vf(I_L=0)} \tag{9.14}$$

And $t_{d(vf)}$ is defined in Eq. (6.7). Figure 9.11 shows a typical variation of t_{vr} and t_{vf} over a complete cycle of the modulating waveform for M=0.8.

(a)   **(b)**
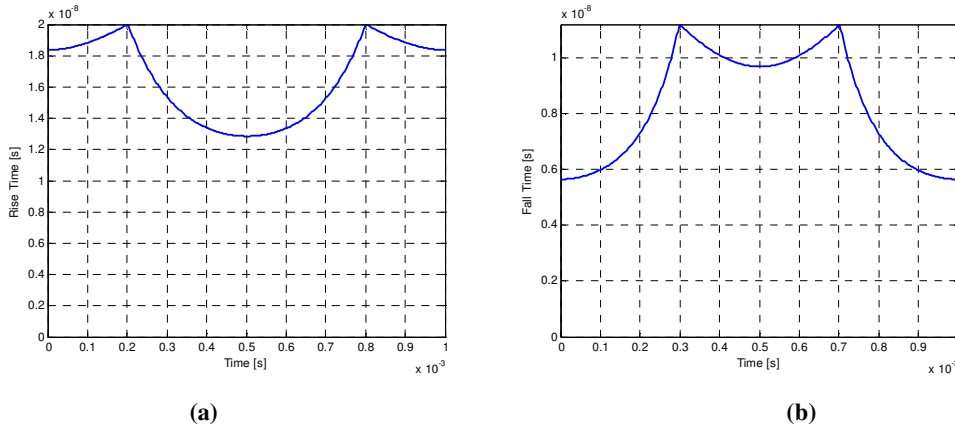
Figure 9.11: Variation in (a) t_{vr} and (b) t_{vf} over a complete cycle of the modulating waveform.

The discontinuities observed exist at the time instants when the inductor current changes polarity, which are governed by the boundary conditions just described.

Analytical Model

With the boundary conditions of the previous section in mind, the analysis in Chapter 3 can once again be applied to construct the 3-D unit area for the combination model within Scenario ②. This is shown in Figure 9.12.
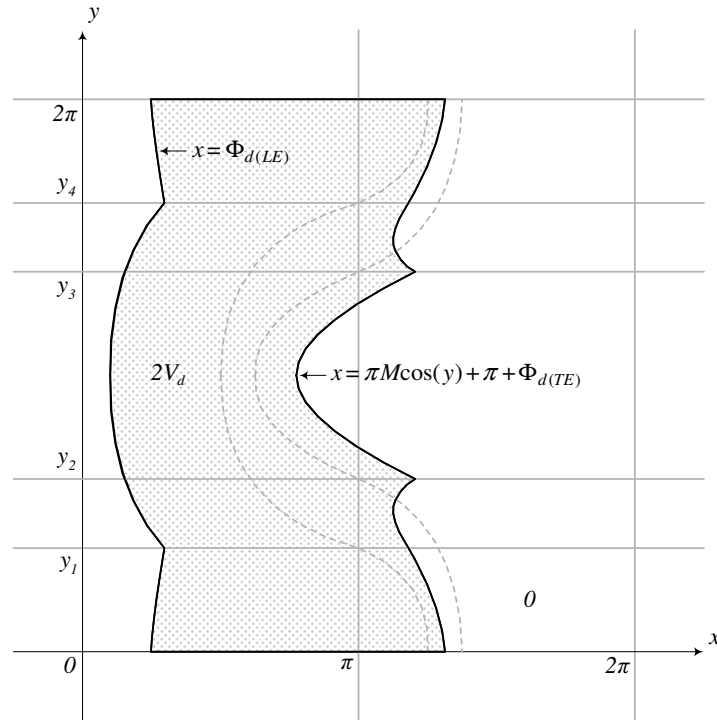
Figure 9.12: Combination 3-D unit area for TENPWM for Scenario ②.

By next inserting the limits defined in Figure 9.11, the complex Fourier coefficient of Eq. (2.15) can be written as:

$$C_{mn} = \frac{V_d}{\pi^2}\left[\int_0^{y_1}\left[\int_{\Phi_{d(LE)}}^{\pi+\pi M\cos(y)+\Phi_{d(TE)}} e^{j(mx+ny)}dx\right]dy + \int_{y_1}^{y_2}\left[\int_{\Phi_{d(LE)}}^{\pi+\pi M\cos(y)+\Phi_{d(TE)}} e^{j(mx+ny)}dx\right]dy\right.$$

$$+\int_{y_2}^{y_3}\left[\int_{\Phi_{d(LE)}}^{\pi+\pi M\cos(y)+\Phi_{d(TE)}} e^{j(mx+ny)}dx\right]+\int_{y_3}^{y_4}\left[\int_{\Phi_{d(LE)}}^{\pi+\pi M\cos(y)+\Phi_{d(TE)}} e^{j(mx+ny)}dx\right]dy+\int_{y_4}^{2\pi}\left[\int_{\Phi_{d(LE)}}^{\pi+\pi M\cos(y)+\Phi_{d(TE)}} e^{j(mx+ny)}dx\right]\right]$$

(9.15)

Where $\Phi_{d(LE)}$ is defined by Eq. (9.6) within the region $y_1 \leq y < y_4$, and $\Phi_{d(TE)}$ defined by Eq. (9.7) within intervals $0 \leq y < y_2$ and $y_3 \leq y < 2\pi$. For the remaining intervals:

$$\Phi_{d(LE)} = 2\pi f_c \left[R_G C_{iss} \ln\left(\frac{V_{GS}}{V_{GS} - V_{GS(th)} - \frac{I_L}{g_{fs}}}\right) + \frac{t_{vr(I_L=0)}}{1 + k_{scaling(t_{vr})} I_L} \right] \tag{9.16}$$

And:

$$\Phi_{d(TE)} = 2\pi f_c \left[R_G C_{iss} \ln\left(\frac{V_{GS}}{V_{GS} - V_{GS(th)} - \frac{I_L}{g_{fs}}}\right) + \frac{t_{vf(I_L=0)}}{1 + k_{scaling(t_{vf})} I_L} \right] \tag{9.17}$$

Note that $t_{vr(I_L=0)}$ is defined by Eq. (9.12), and $t_{vf(I_L=0)}$ defined by Eq. (9.14). The complete solution describing the unit area for the combination of the error sources is achieved by substituting Eq. (9.15) into Eq. (2.12). Eq. (9.15) is once again solved numerically.

Simulation Strategy

In this sub-section it will be shown how the simulation technique of Section 2.5 can be adapted to accommodate the additional constraints introduced within Scenario ②.

Figure 9.13: Combination simulation model for Scenario ②, (a) $i_{L(lower\_env)} > 0$ and (b) $i_{L(upper\_env)} < 0$.

Figure 9.13 represents the pth pulse of a TENPWM waveform within the boundaries of inductor current Scenario ②. In addition to the ideal case, non-zero values of $t_{d(vr)}$, $t_{d(vf)}$, $t_{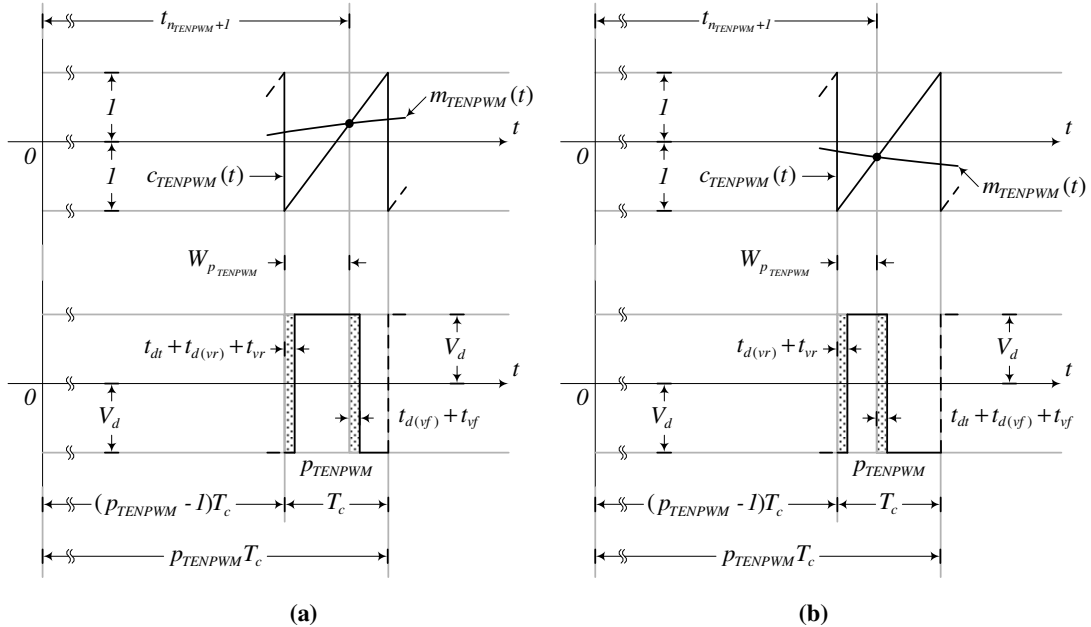vr}$, t_{vf} and t_{dt} are included. The rest of the parameters correspond to those of the ideal case originally introduced in Figure 2.14. The pulse width of the ideal TENPWM model shown in Figure 2.14 can be adapted to include the necessary delays. In the region where $i_{L(lower\_env)}>0$, shown in Figure 9.13 (a), the pulse width changes to:

$$W_{P_{TENPWM\,(combo)}} = W_{P_{TENPWM}} - \left[t_{dt} + t_{d(vr)} + t_{vr} \right] + \left[t_{d(vf)} + t_{vf} \right] \tag{9.18}$$

The time shift of Eq. (2.94) can be defined by substituting for Eq. (9.18), which yields:

$$t_0 = \left(p_{TENPWM} - 1 \right) T_c + \frac{W_{P_{TENPWM}} - \left[t_{dt} + t_{d(vr)} + t_{vr} \right] + \left[t_{d(vf)} + t_{vf} \right]}{2} \tag{9.19}$$

In the region where $i_{L(upper\_env)}<0$, illustrated in Figure 9.13 (b), the pulse width is given by:

$$W_{P_{TENPWM\,(combo)}} = W_{P_{TENPWM}} - \left[t_{d(vr)} + t_{vr} \right] + \left[t_{dt} + t_{d(vf)} + t_{vf} \right] \tag{9.20}$$

While the time shift of Eq. (2.94) can be found by substituting for Eq. (9.21). This gives:

$$t_0 = \left(p_{TENPWM} - 1 \right) T_c + \frac{W_{P_{TENPWM}} - \left[t_{d(vr)} + t_{vr} \right] + \left[t_{dt} + t_{d(vf)} + t_{vf} \right]}{2} \tag{9.21}$$

Verification of the Proposed Analytical and Simulation Models

In this sub-section the results of the proposed analytical and simulation models for inductor current Scenario ② will be compared to each other. The spectrum shown in Figure 9.14 (a) was constructed from the analytical solution of Eq. (9.15), while the spectrum illustrated in (b) was constructed from the proposed simulation method. The parameters used correspond $t_{vr(I_L=0)}=20$ns, $t_{vf(I_L=0)}=10$ns, $k_{scaling(t_{vr})}=0.5$, $k_{scaling(t_{vf})}=1$ and $M=0.8$. The analytical spectrum only considered the baseband harmonics, i.e. $m=0$. The simulation of Figure 9.14 (b), which allows for phasor summation of the various harmonics, produced similar results. For the given variables, this suggests that the modulation products are negligible.

(a)   **(b)**
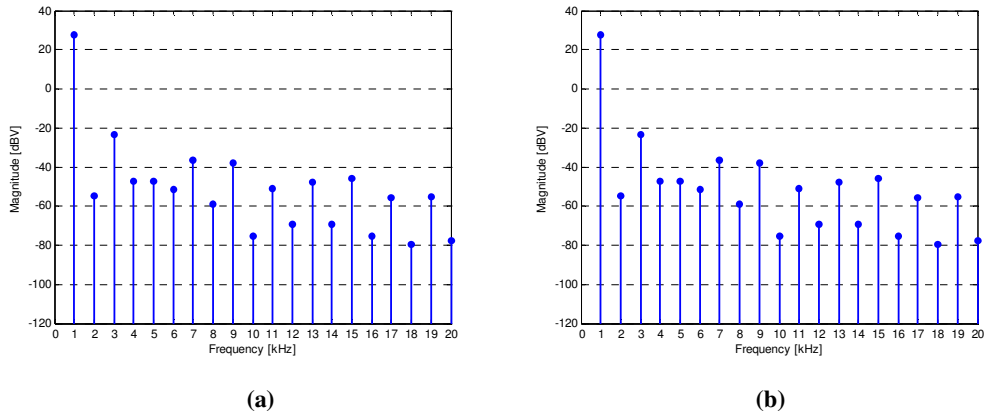
Figure 9.14: (a) Analytical (*m*=0) and (b) simulated baseband harmonics for TENPWM for *M*=0.8.

9.4   EXPERIMENTAL VERIFICATION

In this section the combination model of Section 9.3 is verified experimentally. Table 9.2 contains a brief description of the physical devices, as well as the measurement equipment used. Note that PNPWM is generated from the source, which is a field programmable grid array (FPGA). The remaining circuit parameters correspond to those defined in Table 9.1.

TABLE 9.2

PRACTICAL DEVICE DESCRIPTION AND MEASUREMENT SETUP.

Device Description	Manufacturer	Model Number
PWM Source	Altera®	EP3C25Q240C8NES
Gate Driver IC	International Rectifier®	IRS20124(S)PbF
MOSFET	International Rectifier®	IRFI4019H-117P
Measurement System	Audio Precision®	SYS-2722
AES17 Filter	Audio Precision®	AUX-0025

Figure 9.15 (a) is a measurement of THD+N vs. *M*. The corresponding simulation is shown in Figure 9.15 (b). The voltage rise- and fall times used for the simulation were measured as described in Section 9.2.3, i.e. with the output demodulation filter disconnected. These values correspond to $t_{vr(I_L=0)}$=25ns and $t_{vf(I_L=0)}$=14ns. The scaling variables $k_{scaling(t_{vr})}$ and $k_{scaling(t_{vf})}$ were determined iteratively as $k_{scaling(t_{vr})}$=0.17 and $k_{scaling(t_{vf})}$=0.30.
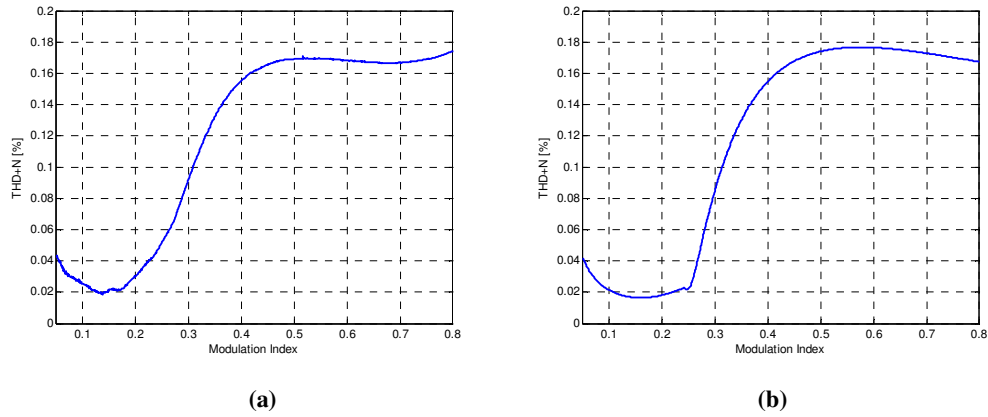
Figure 9.15: THD+N vs. *M* determined by (a) measurement and (b) simulation.

Note that, for the parameters defined in Table 9.1, the boundary between Scenario ① and Scenario ② is in the vicinity of *M*=0.25. At low values of the modulation index (up to *M*=0.15), noise dominates the THD+N measurement. The distortion resulting from the non-linear current modulation of $t_{d(vr)}$, $t_{d(vf)}$, t_{vr} and t_{vf} becomes more dominant than noise above *M*=0.15. Once Scenario ② is entered, distortion increases rapidly. Since t_{vr} and t_{vf} decreases as the current increases, the dead time is effectively phased in during the interval 0.25<*M*<0.45, and hence the ramp in THD+N. Since the switching times t_{vr} and t_{vf} are described by hyperbolic functions, the decrease in switching time will become less affected by an increasing current. This is observed at *M*>0.45. Figure 9.16 shows a comparison between a series of measured and simulated spectra at various values of *M*.

(a) Measurement: *M*=0.2.   **(b) Simulation: *M*=0.2.**

(c) Measurement: *M*=0.4.   **(d) Simulation: *M*=0.4**

(e) Measurement: *M*=0.6.   **(f) Simulation: *M*=0.6.**

(g) Measurement: *M*=0.8.   **(h) Simulation: *M*=0.8.**
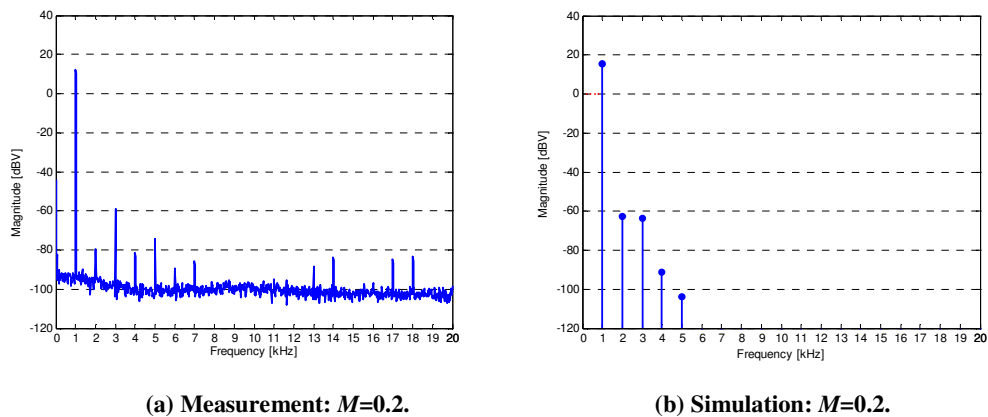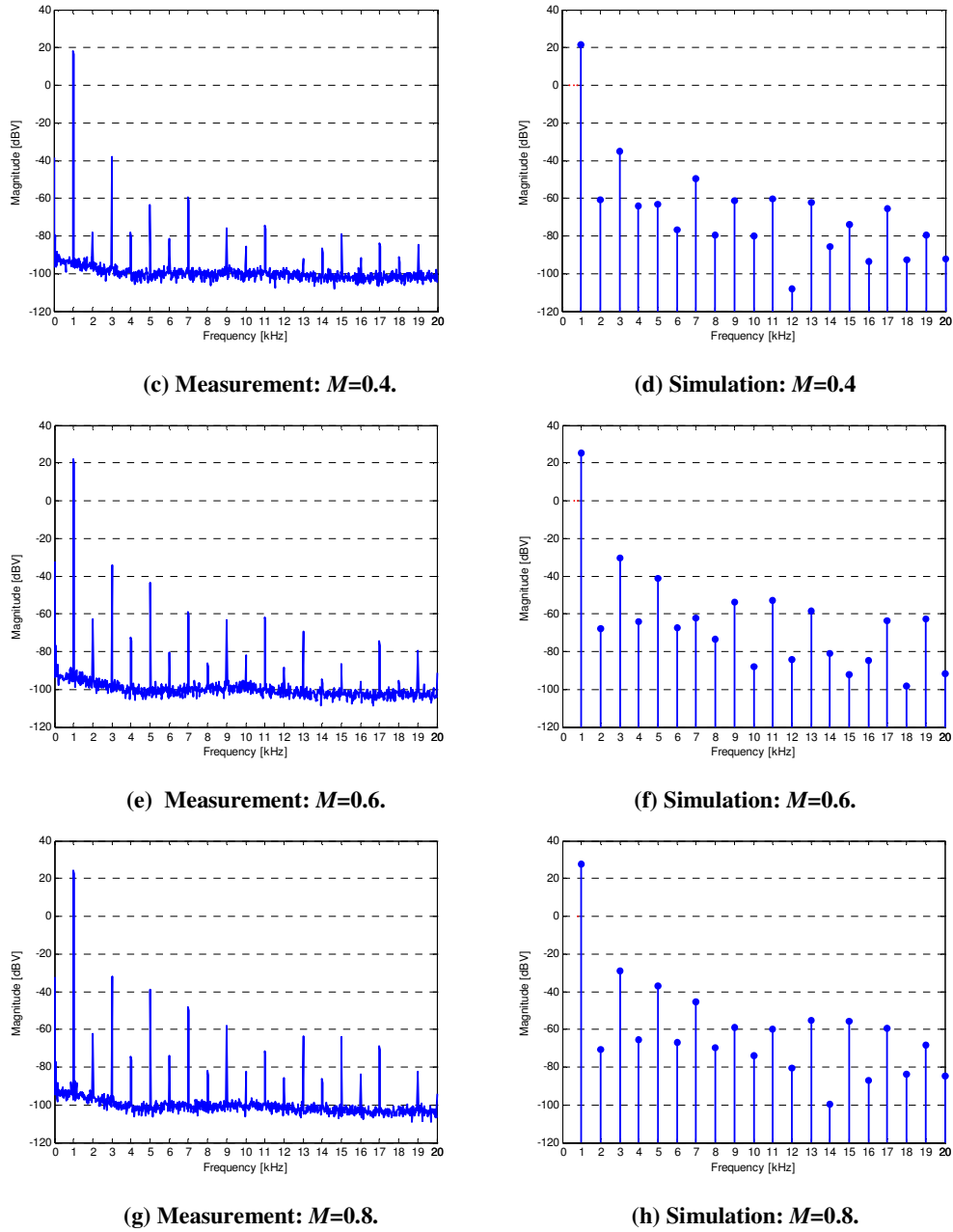
Figure 9.16: Various measured and simulated spectra.

Figure 9.17 (a) shows the duty cycle error introduced over one cycle of the modulating waveform for *M*=0.2, i.e. for Scenario ①. As mentioned, in this region the error is a result of the non-linear current modulation of $t_{d(vr)}$, $t_{d(vf)}$, t_{vr} and t_{vf}.

(a)   **(b)**
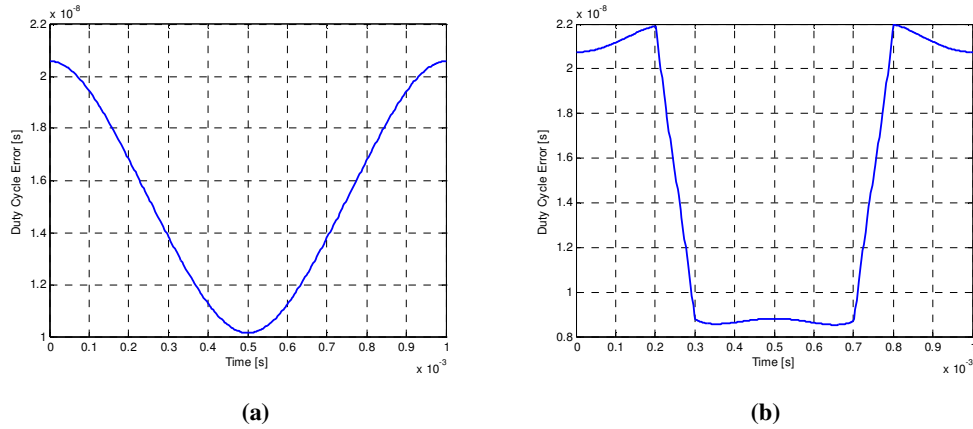
Figure 9.17: Duty cycle error for (a) *M*=0.2 and (b) *M*=0.8.

Figure 9.17 (b) shows the duty cycle error for *M*=0.8. The discontinuity observed is a result of the change in current polarity. Figure 9.18 (a) illustrates measurements of THD+N vs. *M* for various values of L_{filt}. Figure 9.18 (b) shows the corresponding simulation. The scaling variables used to construct the simulation are shown in Table 9.3.

(a)   **(b)**
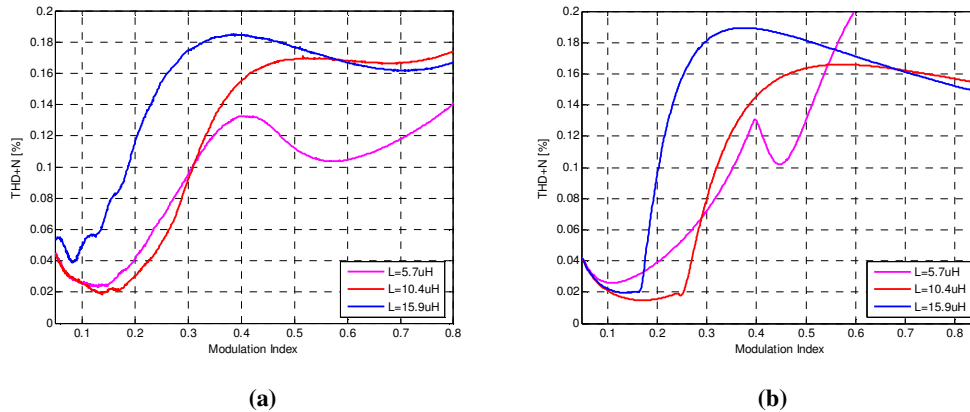
Figure 9.18: THD+N vs. *M* determined by (a) measurement and (b) simulation for various L_{filt}.

Consider the curves for L_{filt}=5.7µH. The boundary between Scenario ① and Scenario ② is in the vicinity of *M*=0.4. The decrease in distortion within this region is a result of the symmetry between the rising edge and falling edge. This condition only occurs at the boundary of Scenario ① and Scenario ②. The difference in results achieved can be ascribed to the switching node capacitance, which has been omitted from the analysis.

TABLE 9.3

DEFINITION OF THE SCALING VARIABLES FOR VARIOUS L_{filt}.

L_{filt}=5.7 µH	L_{filt}=10.4 µH	L_{filt}=15.9 µH
$k_{scaling(t_{vf})}$=0.65	$k_{scaling(t_{vf})}$=0.30	$k_{scaling(t_{vf})}$=0.35
$k_{scaling(t_{vr})}$=0.36	$k_{scaling(t_{vr})}$=0.17	$k_{scaling(t_{vr})}$=0.20

9.5 SUMMARY

This chapter verified the theory that was proposed in Chapters 5 to 8. A brief overview of the individual non-ideal effects was considered, after which an analytical and simulation model describing the combination of the individual non-ideal effects were constructed. The proposed model was compared to practical measurements.

The proposed model's results correlated well with the practical measurements. The deviation from the practical measurement is a result of the switching node capacitance, which has been omitted in this dissertation.
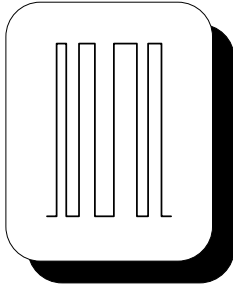
10

CONCLUSIONS AND

FUTURE WORK

10.1 INTRODUCTION

This chapter contains a brief summary of the findings, contributions and conclusions of the analysis which was performed in this dissertation.

10.2 A FUNDAMENTAL ANALYSIS OF PWM

A fundamental analysis of PWM was performed in Chapter 2. Basic modulation methods were introduced, after which the double Fourier series method of analysis for calculating the spectrum of PWM analytically was reviewed.

A simulation strategy, based on Newton's numerical method, was introduced which allows for rapid, accurate calculation of the spectrum of NPWM. Simulations were performed for ideal TENPWM, which produced exactly the same results as the analytical computation.

10.3 INCORPORATION OF PTEs IN THE DOUBLE FOURIER SERIES METHOD

In Chapter 3 a general analytical tool has been developed, which allows for the incorporation of non-ideal effects within W.R. Bennet's [11] method. As a starting point, the analysis introduced in [22] was generalized.

It was shown how a constant time delay can be incorporated into the 3-D unit area. The analysis was then extended to include a purely sinusoidal current polarity, as well as a magnitude dependency. Finally, a more realistic inductor current model with a non-zero ripple component was considered. The proposed analysis was verified by simulation.

10.4   SWITCHING DEVICE CHARACTERISTICS

In Chapter 4, an overview of the power MOSFET's structure, operation and dynamic characteristics were considered. The non-ideal switching operation within a single phase leg, summarized from [32], was considered in the final part of this chapter.

10.5   THE EFFECT OF DEAD TIME

A detailed analysis of the isolated effect of dead time was performed in Chapter 5. The analysis started off with an overview of its well-known effect, after which an analytical model based on the double Fourier series method of analysis was introduced for TENPWM. This model allows for the filter inductor and switching frequency to be parsed as parameters. The analytical solutions were verified by simulation.

It was shown that the dead time produces even, as well as odd order harmonics within the audible band. It was shown that the former harmonics are a result of the modulation products, i.e., the sideband switching harmonics. It was also shown that, for a specific dead time, an optimum distortion level can be established by varying the filter inductance.

10.6   THE EFFECT OF THE MOSFET TURN-ON AND TURN-OFF DELAYS

The detailed analysis in Chapter 6 considered the isolated effect of the MOSFET turn-*on* and turn-*off* delays on harmonic distortion. A simulation model was introduced in which well-known analytical solutions [24], [28] describing these delays were incorporated.

The simulation results obtained for TENPWM showed that distortion arise as a result of two mechanism, of which the first is non-linear current modulation. The second mechanism arise due to the abrupt change in these delays upon a change in current polarity, resulting in an effect similar to dead time.

10.7   THE EFFECT OF NON-ZERO, NON-LINEAR SWITCHING TRANSITIONS

The sole effect of non-zero linear, as well as non-zero non-linear switching transitions were considered in Chapter 7. The analysis included a linear model based on well-known analytical expressions [24], [28] as well as a newly proposed non-linear model based on an

approximation of the non-linear v_{DS} vs. C_{GD} curve of a specific power MOSFET. A closed form solution describing the switching curve was obtained, after which a simulation model was constructed.

It was shown that switching transitions within inductor current Scenario ② results much higher levels of distortion than Scenario ① due to the abrupt change in transition times upon a change in current polarity. It was also shown that the THD increases for increasing switching times. The sideband harmonics contribute to distortion within the baseband for Scenario ②. The proposed non-linear model resulted in much higher levels of distortion than the linear model for both cases of the inductor current.

10.8   THE EFFECT OF PARASITICS AND REVERSE RECOVERY

Chapter 8 considered the effects of the parasitics and reverse recovery on harmonic distortion. The analysis made use of an existing solution to model the overvoltage and undervoltage ringing effect. A simulation model was constructed for TENPWM, after which the results were considered for a half-bridge topology. It was shown that, for both scenarios of the inductor current, that the PAE introduces is negligible compared to the PTEs considered in Chapters 5 to 7.

10.9   COMBINATION MODEL AND EXPERIMENTAL VERIFICATION

The theory that was proposed in Chapters 5 to 8 was verified in Chapter 10. An analytical and simulation model describing the combination of the individual non-ideal effects were constructed. The proposed model was compared to practical measurements. The proposed model's results correlated well with the practical measurements. The deviation from the practical measurement is a result of the switching node capacitance, which has been omitted in this dissertation.

10.10 FUTURE WORK

A method has been introduced in which the harmonic composition of the output stage in the presence of PTEs can be determined. The analysis should be extended to include

amplitude errors. The interaction of the non-linear switching node capacitance with the MOSFET's switching characteristic should be established, as well as the effect of the non-linear on-state resistance.

REFERENCES

[1]   M. Streitenberger, H. Bresch, W. Mathis, "*Theory and Implementation of a New Type of Digital Power Amplifiers for Audio Applications*", IEEE International Symposium on Circuits and Systems, May 2000.

[2]   D. Dapkus, "*Class-D Audio Amplifiers: An Overview*", IEEE Proc. Electronics Letter, 2000.

[3]   D. Dapkus, K. Han, "*Utilizing Class-D Audio Power Amplifiers for High Efficiency*", Conference Proc. International IC-Korea.

[4]   Bruno Putzeys, "*Digital Audio's Final Frontier*", IEEE Spectrum, March 2003.

[5]   M. Sandler, "*Digital Amplification for Consumer Audio*", IEEE Proc. Electronics Letter, 2000.

[6]   M.B. Sandler, "*Towards a Digital Audio Amplifier*", 76th AES Convention, October 1984.

[7]   M.B. Sandler, "*Progress Towards a Digital Audio Amplifier*", 80th AES Convention, March 1986.

[8]   J. Varona, "*Power Digital-to-Analog Conversion using Sigma-Delta and Pulse Width Modulations*", Electronics Letter, ECE1371 Analog Electronics II.

[9]   J.M. Goldberg, M.B. Sandler, "*Noise Shaping and Pulse-Width Modulation for an All-Digital Audio Power Amplifier*", AES Publication, Vol. 39, 1990, p. 449-460.

[10]   A.J. Magrath, I.G. Clark, M.B. Sandler, "*Design and Implementation of a FPGA Sigma-Delta Power DAC*", IEEE Press, 1997, p. 511-520.

[11]   W.R. Bennet, "*New results in the calculation of modulation of products*" Bell Systems Technical Journal, 1933, Vol. 12, pp. 228-243.

[12]   C. Pascual, Z. Song, P.T. Krein, D.V. Sarwate, P. Midya, W.J. Roeckner, "*High-Fidelity PWM Inverter for Digital Audio Amplification: Spectral Analysis, Real-Time DSP Implementation, and Results*" IEEE Transactions on Power Elctronics, Vol. 18, No. 1, January 2003.

[13]   D. Grahame Holmes, Thomas A. Lipo, *Pulsewidth Modulation for Power Converters*, Wiley-IEEE Press, October 3, 2003.

[14]   M.T. Tan, J.S. Chang, C. Chua, B.H. Gwee, "*An Investigation Into the Parameters Affecting Total Harmonic Distortion in Low–Voltage Low-Power Class-D Amplifiers*",

IEEE Transactions on Circuits and Systems, Fundamental Theory and Applications, Vol. 50, No. 10, October 2003, p. 1304-1315.

[15] Karsten Nielsen, "*Linearity and Efficiency Performance of Switching Audio Power Amplifier Output Stages – A Fundamental Analysis*", 105th AES Convention, San Francisco, September 1998.

[16] K. Nielsen, "*PEDEC – A Novel Pulse Referenced Control Method for High Quality Digital PWM Switching Power Amplification*" IEEE Proc. On Power Electronics, 1998, p. 200-207.

[17] Harold S. Black, *Modulation Theory*, D. van Nostrand Company, 1953, pp. 263-281.

[18] S.R. Bowes, "*New Sinusoidal Pulsewidth Modulated Invertor*", Proceedings of IEE, Vol. 122, No. 11, November 1975, pp. 1279-1285.

[19] S.R. Bowes, and B. Bird, "*Novel approach to the analysis and synthesis of modulation processes in power converters.*" Proceedings IEE, May 1975, Vol. 122, No. 5, pp. 507-513.

[20] D.G. Holmes, "*A General Analytical Method for Determining the Theoretical Harmonic Components of Carrier Based PWM Strategies*", IEEE Conference Records, Inductry Applications Society Annual Meeting, Mexico City, Mexico, 1998, pp. 1207-1214.

[21] Z. Song and D.V. Sarwate, "*The Frequency Spectrum of Pulse Width Modulated Signals*," Submitted to Signal Processing, 2002.

[22] C.M. Wu, Wing–Hong Lau, Henry Shu–hung Chung, "*Analytical Technique for Calculating the Output Harmonics of an H–Bridge Inverter with Dead-Time*" IEEE Transactions on Circuits and Systems – I: Fundamental Theory and Applications, Vol. 46, No. 5, May 1999, pp. 617–627.

[23] F. Koeslag, H. du T. Mouton, H.J. Beukes and P. Midya, "*A Detailed Analysis of the Effect of Dead Time on Harmonic Distortion in a Class D Audio Amplifier*", Africon 2007, Windhoek, Namibia, 26-28 October 2007.

[24] Mohan, Undeland, Robbins, *Power Electronics*, John Wiley & Sons, Inc. 1989, pp. 236-239, pp. 571-595.

[25] I.D. Mosely, P.H. Mellor, C.M. Bingham, "*Effect of Dead Time on Harmonic Distortion in Class–D Audio Power Amplifiers*", IEE Proc. Electronics Letters, Vol. 35, No. 12, 15 April 1999.

[26] Tony O'Gorman, "*Discrete Fourier Transform Harmonic Analysis of Digitally Generated PWM Waveforms Which are Distorted by Switch Dead Time*", Inductrials Applications Conference, October 2000, Vol. 4, pp. 2197–2204.

[27] Marco Berkhout, "*A Class-D Output Stage with Zero Dead Time*", ISSCC 2003, Session 7, DACs and Amps, Paper 7.5.

[28] B. Jayant Baliga, *Modern Power Devices*, John Wiley & Sons, Inc. 1987, pp. 263-343.

[29] Flemming Nyboe, Lars Risbo, Petro Andreani, "*Time Domain Analysis of Open Loop Distortion in Class D Amplifier Output Stages*", 27th AES International Conference, Copenhagen, Denmark, September 2005.

[30] Y. Xiao, H. Shah, T.P. Chow, R.J. Gutmann, "*Analytical Modeling and Experimental Evaluation of Interconnect Parasitic Inductance on MOSFET Switching Characteristics*", IEEE Trans. Electronics Letter, 2004.

[31] W. Teulings, J.L. Schanen, J. Roudet, "MOSFET Switching Behaviour Under Influence of PCB Stray Inductance", IEEE Trans. Electronics Letter, 1996.

[32] K. Nielsen, "*Audio Power Amplifier Techniques With Energy Efficient Power Conversion*", Ph.D. Dissertation, Technical University of Denmark, April 30, 1998.

[33] F. Nyboe, "*IC design of Switching Power Stages for Audio Power Amplification*", Ph.D. Dissertation, Technical University of Denmark, August 2006.

[34] F. Koeslag, H. du Toit Mouton, H.J. Beukes, "*Analytical Calculation of the Output Harmonics in a Power Electronic Inverter with Current Dependent Pulse Timing Errors*", Submitted to Journal.

[35] H. du T. Mouton, "*Electronics 414 Notes*", University of Stellenbosch, South Africa.

[36] Simon Haykin, *An Introduction to Analog and Digital Communications*, John Wiley & Sons, Inc. 1989, pp. 259-260.

[37] Germund Dahlquist, *Numerical Methods*, Prentice-Hall, Inc. 1974, pp. 218, 222-227.

[38] Paul F. Hultquist, *Numerical Methods*, The Benjamin/Cummings Publishing Company, Inc. 1988, pp. 96-101.

[39] Richard W. Daniels, *An Introduction to Numerical Methods and Optimization Techniques*, Elsevier North-Holland, Inc. 1978, pp. 43-50.

[40] Simon Haykin, *An Introduction to Analog and Digital Communications*, John Wiley & Sons, Inc. 1989, pp. 13-81.

[41] H.L. Royden, *Real Analysis,* Prentice Hall, 1988, pp. 81-89.

[42] César Pascaul, Zukui Song, Philip T. Krein, Dilip V. Sarwate, "*High-Fidelity PWM Inverter for Audio Amplification Based On Real-Time DSP*", June 19, 2002.

[43] Seung–Gi Jeong, Min–Ho Park, "*The Analysis and Compensation of Dead–Time Effects in PWM Inverters*", IEEE Transactions on Industrial Electronics, Vol. 38, No. 2, April 1991, pp. 108–114.

[44] Alejandro R. Olivia, Simon S. Ang, Juan C. Balda, Héctor G. Chiacchiarini, "*Harmonic Distortion Reduction in Power Inverters*", 35th Annual IEEE Power Electronics Specialists Conference, Vol. 2, 2004, pp. 1226–1231.

[45] Gaël Pillonnett, Nacer Abouchi, Philippe Marguery, "*Reduction of Power Stage THD by Adding Output Capacitance*", 27th AES International Conference, Copenhagen, Denmark, September 2005.

[46] F. Koeslag, H. du Toit Mouton, H.J. Beukes, "*An Investigation into the Separate and Combined Effect of Pulse Timing Errors on Harmonic Distortion in a Class D Audio Amplifier*", 39th Annual IEEE Power Electronics Specialists Conference (PESC), Rhodes, Greece, June 2008.

[47] F. Koeslag, H. du T. Mouton and H.J. Beukes, "*The Isolated Effect of Finite Non-Linear Switching Transitions on Harmonic Distortion in a Class D Audio Amplifier*", 17th South African Universities Power Engineering Conference (SAUPEC), Durban, South Africa, January 2008.

[48] IRFI4019H-117P Datasheet, International Rectifier.

APPENDIX 1: MATHEMATICAL RELATIONSHIPS

1.1 JACOBI-ANGER EXPANSIONS

The Jacobi-Anger expansion is given by:

$$e^{\pm j\xi\cos\theta} = \sum_{k=-\infty}^{\infty} j^{\pm k} J_k(\xi) e^{jk\theta} \tag{A1.1}$$

Rewriting Eq. (A1.1) for positive values of k:

$$e^{\pm j\xi\cos\theta} = J_0(\xi) + 2\sum_{k=1}^{\infty} j^{\pm k} J_k(\xi) \cos(k\theta) \tag{A1.2}$$

1.2 BESSEL FUNCTION INTEGRAL RELATIONSHIPS

Multiplying the Jacobi-Anger expansion in Eq. (A1.1) by $e^{jn\theta}$ and integrating over an interval bounded by arbitrary points a and b gives:

$$\int_a^b e^{\pm j\xi\cos\theta} e^{jn\theta} d\theta = \sum_{k=-\infty}^{\infty} j^{\pm k} J_k(\xi) \int_a^b e^{j(n+k)\theta} d\theta \tag{A1.3}$$

Evaluating the integral on the right-hand side of Eq. (A1.3) for $n = -k$, the following expression can be derived:

$$\int_a^b e^{\pm j\xi\cos\theta} e^{jn\theta} d\theta = (b-a) \sum_{k=-\infty}^{\infty} j^{\pm k} J_k(\xi) \tag{A1.4}$$

Integrating Eq. (A1.3) for the remaining condition when $n \neq -k$ gives:

$$\int_a^b e^{\pm j\xi\cos\theta} e^{jn\theta} d\theta = \sum_{k=-\infty}^{\infty} j^{\pm k} J_k(\xi) \frac{\left[e^{j(n+k)b} - e^{j(n+k)a} \right]}{j(n+k)} \tag{A1.5}$$

Next, consider the integration of Eq. (A1.3) over a 2π interval:

$$\int_0^{2\pi} e^{\pm j\xi\cos\theta} e^{jn\theta} d\theta = \sum_{k=-\infty}^{\infty} j^{\pm k} J_k(\xi) \int_0^{2\pi} e^{j(n+k)\theta} d\theta \tag{A1.6}$$

The integral on the right-hand side of Eq. (A1.6) integrates to a non-zero term only when $n = -k$. Evaluating for this condition and substituting for k, Eq. (A1.6) can be written for $-\infty < n < \infty$ as:

$$\int_0^{2\pi} e^{\pm j\xi\cos\theta} e^{jn\theta} d\theta = 2\pi j^{\pm n} J_n(\xi) \tag{A1.7}$$

The solution of Eq. (A1.7) is valid for all positive and negative integer values of n. Next, consider the product of Eq. (A1.2) and $e^{jn\theta}$ for all positive integer values of n including zero, integrated over an arbitrary interval bounded by points a and b:

$$\int_a^b e^{\pm j\xi\cos\theta} e^{jn\theta} d\theta = J_0(\xi) \int_a^b e^{jn\theta} d\theta + 2\sum_{k=1}^{\infty} j^{\pm k} J_k(\xi) \int_a^b \cos(k\theta) e^{jn\theta} d\theta \tag{A1.8}$$

Evaluating Eq. (A1.8) for the particular case when $n = 0$:

$$\int_a^b e^{\pm j\xi\cos\theta} d\theta = (b-a) J_0(\xi) + 2\sum_{k=1}^{\infty} j^{\pm k} J_k(\xi) \frac{\left[\sin(bk) - \sin(ak)\right]}{k} \tag{A1.9}$$

Consider the integration of Eq. (A1.8) over a 2π interval. Rewriting the expression yields:

$$\int_0^{2\pi} e^{\pm j\xi\cos\theta} e^{jn\theta} d\theta = J_0(\xi) \int_0^{2\pi} e^{jn\theta} d\theta + 2\sum_{k=1}^{\infty} j^{\pm k} J_k(\xi) \int_0^{2\pi} \cos(k\theta) e^{jn\theta} d\theta \tag{A1.10}$$

Evaluating Eq. (A1.10) for the particular case where $n = 0$, the second term on the right-hand side integrates to zero. The expression simplifies to:

$$\int_0^{2\pi} e^{\pm j\xi\cos\theta} d\theta = 2\pi J_0(\xi) \tag{A1.11}$$

1.3 SINE AND COSINE BESSEL FUNCTION RELATIONS

Sine Relation:

$$\sin(z\sin\theta) = 2\sum_{n=1}^{\infty} J_{2n+1}(z)\sin\left[(2n+1)\theta\right] = \sum_{n=-\infty}^{\infty} J_n(z)\sin(n\theta) \tag{A1.12}$$

Cosine Relation:

$$\cos(z\sin\theta) = J_0(z) + 2\sum_{n=1}^{\infty} J_{2n}(z)\cos(2n\theta) = \sum_{n=-\infty}^{\infty} J_n(z)\cos(n\theta) \tag{A1.13}$$

1.4 TRIGONOMETRIC IDENTITIES

Product relations:

$$\sin a \sin b = \frac{1}{2}\left[\cos(a-b) - \cos(a+b)\right] \tag{A1.14}$$

$$\cos a \cos b = \frac{1}{2}\left[\cos(a-b) + \cos(a+b)\right] \tag{A1.15}$$

$$\sin a \cos b = \frac{1}{2}\left[\sin(a+b) + \sin(a-b)\right] \tag{A1.16}$$

$$\cos a \sin b = \frac{1}{2}\left[\sin(a+b) - \sin(a-b)\right] \tag{A1.17}$$

Sum and difference relations:

$$\sin a + \sin b = 2\sin\left(\frac{a+b}{2}\right)\cos\left(\frac{a-b}{2}\right) \tag{A1.18}$$

$$\sin a - \sin b = 2\cos\left(\frac{a+b}{2}\right)\sin\left(\frac{a-b}{2}\right) \tag{A1.19}$$

$$\cos a + \cos b = 2\cos\left(\frac{a+b}{2}\right)\cos\left(\frac{a-b}{2}\right) \tag{A1.20}$$

$$\cos a - \cos b = -2\sin\left(\frac{a+b}{2}\right)\sin\left(\frac{a-b}{2}\right) \tag{A1.21}$$